WIND ENERGY AND POWER SYSTEM INTERCONNECTION, CONTROL, AND OPERATION FOR HIGH PENETRATION OF WIND POWER

A Dissertation
Presented to
The Academic Faculty

By

Jiaqi Liang

In Partial Fulfillment
Of the Requirements for the Degree
Doctor of Philosophy in the
School of Electrical and Computer Engineering

Georgia Institute of Technology
May 2012

WIND ENERGY AND POWER SYSTEM INTERCONNECTION, CONTROL, AND OPERATION FOR HIGH PENETRATION OF WIND POWER

Approved by:

Dr. Ronald G. Harley, Advisor
School of Electrical and Computer Engineering
Georgia Institute of Technology

Dr. David G. Taylor
School of Electrical and Computer Engineering
Georgia Institute of Technology

Dr. Thomas G. Habetler
School of Electrical and Computer Engineering
Georgia Institute of Technology

Dr. Ganesh K. Venayagamoorthy
Department of Electrical and Computer Engineering
Clemson University

Dr. Santiago Grijalva
School of Electrical and Computer Engineering
Georgia Institute of Technology

Date Approved: March 01, 2012

This dissertation is dedicated to

my mother and my wife

ACKNOWLEDGEMENTS

Many people have come into my life, helped and supported me in every way during my study at Georgia Tech. Without you, it would not have been possible for me to finish this long journey.

I would like to express my deepest gratitude to my advisor, Dr. Ronald G. Harley. His constant support and guidance have been invaluable. He has helped me grow technically and professionally. His patience, understanding, and humor have made this journey a much easier one for me.

I have the greatest respect and gratitude to all the faculty members and staff, from inside or outside of Georgia Tech, whom I have had the privilege to work with. I owe a lot to Dr. José A. Restrepo, who generously offered me his hardware experience and support remotely from Venezuela. I would like to thank Dr. Ganesh K. Venayagamoorthy for his invaluable help and technical advices throughout my PhD study. Dr. Deepak M. Divan, Dr. Thomas G. Habetler, and Dr. Santiago Grijalva are faculty members in the power group who have inspired me so much and brought to me different angles of power engineering. I would like to thank Dr. David G. Taylor for serving on my PhD proposal and defense committee and providing me with insightful suggestions. I would also like to extend my gratitude to Ms. Deborah King for being so patient and helping me with the numerous room reservations and lab orders.

My friends and student colleagues at Georgia Tech, especially those in the power group, have been an enormous source of energy, support, and inspiration. I would like to thank all of you for all the great moments. Siwei Cheng, Xueliang Huo, Yi Du, Jing Dai, Pinjia Zhang, Qin Sun, Yao Duan, Yi Yang, Liang Du, Dawei He, Evangelos Farantatos, Dustin Howard,

Diogenes Molina, Frank Kreikebaum, Sangtaek Han, Harjeet Johal, R. Prasad Kandula, Rohit Moghe, Jorge E. Hernández, and Debrup Das are a few friends among the many who I want to express my special thanks for their help, friendship, and kindness.

I would like to thank my mother, Feiyan Lai, who has always believed in me and gave me my strength and confidence in the early stage of my life.

Finally, I would like to thank my wife, Ruilin Zhou, who has always been there for me, given me support during the most difficult time, and come along with me in every step through the entire journey.

TABLE OF CONTENTS

LIST OF TABLES

LIST OF FIGURES

LIST OF ABBREVIATIONS

ACD	Adaptive Critic Design
ACE	Area control error
AGC	Automatic generation control
AVR	Automatic voltage regulator
DFIG	Doubly-fed induction generator
DHP	Dual heuristic dynamic programming
DPC	Direct power control
DR	Down reserve
DTC	Direct torque control
DSOPF	Dynamic stachastic optimal power flow
FACTS	Flexible AC transmission system
GSC	Grid-side converter
LVRT	Low-voltage ride-through
MPPT	Maximum power point tracking
MSE	Mean squared error
OPF	Optimal power flow
PI	Proportional-integral
PIR	Proportional-integral-resonant
PLL	Phase-locked loop
PRBS	Pseudo-random binary signal
PSS	Power system stabilizer
RMS	Root-mean-squared

RNN	Recurrent neural network
RSC	Rotor-side converter
SCADA	Supervisory control and data aquisition
STATCOM	Static synchronous compensator
SVC	Static VAr compensator
UR	Up reserve
WAMS	Wide-area monitoring system
WECS	Wind energy conversion system

SUMMARY

Wind power generation provides opportunities to improve energy security and sustainability, but at the same time creates new challenges to electrical power researchers and engineers. High penetration of wind energy requires innovations in different areas of power engineering. Methods for improving wind energy and power system interconnection, control, and operation are proposed in this Ph.D. dissertation.

Wind turbines using doubly-fed induction generators (DFIGs) have the advantage of low cost, but they are sensitive to grid faults. A feed-forward transient compensation control scheme is proposed to enhance the low-voltage ride-through capability of DFIGs. Stator-voltage transient compensation terms are introduced to suppress rotor current overshoots and torque ripples resulting from grid faults.

Wind power generation introduces unexpected fast power variation to power systems. A dynamic stochastic optimal power flow (DSOPF) control scheme is proposed to optimally reroute real-time active and reactive power flow in the presence of high variability and uncertainty. A neurocontrol design method called the Adaptive Critic Designs is adapted to implement the DSOPF controllers. The performance of the proposed DSOPF control scheme is demonstrated in a 12-bus and a 70-bus power system.

The limited amount of system reserve may prohibit the increase of wind power penetration. A combined energy-and-reserve wind market scheme is thus proposed. The additional wind reserve market is designed with a lower deficit penalty and allows wind producers to manage their risks of deviation revenue loss. Variable wind reserve products are created to absorb part of the wind production variation. These fast wind reserve products can then be used to regulate system frequency deviation and improve system security.

CHAPTER 1 INTRODUCTION AND OBJECTIVES OF RESEARCH

1.1 Background of Wind Energy Generation

Renewable energy has received extensive interests over the past decade, resulting from increasing concerns about energy security and sustainability. Wind energy generation, in particular, has been growing rapidly around the world and has become one of the most mature renewable generation technologies.

The E.U. has set a binding target of 20% of its energy supply coming from wind and other renewable resources by the year 2020 [1]. In the U.S., a scenario of wind energy contributing 20% of the total energy supply by 2030 is envisioned by the Department of Energy [2]. Renewable Portfolio Standard (RPS) mandates (or their equivalents) with renewable-production tax credits have been enacted in many countries and states to accelerate the development of the wind industry [3]. By the end of 2009, the worldwide installed wind capacity reached 159 GW, showing a 31.7 % increase from 2008 [4]. In the U.S., nearly 10 GW of wind capacity came online in 2009, bringing the U.S. total installed wind capacity to over 35 GW [5], yet the wind energy penetration level in 2009 was only around 2% [6].

Variable-speed wind energy conversion systems (WECSs) are commonly used to maximize the wind energy captured in modern wind power plants. The variable-speed operation is achieved by using power electronic converters to decouple the mechanical rotor frequency from the electrical grid frequency. Two major configurations of variable-speed WECSs have been developed [7], [8]: (1) WECSs equipped with doubly-fed induction generators (DFIGs) and partially-rated power electronic converters, as shown in Figure 1.1;

and (2) WECSs equipped with synchronous generators (SGs) and fully-rated power electronic converters, as shown in Figure 1.2 .

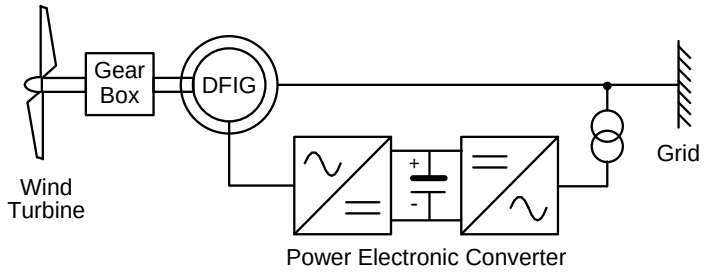

Figure 1.1 A WECS using a DFIG and partially-rated converters.

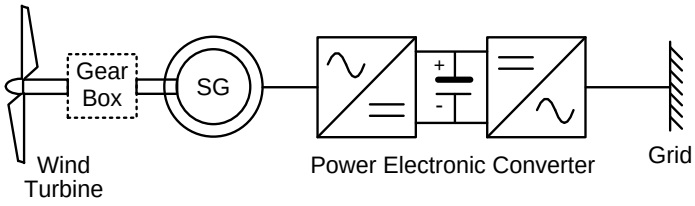

Figure 1.2 A WECS using a SG and fully-rated converters.

In the first WECS configuration, the power electronic converters are typically rated at about 30% of the DFIG power rating. The total system cost is thus reduced. However, the partially-rated converters are vulnerable to grid disturbances. A gearbox is normally required to increase the rotating speed of the DFIG rotor. Because of the high variability of wind, the gearbox is often under high mechanical stress, which requires frequent maintenance to prevent mechanical failure.

In the second WECS configuration, a regular field-excited SG or a permanent-magnet SG is used with an optional gearbox. If the gearbox is not used, a large SG with multiple poles is required. This large SG incurs additional engineering challenges and costs during assembly and installation.

1.2 Interconnection Requirements and Challenges for Large Wind Plants

The rapid growth of wind generation capacity has motivated the establishment of grid

codes for connecting large wind power plants to the grid [9], [10]. In the U.S., the Federal Energy Regulatory Commission (FERC) requires wind plants larger than 20 MW to 1) provide supervisory control and data acquisition (SCADA) capability to transmit data to and receive instructions from transmission providers; 2) maintain their power factors between -0.95 to 0.95, if such a requirement is necessary to ensure system reliability; and 3) withstand three-phase faults and remain connected to the grid for at least nine cycles (0.15 s), where the voltage measured at the high side of the wind-plant step-up transformer may drop to as low as zero volt [12], [13].

The low-voltage ride-through (LVRT) requirement, i.e., the third one mentioned above, requires large wind plants to be robust against grid disturbances. Figure 1.3 shows the measured total wind power production in the Spanish power network on January 18, 2004 [11], and sudden drops of wind production resulting from grid faults were recorded. A successful LVRT solution can minimize these unexpected wind plant outages, and is thus a prerequisite for high penetration of wind energy.

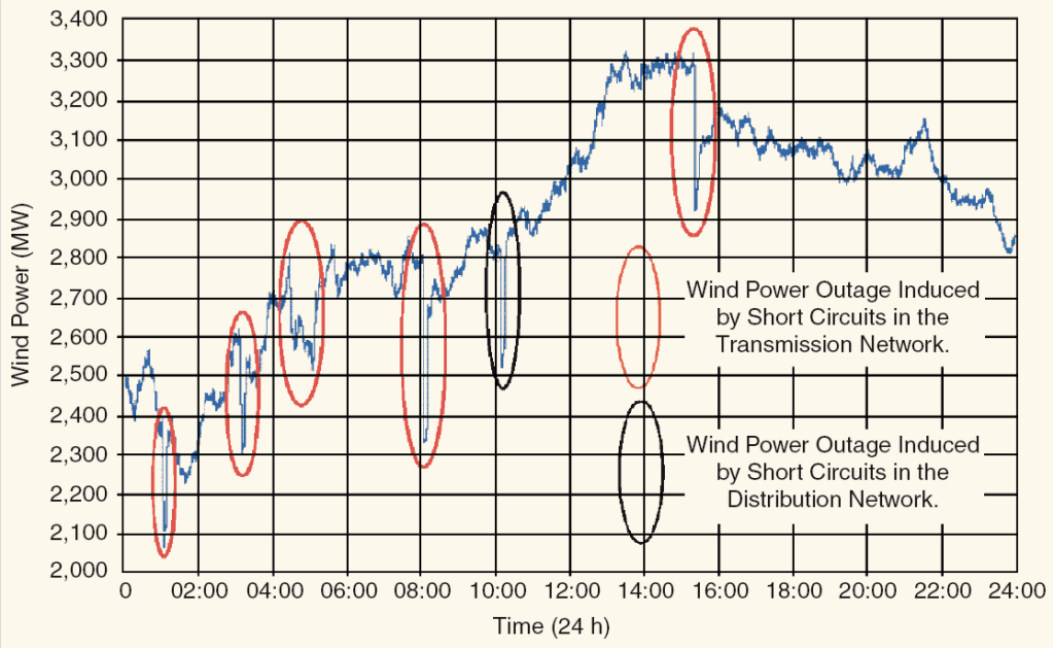

Figure 1.3 Total wind production in Spain with recorded wind power outages [11].

For wind generation systems equipped with DFIGs and partially-rated power electronic converters, the LVRT requirement is difficult to satisfy. Because the stator of a DFIG is directly connected to the grid, the whole DFIG system is sensitive to grid disturbances. Firstly, an abrupt voltage drop (balanced or unbalanced) at the DFIG stator terminals produces a temporary DC component in the stator flux [14], which then induces a large transient voltage in the DFIG rotor circuit. If the power electronic converters cannot compensate for all of the induced voltage, a large rotor-current overshoot appears in the rotor circuit, which may damage the converters and result in disconnection of the wind turbine generator. Secondly, an unbalanced-stator-voltage condition produces a negatively-rotating component in the stator flux [15]. This negatively-rotating stator flux may create large second-order-harmonic torque ripples [16], which increase the gearbox mechanical stress. Therefore, for lower-cost DFIG-based wind generation systems, it is desired to limit the transient current overshoots and torque ripples during abnormal grid conditions.

1.3 Power System Active and Reactive Power Control and Challenges with High Penetration of Wind Power

Power system real-time active power imbalance resulting from unpredicted short-term load variation is typically handled by a simple linear controller, called automatic generation control (AGC) [17]. AGC is also referred as load frequency control or secondary frequency control. Typical AGC uses a proportional-integral (PI) controller to regulate the control-area frequency and inter-area active power exchange by adjusting generation from individual generators. Although AGC provides system-wide active power control, it treats a power grid as a single-bus system, has no coordination with reactive power control, and does not consider system stability and security.

Reactive power support is typically provided by large generators, switched capacitor

banks, and on-load tap-changing (OLTC) transformers. At some critical buses, power-electronics-based flexible-AC-transmission-system (FACTS) devices [18], such as static VAr compensators (SVCs) and static synchronous compensators (STATCOMs), are used to provide dynamic reactive power support. For short-term load variation and disturbances, bus voltages are regulated by these reactive-power-support devices using local controllers [18]. Real-time system-wide coordinated control on reactive power rarely exists in today's power systems.

The present separate control schemes for active and reactive power are based on the assumption that only small variation exists in a power system during a short period of time, and any long-term large variation is handled by steady-state optimization processes. This assumption is true when the major uncertainty in a power system is the load, which varies relatively slowly at transmission levels and is predictable because of the load's cyclic characteristics. However, in a scenario with high penetration of wind power, significant power flow redistributions may occur in a short period of time, resulting from the high variability and uncertainty associated with wind. A large drop of wind power generation at one bus will cause a temporary generation-demand imbalance, followed by generation increases at some other buses and a redistribution of power flow across the power network. With the existing control schemes for active and reactive power, power-line overload and bus over/under-voltage may occur because of the limited control capability of AGC and limited local reactive-power resources.

1.4 Challenges of Power System and Electricity Market Operation with Wind Generation Resources

In both vertically-integrated power companies and electricity markets, power systems are operated based on day-ahead/intra-day scheduling and close-to-real-time dispatching

(adjustments for the next 5 to 15 minutes) processes [19]. Day-ahead/intra-day schedules are generated based on load forecasts, by minimizing the total cost of electricity with different constraints [19]. Day-ahead load forecast errors are typically around 2%. During the day-ahead scheduling process, ancillary reserve services are also planned accordingly to ensure secure operation for the next day under a certain level of uncertainty (e.g., inaccurate forecasts and grid contingencies). In most electricity markets, an energy market is formed to facilitate the energy trading between buyers and sellers, while a reserve market is formed to commit reserve services for system security [20].

Since the introduction of grid-scale wind plants, wind energy has been simply treated as highly-variable negative load with limited predictability. With state-of-the-art wind forecasting methods, average day-ahead wind forecast errors are around 25%-30% for a single wind plant and 15%-18% for a control region [21]. As a result, system operators normally use conservative wind forecasts (forecasts with a high probability of exceedance) in the day-ahead scheduling process to ensure having enough generation capacity online [22]. This method minimizes the impact of wind uncertainty, but at the same time results in under-utilization of wind power. During real-time operation, the actual wind power will exceed the schedules most of the time, and a significant amount of balancing reserve would be needed to absorb all available wind power because of the relatively slow ramp rates of conventional units. Lack of balancing reserve is one of the two major causes (the other one being lack of transmission capacity) of wind curtailments [23].

Wind curtailments reduce wind plant revenues, since no compensation is paid for curtailments in most electricity markets [23]. Moreover, wind producers are subject to monetary penalties if their actual outputs deviate from the forecast-based schedules [24], [25]. In other words, wind producers are exposed to revenue reductions resulting from both

wind forecast errors and conservative supply bids.

As the wind penetration level continues to increase, balancing reserve from conventional units will become scarce, and more wind curtailments and penalties are likely to occur. How to better operate power systems for a high-wind-penetration scenario is still an unanswered challenging question [26].

1.5 Objectives of Research

High penetration of wind power requires reliable and uninterrupted wind energy generation, as well as new methods for power system control and operation that take into account the variability and uncertainty associated with wind. Innovations in different layers of power engineering are required. Figure 1.4 (adapted from [27]) summarizes different enabling technologies for increasing wind energy penetration.

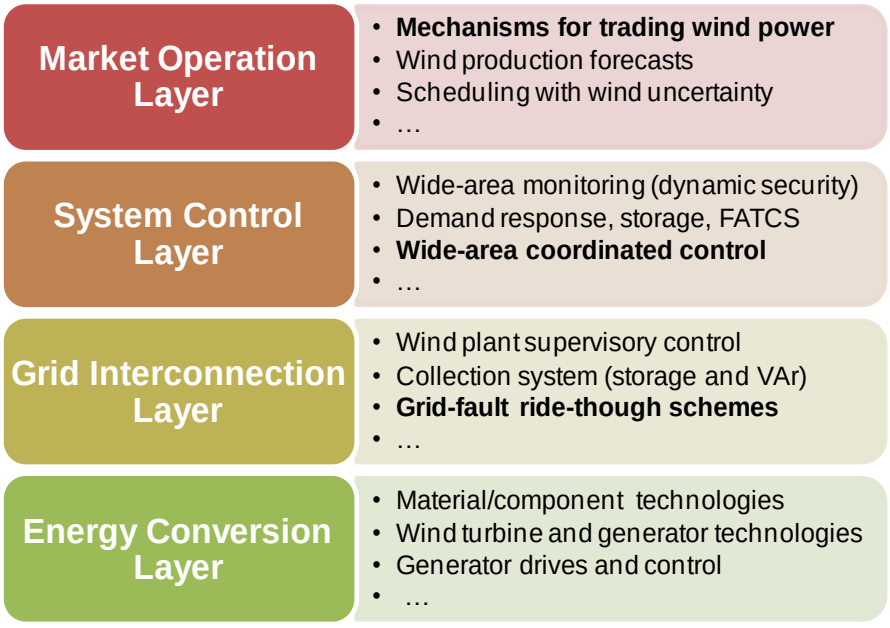

Figure 1.4 Technology paradigm for increasing wind energy penetration.

The proposed research focuses on the following three aspects (bold in Figure 1.4) to provide solutions for achieving high penetration of wind power:

- Low-voltage ride-through (LVRT) enhancement of doubly-fed induction generator (DFIG) based wind generation systems: dynamic control of DFIGs is investigated to enhance their capability to ride through grid transient disturbances and provide uninterrupted active and reactive power generation.
- Wide-area optimal control of power system AC power flow (both active and reactive power flow): the Adaptive Critic Design (ACD) theory [28] is used to provide nonlinear optimal control to power systems with high short-term uncertainty and variability.
- Combined energy-and-reserve wind power market design: fast and variable reserve product from wind plants is proposed to absorb wind production variation, increase wind producer revenue, and enhance power system security.

1.6 Dissertation Outline

The rest of this dissertation is organized as follows:

Chapter 2 provides a comprehensive literature review on the existing methods and techniques pertinent to the proposed research.

Chapter 3 proposes a feed-forward transient compensation control algorithm for enhancing the LVRT capability of DFIGs. Simulation and experimental studies are presented to demonstrate effectiveness of the proposed control method.

Chapter 4 proposes a wide-area optimal power flow control algorithm, called dynamic stochastic optimal power flow (DSOPF) control. Design and control performance of a DSOPF controller for a small 12-bus power system are presented.

Chapter 5 applies the DSOPF control algorithm to a 70-bus power system with two large wind plants. A two-level DSOPF control design is presented for controlling large power networks.

Chapter 6 proposes a new combined energy-and-reserve market mechanism for wind power trading. Analysis on a single wind plant in a perfectly competitive market is presented to demonstrate the benefits of the additional wind reserve market to wind producers.

Chapter 7 further investigates the combined energy-and-reserve market scheme in a single-bus multiple-generator power system. Different wind market schemes are compared by solving the energy-reserve co-optimizaiton problem. The benefits of fast wind reserve to grid security are evaluated using dynamic simulations.

Chapter 8 provides the conclusions and contributions of this dissertation work and recommendations for future investigations.

CHAPTER 2 REVIEW OF LITERATURE

2.1 Chapter Overview

This chapter provides a literature review on topics pertinent to this dissertation work, including: (1) the modeling and control methods for wind turbines and doubly-fed induction generators (DFIGs), (2) the existing low-voltage ride-through (LVRT) techniques for enhancing the robustness of the DFIG-grid interconnection, (3) the existing system-level control methods for controlling power system real-time active and reactive power, and (4) the existing operation methods for procuring wind energy in power markets.

2.2 Control of DFIG-based Wind Generation Systems

This section summarizes the control of DFIG-based wind generation systems and provides the background for subsequent discussions on DFIG LVRT techniques.

2.2.1 Modeling and Operation of Wind Turbines

The wind power captured by a wind turbine is given by [29], [30]

$$P_m = P_{wind} C_P(\lambda,\theta) = \frac{1}{2}\rho A_r v_w^3 C_P(\lambda,\theta), \tag{2.1}$$

where P_{wind} is the wind power in W, C_P is the wind-turbine efficiency, ρ is the air density in kg/m^3, A_r is the area swept by the turbine rotor blades in m^2, and v_w is the wind speed in m/s. The turbine efficiency depends on the blade pitch angle, θ in rad, and the tip-speed ratio, λ, defined by

$$\lambda = \frac{\omega_t R}{v_w}, \tag{2.2}$$

where R is the blade length in m and ω_t is the turbine rotating speed in rad/s. The C_P-λ-θ relationship is a complex nonlinear function that depends on the blade design, and this

relationship is usually given by wind-turbine manufacturers. Figure 2.1 shows the C_p curves of a 3.6 MW wind turbine, where a polynomial is used to approximate the actual C_P-λ-θ relationship [29].

A typical output-power curve of wind turbines is shown in Figure 2.2. For efficiency and safety reasons, wind turbines operate only when the wind speed is between the cut-in and cut-out speeds. When the wind speed is between the cut-in and rated speeds, wind turbines are typically operated in a maximum-power-point-tracking (MPPT) mode, and the turbines are controlled such that C_p reaches its peak value. Different MPPT control algorithms have been reported, including turbine-characteristic-based methods [31], [32], and online-searching-based methods [33], [34]. When the wind speed increases above the rated value, a control loop, called pitch angle control, is activated to increase the pitch angle, θ, and maintain the captured wind power within the turbine rating. Details of the MPPT control used in this dissertation work are included in Appendix A.

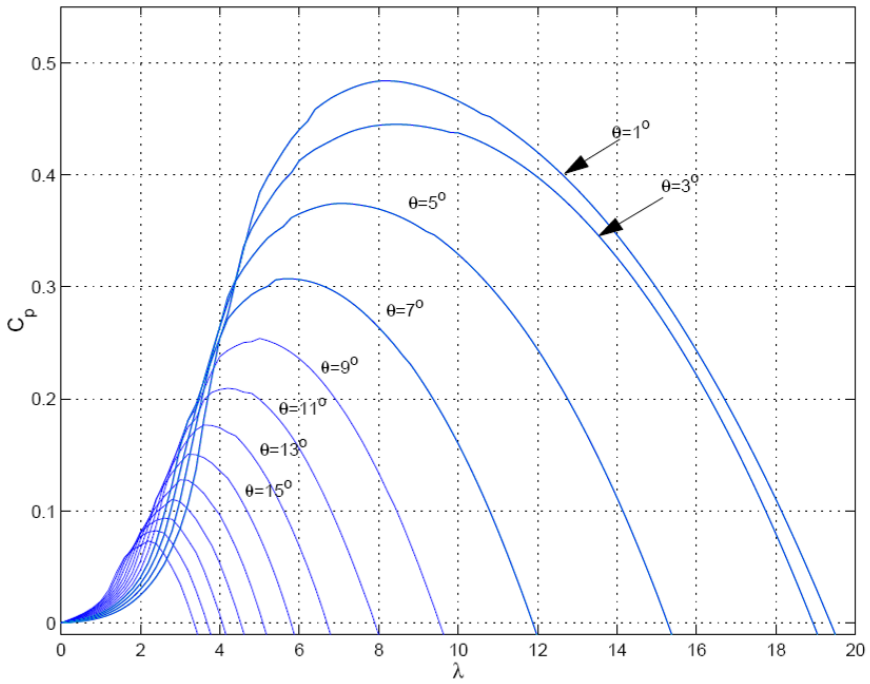

Figure 2.1 Typical wind-turbine C_p curves [29].

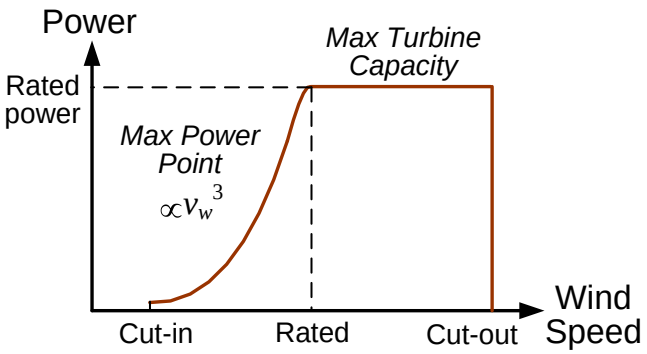

Figure 2.2 Typical wind-turbine power curve.

2.2.2 Vector Control for DFIGs

The power electronic converters of a DFIG wind generation system consist of a rotor-side converter (RSC) and a grid-side converter (GSC), as shown in Figure 2.3. The RSC AC side connects to the rotor outlets of a three-phase wound-rotor induction machine. The GSC AC side connects to the machine stator through a step-up transformer. The RSC controls the DFIG-stator active and reactive power outputs. The GSC maintains the DC-bus voltage and may be controlled to provide additional reactive power to the grid.

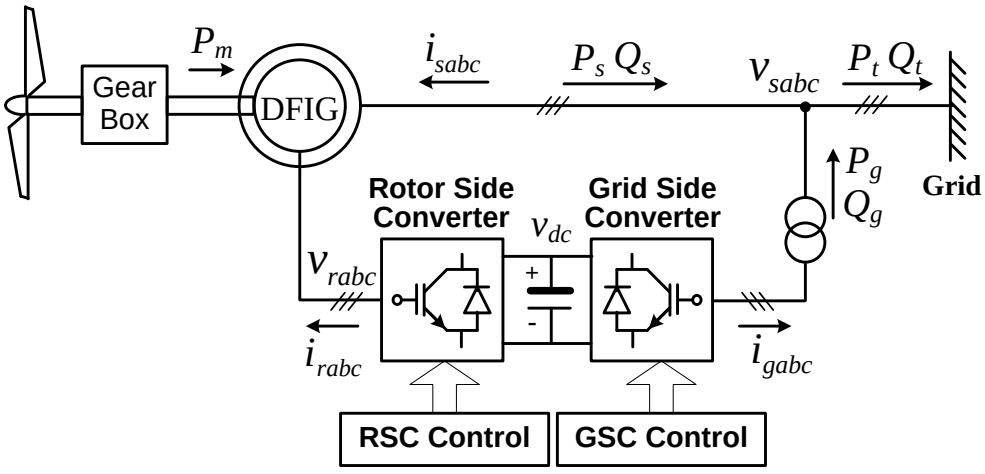

Figure 2.3 Configuration of a DFIG wind turbine system.

The vector control (or field oriented control) algorithm for electric motors [35] has been applied to control DFIGs. In the synchronous *dq* reference frame, when the *d* axis is aligned

with the stator flux (λ_s in Figure 2.4), the DFIG-stator active power output (and electromagnetic torque) is only related to the *q*-axis rotor current, and the reactive power output is only related to the *d*-axis rotor current [30], [32]. Thus, the vector control algorithm decouples the active and reactive power control of DFIGs. The block diagram of the RSC vector control scheme is shown in Figure 2.5. Because the *dq* rotor currents are cross-coupled with the *dq* rotor voltages, feed-forward current regulars with PI controllers [36] are commonly used to decouple the control of *dq* rotor currents [32].

The DFIG mathematical model and derivations for the DFIG vector control scheme are included in Appendix A.

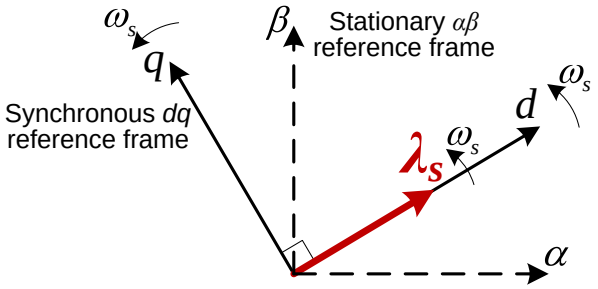

Figure 2.4 Space vector diagram with *dq* synchronous reference frame.

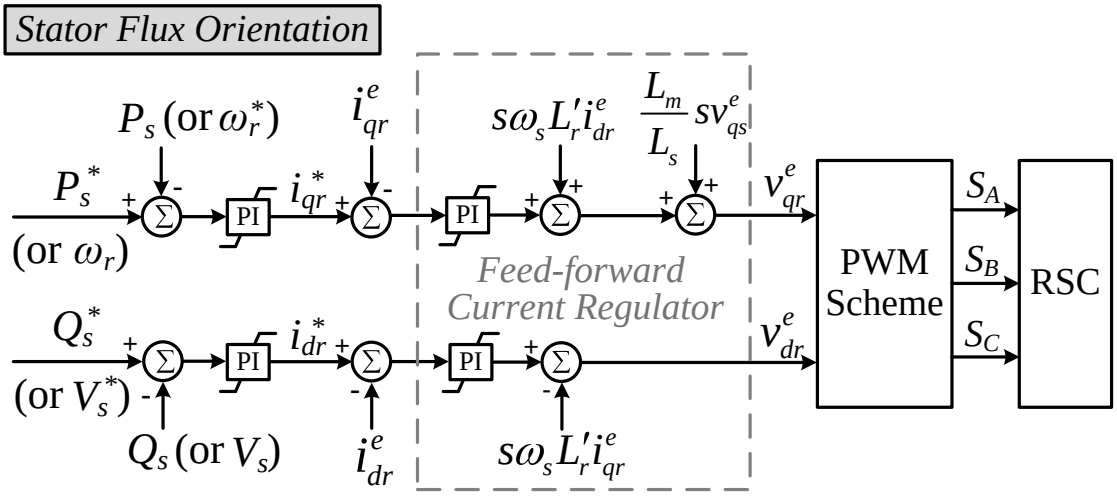

Figure 2.5 Vector control scheme for RSC with a feed-forward current regulator.

2.2.3 Direct Power Control for DFIGs

Direct torque control (DTC) [37], or direct power control (DPC), for electrical motors and FACTS devices has also been applied to directly control the DFIG-stator active and reactive power outputs. The basic principle of DTC/DPC is to generate a voltage space vector that controls (increases or decreases) the electromagnetic torque (or active power) and magnetic flux (or reactive power) during each sampling period. DTC/DPC has good dynamic performance with simple implementation, and requires no knowledge of system parameters [38]. However, the main drawbacks of DTC/DPC include higher current and torque (or power) ripples and a variable switching frequency [38].

The schematic diagram of using DPC to control a DFIG RSC is shown in Figure 2.6, where estimating the rotor flux during zero-slip conditions is one of the major challenges. Seman *et al.* [39] uses the estimated stator flux and rotor current to derive the rotor flux based on the machine flux equations. In contrast, Xu *et al.* [40] avoids estimating the rotor flux by using the vector control concept, where the RSC switching scheme is directly generated based on the estimated stator flux. A DPC scheme with constant switching frequency has also been reported for DFIGs, but some knowledge of the machine parameters are required [41].

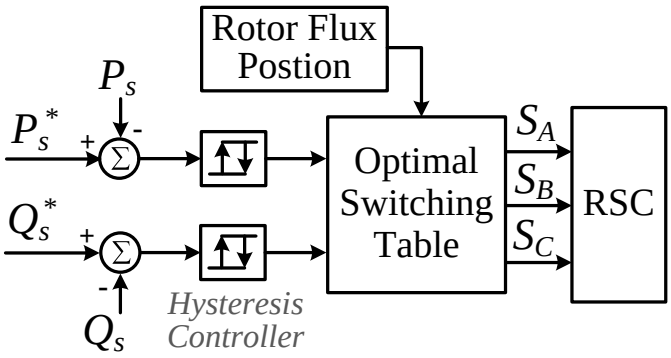

Figure 2.6 Direct power control scheme for RSC.

2.3 Low-Voltage Ride-Through (LVRT) Approaches for DFIG Wind Turbines

This section reviews the different DFIG LVRT techniques that have been developed based on the different DFIG control methods introduced in the previous section. The limitations of the existing LVRT techniques are then summarized at the end of this section.

2.3.1 LVRT Approaches for Balanced Grid Faults

For balanced three-phase grid faults, a large transient current may be induced in the DFIG rotor circuit during the transient periods of stator-voltage drop and recovery. The primary challenge of riding through balanced grid faults is to limit the transient rotor current and the potential DC-bus voltage rise, and protect the power electronic converters from over-current and over-voltage.

2.3.1.1 AC Crowbar Protection Circuit

One common LVRT solution for DFIGs is to install an AC crowbar circuit across the rotor terminals [42]-[44], as shown in Figure 2.7. The crowbar circuit can be implemented using either a thyristor-controlled rectifier [43], [44] or a passive diode rectifier with an active switch at the DC side [42]. The latter one has active turn-off capability and is also referred as an active crowbar. A resistor is often used at the DC side in both crowbar implementations to limit the transient rotor current, and dissipate the excessive energy [45]. When rotor over-current is detected, the RSC triggering is blocked; the crowbar short-circuits the rotor terminals with the resistor and isolates the RSC from the DFIG rotor [46]. The AC crowbar circuit provides conservative protection to the RSC and at the same time changes the DFIG to a regular induction machine, which absorbs reactive power from the grid. This event occurs at the exact same time when the grid needs reactive power support. As a result, dynamic VAr compensators, such as SVCs or STATCOMs, are often installed at the DFIG terminals (or at the wind-plant collection system) to provide reactive power

support during grid faults [47]-[49]. Control of the crowbar circuit that minimizes the crowbar interruption time has also been studied in [50] and [51].

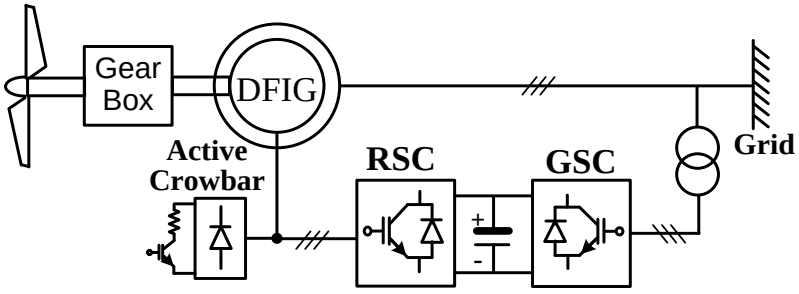

Figure 2.7 DFIG with an active crowbar protection circuit.

2.3.1.2 DC Chopper Protection Circuit

Another LVRT solution equivalent to the AC crowbar is to use a DC chopper circuit with a resistor across the DC bus [44], as shown in Figure 2.8. Instead of adding an extra crowbar circuit, this scheme utilizes the existing RSC diode bridge designed with a higher current rating. When rotor over-current is detected, the RSC triggering is blocked, and the transient current flows throw the RSC diode bridge and charges up the DC-bus capacitor. The DC chopper is used to prevent the DC bus from over-voltage, and dissipate the excessive energy. Similar to the AC crowbar scheme, once the RSC triggering is blocked, the DFIG rotor terminals are short-circuited by the DC-bus capacitor through a passive diode bridge, and the DFIG functions as a regular induction generator.

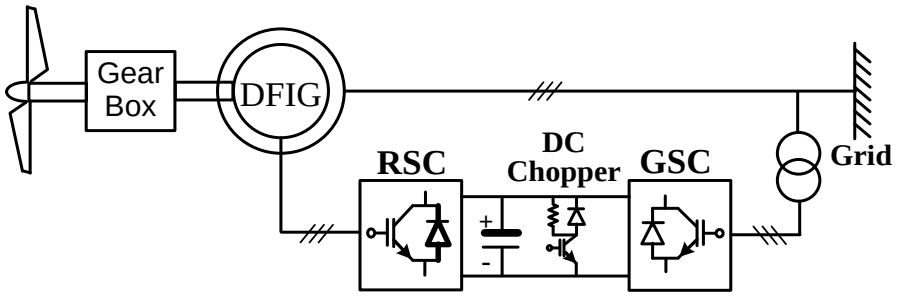

Figure 2.8 DFIG with a DC chopper protection circuit.

2.3.1.3 Protection Circuits using Series-Connected Devices

With an additional series-connected power electronic converter between the DFIG stator and the grid, the net stator voltage can be dynamically restored to minimize the effects of grid disturbances on the DFIG system [52], [53]. However, this solution has a high active-device count and increases the system cost. Alternatively, power-electronics-controlled dynamic impedances may be connected in series with either the DFIG rotor [54] or stator [55] to temporarily increase the impedance seen by the RSC during grid-fault transients.

2.3.2 LVRT Approaches for Unbalanced Grid Faults

For unbalanced grid faults, besides limiting the rotor current during the transient periods of stator-voltage drop and recovery, another important aspect is to limit the torque ripples when the stator voltage is unbalanced. Under unbalanced grid conditions, second-order-harmonic ripples may appear in the electromagnetic torque, stator current, and stator active and reactive power outputs. It has been shown [57], [60] that only one of the following three conditions can be fulfilled at a time by controlling the RSC: 1) eliminating the stator current ripples, 2) eliminating the torque and stator reactive power ripples, and 3) eliminating the stator active and reactive power ripples. To reduce the gearbox stresses, eliminating the torque ripples is typically selected as the control objective.

2.3.2.1 Vector-Control-based Approaches

Based on the RSC vector control scheme shown in Figure 2.4, the sequence component decomposition method is often used to minimize the torque and reactive power ripples. The *dq*-rotor-current positive- and negative-sequence components are controlled separately, resulting in four current PI regulators, additional phase-locked loops (PLLs) and notch filters [56], [57]. Proportional-integral-resonant (PIR) regulators are reported to regulate both the

positive- and negative-sequence currents at the same time [58], eliminating the need for additional negative-sequence current regulators. However, the current commands for the positive- and negative-sequence *dq* rotor currents need to be generated separately. When the RSC is controlled to minimize torque ripples, the GSC may be used to compensate for the active power or stator current ripples [59].

2.3.2.2 DPC-based Approaches

To minimize the second-order-harmonic torque ripples, the DPC-based approaches have a simpler implementation, as compared to the vector-control-based approaches. The DFIG stator active and reactive power outputs due to the positive- and negative-sequence voltages are first separated, denoted as P_+, P_-, Q_+ and Q_- [60], [61]. Combinations of these four power components can be controlled directly by DPC to achieve one of the three above-mentioned ripple-eliminating conditions [60], [61]. A similar idea is used in [62], where the sequence-component calculation is avoided, and P_+ and P_- are calculated indirectly from the active power and estimated electromagnetic torque.

2.3.2.3 Approaches using Series Connected Devices

Similar to the LVRT approaches for balanced grid faults, an additional series-connected power electronic converter may be used to dynamically restore the unbalanced stator voltage [63], but the additional converter increases system cost and complexity.

2.3.3 Section Summary

The AC crowbar and DC chopper schemes are two most cost-effective solutions for limiting DFIG transient rotor currents. However, both schemes interrupt the normal control of the DFIG active and reactive power. An improved method is desired for enhancing the transient-rotor-current control capability and minimizing the occurrence of DFIG control interruptions. For minimizing the torque ripples, most existing techniques rely on sequence

component decomposition that does not consider limiting the transient rotor current.

Based on the vector control algorithm, a feed-forward transient-compensation control scheme for DFIGs is proposed in Chapters 3 to improve the transient-rotor-current control capability and minimize the torque ripples during abnormal grid conditions.

2.4 Power System Wide-Area Control

The development of wide-area monitoring systems (WAMSs), based on synchronized phasor measurement units [64], greatly improves the power grid observability, even during transient events [65]. WAMSs enable distributed dynamic state estimation, which can dramatically reduce the reporting time of the global system states (from minutes down to fractions of a second) and improve the grid visibility from steady states to dynamics [66], [67].With the global dynamic information, advanced wide-area control schemes that require remote synchronized signals become possible to improve grid dynamics. [68], [69]. This section reviews different wide-area control schemes and provides the background for the wide-area power flow control algorithm proposed in Chapters 4 and 5 to optimally routing variable wind power injections.

2.4.1 Transient and Small-Signal Stabilizing Control

This sub-section summarizes different control techniques that have been applied to power system oscillations. Local damping controllers are usually ineffective in damping inter-area oscillations [70], which are characterized by groups of coherent generators swinging against each other. Wide-area coordinated damping controllers at different locations are usually needed. Because of the complexity, nonlinearity, and time-varying characteristics of a power system, designing a wide-area stabilizing controller over a wide operating range is not a trivial task.

Kamwa *et al.* [70] decouples the multiple-input multiple-output (MIMO) power system

into several single-input single-output (SISO) global stabilizing loops based on the coupling between different input-output pairs. These SISO global loops are then sequentially optimized. Instead of multiple SISO loops, the observer-based state-feedback (SF) linear control [71] and the robust H∞ control using linear matrix inequality (LMI) [72] have been applied to design MIMO damping controllers. Because of the linear nature of both the SF and H∞-LMI control designs, multiple control loops are designed at different operating points. From the multiple control loops, an active one is selected by a probabilistic-model-reference method in [71] and a fuzzy-inference system in [72]. Others approach the problem directly from the nonlinear analytical model of a power system [73], [74], where the controller parameters depend on system operating conditions and need to be continuously estimated. More advanced computational-intelligence-based stabilizing controllers using the Adaptive Critic Design (ACD) technique have been reported [75]-[77], where promising control performances are obtained and compared to the observer-based SF and H∞-LMI controllers [77].

2.4.2 Secondary Frequency and Voltage Control

As discussed in Section 1.3, automatic generation control (AGC) uses a simple PI controller to regulate the area control error (ACE) by adjusting generations from individual generators. The ACE is typically defined as

$$ACE = (P_{tie}^* - P_{tie}) + B\,(f - f^*), \tag{2.3}$$

where P_{tie} is the total inbound tie-line active power flow, P_{tie}^* is the scheduled inbound tie-line flow, f is the actual system frequency, f^* is the nominal frequency, and B is a frequency bias term [17]. The generation adjustments to different generators are coordinated by some predefined ratios or ratios from the economic dispatch [17]. In North America, AGC commands are typically updated every 2-4 s [17]. Secondary active power control algorithms that not only

regulate active power imbalance but also consider system constraints have not been reported.

Automatic secondary/regional voltage control for transmission grids is under development in some countries, such as Italy. The Italian power system is divided into several voltage-regulation regions with each region having its own pilot node (bus) [78], [79]. The main generators in each region are used to regulate the pilot-node voltage with PI regulators [78]. Voltage regulation measurements and commands in the Italian system are updated at intervals not exceeding 2 s [79]. Other researchers propose more sophisticated techniques to control system-wide voltages. Wang *et al.* [80] proposes a finite-state-machine-coordinated fuzzy controller to control multiple shunt FACTS devices and maintain the system voltage profile. Nonlinear model predictive control is reported to control system-wide voltages by optimally selecting control commands from a pool of possible control actions [81]. However, all these works have not considered the coordination with power system active power control.

2.4.3 Coordinated AC Power Flow Control and Adaptive Critic Designs (ACDs)

Most of the wide-area control algorithms to date have focused on the transient/small-signal stabilizing control to mitigate angle instability, and the secondary voltage control to mitigate voltage instability. The design of a system-wide coordinated active and reactive power flow controller, which dynamically controls a power system to its optimal operating point, has received little attention. Fardanesh [82] describes an ideal control scenario for power systems, where the optimal operating condition is continuously achieved by some closed-loop control algorithm, but how to design such a control algorithm remains unanswered. A conceptual framework of applying ACDs to power system optimizations, called dynamic stochastic optimizations, has been proposed by Venayagamoorthy [83] and Momoh [84] to incorporate prediction and optimization over power system stochastic

disturbances. However, detailed designs and analyses have not been reported. To provide the control background of the proposed wide-area optimal power flow control, the ACD technique is briefly summarized below.

2.4.3.1 Adaptive Critic Designs

A family of ACDs was proposed by Werbos as a new optimal control technique combining the concepts of reinforcement learning and approximate dynamic programming (ADP) [85]. The ACD theory enables nonlinear optimal control without the need of system analytical models. Figure 2.9 shows the schematic diagram of the ACD technique, which consists of three functional components: a controller, an identifier, and an ADP unit [86].

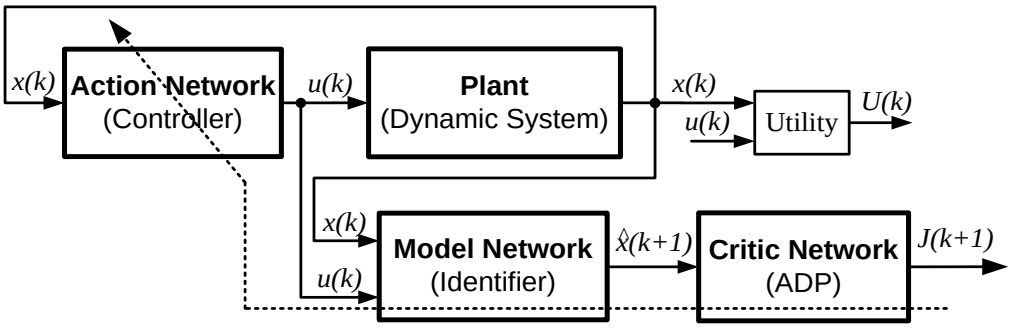

Figure 2.9 Schematic diagram of ACDs.

Having excellent function approximation capability, neural networks [87] are commonly used to implement these three components. As illustrated in Figure 2.9, an action network is trained to approximate the optimal controller. A model network is trained to approximate the plant dynamics, and provides a nonlinear differentiable plant model. A critic network is trained to approximate the cost-to-go function, *J*, in the Bellman's equation of dynamic programming, as in

$$J(k) = \sum_{i=0}^{\infty} \gamma^i \cdot U(k+i) \quad (2.4)$$

,

where γ ($0 < \gamma < 1$) is a discount factor, and $U(k)$ is the utility function (a present cost to be minimized). The optimal control problem is to generate control actions that minimize $J(k)$ at each time step k.

The nonlinear dynamic plant can be described as [86]

$$\begin{aligned} x(k+1) &= F[x(k), u(k)] \\ y(k+1) &= H[x(k+1)] = HF[x(k), u(k)] \end{aligned}, \tag{2.5}$$

where $x(k)$ is the plant state vector and $y(k)$ is the plant output vector. When the plant states, $x(k)$, are accessible (available as feedback) and the control law is a function (dynamic or static) of the plant states, i.e., $u(k) = C[x(k)]$, it has been shown that the cost-to-go function depends only on the present plant states, i.e., $J(k) = V[x(k)]$ [86]. The critic network approximates this V function with the plant states as its inputs. The action network approximates the optimal control laws, $C_{\text{opt}}[\cdot]$, also with the plant states as its inputs. The model network approximates the plant, $F[\cdot]$, and provides sensitivity signals for training the action and critic networks.

For complex dynamic systems, such as power systems, not all the system states are available. As a result, the system states must be estimated from the plant inputs and outputs. An autoregressive-moving-average model is commonly used to estimate the plant states implicitly and predict the plant outputs at the next step [88], as in

$$\begin{aligned} & \hat{x}(k-m) \sim y(k), \ldots, y(k-m), u(k-1), \ldots, u(k-m) \\ \Rightarrow\ & \hat{x}(k+1) \sim u(k), \ldots, u(k-m), \hat{x}(k-m) \\ & \qquad \sim u(k), \ldots, u(k-m), y(k), \ldots, y(k-m) \\ \Rightarrow\ & \hat{y}(k+1) = N_{FF}[y(k), \ldots, y(k-m), u(k), \ldots, u(k-m)] \end{aligned} \tag{2.6}$$

where $\sim$ denotes "a function of", m denotes the number of observations needed for state estimation, and N_{FF} denotes the autoregressive-moving-average model implemented by static feed-forward neural networks. As a result, when the system states are not all accessible, the plant outputs are used as inputs to the three ACD networks, and feed-forward neural networks with

time-delayed loops are used to provide implicit plant state estimations [76], [89]. More details on the mathematical background and training algorithms for ACDs are provided in [86].

2.4.4 Section Summary

The observer-based SF control, robust H∞-LMI control, and other linear control techniques result in linear controllers that are not adequate for controlling the AC power flow of a complex nonlinear power system. Nonlinear control techniques, such as the nonlinear model predictive control, incorporate the power system nonlinearity, but require analytical models and detailed parameters that are difficult to obtain for power systems. The ACD theory is thus adapted to design the proposed wide-area power flow controller in Chapters 4 and 5.

2.5 Power System and Market Operation with Wind Energy

This section reviews some existing market operation methods and monetary rules for incorporating intermittent wind energy. Previous studies on wind plant optimal bidding strategies to minimize deviation penalties are also summarized.

2.5.1 Electricity Markets

Most electricity markets are organized in a sequence of overlapping markets [20], because of the need of planning generation and reserve in advance and matching production and demand in real-time operation. The sequence begins with the long-term forward markets, where monthly or weekly scheduling is made. The day-ahead markets follow, with commitments being made typically 12 to 36 hours before the actual operating day. Some electricity markets also have hour-ahead (or intraday) markets to adjust the hourly (or intraday) schedules. The real-time physical markets have shorter intervals usually of 5 minutes driven by security-constrained economic dispatch software, which determines the real-time locational marginal prices. Most electricity markets also have ancillary reserve

markets, including products such as the regulation reserve, spinning reserve and non-spinning reserve. Depending on different market rules, different reserve products may be auctioned seasonally, monthly or daily.

2.5.2 Wind Power in Today's Electricity Markets

Wind production forecasting is the first step to incorporate wind energy into the power system and market operation. In most U.S. electricity markets, grid-wide wind power forecasts are produced by a centralized forecasting process [21], [22]. Based on the wind forecasts, wind producers submit their energy supply curves to the day-ahead or intraday energy markets. During real-time operation, wind-plant output levels are dispatched from the system operator based on the security-constrained economic dispatch or optimal power flow (OPF) software. Depending on specific market rules, wind-plant output deviations from the dispatched levels may be subject to deviation penalties.

2.5.2.1 Wind Power in the Texas Nodal Market

In the Texas nodal market, hourly wind generation forecasts for the next 48 hours (updated every hour) are provided by the Electric Reliability Council of Texas (ERCOT) to each wind producer [90]. The wind power forecasts with 80% probability of exceedance, called the wind generation resource production potentials (WGRPPs), are used for the bidding process. When the wind producers submit their day-ahead energy offer curves to ERCOT, their hourly maximum offers must be no greater than their hourly WGRPPs [90]. In the actual operating day, wind producers are allowed to adjust their energy offers hourly when updated wind forecasts are available [90].

During real-time operation, the security-constrained economic dispatch software determines the base operating point for each wind producer and updates the locational marginal prices every 5 minutes. If there is no congestion, the base operating point is close

to the maximum offers from the wind producers, and no deviation penalty will be charged to the wind producers [90]. In case of congestions, the dispatch software lowers the base point, and the wind energy is curtailed. In such a case, no penalty is charged for under-generation, but any generation more than 10% above the base point is fully penalized (no further payment for the excessive generation), unless the grid frequency is lower than 59.95 Hz [91].

The ancillary reserve market in ERCOT includes up and down regulation reserve, spinning reserve, and non-spinning reserve. However, the wind producers in ERCOT are not qualified to participate in the reserve market at this moment.

2.5.2.2 Wind Power in the Spanish Market

In the Spanish electricity market, mandatory output forecasts are required for wind producers [92]. Wind plants are subject to deviation penalties same as other generation resources without a dead band [93]. The deviation penalties in the Spanish market depend on the system conditions. If the system is short of generation, only under-generation is penalized, and vice versa [93].

An important technical obligation in the Spanish market is that any wind generation facilities above 10 MW are required to connect to a delegate dispatch center. The delegate dispatch centers communicate between their wind plants and the upper-level system operator in real time [93]. This feature provides observability and controllability to large wind plants, as well as infrastructures for wind producers to participate in the reserve market and respond to frequency-regulation signals.

2.5.3 Participation of Wind Producers in Energy Markets

Because of the significant prediction errors associated with wind power [21], it is important for wind producers to minimize their exposure to the deviation penalties. It is estimated that in the Spanish market, the total revenue loss in the wind industry due to

deviations can represent up to 10% of the total revenue without deviation penalties [94]. Assuming a 10% rate of return, this revenue loss is approximately the same as the total wind industry profit. For a group of wind producers, one effective way to minimize their deviation losses is to use a portfolio approach where multiple wind producers join their forecasts and submit one combined bid [94]. Another way is to form a virtual power plant, which combines wind with storage resources [95], but the availability of utility-scale storage resources is still limited.

A more general method to minimize the deviation revenue loss is to strategically place bids in the day-ahead or intraday energy markets. Bathurst *et al.* [96] proposes an optimal bidding strategy by assuming that the wind production time series is a Markov process, while others use probabilistic wind forecasts to design optimal biding strategies [97]-[102]. The Nordic market regulatory rules are followed in [97]. Pinson *et al.* [98] simulates the Dutch market and compares the performances of using point predictions with probabilistic predictions. The Spanish market regulatory rules on wind plants are described in [99] and [100], where revenue losses under different levels of deviation penalties are compared. A linear optimization model based on discrete probabilistic forecasts with fuzzy optimization is proposed by Xue *et al.* [101]. An alternative risk-based objective function is proposed by Botterud *et al.* [102].

2.5.4 Section Summary

Under the existing market rules for wind power, wind producers only participate in the energy market. During real-time operation, the penalty for over-generation is often less than the spot market price [97]-[100]. As a result, given any committed output levels, a wind producer (having close to zero marginal cost) maximizes its profit by outputting all of its available wind power. Consequently, the grid needs to absorb all of the short-term wind

variation under such a market model. A new market mechanism for trading wind power in a combined energy-and-reserve market is proposed in Chapter 6 to incentivize wind producers to regulate their short-term wind power productions. The optimal bidding scheme in this combined market is derived. The proposed wind market scheme is then compared with the existing market schemes in Chapter 7.

2.6 Chapter Summary

This chapter provides a comprehensive literature review on topics pertinent to this dissertation work. First, the existing control and low-voltage ride-through (LVRT) techniques for doubly-fed induction generator (DFIG) based wind turbine systems, as well as the limitations of these LVRT techniques, are summarized. Next, the existing power system wide-area control methods for stabilizing oscillations and regulating frequency and voltage are reviewed; the Adaptive Critic Design (ACD) technique has been suggested by several researchers as a promising technique to realize the next-generation wide-area power flow controller. Finally, the existing market mechanisms for incorporating wind power are summarized.

Based on this literature review, the rest of this dissertation proposes new methods to improve the interconnection, control, and operation of wind plants and power systems for achieving high penetration of wind power.

CHAPTER 3 FEED-FORWARD TRANSIENT COMPENSATION CONTROL FOR DFIG WIND TURBINES DURING GRID FAULTS

3.1 Chapter Overview

High penetration of wind power requires reliable and predictable wind energy generation. A successful low-voltage ride-through (LVRT) scheme is a key requirement to achieve reliable and uninterrupted wind power generation for doubly-fed induction generator (DFIG) based wind turbines. In this chapter, a feed-forward transient compensation control scheme with proportional-integral-resonant (PIR) current regulators is proposed to enhance the LVRT capability of DFIGs during abnormal grid conditions. Transient compensation terms are feed-forward injected into both the current and power control loops. The feed-forward transient compensation current controller improves the transient current control capability and minimizes DFIG control interruptions during grid-fault transients. Without the need of sequence component decomposition, the torque ripples are reduced by injecting 60 Hz and 120 Hz rotor current components during unbalanced stator-voltage conditions. The proposed transient compensation control introduces minimal additional complexity to a regular DFIG vector control scheme, and shows promising enhancements to the LVRT capability of DFIGs.

3.2 DFIG Transient Model and Dynamics

3.2.1 DFIG Electromagnetic Model

The well known *dq* voltage and flux equations (motor convention, in physical units) for slip-ring or wound rotor induction machines in an arbitrary reference frame are [35]

$$\begin{aligned} v_{ds} &= R_s i_{ds} + p\lambda_{ds} - \omega\lambda_{qs} & \lambda_{ds} &= L_s i_{ds} + L_m i_{dr} \\ v_{qs} &= R_s i_{qs} + p\lambda_{qs} + \omega\lambda_{ds} & \lambda_{qs} &= L_s i_{qs} + L_m i_{qr} \\ v_{dr} &= R_r i_{dr} + p\lambda_{dr} - (\omega - \omega_r)\lambda_{qr} & \lambda_{dr} &= L_m i_{ds} + L_r i_{dr} \\ v_{qr} &= R_r i_{qr} + p\lambda_{qr} + (\omega - \omega_r)\lambda_{dr} & \lambda_{qr} &= L_m i_{qs} + L_r i_{qr} \end{aligned}, \tag{3.1}$$

where all symbols have their usual meanings and ω is the rotating speed of the arbitrary reference frame in rad/s. Equation (3.1) holds in both steady-state and transient conditions. The synchronous reference frame is used with the *q* axis aligned to the positive-sequence stator voltage (the *d* axis aligned to the steady-state positive-sequence stator flux). Compared to the stator reactance at the grid frequency, the stator resistance is often negligible. Neglecting R_s and substituting the flux equations into the voltage equations in (3.1) yield [103], [104] (see Appendix A for detailed derivations)

$$\begin{bmatrix} v_{dr}^e \\ v_{qr}^e \end{bmatrix} = \begin{bmatrix} R_r + L_r' p & -(\omega_s - \omega_r)L_r' \\ (\omega_s - \omega_r)L_r' & R_r + L_r' p \end{bmatrix} \cdot \begin{bmatrix} i_{dr}^e \\ i_{qr}^e \end{bmatrix} + \frac{L_m}{L_s} \begin{bmatrix} v_{ds}^e + \omega_r \lambda_{qs}^e \\ v_{qs}^e - \omega_r \lambda_{ds}^e \end{bmatrix}, \tag{3.2}$$

where L_r' is the rotor transient inductance, $L_r' = \sigma L_r$ with $\sigma = 1 - L_m^2/(L_s L_r)$, and the superscript *e* denotes quantities in the synchronous reference frame.

Equation (3.2) directly relates the instantaneous values of the stator and rotor terminal *dq* voltages to the *dq* rotor currents in both steady-state and transient conditions. The stator flux can be estimated by integrating the stator voltage. If an abrupt stator-voltage dip occurs, the necessary rotor compensating voltage up to the rotor-side converter (RSC) rating could be directly generated based on the second term on the right-hand side of (3.2).

Under steady-state balanced stator voltage conditions [35],

$$v_{ds}^e + \omega_r \lambda_{qs}^e = 0,\ v_{qs}^e - \omega_r \lambda_{ds}^e = s v_{qs}^e, \tag{3.3}$$

where *s* is slip. Equation (3.2) reduces to

$$\begin{bmatrix} v_{dr}^{e} \\ v_{qr}^{e} \end{bmatrix} = \begin{bmatrix} R_r + L_r' p & -s\omega_s L_r' \\ s\omega_s L_r' & R_r + L_r' p \end{bmatrix} \cdot \begin{bmatrix} i_{dr}^{e} \\ i_{qr}^{e} \end{bmatrix} + s\frac{L_m}{L_s} \begin{bmatrix} 0 \\ v_{qs}^{e} \end{bmatrix}. \tag{3.4}$$

Equation (3.4) provides the analytical basis for the steady-state stator-voltage compensations widely used in a conventional feed-forward current regulator (see Figure 2.5) for the DFIG RSC control. These steady-state compensations are directly inherited from the traditional motor control scheme [35] (a dual system of DFIGs), where no disturbances would normally occur at the rotor side. As a result, equation (3.4) offers correct compensations only in balanced steady-state stator-voltage conditions. For DFIGs, the stator is exposed to different grid disturbances. The full transient model, (3.2), is needed to provide correct transient compensations in the current control loops during fault transients or unbalanced stator-voltage conditions.

3.2.2 DFIG Electromagnetic Dynamics during Grid Faults

Figure 3.1 shows the simulated DFIG stator flux dynamics during a balanced three-phase-to-ground fault. The stator voltage drops abruptly to about 0.3 pu, resulting in a decaying DC component in the stator flux (the center of the stator-flux rotating track is temporarily off the origin), as shown in Figure 3.1 (a). In the synchronous reference frame, this DC component becomes 60 Hz, as shown in Figure 3.1 (b). Compared to the stator voltage, the stator flux decays slower, and equation (3.3) does not hold during the flux transient period. As a result, the traditional feed-forward current regulator would result in inaccurate stator-voltage compensations. Figure 3.2 shows a typical waveform of the magnitude of the rotor current space vector controlled by a traditional feed-forward current regulator during the same balanced grid fault. A large transient current overshoot is observed.

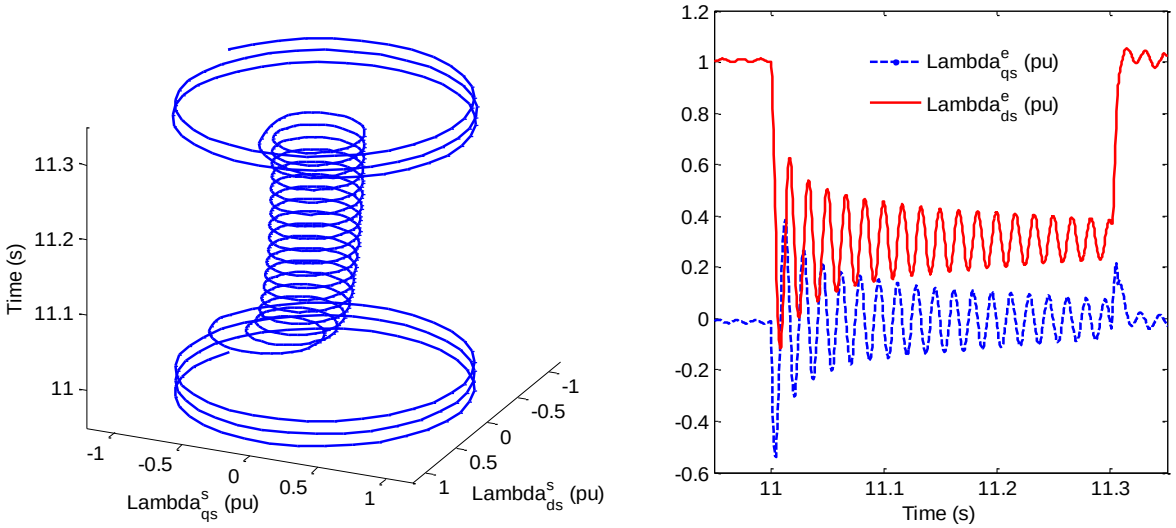

(a) (b)

Figure 3.1 Typical DFIG stator flux linkage in (a) stationary and (b) synchronous reference frames during a three-phase-to-ground grid fault.

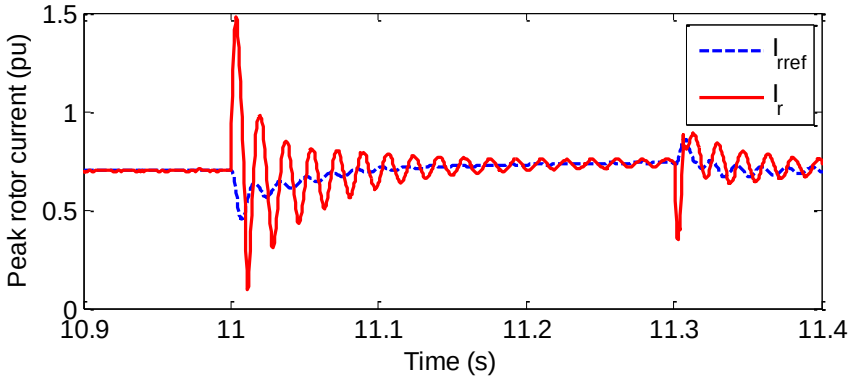

Figure 3.2 Typical DFIG rotor current during a balanced three-phase fault (controlled by a traditional feed-forward current regulator with crowbar disabled).

Figure 3.3 shows the simulated DFIG stator flux dynamics during an unbalanced single-phase-to-ground fault. Besides the temporary DC component, the stator flux contains a negatively rotating component. Its rotating path becomes an ellipse, as shown in Figure 3.3 (a). In the synchronous reference frame, this negatively rotating component is a 120 Hz signal, which is superimposed on the decaying 60 Hz signal in Figure 3.3 (b). The rotor current overshoots during an unbalanced grid fault depends on the initial point-on-wave at the fault instant [105]. A higher post-fault natural flux (the decaying DC component) results

in a higher rotor-current overshoot [105]. Figure 3.4 shows a typical waveform of the magnitude of the rotor current space vector during the same unbalanced single-phase-to-ground fault. A current overshoot caused by the post-fault DC flux is observed at the fault instant, and a 120 Hz component persists during the unbalanced grid fault.

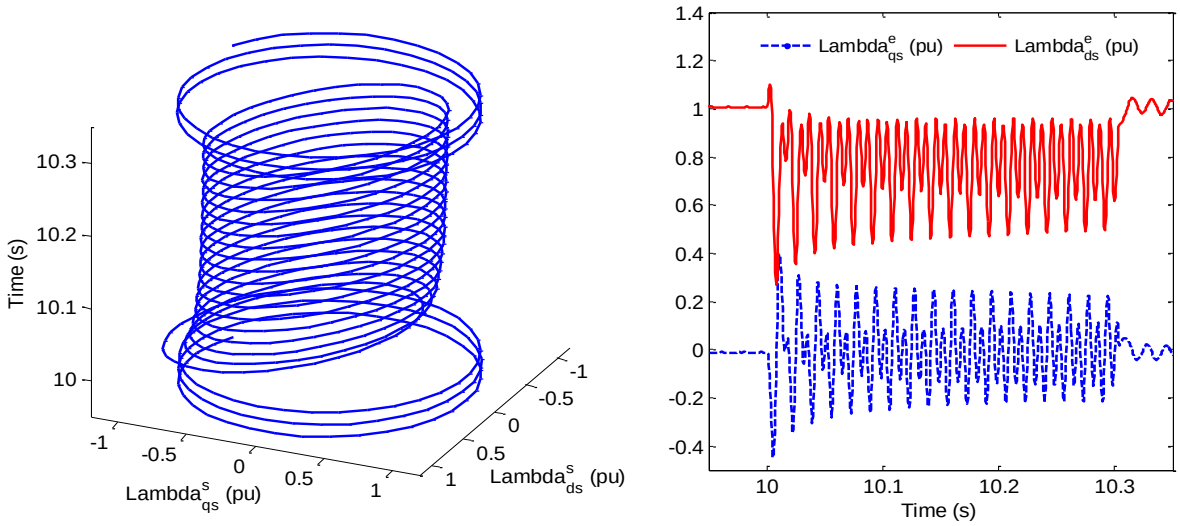

(a) (b)

Figure 3.3 Typical DFIG stator flux linkage in (a) stationary and (b) synchronous reference frames during a single-phase-to-ground grid fault.

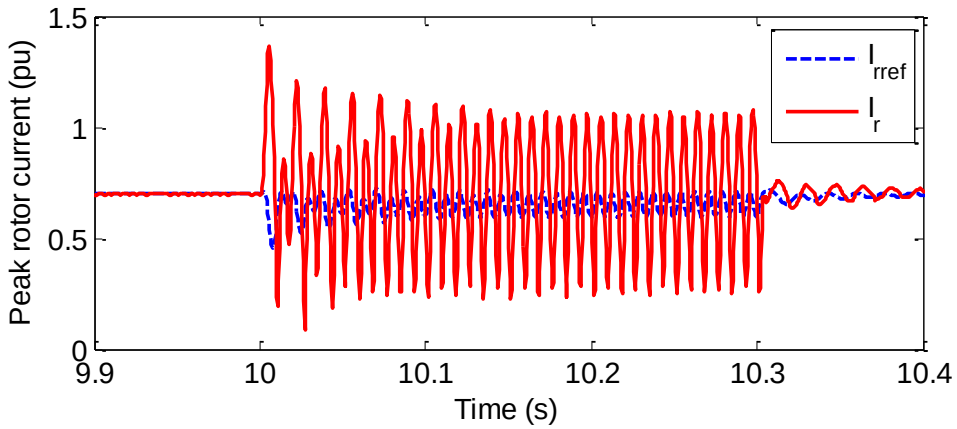

Figure 3.4 Typical DFIG rotor current during an unbalanced single-phase fault (controlled by a traditional feed-forward current regulator with crowbar disabled).

3.2.3 DFIG Electromechanical Model

The instantaneous electromagnetic torque (in physical units) of a DFIG is given by [35]

$$T_e = -\frac{3}{2}\frac{P}{2}\frac{L_m}{L_s}(\lambda_{qs}^e i_{dr}^e - \lambda_{ds}^e i_{qr}^e) \quad (3.5)$$

where a positive torque means generating positive electric power from the generator to the grid, and the coefficient 3/2 comes from the *dq* transformation. Under steady-state balanced stator-voltage conditions, $\lambda_{qs}{}^e = 0$ and $\lambda_{ds}{}^e$ is a constant. Thus, T_e is only related to $i_{qr}{}^e$.

However, during stator-voltage transient or unbalanced conditions, $\lambda_{qs}{}^e$ is not equal to zero, and $\lambda_{ds}{}^e$ varies, as shown in Figure 3.1 (b) and Figure 3.3 (b). To minimize torque ripples, both the *dq* stator flux linkages and *dq* rotor currents need to be considered

3.3 Feed-Forward Transient Compensation Control

3.3.1 Schematic Framework of Feed-Forward Transient Compensation Control

The schematic framework of the proposed feed-forward transient compensation control is shown in Figure 3.5. A synchronous-reference-frame-based three-phase phase-locked loop (PLL) is used to provide the *dq* transformation angle. The *q* axis is locked to the positive-sequence stator voltage. Two additional feed-forward transient compensation blocks are added to the traditional vector control scheme.

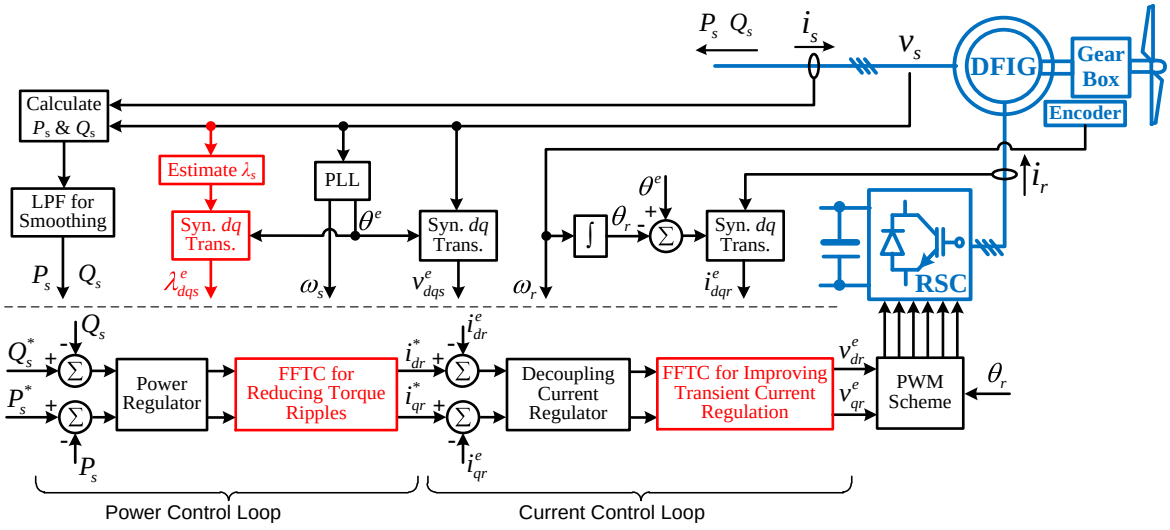

Figure 3.5 Feed-forward transient compensation control for DFIGs.

3.3.2 Synchronous-Reference-Frame-based Three-Phase Phase-Locked Loop

Figure 3.6 shows the general block diagram of a synchronous-reference-frame-based three-phase PLL [106], where $G(s)$ is a controller that maintains v_{ds}^{e} to be zero, i.e., the q axis is locked to the three-phase voltage vector. For most grid-interfacing power electronic systems, a PLL that tracks the positive-sequence voltage is desired to avoid the injection of negative-sequence current [107]. When a proportional-integral (PI) regulator is used for $G(s)$, the PLL closed-loop small-signal system is given by [106]

$$H(s) = \frac{2\zeta\omega_n s + \omega_n^2}{s^2 + 2\zeta\omega_n s + \omega_n^2}$$
$$\omega_n = \sqrt{V_m K_i},\ \zeta = \frac{\sqrt{V_m K_p^2 / K_i}}{2}, \tag{3.6}$$

where ω_n is the natural frequency, ζ is the damping ratio, V_m is the peak phase voltage, K_p and K_i are the proportional and integral gains of the PI regulator. In this research, a low natural frequency of 10 Hz and a damping ratio of 0.707 are used to reject negative-sequence stator voltage.

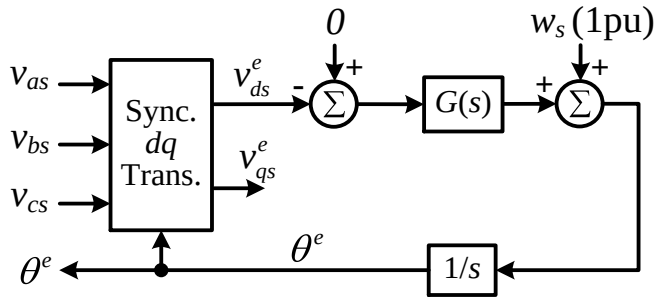

Figure 3.6 Block diagram of a three-phase PLL.

A laboratory three-phase voltage sag generator [108], as shown in Figure 3.7, is set up to test the resulting PLL performance during both balanced and unbalanced grid faults. Detailed hardware implementation of the voltage sag generator is described in Appendix B.

Figure 3.8 and Figure 3.9 show the experimental PLL performances during a three-phase-to-neutral and a phase-A-to-neutral grid fault. The angle error (*Ang Err* in Figure 3.8 and Figure 3.9) between the PLL output angle and a synchronously rotating angle is less than 3% in both cases. The PI-based PLL is able to provide a good tracking to the positive-sequence stator voltage even during grid disturbances.

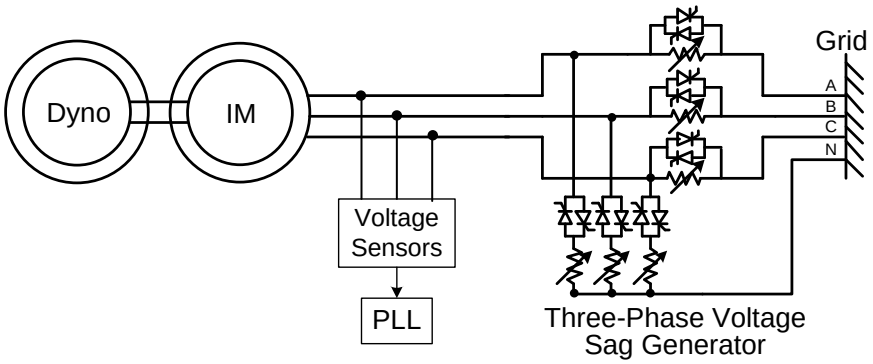

Figure 3.7 A laboratory voltage sag generator for testing PLL during grid faults.

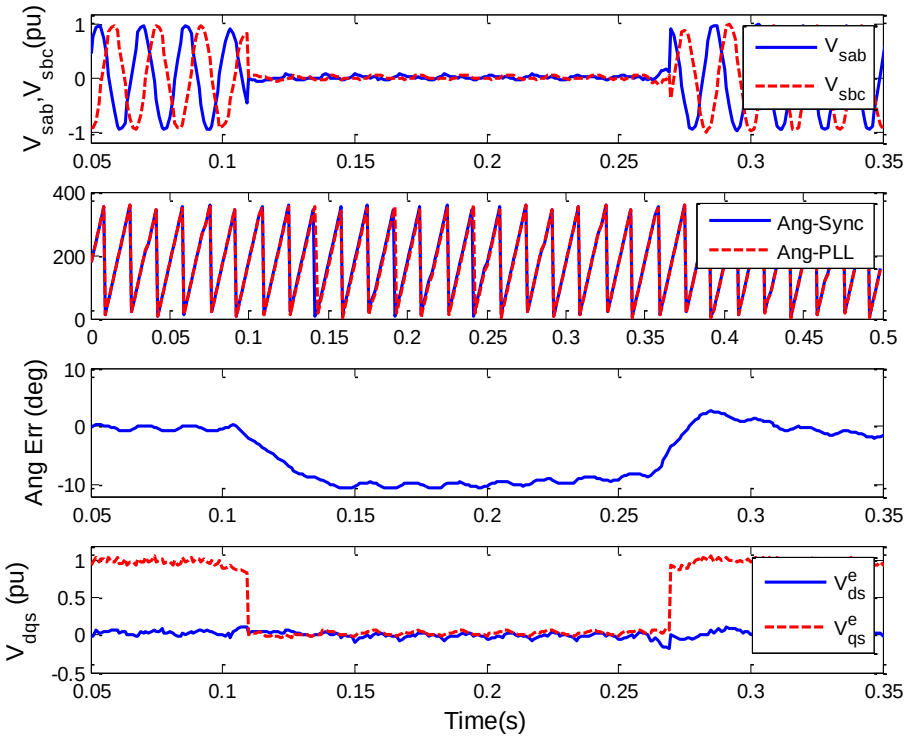

Figure 3.8 PLL performance during a three-phase-to-neutral grid fault.

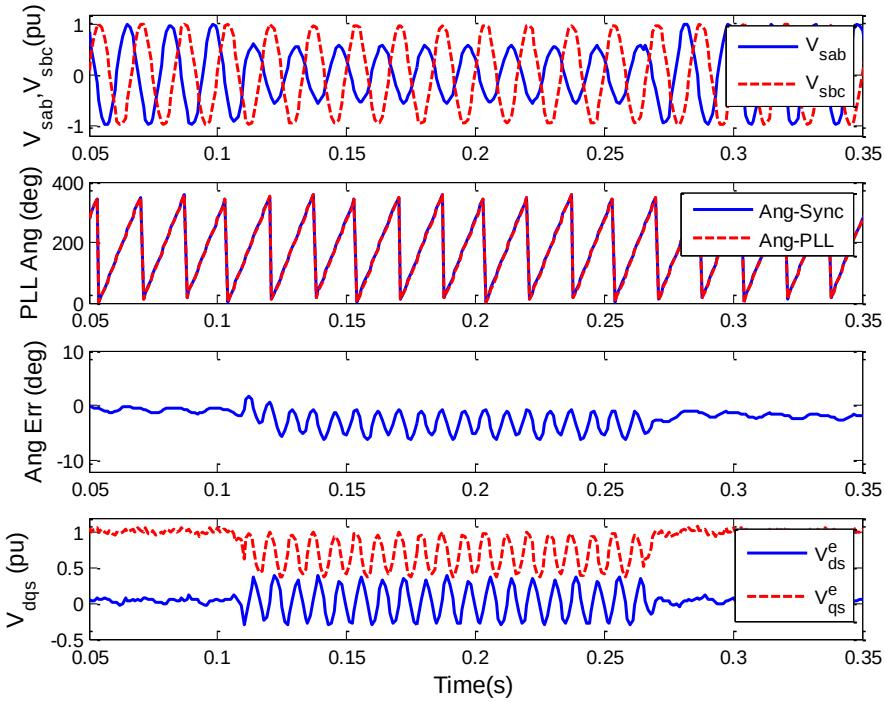

Figure 3.9 PLL performance during a phase-A-to-neutral grid fault.

3.3.3 Feed-Forward Transient Compensation Design for Current Control Loop

Based on (3.2), the feed-forward transient compensation scheme for the current control loop is shown in Figure 3.10. The complete transient voltages induced from the stator side are feed-forward injected into the rotor-current control loop without the assumption on steady-state balanced stator voltage. However, because the feed-forward compensations depend on the knowledge of system parameters, without accurate compensations, the rotor currents may contain 60 Hz and 120 Hz components during abnormal grid-voltage conditions. To better regulate the transient rotor currents, proportional-integral-resonant (PIR) current regulators [109] are employed, as shown in Figure 3.11, where resonant blocks for ω_s and $2\omega_s$ are added in parallel to a PI regulator. β is the bandwidth (in rad/s) of the resonant block, and K_R is the gain at the resonant frequency. Figure 3.12 shows the equivalent implementation of a resonant regulator in digital processors using proportional and integral blocks.

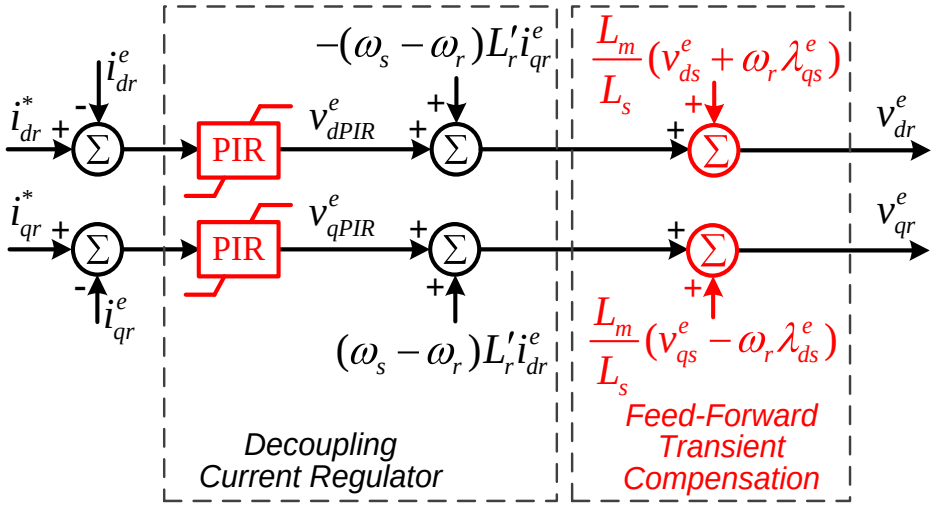

Figure 3.10 Current-loop feed-forward transient compensation scheme.

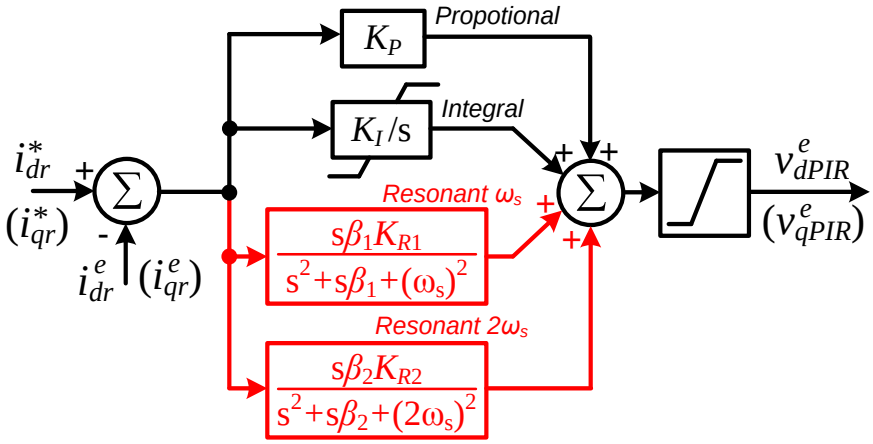

Figure 3.11 Proportional-integral-resonant (PIR) current regulator.

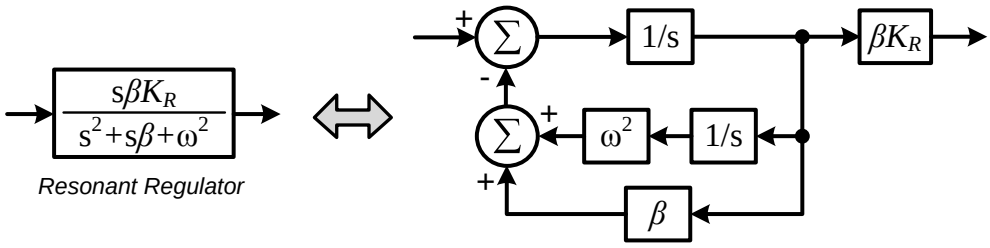

Figure 3.12 Implementation of a resonant regulator block.

In Figure 3.10, the stator flux is estimated by integrating the stator voltage in the stationary $\alpha\beta$ reference frame, as shown in Figure 3.13. The synchronous dq transformation

angle, θ^e, obtained from the PLL is then used to transform the stator flux from the stationary reference frame to the synchronous reference frame.

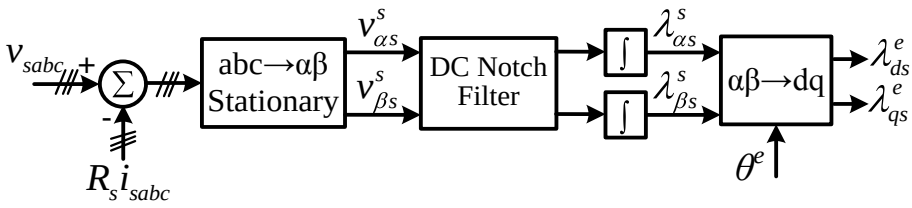

Figure 3.13 Estimation of stator flux linkage.

Based on the feed-forward transient compensation scheme shown in Figure 3.10, the rotor-side converter (RSC) *dq* output voltages are given by

$$\begin{aligned} v^e_{dr} &= PIR(i^*_{dr} - i^e_{dr}) - (\omega_s - \omega_r)L'_r i^e_{qr} + \frac{L_m}{L_s}(v^e_{ds} + \omega_r \lambda^e_{qs}) \\ v^e_{qr} &= PIR(i^*_{qr} - i^e_{qr}) + (\omega_s - \omega_r)L'_r i^e_{dr} + \frac{L_m}{L_s}(v^e_{qs} - \omega_r \lambda^e_{ds}) \end{aligned} \quad . \tag{3.7}$$

Substituting (3.7) into (3.2) yields the closed-loop transfer function of the current control loop, as in

$$\frac{i^e_{dr}(s)}{i^*_{dr}(s)} = \frac{i^e_{qr}(s)}{i^*_{qr}(s)} = \frac{PIR(s)}{R_r + sL'_r + PIR(s)} \quad . \tag{3.8}$$

where *s* in (3.8) is the Laplace operator. Using (3.8), the current control loop can be designed using the Bode plot technique. For example, using the 4 MVA, 4.16 kV DFIG parameters listed in Appendix A, with a switching frequency of 1k to 2k Hz, the proportional and integral paths are first designed to have a cut-off frequency of about 100 Hz, and then the resonant paths are added to allow approximately unity gain and zero phase shift at 60 Hz and 120 Hz. The resulting Bode plots of the closed-loop current controller with feed-forward transient compensations and PIR regulators are shown in Figure 3.14.

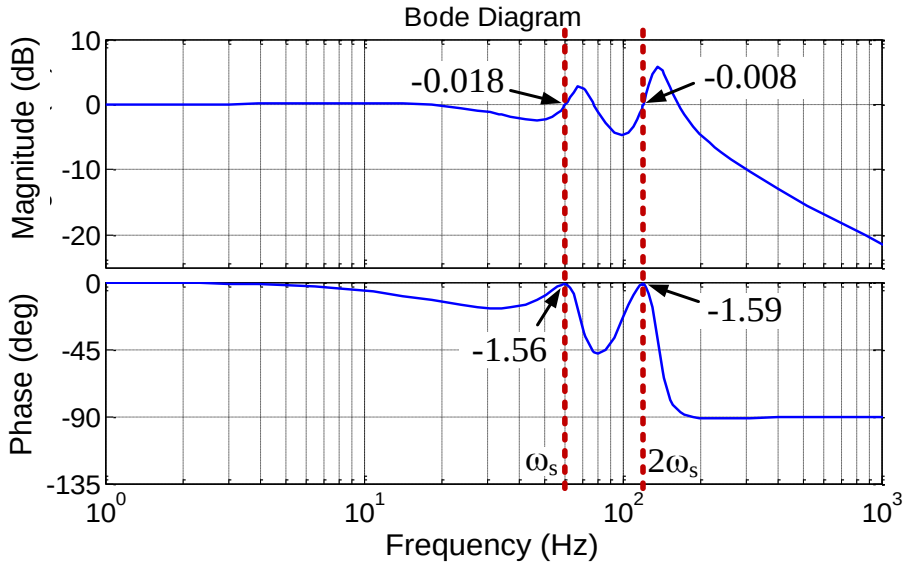

Figure 3.14 Bode plots of close-loop current control system.

3.3.4 Feed-Forward Transient Compensation Design for Power Control Loop

Based on (3.5), the power-loop feed-forward transient compensation design for reducing torque ripples is shown in Figure 3.15. V_{pk} is the nominal peak phase voltage, and V_{pk}/ω_s is the nominal stator flux linkage. The limiting block is used to set the *q*-axis current limits during transient conditions. The *q*-axis rotor current command before the limiting block is then given by

$$i_{qr}^{*} = \frac{1}{\max(\lambda_{ds}^{e}, 0)}\left[\frac{V_{pk}}{\omega_s} PI(P_s^{*} - P_s) + \lambda_{qs}^{e} i_{dr}^{e}\right] \quad (3.9)$$

Abrupt jumps of i_{qr}^{*} between its upper and lower limits may occur when λ_{ds}^{e} crosses zero during the first few cycles of a severe grid fault [see Figure 3.1 (b)]. To avoid instability, only the positive λ_{ds}^{e} is fed into the power control loop.

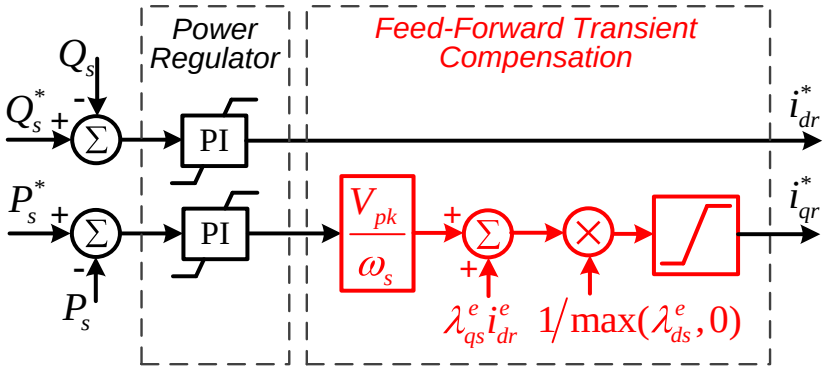

Figure 3.15 Power-loop feed-forward transient compensation scheme.

During steady-state balanced grid-voltage conditions, $\lambda_{ds}^e = V_{pk}/\omega_s$ and $\lambda_{qs}^e = 0$. The feed-forward transient compensation block shown in Figure 3.15 has no effects on i_{qr}*. During abnormal grid-voltage conditions, 60 Hz and 120 Hz components are intentionally injected into i_{qr}^* by the feed-forward terms. Since a good tracking of the rotor current at both 60 Hz and 120 Hz is achieved by the proposed feed-forward transient compensation current controller, when $\lambda_{ds}^e > 0$, substituting (3.9) into (3.5) yields

$$T_e = \frac{3}{2}\frac{P}{2}\frac{L_m}{L_s}\frac{V_{pk}}{\omega_s} PI(P_s^* - P_s) \quad (3.10)$$

The outer power control loop is usually designed with a relatively low bandwidth (usually less than one tenth of the current-loop bandwidth). The outputs of the PI power regulators thus have minimal 60 Hz and 120 Hz components. As a result, from (3.10), the electromagnetic torque ripples are reduced.

3.4 LVRT Capability of the Feed-Forward Transient Compensation Control Considering Converter Ratings

3.4.1 DFIG Rotor Back EMF during Grid Faults

The second term on the right-hand side of (3.2) represents the back electromotive force (EMF) seen from the DFIG rotor terminals. To simplify the conversion between stator and

rotor quantities, the per-unit (pu) system is used in the following discussion. In pu, the mutual inductance and the stator inductance are about the same, i.e., $L_m/L_s \approx 1$. The instantaneous rotor back EMF space vector can be written as a complex number and further decomposed into the positive- and negative-sequence components, as in

$$\begin{aligned}\vec{v}^{\,e}_{rEMF} &= v^e_{drEMF} + jv^e_{qrEMF} \\ &= (v^e_{ds} + \omega_r \lambda^e_{qs}) + j(v^e_{qs} - \omega_r \lambda^e_{ds}) \\ &= (v^e_{ds+} + \omega_r \lambda^e_{qs+}) + j(v^e_{qs+} - \omega_r \lambda^e_{ds+}) \\ &\quad + (v^e_{ds-} + \omega_r \lambda^e_{qs-}) + j(v^e_{qs-} - \omega_r \lambda^e_{ds-})\end{aligned}. \tag{3.11}$$

As illustrated in Figure 3.16, if the *dq* transformation angle is attached to the positive-sequence stator voltage by the PLL, then

$$\begin{aligned} v^e_{ds+} &= 0,\ v^e_{qs+} = v_{s+} \\ \lambda^e_{ds+} &= \lambda_{s+},\ \lambda^e_{qs+} = 0 \end{aligned}. \tag{3.12}$$

In steady state, $p\lambda_{ds+}{}^e = p\lambda_{qs+}{}^e = 0$, $p\lambda_{ds-}{}^e = 2\omega_s\lambda_{qs-}{}^e$, and $p\lambda_{qs-}{}^e = -2\omega_s\lambda_{ds-}{}^e$. Thus, from the stator-voltage equations in (3.1), the relationship between the steady-state stator voltage and flux is given by (neglecting stator resistance)

$$\begin{aligned} v^e_{ds+} &= -\omega_s \lambda^e_{qs+},\ v^e_{qs+} = \omega_s \lambda^e_{ds+} \\ v^e_{ds-} &= \omega_s \lambda^e_{qs-},\ v^e_{qs-} = -\omega_s \lambda^e_{ds-} \end{aligned}. \tag{3.13}$$

From (3.11) to (3.13), the prefault ($t = t_f^-$) steady-state DFIG rotor back EMF (assuming balanced stator voltage, i.e. $v_{ds-}{}^e = v_{qs-}{}^e = 0$) is given by

$$\vec{v}^{\,e}_{rEMF}\,|_{t=t_f^-} = j(v^e_{qs+} - \omega_r \lambda^e_{ds+}) = jsv_{s+}, \tag{3.14}$$

where s is the slip. During normal operation, the magnitude of the rotor-side converter (RSC) output-voltage is thus approximately sV_s in pu. If the exciting current is neglected, the DFIG stator and rotor currents are the same in pu. As a result, if the DFIG slip is limited between -0.3 and 0.3, the RSC requires a rating of only 30% of the generator rating. The actual RSC voltage

rating is usually higher to have sufficient transient-current regulation capability.

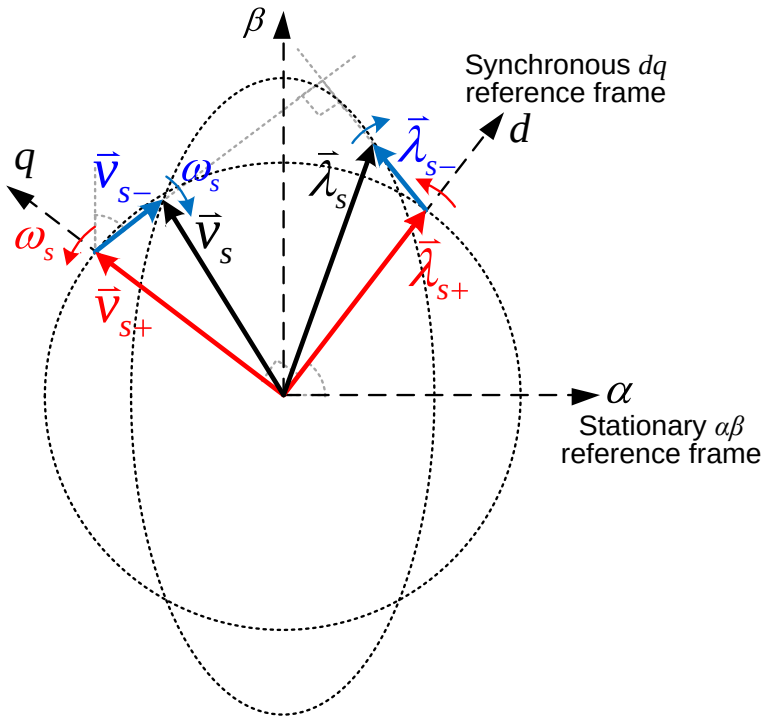

Figure 3.16 Positive- and negative-sequence stator voltage and flux vectors in pu.

3.4.1.1 DFIG Rotor Back EMF during Balanced Grid Faults

Since flux cannot change abruptly, at the instant of an abrupt stator-voltage drop, the stator flux will be the same as its prefault value, $V_{sPrefault}/\omega_s$, where $V_{sPrefault}$ is the magnitude of the prefault stator voltage. For a balanced grid fault, neglect the effect of stator voltage phase-angle jump, which is usually small for transmission systems [105], [110], and let V_{sFault} denote the magnitude of the stator voltage at the first instant after the fault ($t = t_f^+$). From (3.14), the magnitude of the rotor back EMF at $t = t_f^+$ is given by

$$V_{rEMF}\big|_{t=t_f^+} = \left|(v^e_{qs+}\big|_{t=t_f^+}) - \omega_r(\lambda^e_{ds+}\big|_{t=t_f^-})\right| = \left|V_{sFault} - (1-s)V_{sPrefault}\right| . \qquad (3.15)$$

Assuming the prefault stator voltage is 1 pu, from (3.15), Figure 3.17 shows the post-fault rotor back EMF at t = 0+ as a function of V_{sFault}. The most severe case (highest rotor back EMF)

happens when the DFIG is operated at the maximum super-synchronous speed (s = -0.3). In this case, if the stator voltage suddenly drops to zero, the rotor back EMF becomes 1.3 pu.

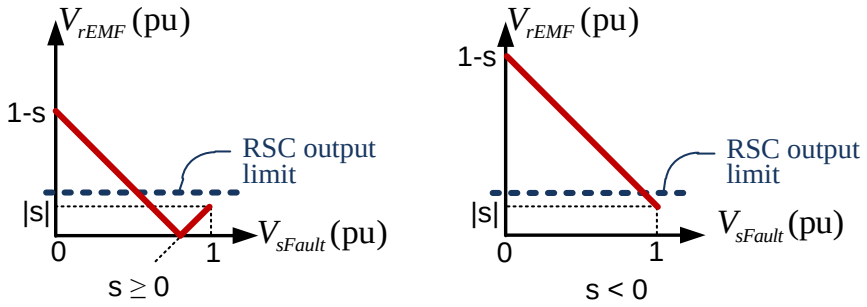

Figure 3.17 DFIG rotor back EMF at the first instant after an abrupt balanced grid fault.

3.4.1.2 DFIG Rotor Back EMF during Unbalanced Grid Voltage

When the stator voltage is unbalanced, from (3.11) to (3.13),

$$\begin{aligned}\vec{v}^{e}_{rEMF} &= jsv^{e}_{qs+} + (2-s)v^{e}_{ds-} + j(2-s)v^{e}_{qs-} \\ &= s\vec{v}^{e}_{s+} + (2-s)\vec{v}^{e}_{s-}\end{aligned} \quad (3.16)$$

The magnitude of the rotor back EMF with an unbalanced grid voltage is thus

$$V_{rEMF} = |s|V_{s+} + (2-s)V_{s-}, \quad (3.17)$$

where V_{s+} is the magnitude of the positive-sequence stator voltage, and V_{s-} is the magnitude of the negative-sequence stator voltage.

For a single-phase-to-ground fault, assume $\tilde{V}_{as} = V_f \angle 0°$, $\tilde{V}_{bs} = 1\angle -120°$, $\tilde{V}_{cs} = 1\angle 120°$, where V_f is the phase A voltage magnitude in pu during the fault. From the symmetrical component transformation [17], the stator-voltage sequence components are given by

$$V_{s+} = (2+V_f)/3,\ V_{s-} = (1-V_f)/3. \quad (3.18)$$

Substituting (3.18) into (3.17) yields

$$V_{rEMF} = \begin{cases} [2 + s - 2(1-s)V_f]/3 & s \geq 0 \\ [2 - 3s - 2V_f]/3 & s < 0 \end{cases} . \tag{3.19}$$

The most severe case happens at the maximum super-synchronous operation (s = -0.3) when the phase A voltage becomes zero. In such a case, the peak rotor back EMF is 0.97pu

For a phase-to-phase grid fault represented by $\tilde{V}_{as} = 1$, $\tilde{V}_{bs} = -\frac{1}{2} - j\frac{\sqrt{3}}{2}V_f$, $\tilde{V}_{cs} = -\frac{1}{2} + j\frac{\sqrt{3}}{2}V_f$, the stator-voltage sequence components are given by,

$$V_{s+} = (1+V_f)/2,\ V_{s-} = (1-V_f)/2 . \tag{3.20}$$

Substituting (3.20) into (3.17),

$$V_{rEMF} = \begin{cases} 1-(1-s)V_f & s \geq 0 \\ (1-s)-V_f & s < 0 \end{cases} . \tag{3.21}$$

The most severe case happens when the DFIG is operated at maximum super-synchronous speed (s = -0.3) and V_f becomes zero. In such a case, the peak rotor back EMF is 1.3 pu.

Equation (3.15) provides the peak rotor back EMF at the transient period of balanced grid voltage drops, and Equation (3.17) provides the peak rotor back EMF during unbalanced grid-voltage conditions. During abnormal grid conditions, the rotor back EMF needs to be compensated by the RSC to avoid transient rotor current overshoots, as illustrated by the single-phase equivalent of the DFIG rotor circuit shown in Figure 3.18.

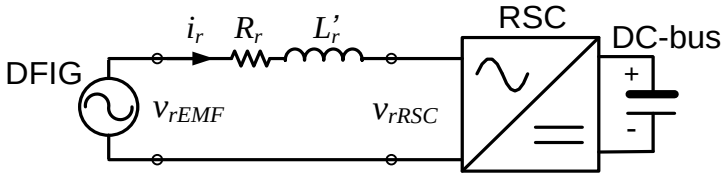

Figure 3.18 Single-phase equivalent of the DFIG rotor circuit.

3.4.2 Rotor-Current Overshoot Minimization Capability of Feed-Forward Transient Compensation Control

The rotor-current overshoot is generally higher for a three-phase-to-ground grid fault, which has a higher post-fault natural flux component (higher transient rotor back EMF). The proposed feed-forward transient compensation control scheme reduces current overshoots by directly counteracting the transient rotor back EMF using the additional transient compensation terms. The actual current control capability of a voltage source inverter depends on the DC-bus voltage, limited by the voltage ratings of the rotor-side converter (RSC) power electronic devices and the DC capacitor. Suppose that the maximum RSC output voltage is k pu. For a balanced grid fault, from (3.15), the feed-forward transient compensation control scheme is capable of eliminating the transient rotor current when

$$V_{sFault} > 1\text{-}s\text{-}k \text{ pu.} \tag{3.22}$$

For severe grid faults, the transient back EMF in the rotor circuit may be greater than the maximum RSC output, resulting in RSC over-modulation and an uncontrolled transient rotor current. However, if the RSC output voltage, $\vec{v}_{rRSC}$, is aligned with the rotor back EMF, $\vec{v}_{rEMF}$, the residual voltage across the rotor circuit is minimized, as shown in Figure 3.19.

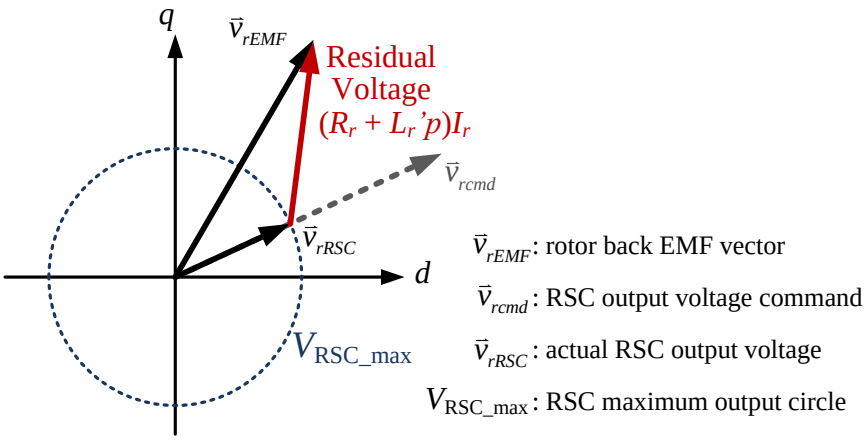

Figure 3.19 Rotor voltage space vectors.

With correct compensations in the rotor current controller, the proposed feed-forward transient compensation control scheme directly aligns the RSC output voltage with the rotor back EMF and results in a minimal transient rotor current overshoot.

3.4.3 Torque-Ripple Minimization Capability of Feed-Forward Transient Compensation Control

During unbalanced grid faults, to eliminate torque ripples by injecting transient compensation terms into the power control loop, the RSC needs to at least compensate for the peak rotor back EMF given by (3.17). For severe unbalanced grid faults, it has been shown that the rotor back EMF may exceeds the maximum RSC output voltage. Suppose that the maximum RSC output voltage is k pu. For example, for a single-phase-to-ground fault, from (3.19), the feed-forward transient compensation control scheme is able to suppress torque ripples when

$$\begin{cases} V_f \geq \dfrac{2+s-3k}{2(1-s)} & s \geq 0 \\ V_f \geq 1-1.5s-1.5k & s < 0 \end{cases}, \tag{3.23}$$

where V_f is the phase A voltage in pu during the grid fault.

3.5 Simulation Studies in a Single-Machine Infinite-Bus Power System

3.5.1 Simulation System

A 3.6 MW, 4.16 kV DFIG wind turbine system [29] is simulated in PSCAD/EMTDC to demonstrate the effectiveness of the proposed feed-forward transient compensation control scheme. The DFIG wind turbine is modeled as a two-mass system. The rotor-side converter (RSC) and grid-side converter (GSC) are represented by a switch-level model. The rated DC-bus voltage is set to 3.5 kV. With a stator-to-rotor turns ratio of 1, the rated stator and rotor currents for this machine are both 0.555 kA in RMS value and 0.785 kA in peak value.

The detailed parameters of this DFIG wind turbine system are listed in Appendix A. The one-line diagram of the simulated system appears in Figure 3.20. The overall control schematics for the RSC and GSC are shown in Figure 3.21 and Figure 3.22.

An active crowbar circuit (shown in Figure 3.21) with a 0.5 pu resistor [45] is implemented to protect the RSC from over-current. The crowbar turns on when the rotor current exceeds 0.9 kA, and it turns off when the stator voltage is back to normal conditions. When the crowbar is on, the RSC triggering is block. A DC chopper circuit (shown in Figure 3.22) with a 0.5 pu resistor is also implemented across the DC bus to protect both the converters from over-voltage. The DC chopper limits the DC-bus voltage to 4 kV.

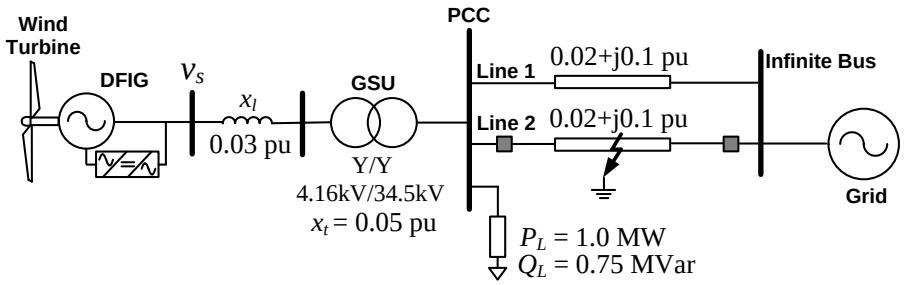

Figure 3.20 One-line diagram of the simulation system.

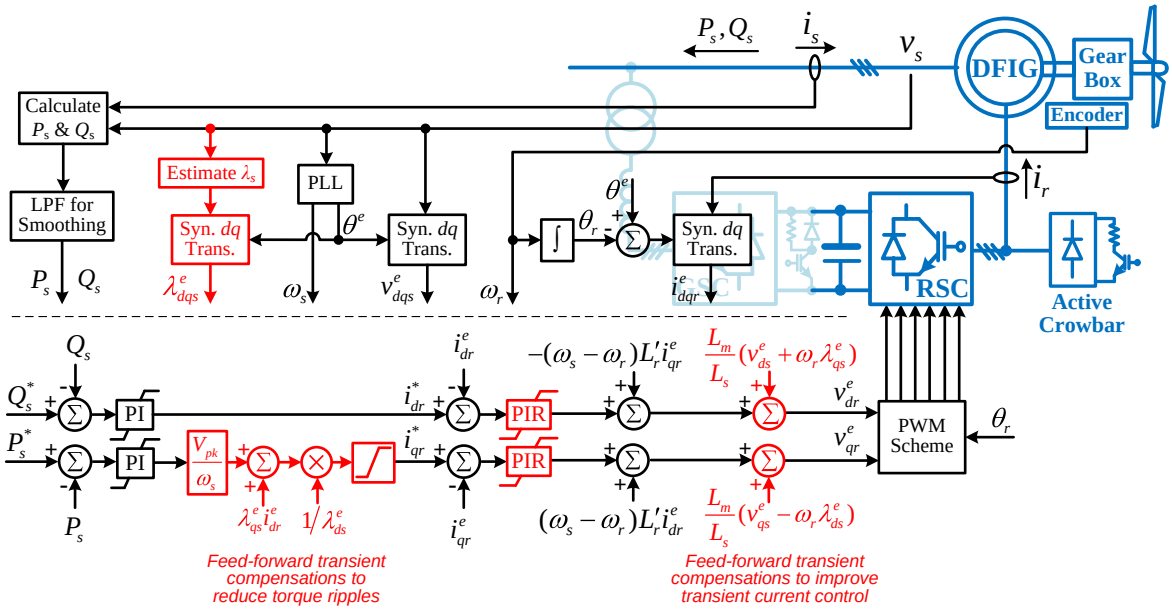

Figure 3.21 Overall control diagram for RSC.

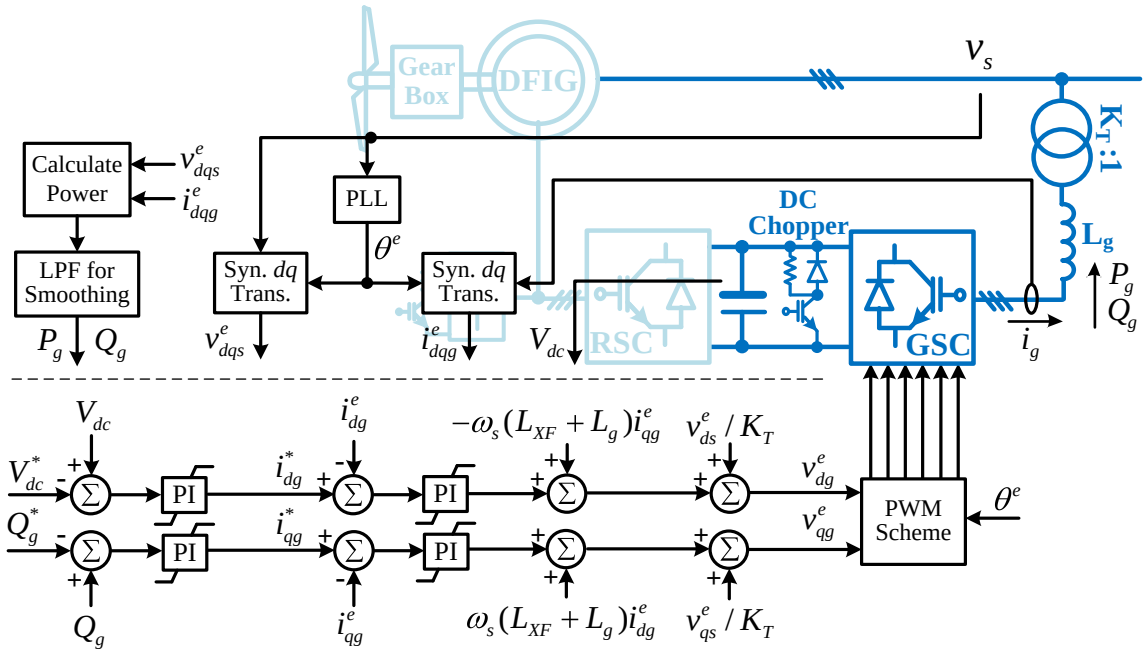

Figure 3.22 Overall control diagram for GSC.

From the analysis in Section 3.4, it is more difficult to ride through faults in super-synchronous conditions. Thus for evaluation purposes, the DFIG is operated at a super-synchronous speed at a slip of -0.21. Four different control cases are compared, as listed in Table 3.1. *Case 1* uses the traditional steady-state compensations with PI current regulators, the crowbar protection is disabled, and the RSC continues switching regardless of the current level. *Case 1* is simulated to show the transient current waveforms during grid faults. For *Cases 2* to *4*, the crowbar protection is enabled. *Case 2* uses the same control scheme as in *Case 1*. *Case 3* applies the proposed feed-forward transient compensation control to only the current loop with PIR current regulators. *Case 4* applies the proposed feed-forward transient compensation control to both the power and current loops with PIR current regulators.

Table 3.1 Control cases for comparison during grid faults.

Case	Control Schemes	Crowbar
1	Steady-state compensations with PI current regulators	Disabled
2	Steady-state compensations with PI current regulators	Enabled
3	Feed-forward transient compensations for only the current loop with PIR current regulators	Enabled
4	Feed-forward transient compensations for both power and current loops with PIR current regulators	Enabled

3.5.2 Simulation Results during a Three-Phase-to-Ground Fault

In order to compare the control performance during balanced grid faults, a three-phase-to-ground fault is applied at Line 2 in Figure 3.20 from 1 s to 1.15 s, causing the stator voltage to drop to about 0.6 pu. Figure 3.23 and Figure 3.24 show the simulation results for the four control cases in Table 3.1.

For *Case 1* with crowbar disabled, the RSC current goes up to 0.95 kA at the instant of the grid fault, as shown in Figure 3.23. As a result, in *Case 2*, the crowbar circuit turns on to divert the large transient current. Once the crowbar is on, the DFIG starts to consume reactive power from the grid, and further reduces the stator voltage to about 0.55 pu. Meanwhile, the generator follows the torque-speed curve of an induction machine, and produces much less active power, as shown in Figure 3.23.

With the proposed feed-forward transient compensation control scheme, *Cases 3* and *4* (see Figure 3.24) show almost the same responses for this balanced grid fault. The transient rotor currents are well controlled without any overshoots. The proposed feed-forward transient compensation control prevents the occurrence of DFIG control interruption. Both *Cases 3* and *4* provide good transient current control performance, and result in an uninterrupted active and reactive power generation.

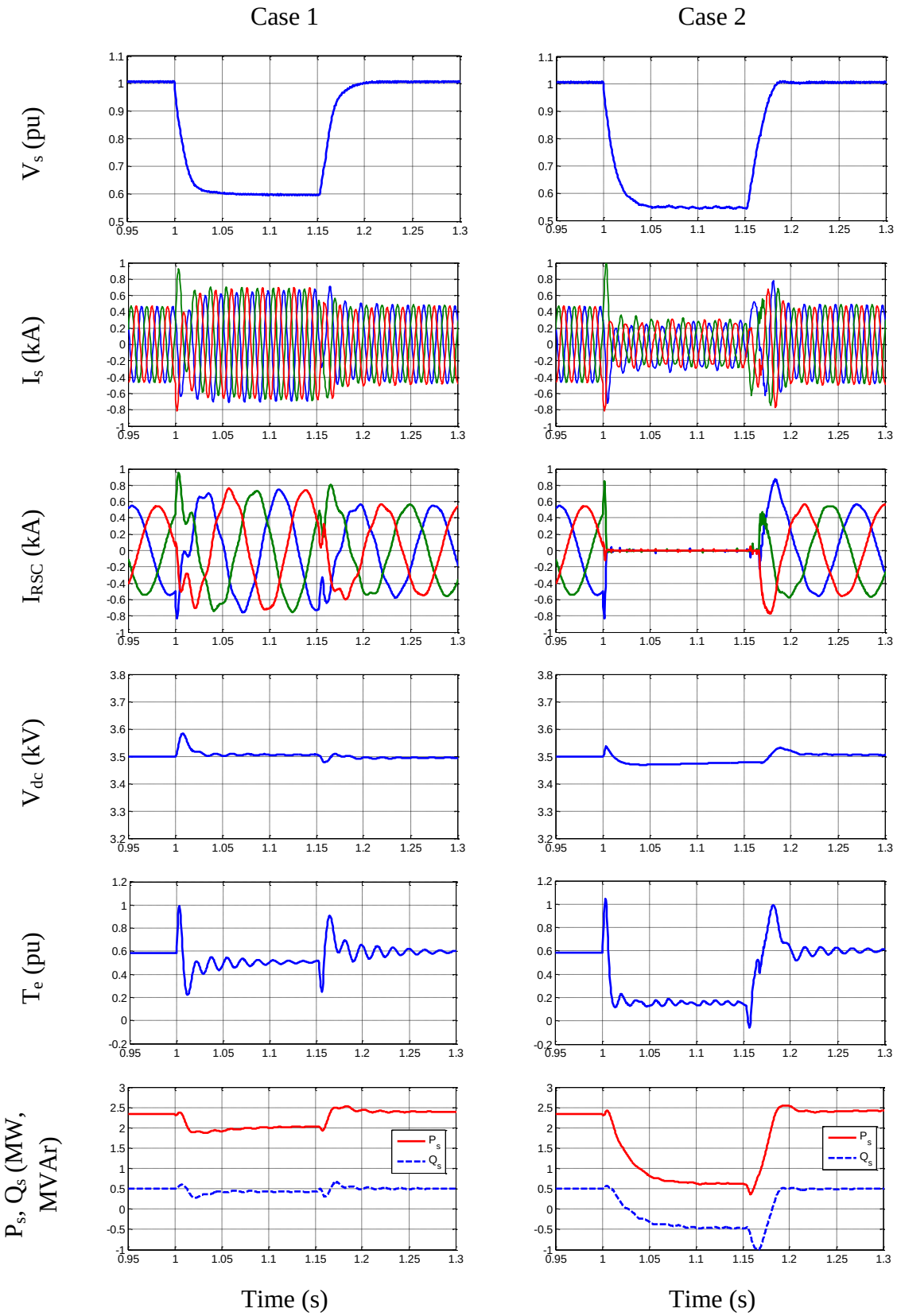

Figure 3.23 Simulated DFIG responses with different control schemes during a balanced three-phase fault: *Cases 1* and *2*.

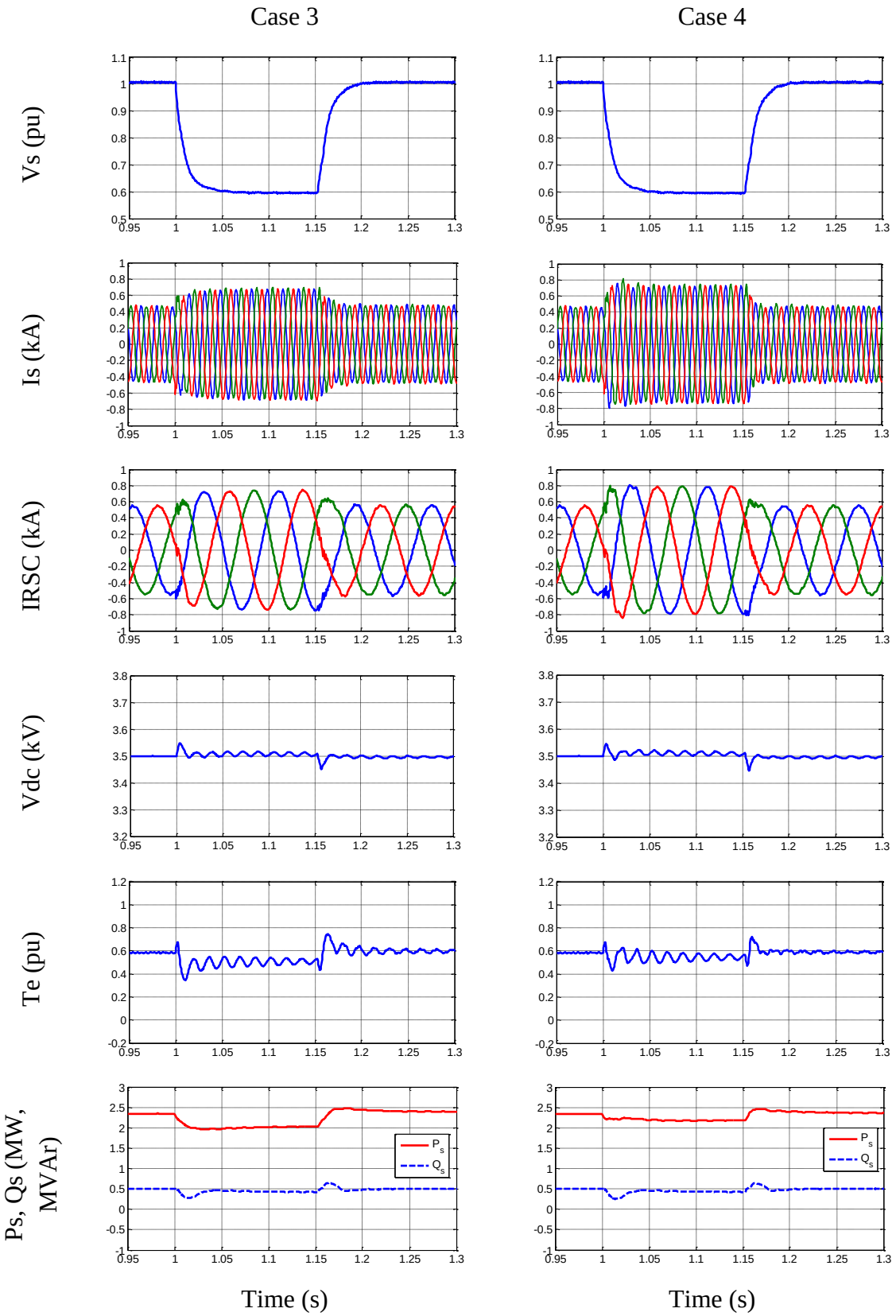

Figure 3.24 Simulated DFIG responses with different control schemes during a balanced three-phase fault: *Cases 3* and *4*.

3.5.3 Simulation Results during a Single-Phase-to-Ground Fault

In order to evaluate the control performance during an unbalanced grid fault, a phase-A-to-ground fault is applied at Line 2 in Figure 3.20 from 1 s to 1.3 s. The phase A voltage at the point of common coupling (PCC, see Figure 3.20) drops to 0.6 pu, and the DFIG stator voltage has a 20% unbalance factor (the ratio between the negative- and positive-sequence components). Figure 3.25 and Figure 3.26 show the simulation results for the four control cases listed in Table 3.1.

With regular steady-state compensations in *Cases 1* and *2*, a large negative-sequence current appears at the stator side, as shown in Figure 3.25. The electromagnetic torque experiences large second-order harmonic ripples. Again, once the crowbar turns on, the generator loses active control over its active and reactive power outputs; the active power output drops and the machine starts to absorb reactive power from the grid, as shown in *Case 2* of Figure 3.25.

In *Case 3*, when the feed-forward transient compensation control is applied to the current control loop, the transient rotor and stator currents remain under control without any overshoots or negative-sequence components, as shown in Figure 3.26. As a result, the crowbar circuit does not need to turn on. Both active and reactive power supplies remain uninterrupted. The torque ripples are also reduced in this case, as compared to *Cases 1* and *2*.

In *Case 4*, the feed-forward transient compensation control scheme is further applied to the power control loop. Second-order harmonic current is intentionally injected, and the torque ripples are further reduced, as shown in *Case 4* of Figure 3.26. This small amount of current harmonics may then be filtered out using the shunt-connected GSC. Case 4 provides the best torque performance although with a small amount of current ripple.

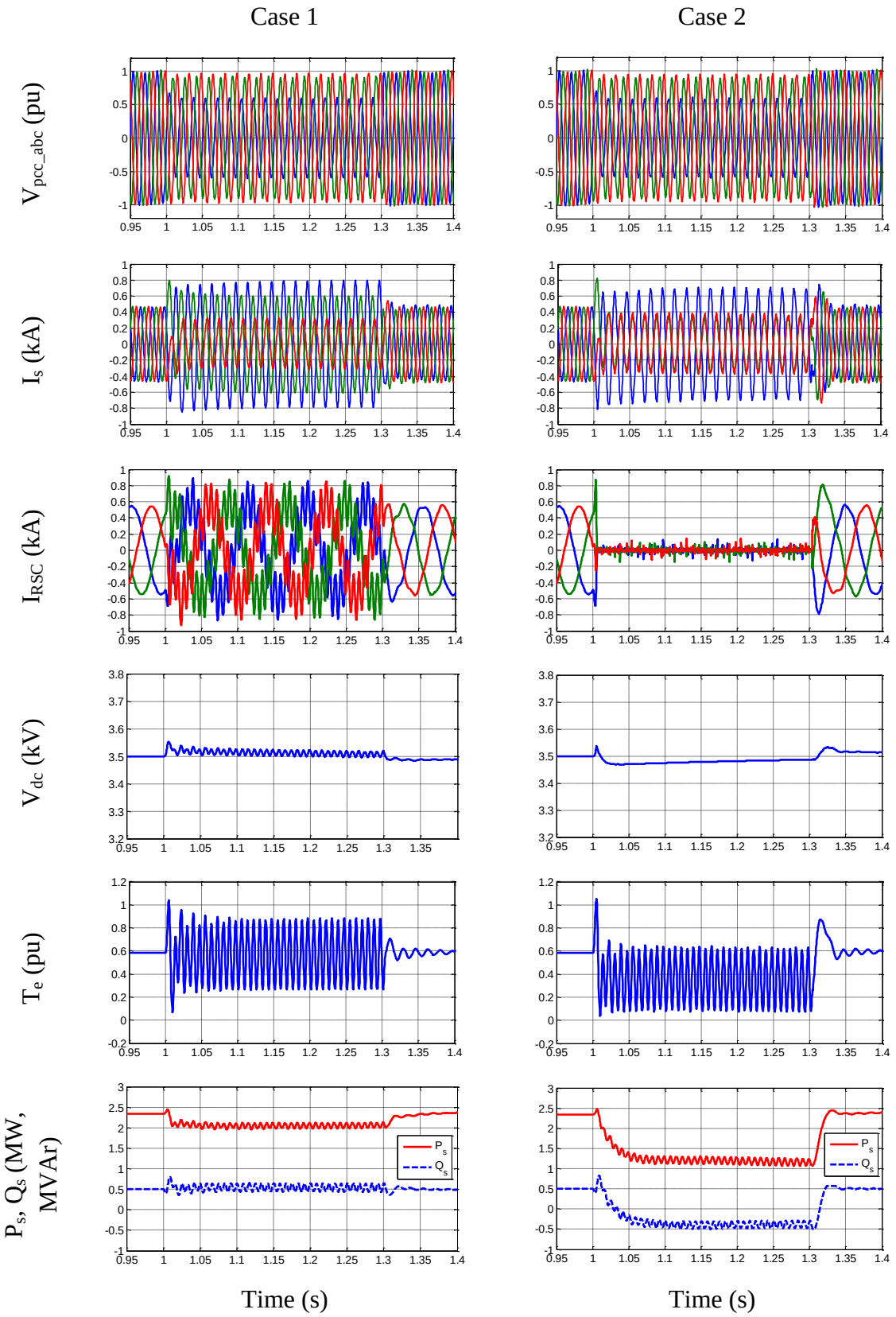

Figure 3.25 Simulated DFIG responses with different control schemes during an unbalanced single-phase fault: *Cases 1* and *2*.

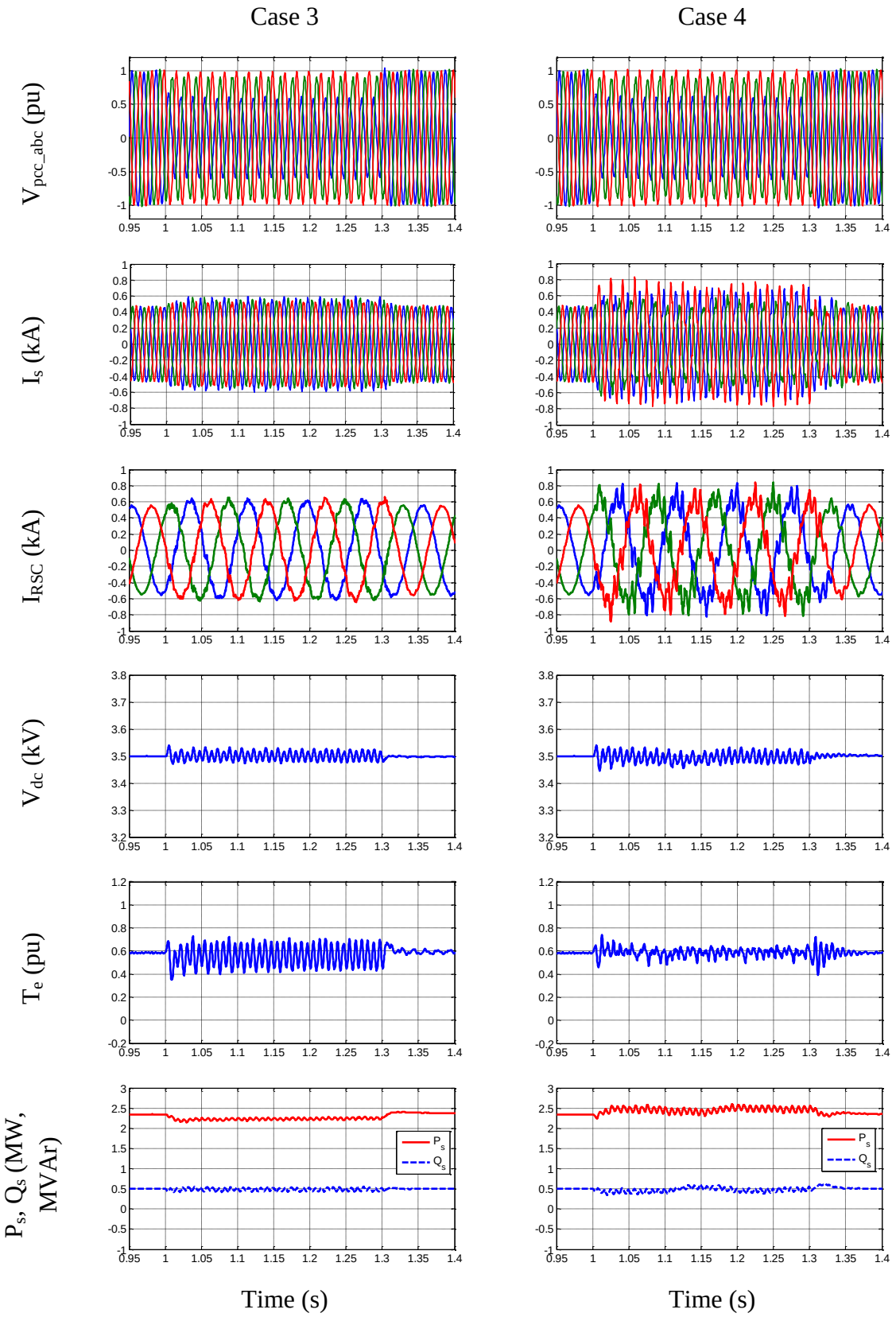

Figure 3.26 Simulated DFIG responses with different control schemes during an unbalanced single-phase fault: *Cases 3* and *4*.

3.6 Experimental Validation

3.6.1 Schematic and Layout of the Experimental Test Bench

A 230 V, 7.5 hp DFIG system, as shown in Figure 3.27 and Figure 3.28, is developed to validate the proposed feed-forward transient compensation control scheme in enhancing the low-voltage ride-through (LVRT) capability of DFIGs. The DC motor produces mechanical

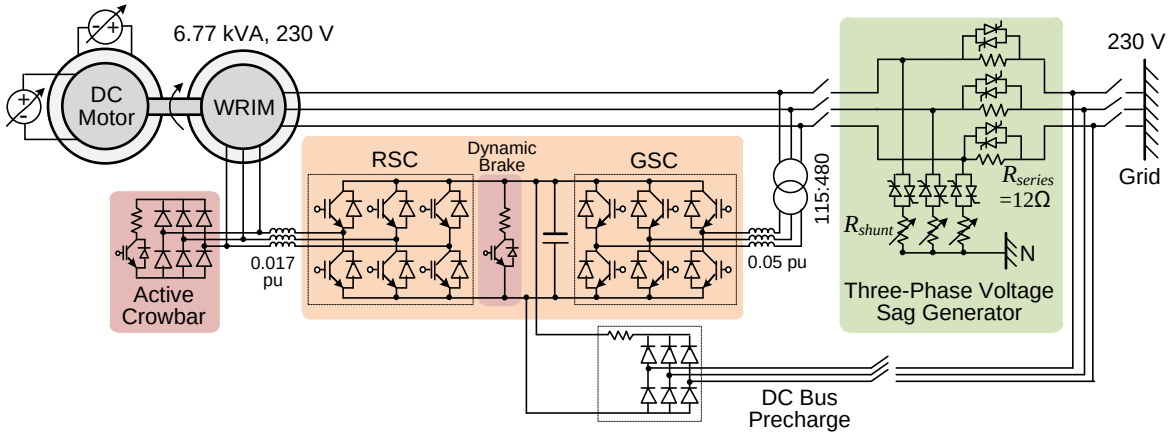

Figure 3.27 Schematic of the DFIG LVRT experimental setup

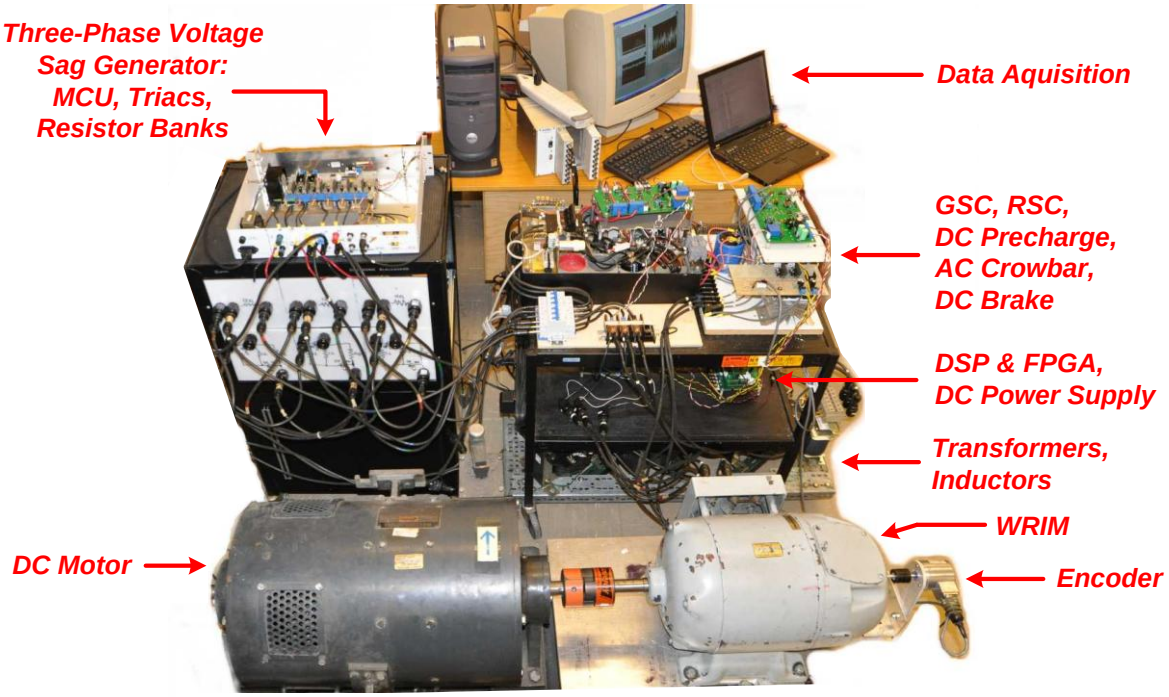

Figure 3.28 Physical system layout of the DFIG LVRT test bench.

power to rotate the wound-rotor induction machine (WRIM). Additional inductors are added at the rotor-side converter (RSC) and grid-side converter (GSC) AC-side outputs to reduce *di*/*dt*. A three-phase Y-Y transformer is used to interface the GSC with the grid. 1200 V, 75 A IGBT Intelligent Power Modules are used to implement both the RSC and GSC. An additional precharge circuit is used to charge the DC-bus capacitor before the DFIG stator is energized. The DFIG stator is connected to the grid through a three-phase voltage sag generator, as shown in Figure 3.27.

Figure 3.29 shows the control hardware architecture of this laboratory DFIG system. Voltage and current measurements from the RSC and GSC are sampled at 10 kHz and stored in the FPGA memory. Rotor speed and position information is updated in the FPGA memory *N*/4 and *N* times, respectively, per revolution, where *N* is the pulses per revolution of the encoder. The DSP accesses the current, voltage, speed, and position information

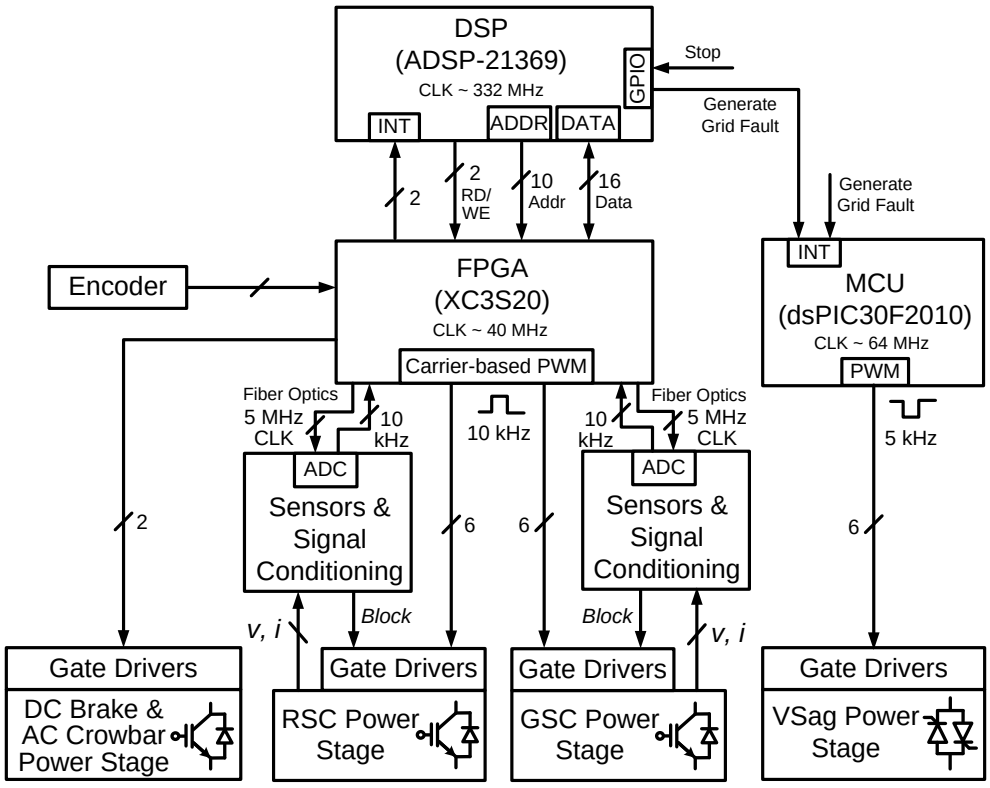

Figure 3.29 Control hardware architecture for the DFIG LVRT test bench.

stored in the FPGA when interrupts are generated by the FPGA. The DSP sends the PWM duty cycles and on/off states for the AC crowbar and DC chopper back to the FPGA. The DSP can also send grid-fault triggering signals to the voltage-sag-generator controller, so that grid faults can be applied at the same point-on-wave for multiple tests.

The detailed hardware implementation, control algorithm, and start/shut-down procedures for this laboratory DFIG system are described in Appendix C.

3.6.2 Control and Protection Settings for the DFIG Test Bench

The DFIG rotor speed is regulated by the RSC. The DFIG stator output power then depends on the DC motor armature voltage and field current. The GSC maintains the DC-bus voltage at 180 V. Using the space vector modulation, a maximum of 104 V peak phase voltage (0.55 pu) can then be obtained at the AC outputs of both RSC and GSC.

The reactive power outputs from the GSC and DFIG stator are not directly controlled in closed loops. Instead, the GSC reactive current reference is set to zero to have a unity power factor at the GSC outputs. The RSC reactive current reference (for DFIG excitation) is set to be proportional to the stator voltage, and is set to 15 A in peak value at 1 pu stator voltage. The lab DFIG has a relatively large air gap. The no-load stator current (rotor terminals shorted) for this machine is 17 A (0.71 pu) in peak value at rated stator voltage.

The generator has a current rating of 17 A (24 A in peak value) for both the stator and rotor. The crowbar, when enabled, activates if any of the three-phase instantaneous rotor currents exceed 30 A. Once the crowbar is on, all the RSC IGBTs are turned off. In this study, all grid faults are generated for a period of 0.15 s. The crowbar remains on for 0.2 s before turning off. Normal operation of RSC resumes after the crowbar turns off.

The DC-bus dynamic brake turns on when the DC-bus voltage exceeds 210 V, and turns off when the DC-bus voltage drops below 190 V.

3.6.3 Experimental Results during a Three-Phase Voltage Dip

A 0.15 s balanced three-phase-to-neutral fault is generated to test different DFIG control algorithms. The shunt resistance, R_{shunt}, in the voltage sag generator (see Figure 3.27) is set to 6.2 Ω to generate this fault (If R_{shunt} is too small, the resulting grid fault will be so severe that no matter what control algorithm is used, the crowbar has to turn on; 6.5 Ω is one of the values that can distinguish the performance of different control algorithms.).

3.6.3.1 Balanced Fault during Sub-Synchronous Operation

Experimental results for sub-synchronous operation (rotor speed command equals 0.85 pu) are shown in Figure 3.30. The following measurements are compared for the traditional PI-based control with steady-state compensations and the proposed feed-forward transient compensation control: stator terminal voltage, V_s; stator currents, I_{abcs}; rotor-side converter (RSC) AC-side output currents, I_{RSC}; DC-bus voltage, V_{dc}; rotor speed; and DFIG stator output active and reactive power, P_s and Q_s (positive means output into the grid).

When the traditional PI-based control with steady-state compensations is used, the crowbar turns on (point A in Figure 3.30) as soon as the DFIG stator voltage dips. The DFIG output power drops to almost zero, and the rotor speed rises during the fault. When the stator voltage suddenly recovers (point B in Figure 3.30), the crowbar remains on, and a large in-rush stator current (point B in Figure 3.30) occurs, which also induces large current in the machine rotor. The crowbar fails to turn off and gets reactivated (point C in Figure 3.30) because of the large in-rush current. The rotor-side converter (RSC) fails to resume operation immediately after the fault in this case. The DFIG starts to absorb active power from the grid, since the machine is running in sub-synchronous mode. At the same time, a large amount of reactive power (more than 4 kVAr) is drawn from the grid, causing the stator terminal voltage to drop slightly (D in Figure 3.30) even though the stator is directly

connected to the grid.

In contrast, when the feed-forward transient compensation control is used, the rotor current over-shoots are reduced at both voltage drop (point E in Figure 3.30) and recovery (point F in Figure 3.30). Crowbar interruption is prevented in this case with the proposed transient compensation scheme. The rotor speed rise is reduced, and the DFIG continues to supply active power up to its current rating.

Notice that the stator voltage sags in Figure 3.30 are different for the two control algorithms. This is because the generated voltage sag depends on the current that goes through the shunt and series resistors. Although the same resistor setting is used in the voltage sag generator, the DFIG stator currents are different depending on the control algorithm and crowbar status. For the same reason, the stator voltage tends to drop slower when a fault is generated by inserting the shunt resistors (stator current raises the stator voltage through the shunt resistors), and to rise faster when the shunt resistors are removed. Thus, a higher current overshoot is generally observed when the fault is removed (point F in Figure 3.30).

Also note that the DC-bus voltage drops during the fault, when the feed-forward transient compensation scheme is used to ride though the fault. This is because the machine operates at sub-synchronous condition, and the RSC outputs active power into the DFIG rotor. Meanwhile, the stator voltage drops and reduces the active power input to the DC-bus through the grid-side converter (GSC). For a deep voltage sag during sub-synchronous operation, even if the RSC control rides though the fault instant, the RSC operation may still need to be stopped to maintain the DC-bus voltage and prevent large in-rush current during sudden voltage recovery.

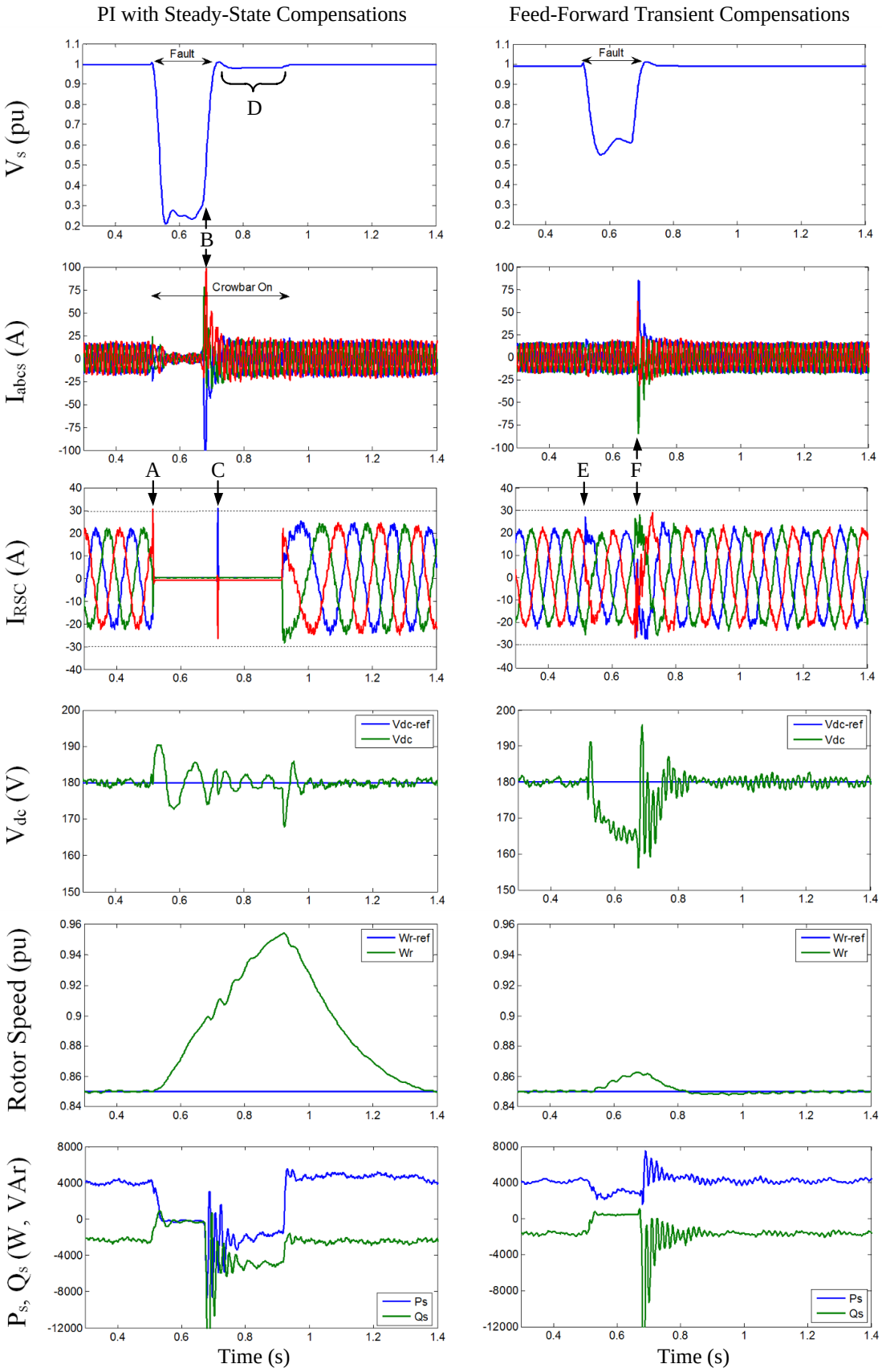

Figure 3.30 Experimental DFIG responses: ω_r = 0.85 pu, ABC-N fault.

3.6.3.2 Balanced Fault during Super-Synchronous Operation

For the same balanced grid fault as in Figure 3.30, experimental results for super-synchronous operation (rotor speed command equals 1.1 pu) are shown in Figure 3.31.

The traditional PI-based controller survives the transient of stator voltage drop (point A in Figure 3.31), but fails to regulate the rotor current at the stator voltage recovery (point B in Figure 3.31). After the crowbar turns on (point B in Figure 3.31), the DFIG starts to absorb a large amount of reactive power (C in Figure 3.31). The DFIG is only able to resume normal operation after the crowbar turns off (point D in Figure 3.31). Notice that during the fault, a large under-damped oscillation mode (E in Figure 3.31) is observed. This oscillation mode gets excited by the three-phase grid fault, and manifests itself as a 28 Hz negative-sequence component in the abc rotor currents and a 38 Hz positive-sequence component in abc stator currents. The oscillation mode is well-damped in sub-synchronous operation and becomes under-damped in super-synchronous operation. Thus, this oscillation mode is likely to be a slip-dependent inherent mode of the induction machine. External controllers may change the damping of this mode. As shown in Figure 3.31, the traditional PI-based controller with steady-state compensations is not able to damp this mode, although good current regulation performance is achieved during normal conditions (before point A and after point D in Figure 3.31). However, the proposed feed-forward transient compensation control is able to damp out this mode (F in Figure 3.31).

When the feed-forward transient compensation control is used, the transient rotor current is well controlled even at the voltage recovery (point G in Figure 3.31). The DFIG system rides through this fault. The DC-bus voltage does not drop in this case, because the DFIG is in super-synchronous operation and the DFIG rotor outputs active power into the DC-bus.

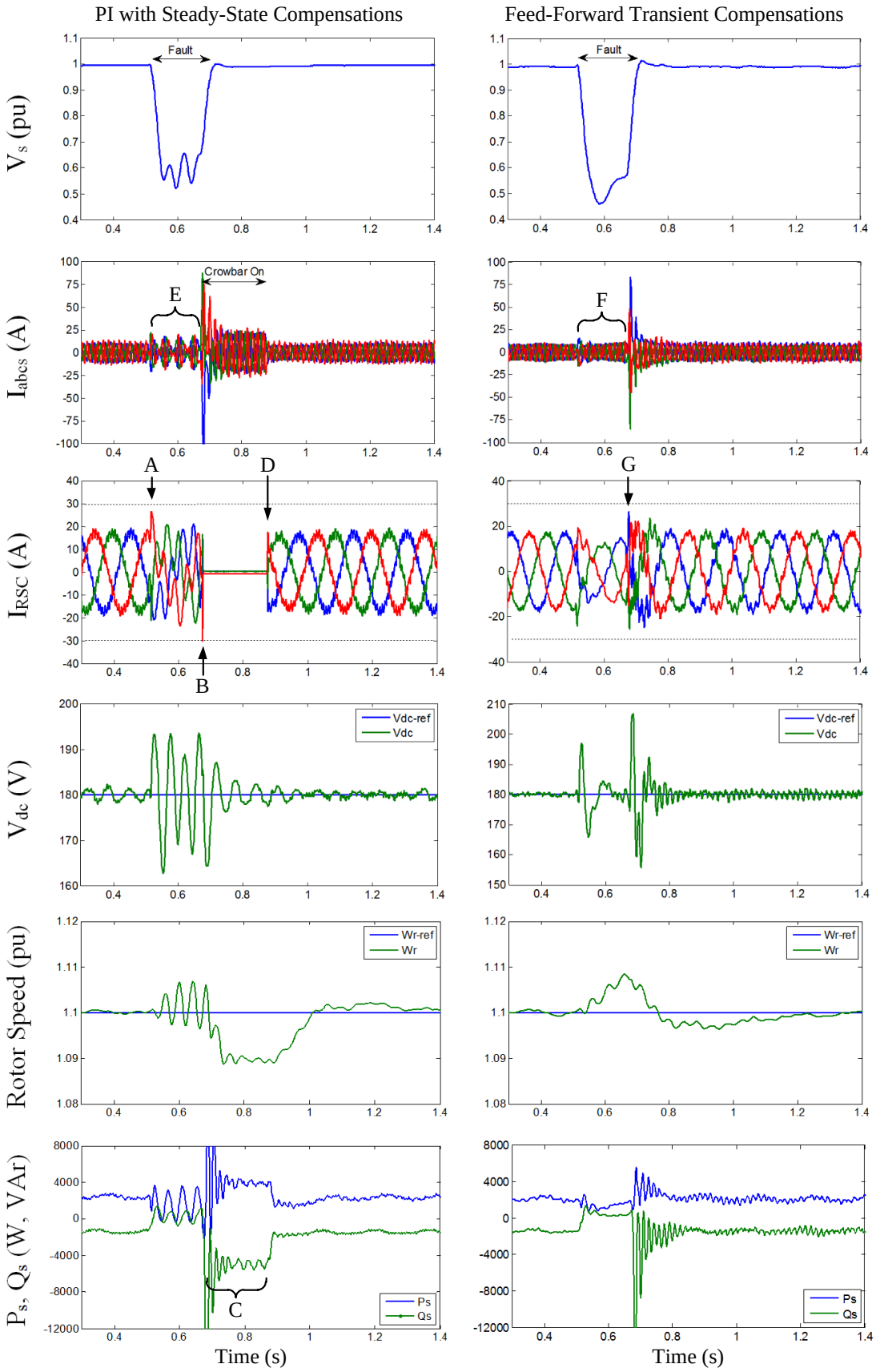

Figure 3.31 Experimental DFIG responses: ω_r = 1.1 pu, ABC-N fault.

3.6.3.3 Experimental and Simulation Results Comparison under Balanced Fault

To verify the DFIG simulation model developed in the PSCAD software, the experimental system (parameters listed in Appendix C) under the same balanced fault is simulated. The traditional PI-based control with steady-state compensations is used for comparison. Results for sub-synchronous and super-synchronous operation are shown in Figure 3.32 and Figure 3.33, respectively. The current and power responses match well between the experiments and simulations, expect that during super-synchronous operation in

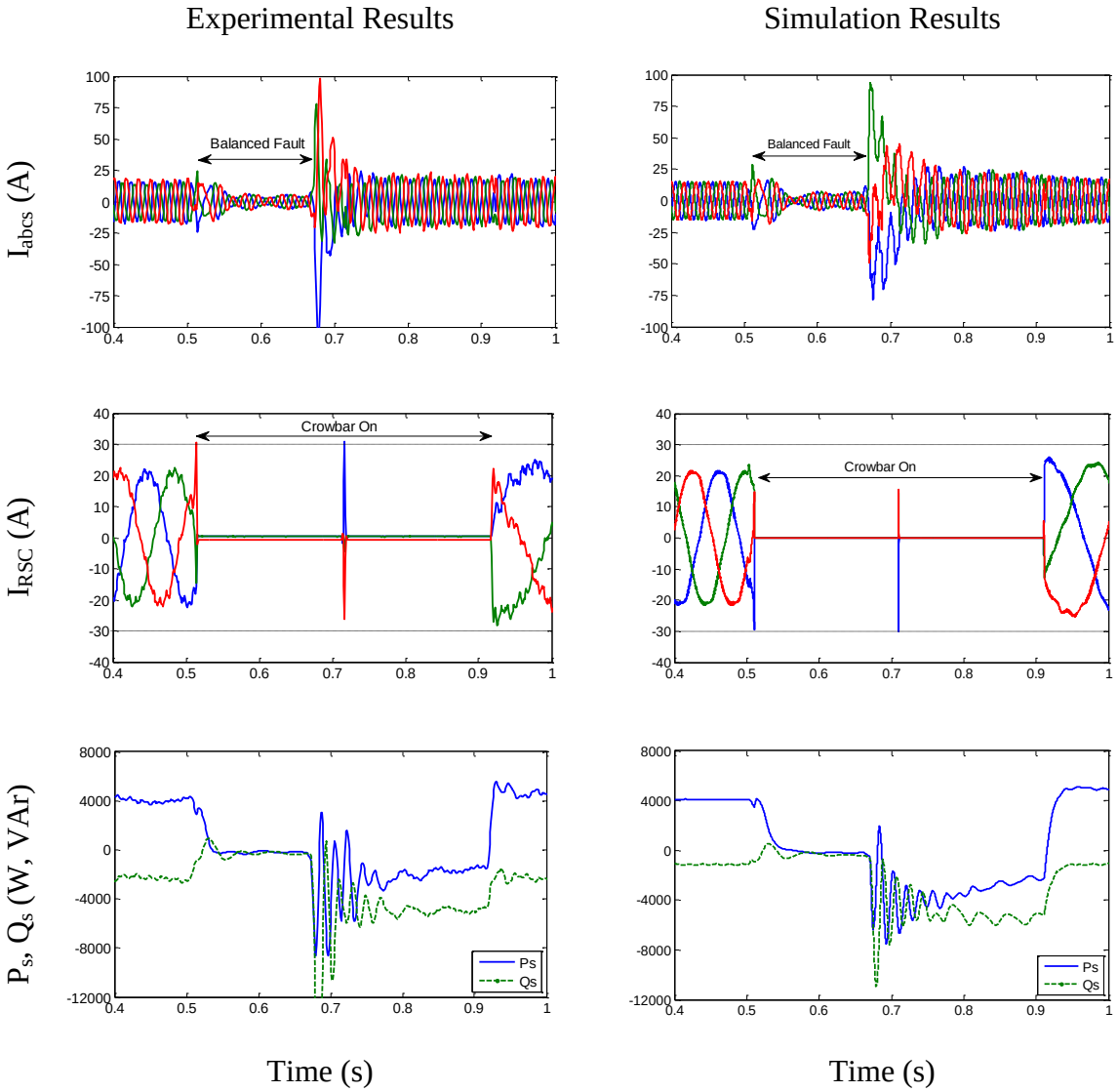

Figure 3.32 Experimental and simulation results comparison: ω_r = 0.85 pu, ABC-N fault.

Figure 3.33, the simulated currents do not contain the under-damped oscillation between 0.51 s and 0.66 s. At the fault recovery (at about 0.66 s), the experimental stator currents have a transient AC component (a larger initial post-fault AC current) that does not seem to appear in the simulated stator current waveforms. The phase angles of the experimental and simulated rotor currents are different, which is due to the fact that the rotor angles are not synchronized between the experimental and simulation systems.

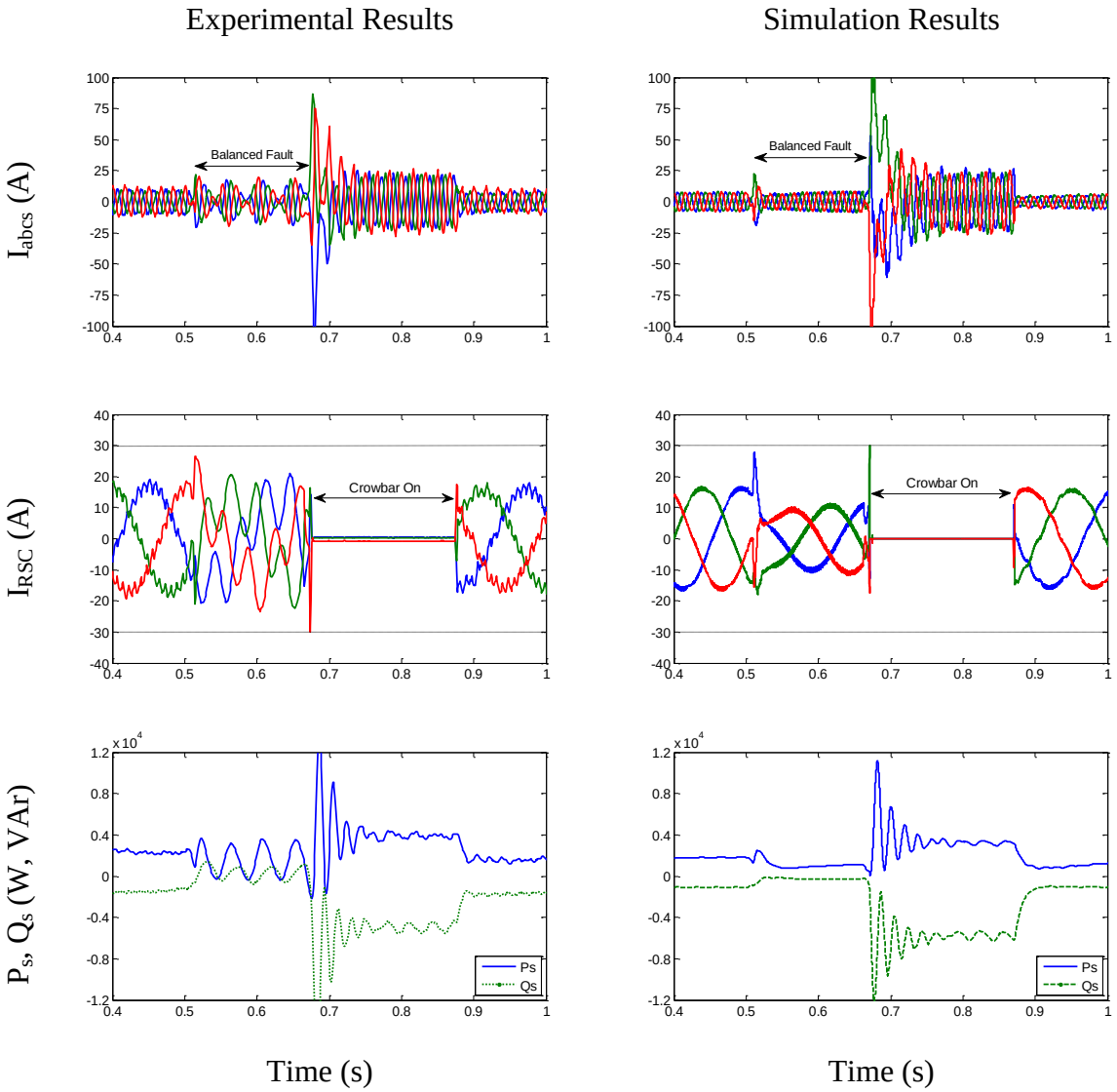

Figure 3.33 Experimental and simulation results comparison: ω_r = 1.1 pu, ABC-N fault.

3.6.4 Experimental Results during a Single-Phase Voltage Dip

To further validate the proposed feed-forward transient compensation control scheme, a 0.15 s unbalanced phase-A-to-neutral fault is generated to test the different DFIG control algorithms. The phase-A shunt resistance in the voltage sag generator (see Figure 3.27) is set to 5.8 Ω, while the DFIG stator phases B and C are directly connected to the grid. To have the same post-fault flux transient, the inceptions of this unbalanced fault are synchronized at the zero crossing of phase A voltage. Note that the rotor angle may be different every time this fault is generated. Thus, the transient rotor current may be different in the *abc* coordinates, but will be the same in the *dq* synchronous frame.

3.6.4.1 Unbalanced Fault during Sub-Synchronous Operation

Experimental results for sub-synchronous operation (rotor speed command equals 0.85 pu) are shown in Figure 3.34 and Figure 3.35. Four control scenarios, same as those listed in Table 3.1, are compared for this unbalanced grid fault. The following measurements are plotted for comparisons: stator voltages, V_{abcs}; stator currents, I_{abcs}; rotor-side converter (RSC) AC-side output currents, I_{RSC}; DC-bus voltage, V_{dc}; estimated torque based on (3.5), $Torq_{est}$; and DFIG stator output active and reactive power, P_s and Q_s (positive means output into the grid).

Figure 3.34 shows the experimental results for the traditional PI-based controller with steady-state compensations. When the crowbar is disabled (the converters for the lab test bench are sized with higher ratings for testing purposes), the RSC/rotor currents exceed 30 A (points A, B, and C in Figure 3.34) from time to time because of the large negative sequence component. When the crowbar is enabled, to bypass the high rotor current peaks from the RSC, the crowbar turns on at point D in Figure 3.34, resulting in results shown in the second column of Figure 3.34. Although the RSC is now protected from over-current,

large negative-sequence currents (E in Figure 3.34) still exist in the machine, resulting in large torque ripples. Because the machine is operated in the sub-synchronous mode, once the crowbar activates, the machine runs in motoring mode and starts to absorb active power from the grid until its speed exceeds the synchronous speed.

When the feed-forward transient compensation control is used for the current loop, the rotor current overshoots (points A and B in Figure 3.35) are reduced, and the negative-sequence currents (C in Figure 3.35) are well controlled. The crowbar does not need to activate, and the torque ripples (D in Figure 3.35) are also reduced. In the second column of Figure 3.35, some negative-sequence rotor currents (E in Figure 3.35) are intentionally injected following the power-loop feed-forward transient compensation scheme in Figure 3.15. The torque ripples (F in Figure 3.35) are further reduced without causing over-current problems. With the proposed feed-forward transient compensation control, the crowbar does not need to turn on, the torque ripples are reduced, and the active power production is uninterrupted during this unbalanced fault.

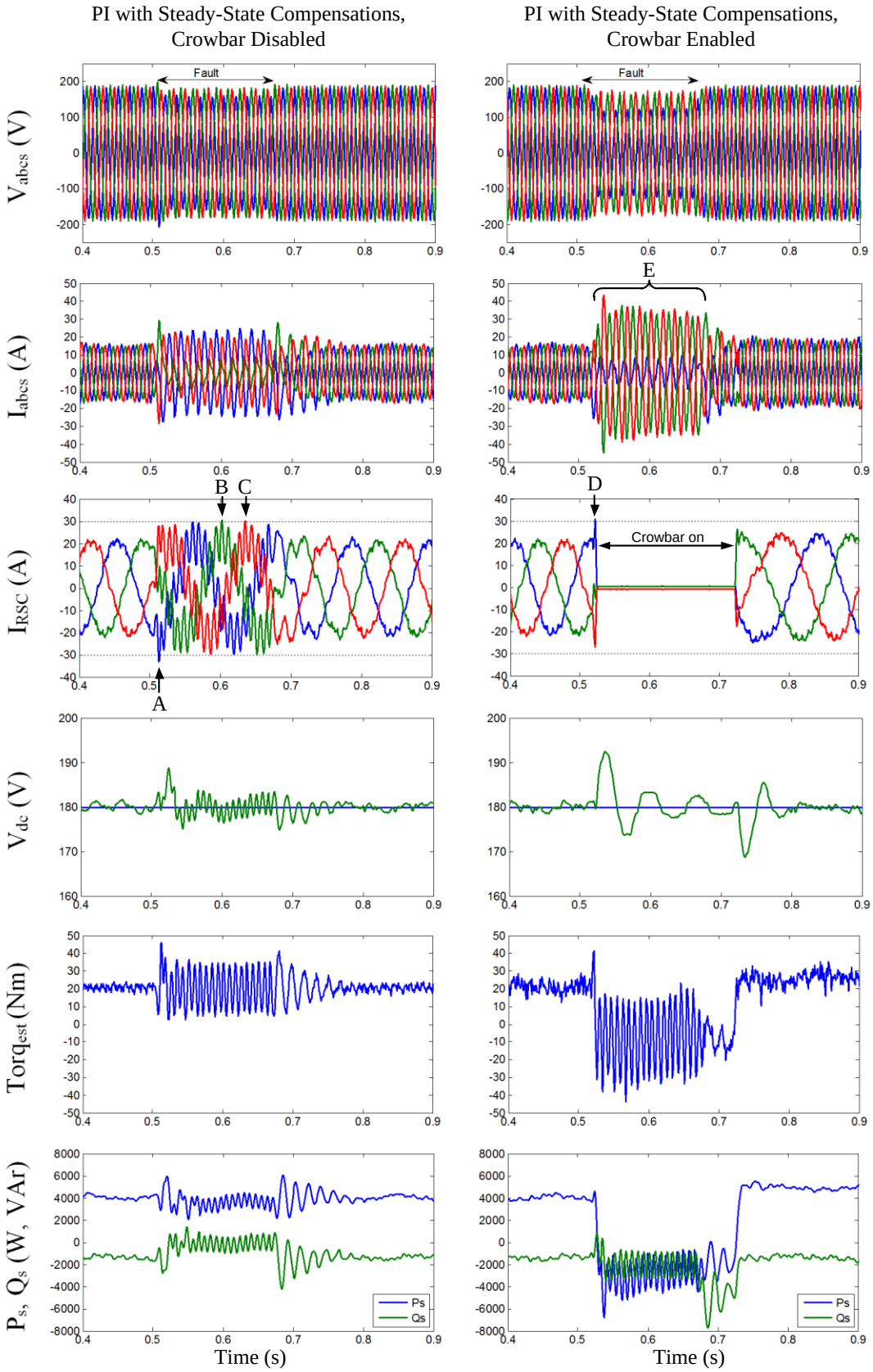

Figure 3.34 Experimental DFIG responses: ω_r = 0.85 pu, A-N fault, PI-based controller with steady-state compensations.

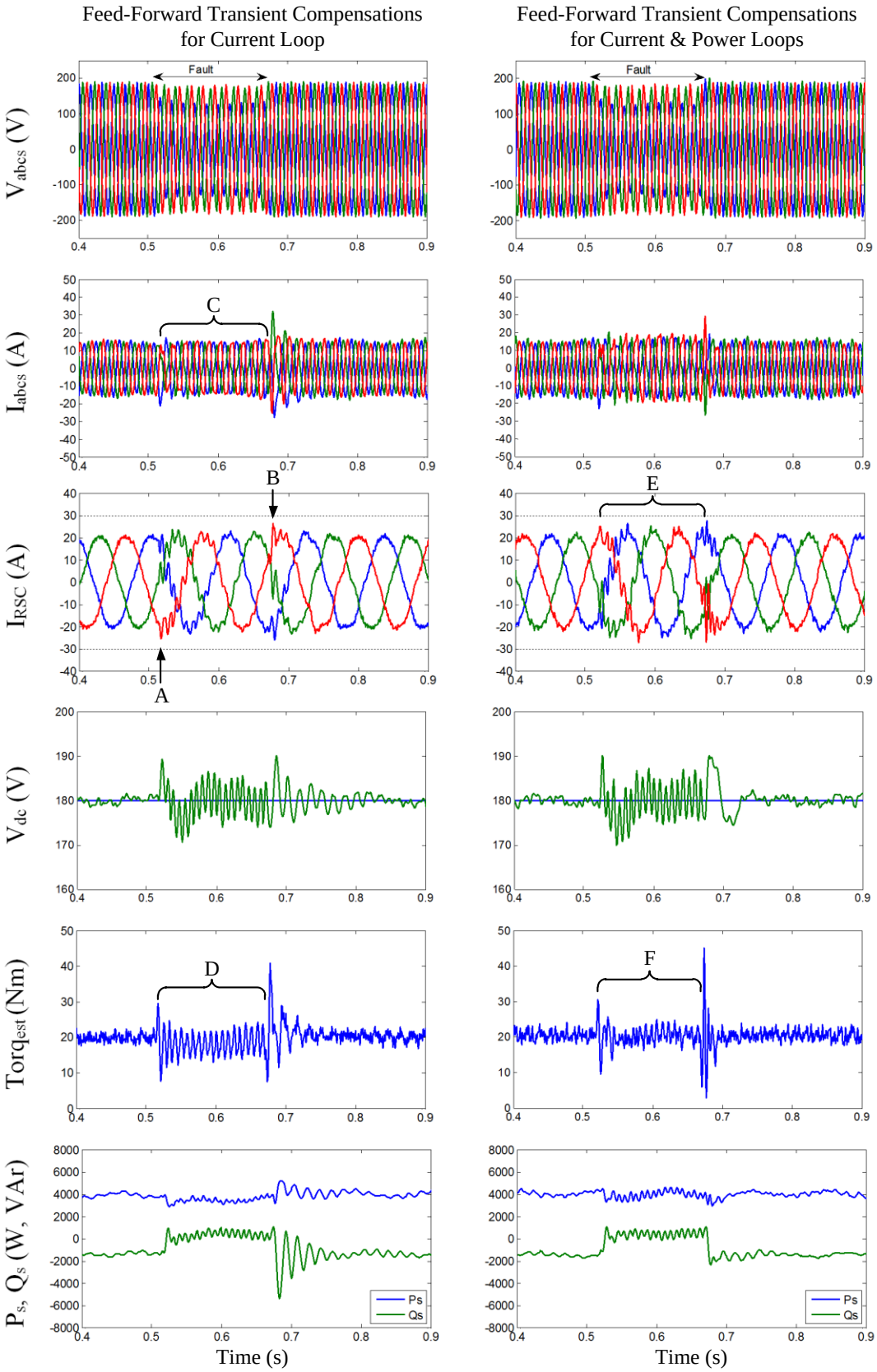

Figure 3.35 Experimental DFIG responses: ω_r = 0.85 pu, A-N fault, feed-forward transient compensation control.

3.6.4.2 Unbalanced Fault during Super-Synchronous Operation

Experimental results for super-synchronous operation (rotor speed command equals 1.1 pu) are shown in Figure 3.36.

When the traditional PI-based current control with steady-state compensations is used, the rotor current overshoot causes the crowbar to turn on (point A in Figure 3.36). The torque then experiences large ripples (B in Figure 3.36) because of the large negative-sequence currents (C in Figure 3.36). The DFIG can only resume normal operation after the crowbar turn off (point D in Figure 3.36).

When the feed-forward transient current control scheme is used, results are shown in the second column of Figure 3.36. Both the transient and negative-sequence rotor currents are well controlled, resulting in a lower level of torque ripples and uninterrupted power supply to the grid.

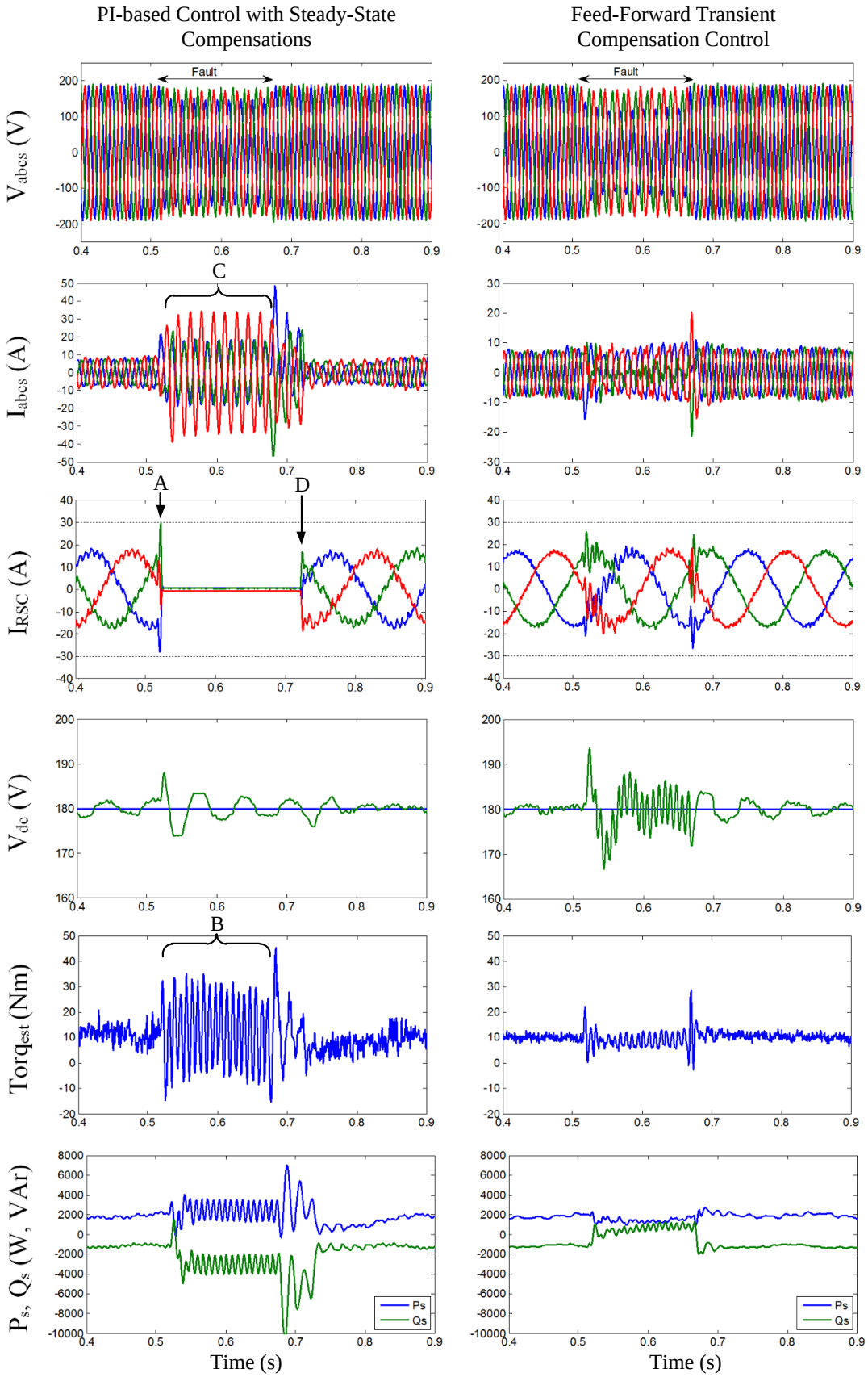

Figure 3.36 Experimental DFIG responses: ω_r = 1.1 pu, A-N fault.

3.6.4.3 Experimental and Simulation Results Comparison under Unbalanced Fault

To further verify the DFIG simulation model developed in the PSCAD software, the experimental system (parameters listed in Appendix C) under the same unbalanced fault is simulated. The faults in the experimental and simulation systems are generated at the same point-on-wave of the stator voltage. The traditional PI-based control with steady-state compensations is used for comparison. Results are shown in Figure 3.37 for sub-synchronous operation and in Figure 3.38 for super-synchronous operation. The current and

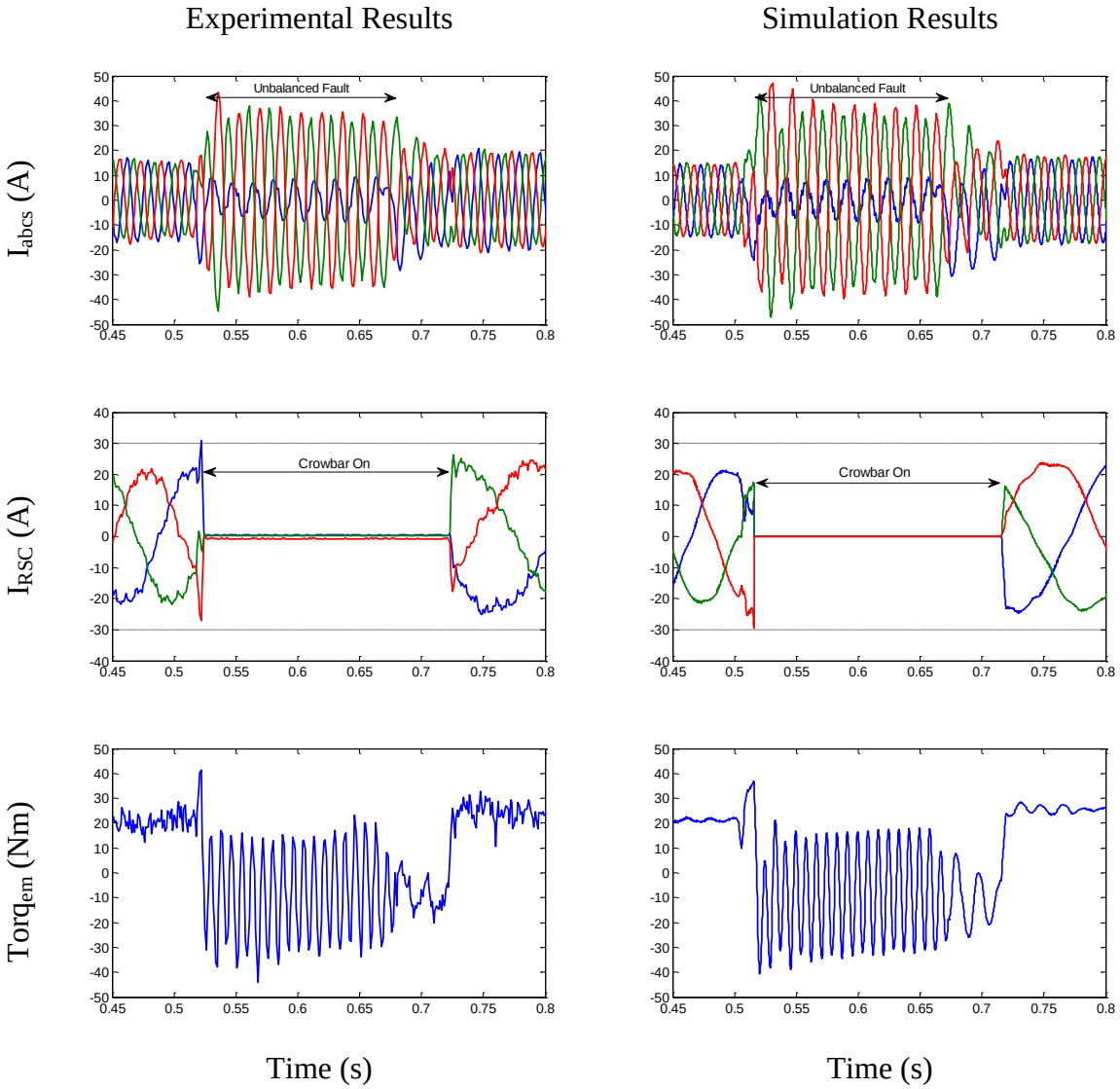

Figure 3.37 Experimental and simulation results comparison: ω_r = 0.85 pu, A-N fault.

torque responses between the experimental and simulation systems match well with each other. Again, because the rotor angles are not synchronized between the experimental and simulation systems, the phase angles of the experimental and simulated rotor currents are different.

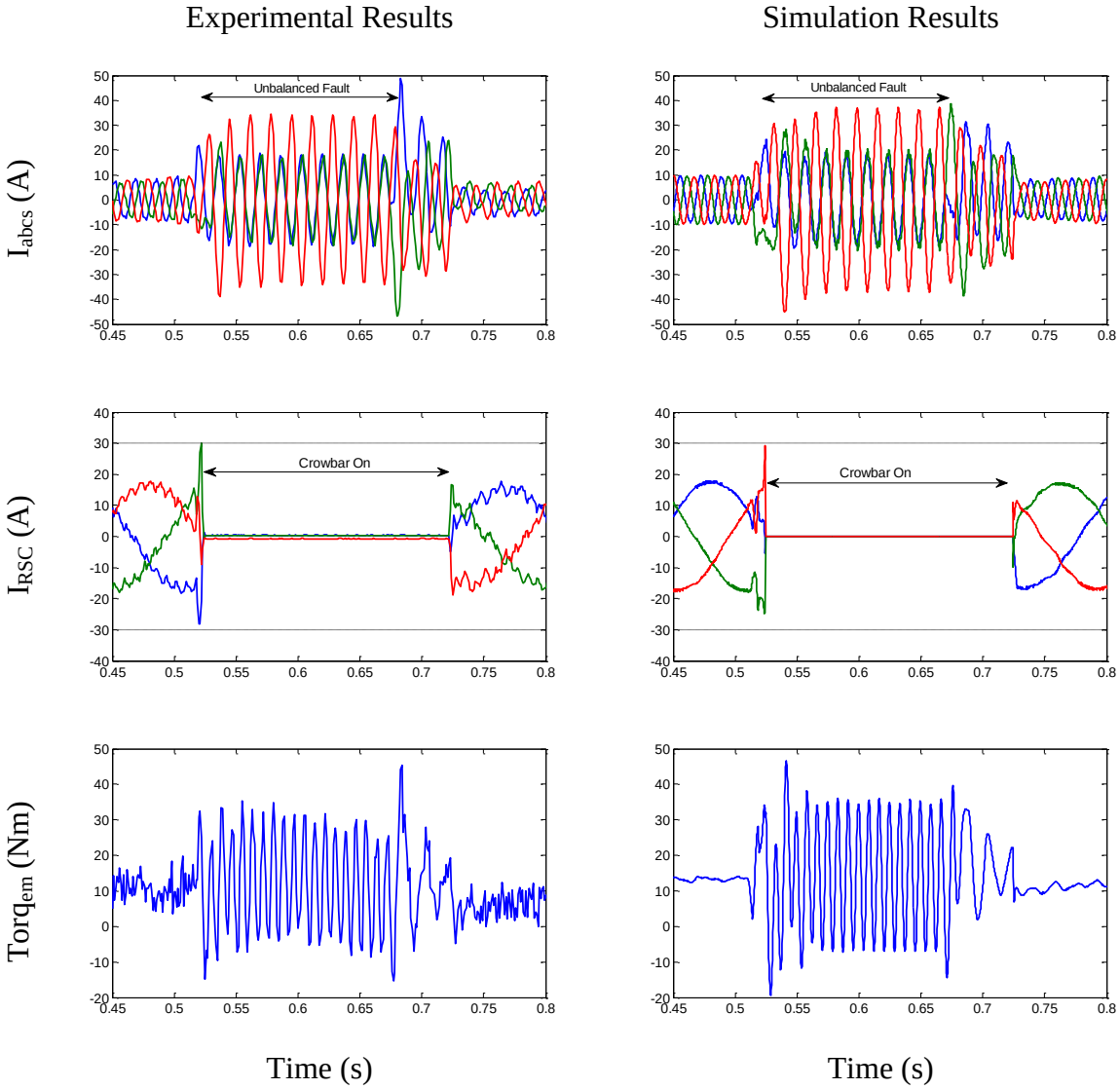

Figure 3.38 Experimental and simulation results comparison: ω_r = 1.1 pu, A-N fault.

3.7 Chapter Summary

A feed-forward transient compensation control scheme is proposed in this chapter to enhance the low-voltage ride-through (LVRT) capability of doubly-fed induction generator

(DFIG) based wind generation systems during both balanced and unbalanced grid faults. Transient compensation terms are feed-forward injected into both the current and power control loops to improve the transient current control capability and reduce the torque ripples resulting from grid faults. Simulation studies and experimental validations confirm the effectiveness of the proposed feed-forward transient compensation control algorithms. With minimal additional complexity, the proposed control enhances the LVRT capability of DFIG wind generation systems.

The next chapter discusses the power system control layer (see Figure 1.4) for secure integration of wind power, and proposes a dynamic stochastic optimal power flow (DSOPF) control algorithm for dynamically and optimally coordinating multiple grid-connected energy systems.

CHAPTER 4 DYNAMIC STOCHASTIC OPTIMAL POWER FLOW CONTROL FOR POWER SYSTEMS WITH HIGH UNCERTAINTY AND VARIABILITY

4.1 Chapter Overview

To achieve a high penetration level of intermittent renewable energy, the control of power systems needs to consider the associated high variability and uncertainty. Power system stability and security need to be ensured dynamically as the system operating condition continuously changes. In this chapter, a dynamic stochastic optimal power flow (DSOPF) control algorithm using the Adaptive Critic Designs (ACDs) is proposed to control the future smart grid in an environment with high short-term uncertainty and variability. The ACD technique, specifically the dual heuristic dynamic programming (DHP) [28], is used to provide nonlinear optimal control, where the control objective is explicitly formulated to incorporate power system economy, stability and security. The proposed DSOPF controller dynamically controls the power system active and reactive power flow based on the control objective. A 12-bus test power system is used to demonstrate the success of the proposed DSOPF controller.

4.2 Framework of Dynamic Stochastic Optimal Power Flow (DSOPF) Control

A power system is a multi-input multi-output, nonlinear, and non-stationary complex dynamic plant. A DSOPF controller is designed to replace the traditional automatic generation control (AGC) and secondary/regional voltage control, as illustrated in Figure 4.1, and to provide nonlinear optimal control to the system-wide AC power flow. The power system is assumed to be sufficiently observable with wide-area monitoring systems. Data

processing and transmitting, state estimations, and derivations of power system quantities are not considered. Continuous snapshots of the dynamic power system are assumed to be readily available in the control room. With the snapshots as system feedbacks, the DSOPF controller dynamically adjusts the steady-state commands dispatched by the optimal power flow (OPF) algorithm, as illustrated in Figure 4.2. In an environment with high short-term variability, only those continuously adjustable resources are controlled by the DSOPF controller to continuously track the optimal operating point. Mechanical-switch-based

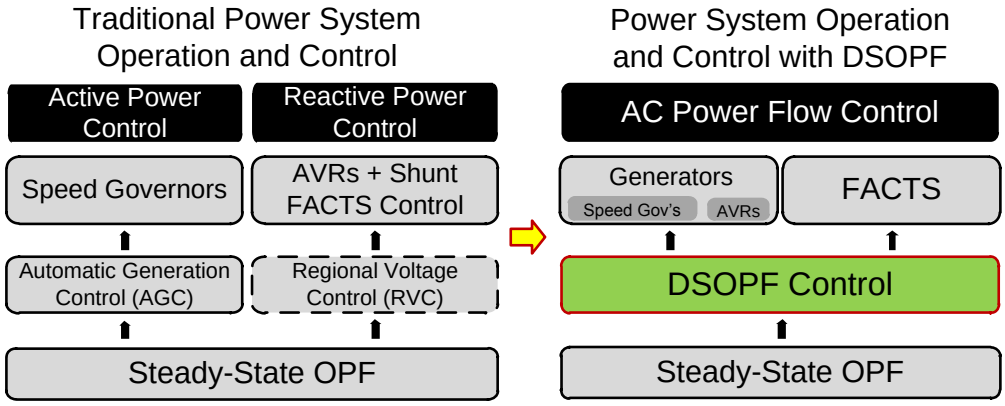

Figure 4.1 Traditional power system operation-control structure and the proposed structure with DSOPF control.

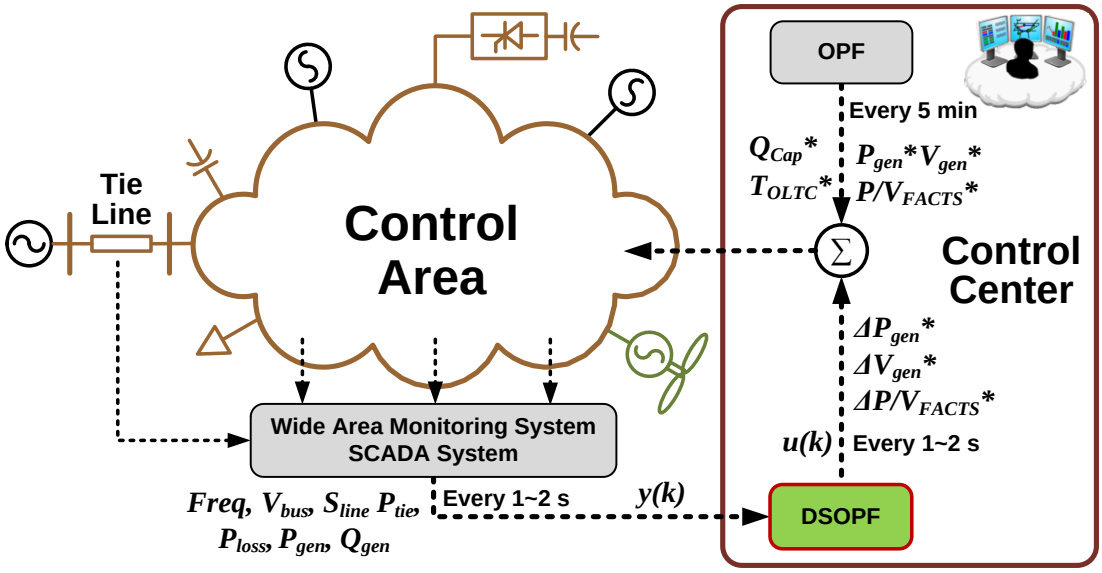

Figure 4.2 General framework of the DSOPF control.

devices are not designed to continuously react to fast events. Their lifetimes are typically inversely dependent on the number of switching actions. These devices are thus not controlled by the DSOPF controller.

A nonlinear optimal control strategy is necessary to achieve the DSOPF control, where an objective function (the cost-to-go function) is minimized in a closed-loop control fashion and the nonlinearity is used to handle different operating points and physical control limits. Besides the optimality and nonlinearity considerations, the DSOPF control must be able to adapt to the time-varying dynamics of the power system, whose topology may change at any point in time. To implement the DSOPF, it is thus essential to have a nonlinear optimal control strategy that is able to continuously identify the system topology changes and accordingly adjust its optimal control laws.

The Adaptive Critic Design (ACD) technique, introduced in Section 2.4.3.1, is a promising candidate, since it requires no knowledge of the power network analytical model. A typical ACD scheme consists of three neural networks: a model network, an action network, and a critic network, as illustrated in Figure 4.3. The model network can identify the time-varying dynamics of the nonlinear power system. The critic network, which approximates the cost-to-go control objective, trains the nonlinear action network to create an optimal control mapping between the plant feedbacks and control actions.

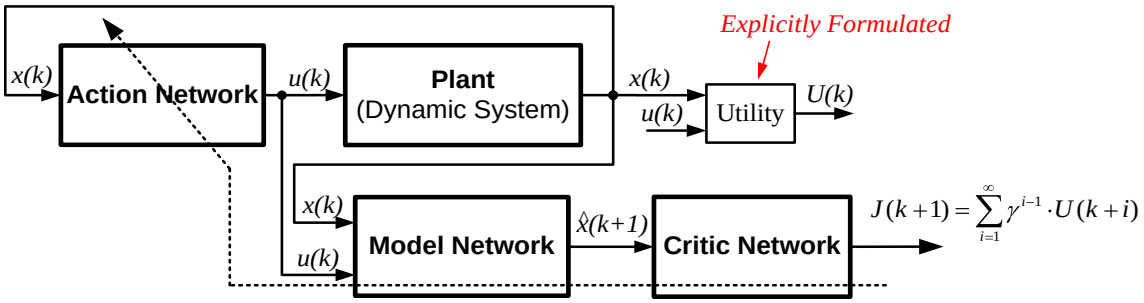

Figure 4.3 Diagram of an ACD scheme.

The optimization objective is explicitly formulated in the ACD technique. Thus, the total energy cost, frequency deviation, tie-line flow deviations, bus voltage deviations, line loadings, line losses, generator stability margins, and/or other indices related to the system economy, stability and security can be readily formulated in the control objective. By continuously optimizing this objective, the ACD-based DSOPF controller optimally controls the system active and reactive power flow. The implementation of the ACD-based neurocontrol using recurrent neural networks (RNNs) is discussed in the next section.

4.3 Recurrent-Neural-Network-based Adaptive Critic Designs

4.3.1 Recurrent Neural Networks (RNNs)

As introduced in Section 2.4.3.1, for complex dynamic plants whose states are not all accessible, feed-forward neural networks with time-delayed loops are typically used to implicitly estimate the plant states and implement the ACD scheme.

An alternative approach is to directly use a dynamic neural network without time-delayed loops, such as an RNN shown in Figure 4.4. RNNs have advantages over static feed-forward neural networks in modeling and control of dynamic systems because of their internal dynamic memories [111], [112]. With RNNs, the internal feedback loops effectively provide the time-delayed information for state estimation, as in

$$\begin{aligned} o(k) &= g[W_o \cdot s(k)] \\ &= g\{W_o \cdot f[W_s \cdot s(k-1) + W_i \cdot i(k)]\} \\ &= N_R[i(k), i(k-1), \ldots] \end{aligned} \tag{4.1}$$

where $i(k)$ is the input vector, $o(k)$ is the output vector, $s(k)$ is the RNN internal state vector, $f(\cdot)$ and $g(\cdot)$ are activation functions, and N_R denotes the equivalent static nonlinear mapping from the RNN's present and historic inputs to its present output.

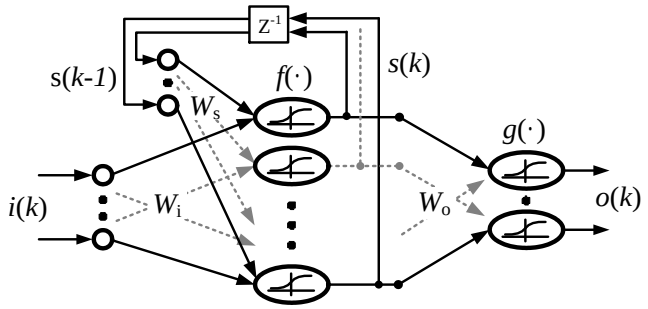

Figure 4.4 Structure of a hidden-layer-feedback RNN with no bias terms.

The training of an RNN requires more computation effort than an feed-forward neural network with the same number of neurons. The gradients of an RNN's outputs with respect to its weights are found by the back-propagation through time algorithm [113]. With a truncated depth of one, i.e. back-propagated by one time step, the error gradients for an RNN are given by

$$\begin{aligned}
\frac{\partial E(k)}{\partial W_o} &= [\nabla g]\cdot\frac{\partial E(k)}{\partial o(k)}\cdot s(k)' \\
\frac{\partial E(k)}{\partial W_s} &= [\nabla f]\cdot W_o'\cdot[\nabla g]\cdot\frac{\partial E(k)}{\partial o(k)}\cdot s(k-1)' \\
\frac{\partial E(k)}{\partial W_i} &= [\nabla f]\cdot W_o'\cdot[\nabla g]\cdot\frac{\partial E(k)}{\partial o(k)}\cdot i(k)'
\end{aligned} \qquad (4.2)$$

$E(k)$ is an error measurement related the RNN outputs. More details on calculating this error for the model, critic and action networks are described in the following sections. $[\nabla g]$ and $[\nabla f]$ are diagonal matrices containing the gradients of $g(\cdot)$ and $f(\cdot)$, respectively. The upper-right prime symbol means transpose. For the numerical simulations performed in this dissertation, a truncated depth of one yields sufficiently good training results and is thus used to calculate the gradients of all RNNs in the DSOPF controllers presented in this dissertation. More details on the back-propagation through time algorithm and training of RNNs are described in Appendix E.

After obtaining the gradients, to minimize $E(k)$, the incremental gradient descent algorithm is used to update the RNN weights:

$$W_o(k+1) = W_o(k) - r_o \frac{\partial E(k)}{\partial W_o}$$
$$W_s(k+1) = W_s(k) - r_s \frac{\partial E(k)}{\partial W_s}, \tag{4.3}$$
$$W_i(k+1) = W_i(k) - r_i \frac{\partial E(k)}{\partial W_i}$$

where r_o, r_s, and r_i are gains controlling the step size of the weight updates. When *tansig*(·) or *sigmoid*(·) is used for the activation functions, their gradients are small in the saturation regions. Thus, r_s and r_i are usually larger (say five times larger for a truncated depth of one) than r_o to compensate for the error gradient magnitude drops introduced by . r_o could be in the range of 0.0001 to 0.01 depending on specific applications.

The output-to-input derivatives of an RNN is given by

$$\frac{\partial o(k)}{\partial i(k)} = [\nabla g] \cdot W_o \cdot [\nabla f] \cdot W_i, \tag{4.4}$$

which provides the output-input sensitivities for training other networks in an ACD scheme.

4.3.2 Recurrent Neural Networks for Adaptive Critic Designs (ACDs)

Figure 4.5 shows the schematic diagram of the dual heuristic dynamic programming (DHP, a technique in the ACD family) with RNNs, where the critic network directly estimates $\lambda(k)$, the gradient of $J(k)$ with respect to the plant outputs.

For the RNN model network, $o(k)$ in (4.1) is replaced by $\hat{y}(k+1)$ to learn the plant dynamics, and the inputs to the RNN model network are $y(k)$ and $u(k)$. Thus,

$$\hat{y}(k+1) = N_{R\_\text{model}}[y(k), y(k-1), ..., u(k), u(k-1), ...], \tag{4.5}$$

where N_{R_model} is the equivalent static mapping N_R produced by the RNN model network, and a similar notation applies to N_{R_action} for the action network and N_{R_critic} for the critic network. Compared to (2.6), the RNN model network described by (4.5) has the necessary mathematical form to reproduce the dynamic plant of (2.5).

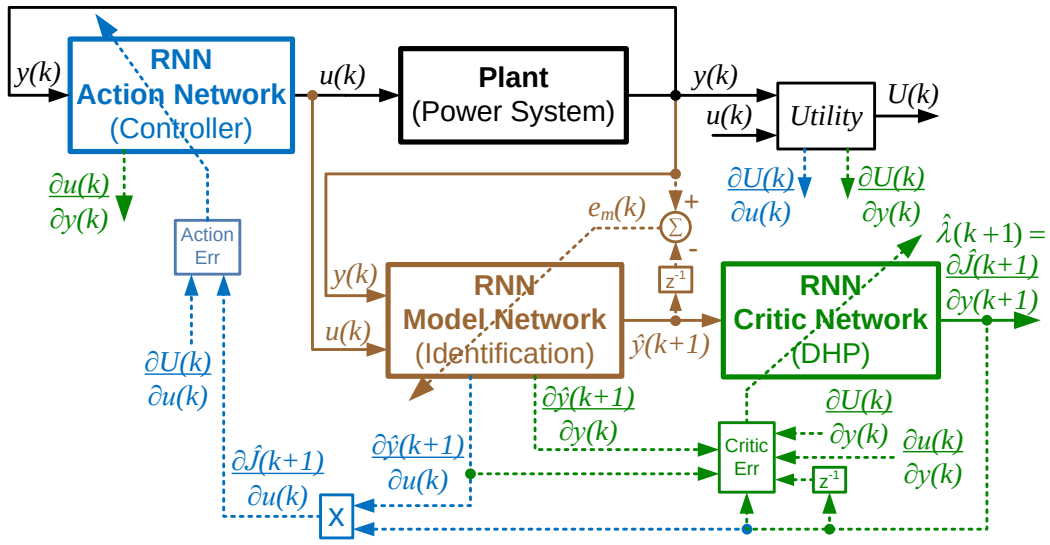

Figure 4.5 Schematic diagram of DHP neurocontrol design with RNNs. Brown: signals for model training; green: signals for critic training; blue: signals for action training.

For the RNN action network shown in Figure 4.5,

$$u(k) = N_{R\_\text{action}}[y(k), y(k-1), \ldots] \tag{4.6}$$

From the self recursion of (4.6),

$$\begin{aligned} u(k-1) &\sim y(k-2), y(k-3), \ldots \\ u(k-2) &\sim y(k-3), y(k-4), \ldots \end{aligned} \tag{4.7}$$

where "~" denotes "a function of". The RNN action network then implements the mapping from [y(k), y(k-1),…, u(k-1), u(k-2),…] to $u(k)$. From (2.6), the RNN action network has the necessary form to implement the optimal mapping (optimal control laws) from $\hat{x}(k)$ to $u(k)$.

For the RNN critic network shown in Figure 4.5,

$$\hat{\lambda}(k+1) = \frac{\partial \hat{J}(k+1)}{\partial y(k+1)} = N_{R\_\text{critic}}[\hat{y}(k+1), \hat{y}(k), \ldots] \tag{4.8}$$

Since $J(k+1)$ is a function of $x(k+1)$, it is thus a function of $[y(k), y(k-1),\ldots, u(k), u(k-1),\ldots]$. For a controller given by (4.6), $J(k+1)$ is then a function of $[y(k), y(k-1),\ldots]$, and its derivative $\lambda(k+1)$ also becomes a function of the same series. Hence, the RNN critic network, represented by (4.8),

has the necessary mathematical form to approximate $\lambda(k)$.

4.3.3 Training of a DHP-based Neurocontroller using RNNs

The training of a DHP-based neurocontroller is done in two steps in this dissertation: 1) offline training of the model network; and 2) online training of all three networks. In the following discussions, W_{im}, W_{sm}, and W_{om} are weights for the model network, W_{ic}, W_{sc}, and W_{oc} are weights for the critic network, W_{ia}, W_{sa}, and W_{oa} are weights for the action network.

4.3.3.1 Offline Training of Model Network

The plant is first operated without a closed-loop action network. Pseudo-random binary signals [30] are injected into the plant inputs, $u(k)$, over a wide operating range. The plant responses, $y(k)$, are recorded together with $u(k)$. With the recorded $u(k)$ and $y(k)$ at different operating points, the model network is trained offline to minimize the following mean squared error (MSE):

$$E_m(k) = \|e_m(k)\|^2 = \|y(k) - \hat{y}(k)\|^2, \tag{4.9}$$

$$MSE = average\left[\sum_{\substack{\text{operating}\\ \text{points}}} \sum_{k} E_m(k)\right], \tag{4.10}$$

where $\hat{y}(k)$ is the one-step delay of the model network output. In other words, the model network is trained to identify the plant dynamics and provide one-step-ahead prediction.

Figure 4.6 shows the flowchart for offline training of the RNN model network using the incremental gradient descent algorithm. The model network is first initialized with small random weights. During the training step, the one-step model prediction error and error gradients are calculated based on (4.9) and (4.2), respectively. The model weights are then updated based on (4.3). The model training continues until the MSE calculated in the testing step drops below a certain level.

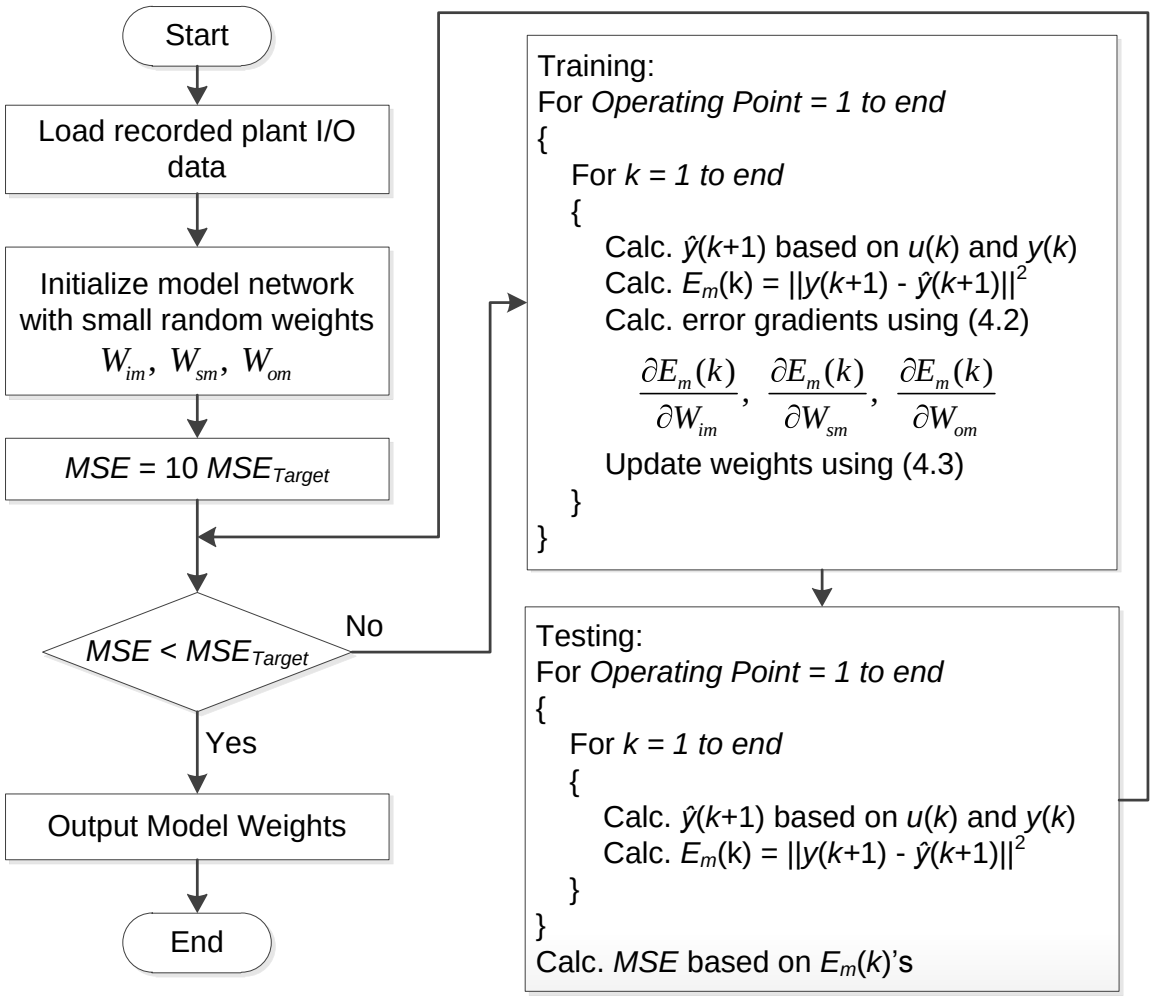

Figure 4.6 Flowchart of RNN model network offline training.

4.3.3.2 Online Training of Model, Critic, and Action Networks

After the offline training, the model network is used to provide system-wide cross-coupling sensitivity signals, $\partial y(k+1)/\partial u(k)$, over a wide operating range. When training the critic and action networks, the model weights are continuously updated with a small learning rate to ensure tracking of new operating conditions.

An RNN DHP critic network is trained online to approximate $\lambda(k+1)$, the partial derivative of $J(k+1)$ with respect to $y(k+1)$, by minimizing the following error [86]:

$$
\begin{aligned}
&E_c(k) = \|e_c(k)\|^2 \\
&e_c(k) = \hat{\lambda}(k) - \{\frac{\partial U(k)}{\partial y(k)} + [\frac{\partial u(k)}{\partial y(k)}]' \frac{\partial U(k)}{\partial u(k)} \\
&\qquad + \gamma[\frac{\partial \hat{y}(k+1)}{\partial y(k)} + \frac{\partial \hat{y}(k+1)}{\partial u(k)} \frac{\partial u(k)}{\partial y(k)}]' \hat{\lambda}(k+1)\}
\end{aligned}
\tag{4.11}
$$

The training of the critic network is done online with the action network in the loop. The training starts with a small discount factor γ, say 0.5. As the critic weights converge, the discount factor is gradually increased to 0.8.

The optimal control objective of the DSOPF controller is to minimize $J(k)$ at every time step k, which is accomplished by training an RNN action network. The action network is trained to approximate the optimal control law by minimizing [86]

$$
\begin{aligned}
&E_a(k) = \left\| \frac{\partial \hat{J}(k)}{\partial u(k)} \right\|^2 \\
&\frac{\partial \hat{J}(k)}{\partial u(k)} = \frac{\partial U(k)}{\partial u(k)} + \gamma[\frac{\partial \hat{y}(k+1)}{\partial u(k)}]' \hat{\lambda}(k+1)
\end{aligned}
\tag{4.12}
$$

During the training, when $E_a(k)$ becomes zero, $u(k)$ is the optimal control action that minimizes $J(k)$ in the local region. Global optimal is obtained by exposing the RNN action network to different system conditions.

To minimize the initial impact on the plant, the random initial weights of both the critic and action networks are limited to small values (typically in the range of 0.0001 to 0.01 with 20% connectivity) such that the initial outputs of both the critic and action networks are close to zero [76], [119].

Figure 4.7 shows the flowchart of online training for all three networks. At sampling step k, the output-to-input derivatives of the model, critic, and action networks are given by (4.4). The model prediction error is given by (4.9), and the model error gradients are given by (4.2). The utility derivatives can be calculated based on the utility formulation, which is

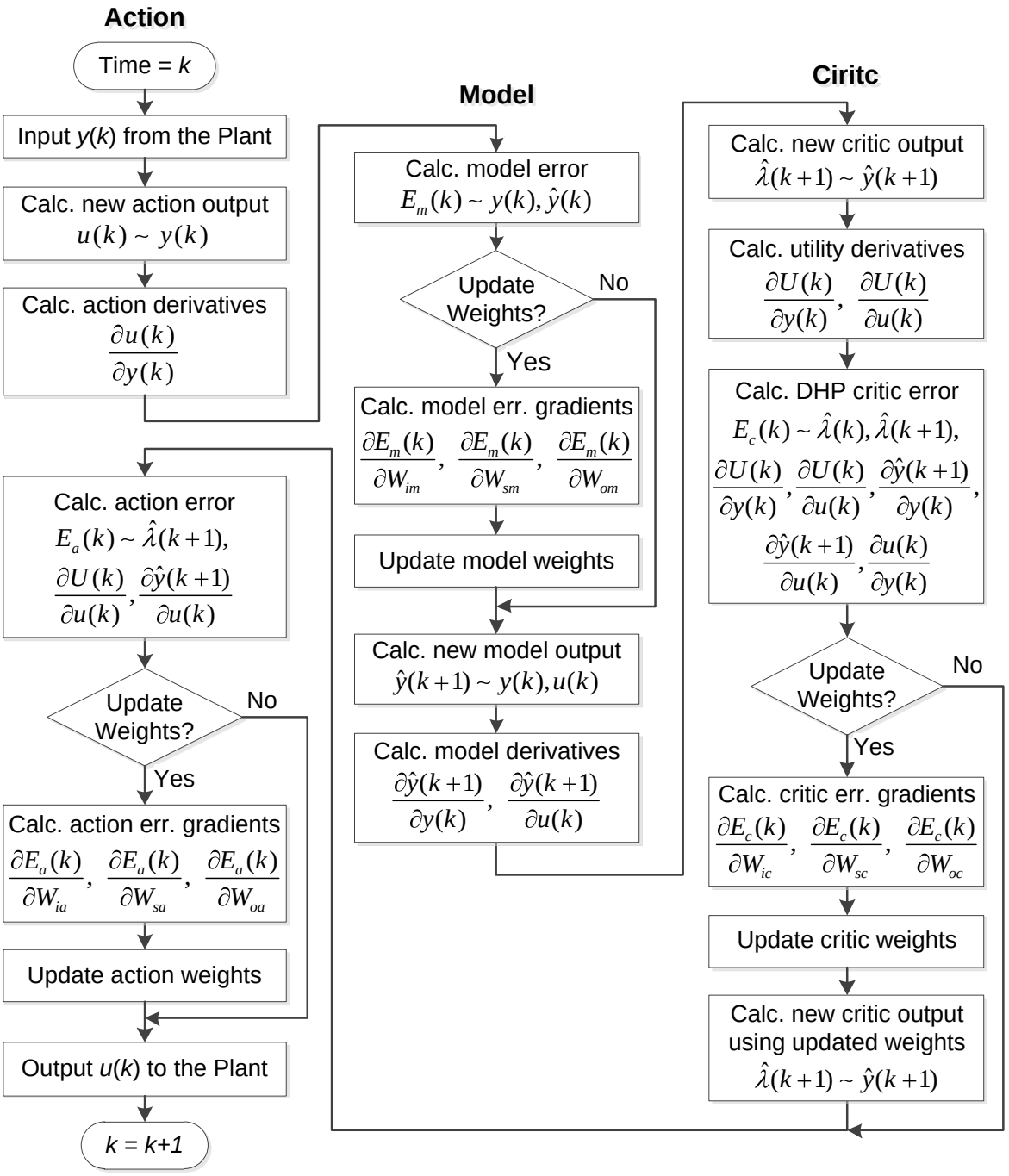

Figure 4.7 Online training flowchart of RNN model, critic, and action networks.

usually a function of the plant outputs and the control effort. Assuming a linear output activation function for the critic network, the DHP critic network output at time *k* is obtained by

$$\hat{\lambda}(k+1) = W_{oc} s_c(k) = W_{oc} f_c[W_{ic} \hat{y}(k+1) + W_{sc} s_c(k-1)], \tag{4.13}$$

where $s_c(k)$ is the internal state vector of the critic network, and $f_c(\cdot)$ is the hidden layer activation function of the critic network. When calculating the critic error, given by (4.11), $\hat{\lambda}(k)$ and $\hat{\lambda}(k+1)$ should be based on the same set of critic weights. With a truncated depth of one, the critic error gradient with respect to W_{oc} is given by

$$\begin{aligned}\frac{\partial E_c(k)}{\partial W_{oc}} &= 2\cdot e_c(k)'\cdot\frac{\partial\hat{\lambda}(k)}{\partial W_{oc}} - 2\gamma\cdot e_c(k)'\cdot[\frac{d\hat{y}(k+1)}{dy(k)}]'\cdot\frac{\partial\hat{\lambda}(k+1)}{\partial W_{oc}} \\ &= 2\cdot e_c(k)\cdot s_c(k-1)' - 2\gamma\cdot\frac{d\hat{y}(k+1)}{dy(k)}\cdot e_c(k)\cdot s_c(k)' \\ \text{where } \frac{d\hat{y}(k+1)}{dy(k)} &= \frac{\partial\hat{y}(k+1)}{\partial y(k)} + \frac{\partial\hat{y}(k+1)}{\partial u(k)}\frac{\partial u(k)}{\partial y(k)}\end{aligned} \quad (4.14)$$

.

The critic error gradient with respect to W_{sc} is given by

$$\begin{aligned}\frac{\partial E_c(k)}{\partial W_{sc}} &= 2\cdot e_c(k)'\cdot\frac{\partial\hat{\lambda}(k)}{\partial W_{sc}} - 2\gamma\cdot e_c(k)'\cdot[\frac{d\hat{y}(k+1)}{dy(k)}]'\cdot\frac{\partial\hat{\lambda}(k+1)}{\partial W_{sc}} \\ &= 2\cdot[\nabla f_{c2}]\cdot W_{oc}'\cdot e_c(k)\cdot s_c(k-2)' - 2\gamma\cdot[\nabla f_{c1}]\cdot W_{oc}'\cdot\frac{d\hat{y}(k+1)}{dy(k)}\cdot e_c(k)\cdot s_c(k-1)'\end{aligned} \quad (4.15)$$

where $[\nabla f_{ci}]$'s are $m\times m$ diagonal matrices containing the gradients of $f_c(\cdot)$, and the subscript i is a time index representing the back-propagation depth (see Appendix E). The critic error gradient with respect to W_{ic} is given by

$$\begin{aligned}\frac{\partial E_c(k)}{\partial W_{ic}} &= 2\cdot e_c(k)'\cdot\frac{\partial\hat{\lambda}(k)}{\partial W_{ic}} - 2\gamma\cdot e_c(k)'\cdot[\frac{d\hat{y}(k+1)}{dy(k)}]'\cdot\frac{\partial\hat{\lambda}(k+1)}{\partial W_{ic}} \\ &= 2\cdot[\nabla f_{c2}]\cdot W_{oc}'\cdot e_c(k)\cdot\hat{y}(k)' - 2\gamma\cdot[\nabla f_{c1}]\cdot W_{oc}'\cdot\frac{d\hat{y}(k+1)}{dy(k)}\cdot e_c(k)\cdot\hat{y}(k+1)'\end{aligned} \quad (4.16)$$

.

After obtaining the model output-to-input derivatives and critic outputs, the action error is given by (4.12). With a truncated depth of one, the action error gradients with respect to its weights can be obtained using (4.2).

During each sampling step, the weights of both the action and critic networks are updated. The online training continues until both the critic and action errors converge to zero.

4.4 Design of a DHP-based DSOPF Controller for a 12-Bus Power System

4.4.1 Twelve-Bus Test Power System

A 12 bus test power system modified from [114], as shown in Figure 4.8, is used to demonstrate the design of the DHP-based DSOPF controller. Buses 4 and 5 are two remote load buses supplied from three transmission corridors. No infinite bus is used to hold the system frequency. All four generators are modeled with full transient dynamics in PSCAD and equipped with automatic voltage regulators (AVRs) and speed governors. Generators 2 to 4 are within one control area, and they are controlled by one automatic generation controller, AGC2. Generator 1 is assumed to be an aggregated representation of an interconnected area, and it is controlled by AGC1. With AGC1 and AGC2, the system frequency and inter-area tie-line power flow, P_{tie}, can be maintained at the nominal/scheduled values. Bus 4 is selected as the pilot bus for a PI-based secondary voltage control. Block diagrams of the AGCs, bus 4 voltage control (V_4Ctrl), AVRs and speed

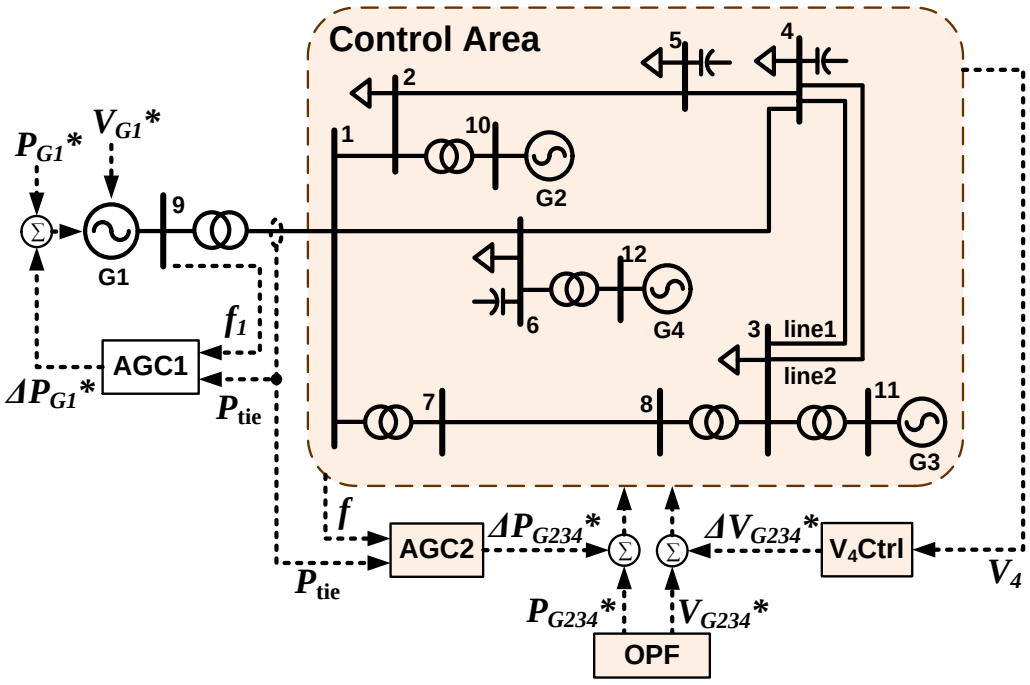

Figure 4.8 Twelve-bus test power system with AGCs and V_4Ctrl.

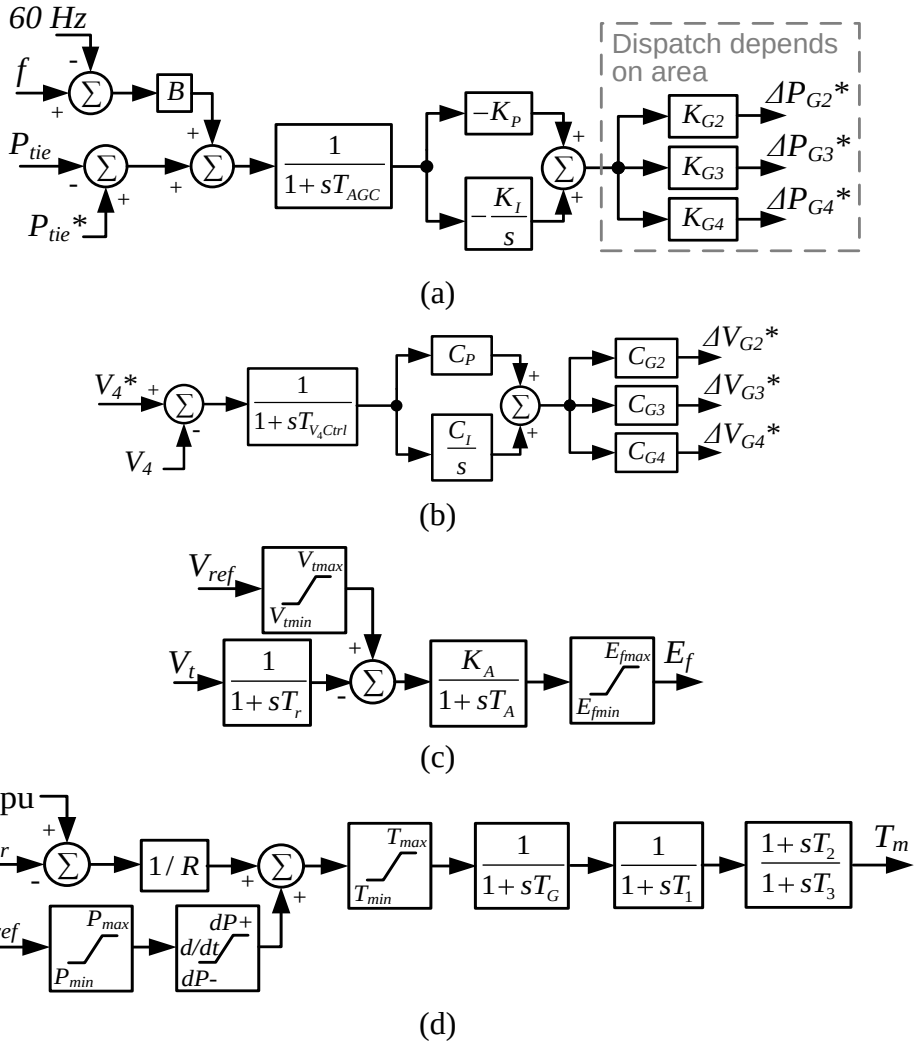

Figure 4.9 Block diagrams of (a) a PI-based AGC (P_{tie} is positive with an inbound flow), (b) a PI-based pilot bus voltage control, (c) an AVR, and (d) a speed governor.

governors used in this study are shown in Figure 4.9. The dispatch ratios in the AGC, K_{G1}, K_{G2} and K_{G3}, are determined by the changing rate of the incremental cost of each generator, so that any changes commanded by AGC2 would result in minimum costs [17]. The dispatch ratios in the V4Ctrl are set to be equal in this study. All four generators are assumed to be gas-turbine based and have a typical ramp rate (both up and down) of 18 MW/min [115].

The generator and line parameters are provided in Appendix D [114]. The base case of this system, including the scheduled tie-line flow, is defined in Table 4.1. At each load bus, half of the load is represented by a constant-impedance load and the other half is represented

by a constant-power load, which introduces some load-voltage characteristics [116]. All lines are represented by a single lumped π-equivalent model [17].

A DSOPF controller is designed below to replace AGC2 and V_4Ctrl and provide coordinated secondary active and reactive power flow control, as shown in Figure 4.10.

Table 4.1 Base case of the 12-bus power system (modified from [114]).

Bus	Gen MVA	V_G* (pu)	P_G* (MW)	Fuel Cost ($/h) a	b	c	Load (MVA) Const. Imp.	Const. Power	Shunt Cap. (MVAr)
2							140 + j100	140 + j100	
3							160 + j120	160 + j120	
4							160 + j120	160 + j120	160
5							50 + j30	50 + j30	80
6							220 + j150	220 + j150	180
9 (G1)	1000	1.02	480						
10 (G2)	700	1.02	500	700	34.10	0.0117			
11 (G3)	500	1.01	200	670	36.85	0.0135			
12 (G4)	500	1.02	300	650	36.24	0.0130			

Scheduled area power import P_{tie}* = 480 MW.

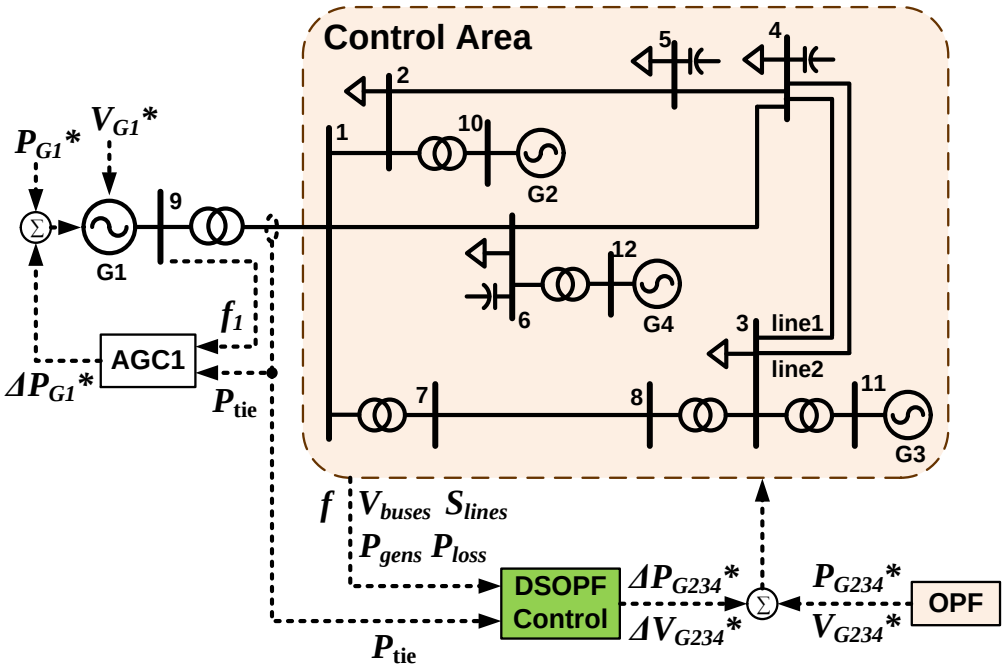

Figure 4.10 Twelve-bus test power system with DSOPF control.

AGC2 and V_4Ctrl are disconnected during the training and testing of the DSOPF controller. Similar to the AGCs, the data update rate for the DSOPF controller is assumed to be 1 s, which neglects the transient oscillations but includes the local controller and load dynamics. During the online training of the neural networks shown in Figure 4.5, the weights of these neural networks are also updated every 1 s.

4.4.2 Model Network for System Identification

The nonlinear dynamic plant "seen" by the DSOPF controller is defined in Figure 4.11. The following 15 smoothed wide-area measurements are sampled at 1 Hz for the DSOPF controller: the system frequency in Hz, f (average rotor speeds of G2, G3 and G4); the RMS voltage of the five load buses in pu, V_2, V_3, V_4, V_5 and V_6; the apparent power flow magnitude of four long lines in pu, S_{25}, S_{16}, S_{64}, and S_{78}; the tie-line power import in MW, P_{tie}; the active power outputs from G2 to G4 in MW, P_{G2}, P_{G3}, and P_{G4}; and the total network active power loss in MW, P_{loss}. These 15 measurements are then linearly scaled to have the same order of magnitude and form the plant output vector, $y(k)$.

The plant has six inputs from the DSOPF controller. $u_1(k)$ to $u_3(k)$ are adjustment signals to change the active power outputs of G2 to G4, and $u_4(k)$ to $u_6(k)$ are adjustment

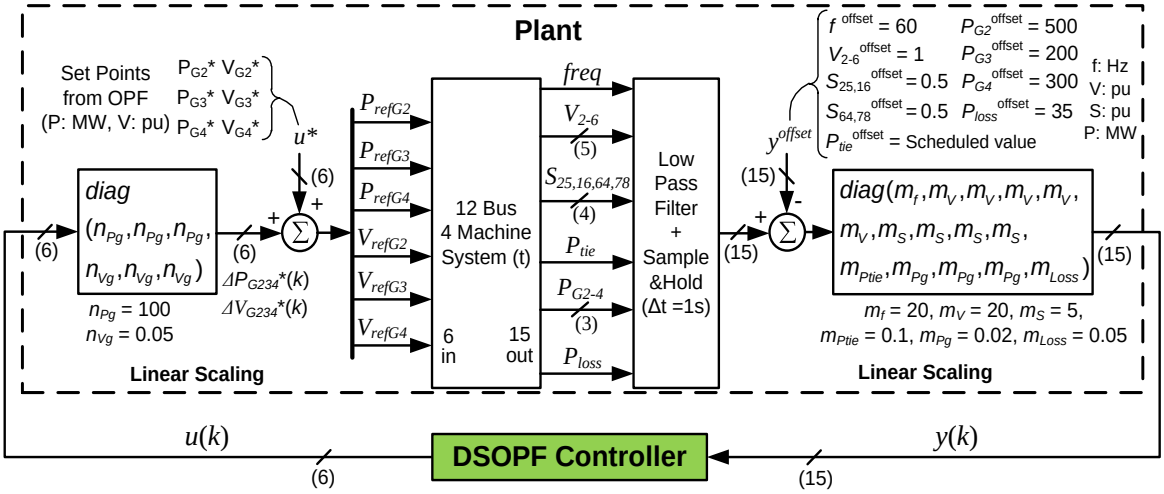

Figure 4.11 The nonlinear plant connected to the DSOPF controller

signals to change the terminal voltages of G2 to G4. These six inputs are scaled and added to the steady-state dispatches, u^*, obtained from the traditional OPF algorithm.

Based on the discussions in Section 4.3, an RNN model network with 30 internal neurons is first trained offline to identify the plant dynamics. Pseudo-random binary signals (PRBSs) are injected to the plant inputs at eight different dispatch cases, as listed in Table 4.2. D1 is the base case, D2 to D4 represent line outage conditions, and D5 to D8 represent different load conditions. All 8 dispatches are generated using the interior-point OPF algorithm with bus-voltage and line-rating constraints in MATPOWER [117]. Small manual adjustments are then added to the MATPOWER results to account for load-voltage characteristics and local controller errors. The PRBS perturbations applied to the system are

Table 4.2 Operating conditions for model network pretraining.

Disp-atch	G2		G3		G4		Line or load changes from base case (P: MW, Q: MVAr)
	P_{G2}* (MW)	V_{G2}* (pu)	P_{G3}* (MW)	V_{G3}* (pu)	P_{G4}* (MW)	V_{G4}* (pu)	
D1	500	1.02	200	1.01	300	1.02	None (Base Case)
D2	490	1.02	220	1.03	330	1.03	Line 2-5 is out
D3	500	1.03	215	1.04	300	1.02	Line 4-6 is out
D4	500	1.03	215	1.04	315	1.04	One of lines 3-4 is out
D5	550	1.05	270	1.04	360	1.02	Const. power loads at buses 3&5 become: P_{L3} =210, Q_{L3} = 140 P_{L5} =100, Q_{L5} = 50
D6	505	0.99	180	1.02	285	1.03	Const. power load at bus 5 become: P_{L5} = 0, Q_{L5} = 0
D7	525	1.02	250	1.04	340	1.03	Const. power load at bus 4 become: P_{L4} = 210, Q_{L4} = 140
D8	500	1.01	190	1.02	290	1.02	Const. power load at bus 4 become: P_{L4} = 110, Q_{L4} = 100

P_{G1}*, V_{G1}*, and P_{tie}* are the same as the base case for all dispatch cases.

shown in Figure 4.12. Because of the response-time difference in AVRs and speed governors, the perturbations applied to the three generator power commands change sequentially every 20 s, and the perturbations applied to the three generator voltage commands change sequentially every 2 s. 500 s of data for each dispatch case are recorded and used for model offline training [118]. The model network is then trained to minimize the mean squared error defined in (4.10) following the steps shown in Figure 4.6.

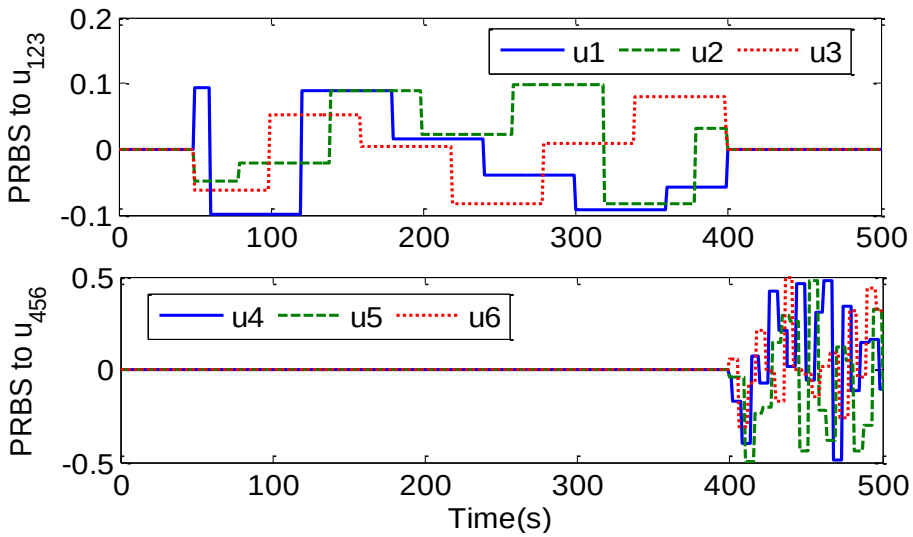

Figure 4.12 PRBS perturbations applied to the 12-bus system.

The testing results of the trained model network (with fixed weights) at D1, D2, D5 and D6 under the same PRBS injections are shown in Figure 4.13, where y_1 (related to the system frequency) is plotted. All 15 outputs from the model network have similar tracking performances at all 8 dispatch cases. A mean relative absolute error of 5% is achieved for the testing results. The trained model network is table to provide one-step prediction for the eight operating conditions listed in Table 4.2. After the offline training, the model network is used to provide system-wide cross-coupling sensitivity signals, $\partial y(k+1)/\partial u(k)$. When training the critic and action networks, the model weights are continuously updated with a small learning rate to ensure tracking of new operating conditions.

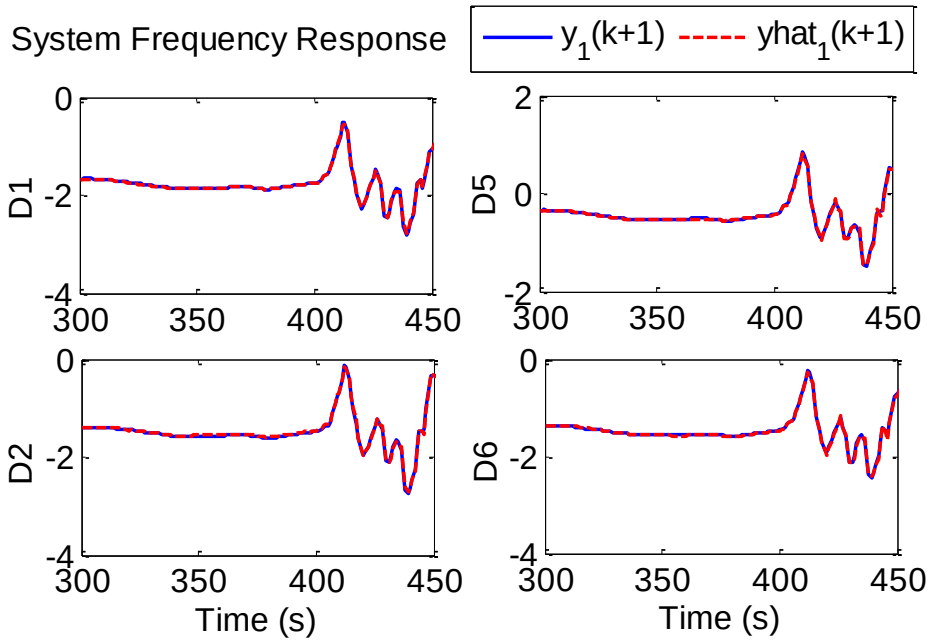

Figure 4.13 Model network testing results at the D1, D2, D5, and D6: plant output $y_1(k+1)$ and model network output $\hat{y}_1(k+1)$.

4.4.3 Utility and Cost-to-Go Functions

The control objective for the 12 bus system includes six components: the area control error, U_{ACE}; the system voltage deviation, U_{Volt}; the system line loading, U_{Line}; the total fuel cost, U_{Fuel}; the total line loss, U_{Loss}; and the control effort, U_{Ctrl}. The utility function, U, is thus defined as

$$U(k) = U_{ACE}(k) + U_{Volt}(k) + U_{Line}(k) + U_{Fuel}(k) + U_{Loss}(k) + U_{Ctrl}(k), \tag{4.17}$$

$$\begin{aligned}
U_{ACE}(k) &= w_{freq}\Delta f^{2}(k) + w_{tie}\Delta P_{tie}{}^{2}(k) \\
&= w_{freq}y_1^2(k)/m_f^2 + w_{tie}y_{11}^2(k)/m_{Ptie}^2 \\
U_{Volt}(k) &= w_{volt}\,\|\Delta V_{2\text{-}6}(k)\|^2 = w_{volt}\,\|y_{2\text{-}6}(k)\|^2/m_V^2 \\
U_{Line}(k) &= w_{line}[e^{(S_{25}^4(k)-1)} + e^{(S_{16}^4(k)-1)} + e^{(S_{64}^4(k)-1)} + e^{(S_{78}^4(k)-1)}] \\
U_{Fuel}(k) &= w_{fuel}[F_{G2}(k) + F_{G3}(k) + F_{G4}(k) - F^{offset}] \\
U_{Loss}(k) &= w_{loss}P_{loss}(k) = w_{loss}[y_{15}(k)/m_{Loss} + P_{loss}^{offset}] \\
U_{Ctrl}(k) &= w_{Pg}\,\|\Delta P_{G2\text{-}4}^{*}(k)\|^2 + w_{Vg}\,\|\Delta V_{G2\text{-}4}^{*}(k)\|^2 \\
&= w_{Pg}n_{Pg}^2\,\|u_{1\text{-}3}(k)\|^2 + w_{Vg}n_{Vg}^2\,\|u_{4\text{-}6}(k)\|^2
\end{aligned} \tag{4.18}$$

,

where w_x's are various weighting factors (listed in Table 4.3), and m_x's and n_x's are the plant input-output scaling factors as shown in Figure 4.11. The weighting factors are heuristically selected. A higher weighting factor gives a higher priority to the corresponding component, and these weights may be changed according to system conditions and specific design requirements.

Table 4.3 Weighting factors and constants used in the utility function.

w_{freq}	w_{tie}	w_{volt}	w_{line}	w_{fuel}	F^{offset}	w_{loss}	w_{Pg}	w_{Vg}
400	0.01	1600	1	0.001	4e4	0.01	1e-4	200

U_{Line}(k) in (4.18) is designed such that if a line loading is above 1 pu, U_{Line}(k) increases dramatically; otherwise, U_{Line}(k) becomes negligible. For example, the pu line loading of line 2-5, $S_{25}(k)$, is obtained by

$$S_{25}(k) = [y_7(k)/m_s + S_{25}^{\text{offset}}], \tag{4.19}$$

where m_s and S_{25}^{offset} are a scaling factors shown in Figure 4.11. Similar relationships exist between $S_{16}(k)$, $S_{64}(k)$, $S_{78}(k)$ and $y_8(k)$, $y_9(k)$, $y_{10}(k)$, respectively. In (4.18), F_{Gi}(k) is the fuel cost of generator i in \$/MWh. A quadratic cost function [19] is used, as in

$$\begin{aligned} &F_{Gi}(k) = a_i + b_i P_{Gi}(k) + c_i P_{Gi}^2(k) \\ &P_{Gi}(k) = y_{10+i}(k)/m_{Pg} + P_{Gi}^{offset} \\ &i = 2,3,4 \end{aligned} \tag{4.20}$$

,

where the coefficients a_i, b_i and c_i for the three generators are listed in Table 4.1. From (4.17) to (4.20), the utility function, $U(k)$, depends only on the plant output vector, $y(k)$, and the control action vector, $u(k)$. The cost-to-go function, $J(k)$, is then the discounted accumulation of $U(k)$.

4.4.4 Critic Network for Approximate Dynamic Programming

A based in the dual heuristic dynamic programming (DHP) critic network is trained online to approximate $\lambda(k+1)$, the partial derivative of $J(k+1)$ with respect to $y(k+1)$, by minimizing the critic error defined in (4.11). A recurrent neural network (RNN) with 30

internal neurons is used to implement the critic network. The critic network is trained online with the action network in the loop, following the online training flowchart shown in Figure 4.7. The training starts with a small discount factor γ, say 0.5. As the critic weights converge, the discount factor is gradually increased to 0.8. Since the training of the action network also depends on the critic network, these two networks are trained and converge together [89].

4.4.5 Action Network for Optimal Control Law Approximation

The optimal control objective of the DSOPF controller is to minimize $J(k)$ at every time step k, which is accomplished by training the action network. An RNN action network with 30 internal neurons is trained online to approximate the optimal control law by minimizing the action error defined in (4.12). During the online training, when action error converges to zero, $u(k)$ is the optimal control action that minimizes $J(k)$ in the local region. Global optimal is obtained by exposing the DSOPF controller to different system conditions.

To minimize the initial impact on the power system, the weights of the critic and action networks are randomly initialized between ±0.005 with 20% connectivity [76], [119], i.e., 20% of the entries in the weight matrices are nonzero and between ±0.005. Starting at D1 (see Table 4.2) and a discount factor of 0.5, the action and critic networks are connected to the 12-bus system and trained simultaneously online. The weights of both the action and critic networks are updated at every time step, i.e., 1 s, based on their error signals. Different disturbances, such as load ramping and line outages, are then applied to the system. After both networks converge at this operating condition, the training process continues at other operating points, and the discount factor is slowly increased to 0.8.

4.5 Simulation Results

4.5.1 Steady-State Performance

The steady-state performance of the DSOPF controller is studied at the different

dispatch cases listed in Table 4.2. Results for cases D1, D3 and D7 are shown in Table 4.4, where the system is controlled by the linear controllers (AGC2+V_4Ctrl) and the DSOPF controller, respectively. For V_4Ctrl, the reference or required voltage at bus 4 is set to 0.97 pu. The voltages of the two load buses, V_4 and V_5, and the apparent power loading of the three most heavily loaded lines are listed in Table 4.4.

When using the DSOPF control, the utility function, as an overall index of optimality, is lower than that of the linear controllers at all three dispatch cases (lower is better). Lower fuel cost, lower line losses, smaller voltage deviations and lower line loadings are achieved by the DSOPF control, but with higher control effort and slightly larger frequency and tie-line flow deviations.

Table 4.4 Steady-state comparison of DSOPF control and AGC+V_4Ctrl.

	D1			D3			D7	
	AGC2 V_4Ctrl	DSOPF Ctrl		AGC2 V_4Ctrl	DSOPF Ctrl		AGC2 V_4Ctrl	DSOPF Ctrl
Utility	7.90	7.21	Utility	9.74	8.81	Utility	10.75	10.12
Fuel	43.67	43.24	Fuel	44.23	43.61	Fuel	46.18	45.98
F	60.000	60.001	f	60.000	60.003	f	60	60.003
P_{tie}	480.0	479.6	P_{tie}	480.0	478.9	P_{tie}	480	479.1
P_{loss}	46.3	40.5	P_{loss}	46.7	39.1	P_{loss}	48.7	41.9
U_{Volt}	1.619	1.142	U_{Volt}	2.937	2.391	U_{Volt}	2.14	1.586
V_4	0.970	0.976	V_4	0.970	0.967	V_4	0.970	0.973
V_5	0.993	1.007	V_5	0.979	1.003	V_5	0.984	1.007
U_{Line}	1.904	1.813	U_{Line}	1.868	1.754	U_{Line}	1.900	1.793
S_{25}	0.76	0.71	S_{25}	0.81	0.75	S_{25}	0.77	0.73
S_{16}	0.80	0.76	S_{16}	0.55	0.56	S_{16}	0.78	0.71
S_{78}	0.67	0.63	S_{78}	0.75	0.68	S_{78}	0.69	0.65
U_{Ctrl}	0.244	0.602	U_{Ctrl}	0.244	0.668	U_{Ctrl}	0.028	0.337

(*Fuel*: k$/h, *f*: Hz, P_{tie}: MW, P_{loss}: MW, *V*: pu, *S*: pu)

4.5.2 Dynamic Performance after Load Tripping

To demonstrate the excellent performance of the DSOPF controller in regulating the system frequency, at dispatch case D1, an unexpected contingency causes the 100 MW 60 MVAr load at bus 5 to trip at 300 s. To prevent over-voltage, the capacitor bank at bus 5 is also tripped at 301 s by over-voltage protection. The system frequency and tie-line flow controlled by the linear controllers (AGC2+V_4Ctrl) and the DSOPF controller, respectively, are shown in Figure 4.14 (a). Results from the linear controllers are shown in black solid lines, and results from the DSOPF controller are shown in red dotted lines. The DSOPF controller results in a smaller frequency rise and faster frequency recovery than the linear controllers. The tie-line flow also has a smaller deviation and faster return to its scheduled value of 480 MW, when the DSOPF controller is used.

Figure 4.14 (b) and (c) show the six controlled quantities, namely the active power outputs and terminal voltages of the three generators, during this event. To regulate the short-term power imbalance, AGC2 decreases generation from all three generators at their maximum ramp rates. In contrast, the DSOPF controller further utilizes the load-voltage characteristics and temporarily increases the generator voltages, which creates higher energy consumption at the local buses to balance the short-term over-generation.

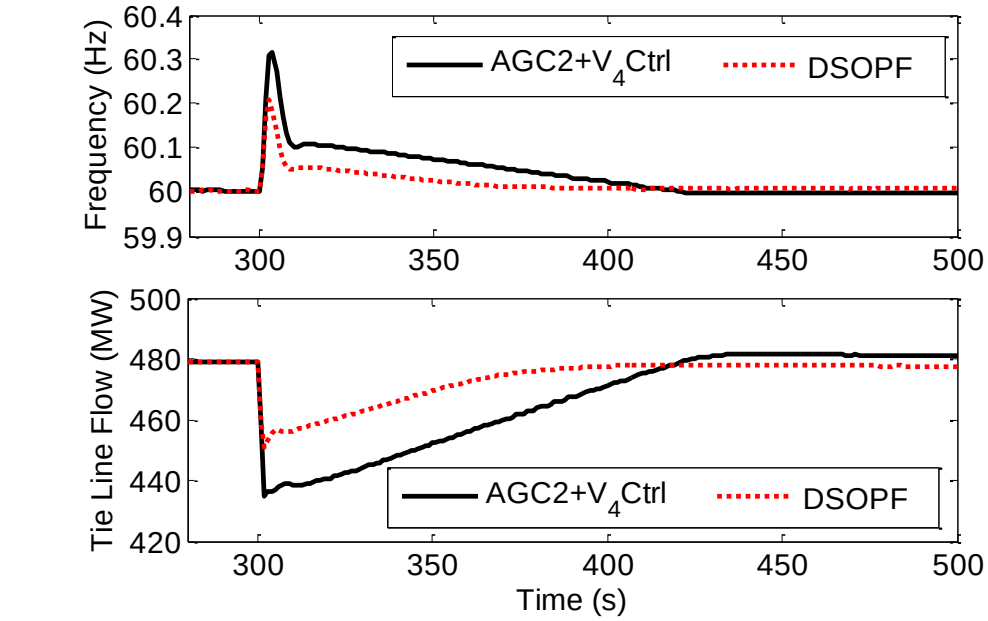

(a)

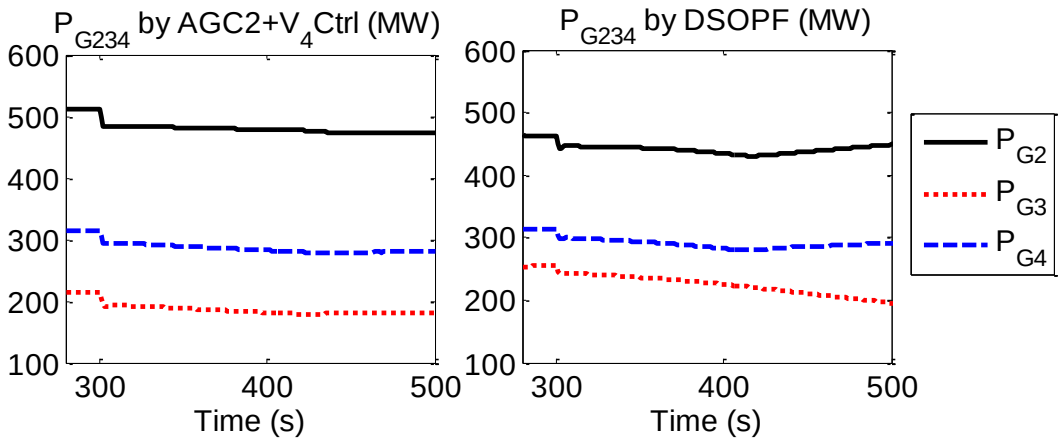

(b)

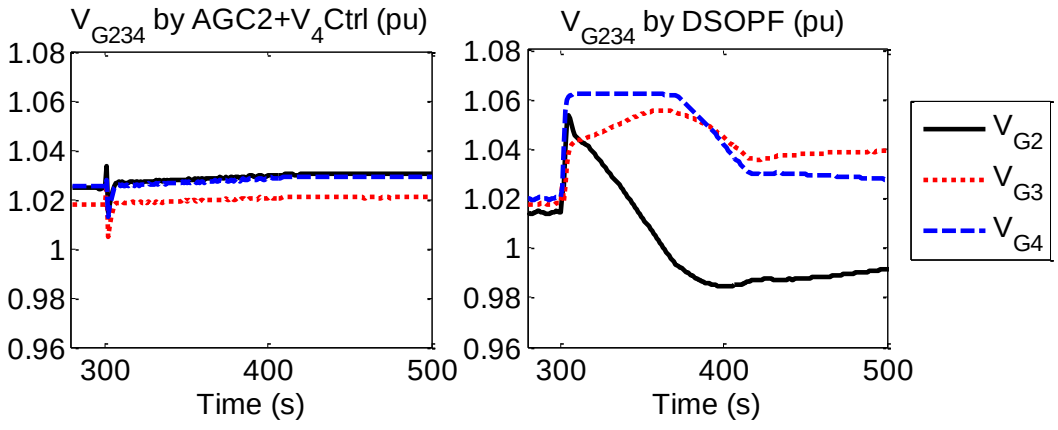

(c)

Figure 4.14 System responses after load tripping at bus 5: (a) frequency and tie-line flow, (b) active power outputs of G2 to G4, (c) terminal voltages of G2 to G4.

4.5.3 Dynamic Performance with Large Varying Load

To simulate the active power variability from intermittent renewable generation resources, 50 MW, 10 MVAr of varying constant-power load, as shown in Figure 4.15 (a), are added to each of buses 4 and 5. As a result, the system experiences large load ramping (both up and down) at a rate of 40 MW/min with a peak of 100 MW.

With AGC2 and V_4Ctrl, the active power outputs and terminal voltages of the three generators varies up and down to follow the system load and regulate the bus 4 voltage, as shown in Figure 4.15 (g) and (h). Meanwhile, the system consumes more fuel, as shown in Figure 4.15 (b), and has higher line losses, as shown in Figure 4.15 (c). The frequency and tie-line flow have a maximum deviation of more than 0.04 Hz and 15 MW, respectively, as shown in Figure 4.15 (d) and (e). Although the voltage at bus 4 is well regulated by V_4Ctrl, the voltage at bus 5 drops below 0.95 pu, as shown in Figure 4.15 (f). If this large load variation continues, frequent switching of the capacitor bank at bus 5 would be needed to avoid under-voltage violations.

On the contrary, with the DSOPF controller, the three generators are optimally coordinated. Lower fuel cost and line loss are achieved, as shown in Figure 4.15 (b) and (c). The voltage at both buses 4 and 5 are now kept above 0.95 pu, as shown in Figure 4.15 (f). The system frequency and tie-line flow are regulated much closer to their nominal values, as shown in Figure 4.15 (d) and (e).

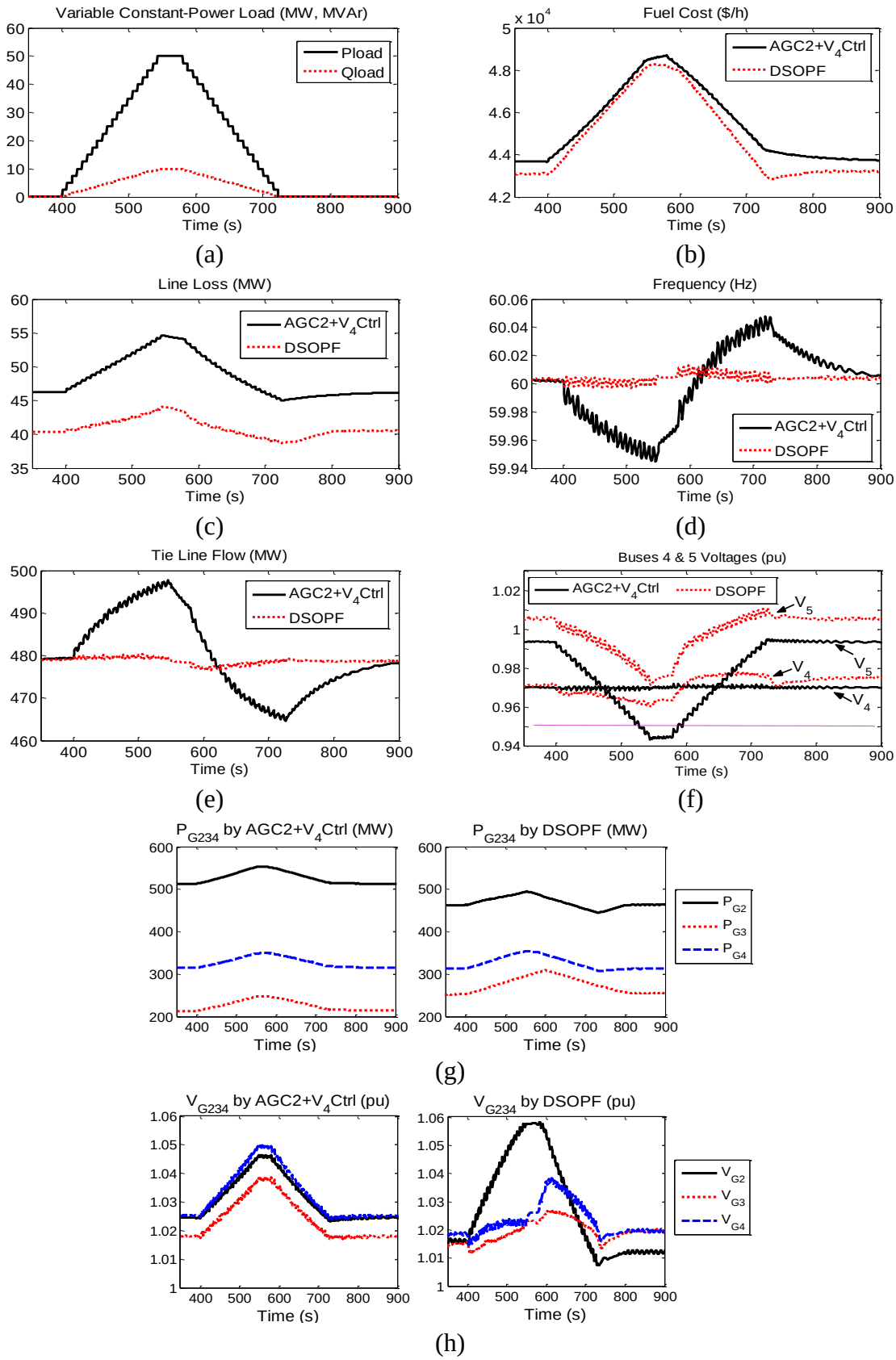

Figure 4.15 System responses during a large load variation: (a) varying load applied to buses 4 and 5, (b)-(f): various system responses, (g)-(h): controlled variables.

4.5.4 Dynamic Performance after Line Outage

To further demonstrate the DSOPF controller's capability to reroute the system power flow, at dispatch case D7 (bus 4 becomes more heavily loaded), line 2-5 is permanently tripped 0.15 s after a three-phase-to-ground fault. The fault happens somewhere along line 2-5 at 400 s. This is a severe event since line 2-5 is heavily loaded at D7 in order to serve the load at buses 4 and 5. Tripping of line 2-5 may cause overloading of the other two transmission corridors. This event requires a redistribution of power flow in order for the 12-bus system to survive. Figure 4.16 shows the simulation results of this event with AGC2+V_4Ctrl and the DSOPF controller, respectively.

When only AGC2 and V_4Ctrl are used, bus 4 voltage (the lowest post-fault voltage) drops below 0.94 pu, as shown in Figure 4.16 (a). The PI-based V_4Ctrl fails to regulate the bus 4 voltage, since the reactive support from G2 is interrupted and the reactive power outputs from G3 and G4 are limited by their MVA capacities. As a result, 50 MW 20 MVAr of load at bus 4 is tripped at 500 s to bring the bus 4 voltage back to a normal condition. However, transmission line 1-6, which has the highest post-fault line loading, remains overloaded, as shown in Figure 4.16 (b). Neither AGC2 nor V_4Ctrl is capable of relieving this line overload.

In contrast, with the proposed DSOPF controller, both the active and reactive power flows are optimally adjusted after the outage of line 2-5. G2 now becomes electrically further away from the load center. The DSOPF controller reduces the power generation and terminal voltage from G2, as shown in Figure 4.16 (d) and (e). Both V_4 and S_{16} are maintained at normal conditions without violating any voltage or line limits. Under-voltage load shedding is thus not necessary. The system frequency, as shown in Figure 4.16 (c), also experiences less fluctuation. The system survives this event with the DSOPF controller.

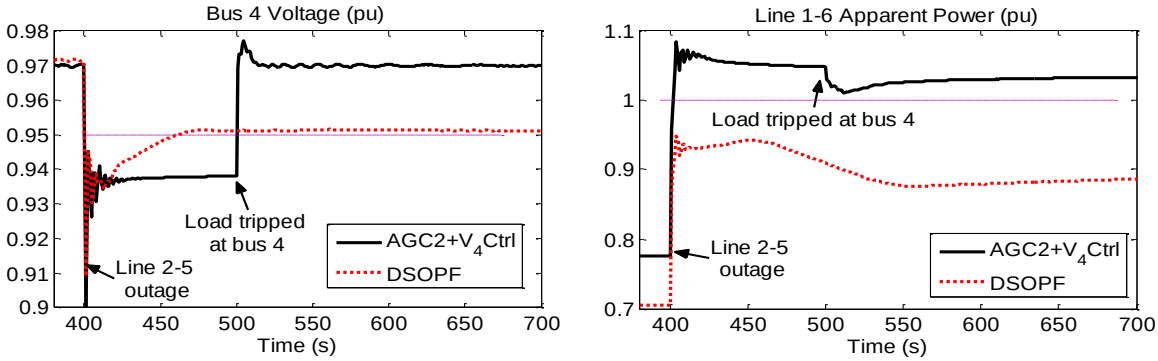

(a) (b)

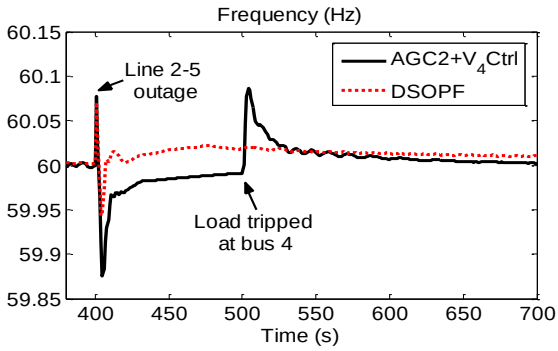

(c)

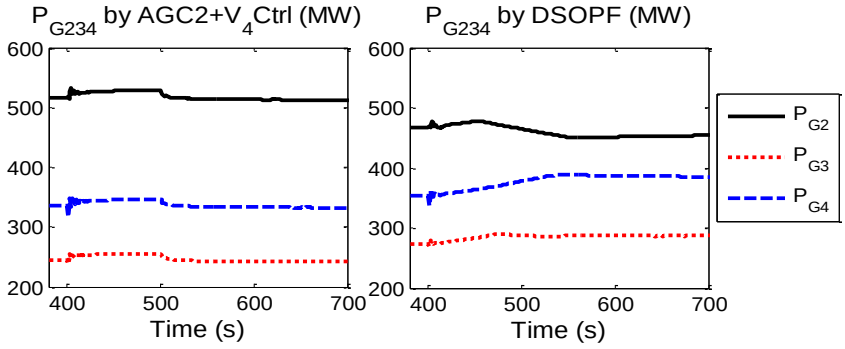

(d)

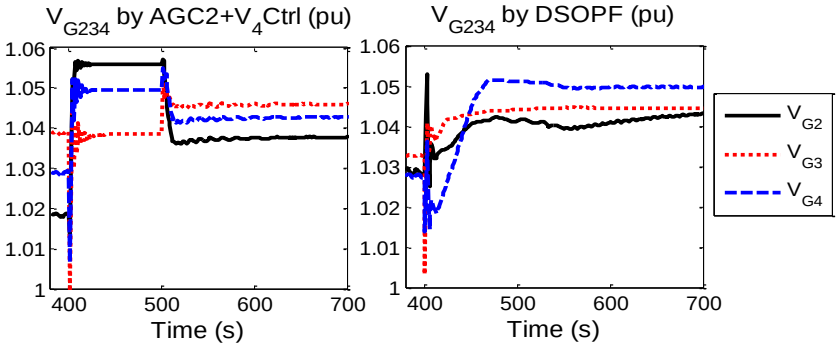

(e)

Figure 4.16 System responses after line 2-5 outage (load tripping also occurs when AGC2 and V_4Ctrl are used): (a) bus 4 voltage, (b) line 1-6 loading, (c) system frequency, (d) active power outputs of G2 to G4, (e) terminal voltages of G2 to G4.

4.6 Chapter Summary

A dynamic stochastic optimal power flow (DSOPF) control algorithm is presented in this chapter as a solution to the future smart grid operation in an environment with high short-term uncertainty and variability. The proposed DSOPF control adapts the nonlinear optimal control technique from the Adaptive Critic Design (ACD) theory, and provides closed-loop dynamic tracking of the optimal operating point of a power system. Identifications of system topology changes and local controller/load dynamics are carried out by the continuous online learning of the ACD method. The dual heuristic dynamic programming (DHP) approach with recurrent neural networks (RNNs) is used to design a DSOPF controller for a 12-bus test power system. Simulation results demonstrate the promising steady-state and dynamic performances of the DSOPF controller under various operating conditions and system disturbances. It is a promising candidate for routing real-time variable wind energy injections.

The next chapter further investigates this DSOPF control method on a larger power system with different generation resources, including coal, gas, hydro, and wind. A two-level DSOPF control scheme is proposed to aid scaling up the DSOPF control algorithm and make it applicable large practical power systems.

CHAPTER 5 TWO-LEVEL DSOPF CONTROL FOR A 70-BUS POWER SYSTEM WITH LARGE WIND PLANTS

5.1 Chapter Overview

The dynamic stochastic optimal power flow (DSOPF) control algorithm proposed in Chapter 4 shows promising dynamic power flow control capability for the small 12-bus system. To further investigate the potential of the DSOPF control algorithm for large power systems, a 70-bus test power system with different generation resources, including large wind plants, is developed. A two-level DSOPF control scheme is proposed in this chapter to scale up the DSOPF algorithm for this 70-bus system. The lower level consists of two area DSOPF controllers, each of which controls its own area power network. The top level consists of one global DSOPF controller, which coordinates the area controllers by adjusting the inter-area tie-line flows. This two-level architecture distributes the control and computation burden to multiple area DSOPF controllers, and reduces the training difficulty for implementing the DSOPF control for a large network. Simulation studies on the 70-bus power system with large wind variation are shown to demonstrate the effectiveness of the proposed two-level DSOPF control scheme.

5.2 Seventy-Bus Power System

The 70-bus test power system, as shown in Figure 5.1, is developed by modifying and extending a 68-bus test power system [120], [121]. The original 68-bus power system is a simplified model of the New England and New York interconnected power systems of the 1970s. Area 1 with generators G1-G9 represents the New England Test System. Area 2 with generators G10-G13 represents the New York Power System (NYPS). Generators G14-G16

are aggregated representations of three interconnected areas to the NYPS. Two additional buses, buses 69 and 70, are added to connect two wind plants, G17 and G18, to the main system. Detailed parameters of the 70-bus power system are listed in Appendix D. A brief description on the major system components is given below.

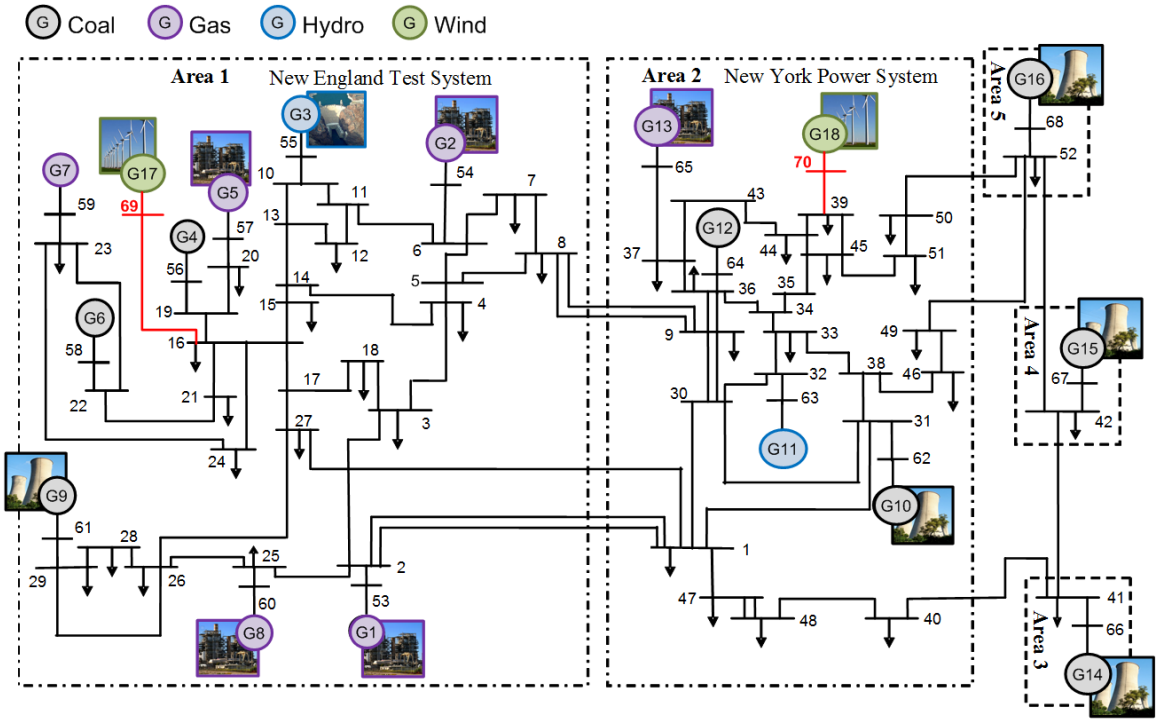

Figure 5.1 The 70-bus power system with different generation resources.

5.2.1 Modeling of the 68-Bus System with Conventional Generator Units

The 16 generators in the 68-bus system developed in this dissertation consist of eight coal plants: G4, G6, G9, G10, G12, G14, G15, and G16; six gas plants: G1, G2, G5, G7, G8, and G13; and two hydro plants: G3 and G11. No infinite bus is used to hold the system frequency. For all 16 conventional generation units, the 8th order synchronous machine model [17] is used. The parameters for each synchronous generator, derived from [120] by properly selecting generator ratings, are listed in Appendix D.

Automatic voltage regulators (AVRs) and speed governors are developed for all 16

conventional generation units. Block diagrams of the AVR exciters and turbine speed governors are shown in Figure 5.2 (a) and (b). Solid-state exciters are assumed with negligible time delays. A feedback block for transient gain reduction is included in the AVR model to increase the damping torque [17]. A ramp rate of 1% per minute is assumed for the coal plants. For the gas and hydro plants, the ramp rates are assumed to be 5% per minute and 5% per second, respectively. Typical AVR and governor parameters for coal, gas, and hydro plants are selected from [122] for the 16 generators (listed in Appendix D).

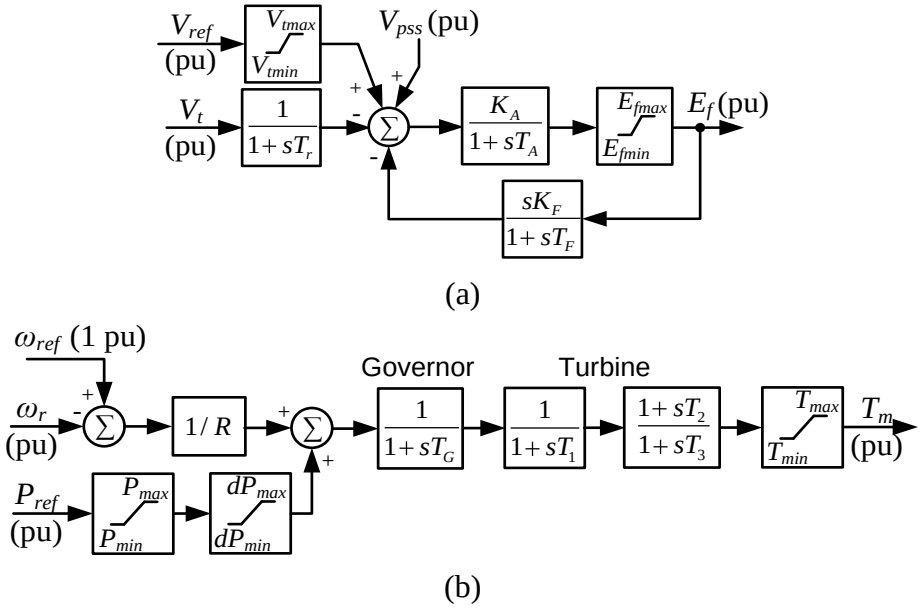

Figure 5.2 Models of (a) an AVR exciter and (b) a turbine speed governor.

The 68-bus system experiences 11 local electromechanical oscillation modes and 4 inter-area oscillation modes [121]. Seven power system stabilizers (PSSs) are added to generators G3, G9, G10, G12, G14, G15, and G16 to improve the damping of these oscillation modes. The seven PSSs are added one at a time to damp the presently worst oscillating mode resulting from eigenvalue analysis [17] of the 68-bus system. The block diagram of the PSSs used in this study is shown in Figure 5.3. Parameters for the PSSs are listed in Appendix D.

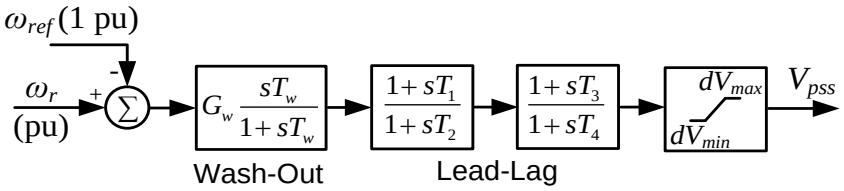

Figure 5.3 Model of a power system stabilizer.

The single-section lumped π model [17] is used to model all transmission lines, i.e., the effects of electromagnetic traveling waves are neglected. Accurate load modeling is a difficult but important task when studying practical power systems. A typical system load usually comprises a large number of diverse load components, and the load composition changes with time. For this test system, since no actual load data is available, all loads are modeled as impedance loads.

5.2.2 Addition of Wind Plants

The 68-bus test system is expanded to a 70-bus system by adding two wind plants (see Figure 5.1). Wind plant G17 has a capacity of 1404 MW, and is connected to bus 16 in area 1 through a transmission line. Wind plant G18 has a capacity of 1836 MW, and is connected to bus 39 in area 2 through a transmission line. A typical capacity factor of around 25% is assumed for both wind plants. To compensate for the additional generation capacity, the loads at buses 16 and 24 in area 1 are each increased by 175 MW, and the loads at buses 33 and 45 in area 2 are each increased by 240 MW. The line and load data for the final 70-bus power network are listed in Appendix D.

An aggregated DFIG wind turbine system (see Appendix A) is used for both wind plants. The power electronic converter is modeled as a three-phase controllable voltage source, i.e., harmonic contents are neglected. Both wind plants follow the maximum-power-point operation up to their maximum power ratings. External control signals for wind curtailments in MW are also implemented. Detailed wind turbine control algorithms are

described in Appendix A.

5.2.3 Automatic Generation Controllers (AGCs) for the 70-Bus System

Five AGCs (one for each area) are implemented for the 70-bus power system to regulate the inter-area tie-line power flow and system frequency, as shown in Figure 5.4. For areas 1 and 2, the AGC controls only the gas and hydro generation units (see Figure 5.1), which have fast ramping capability as compared to the coal-based units. For areas 3 to 5, the AGC controls the aggregated generator in each area. Figure 5.5 shows the AGC for area 1 as an example. The AGCs for other areas have a similar structure but different inputs and outputs.

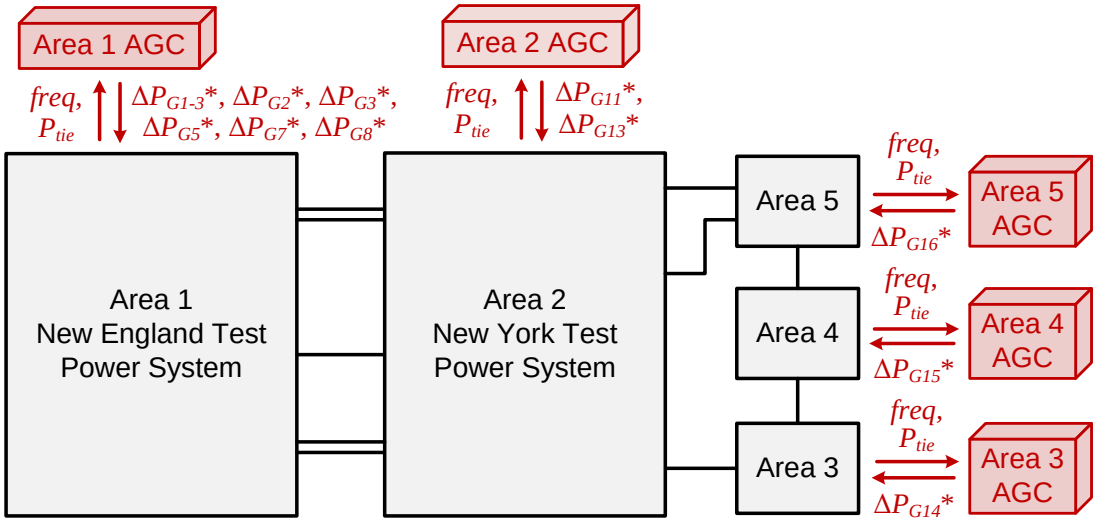

Figure 5.4 The 70-bus system with five AGCs.

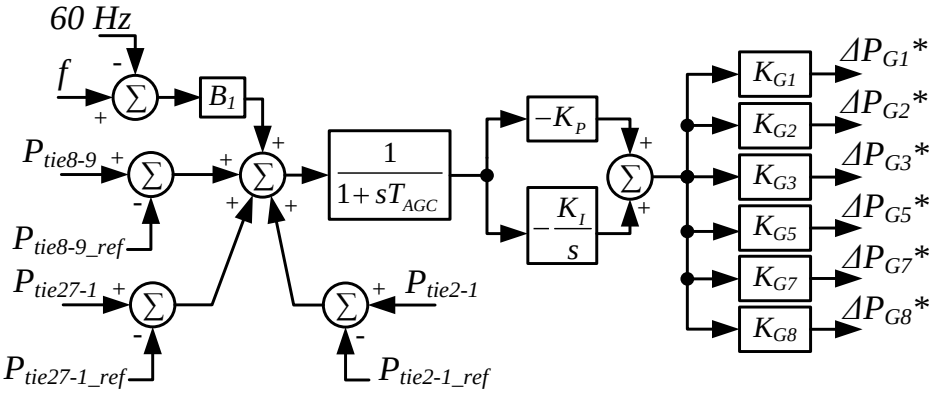

Figure 5.5 AGC for the New England (area 1) system.

With the five AGCs, the frequency of the 70-bus system can be controlled when the wind power production varies. However, AGCs have no visibility to system line loadings or bus voltages, leaving the system vulnerable to insecurity when unexpected fast wind power variation occurs. The dynamic stochastic optimal power flow (DSOPF) control algorithm introduced in Chapter 4 is then applied to this 70-bus system to control its real-time power flow.

5.3 Two-Level DSOPF Control Architecture

To apply the DSOPF control algorithm to practical power systems, methods for efficiently scaling up the DSOPF controller need to be investigated. For the 70-bus power system, hundreds of quantities need to be monitored in order to control its power flow. A two-level DSOPF control architecture, as shown in Figure 5.6, is proposed to divide the DSOPF controller into multiple area controllers and one global controller. Each area DSOPF controller monitors quantities and controls the power flow within its own network, and regulates its boundary tie-line flows to the commanded values. The global DSOPF controller monitors some critical lines from the whole system, and coordinates the area controllers by adjusting the tie-line power flow commands between the areas. This two-level architecture distributes the control and computation burden to multiple area DSOPF controllers, reduces the training difficulty for implementing the DSOPF control for a large network, and potentially makes the whole system more robust to communication failure.

For the 70-bus system, areas 3 to 5 are single-bus aggregated systems. Thus, the AGCs remain in use for regulating the frequencies and tie-line flows for these three areas. Areas 1 and 2 are two mesh networks, each of which is controlled by one area DSOPF controller, to control the area power flow and regulate the frequency and tie-line flow. The global DSOPF controller monitors the MVA loading of some critical transmission lines (lines that often get

congested), and adjusts the tie-line flow commands to help relieve the congestions in the local areas. The design of the two area DSOPF controllers and the global DSOPF controller is discussed in the following sections.

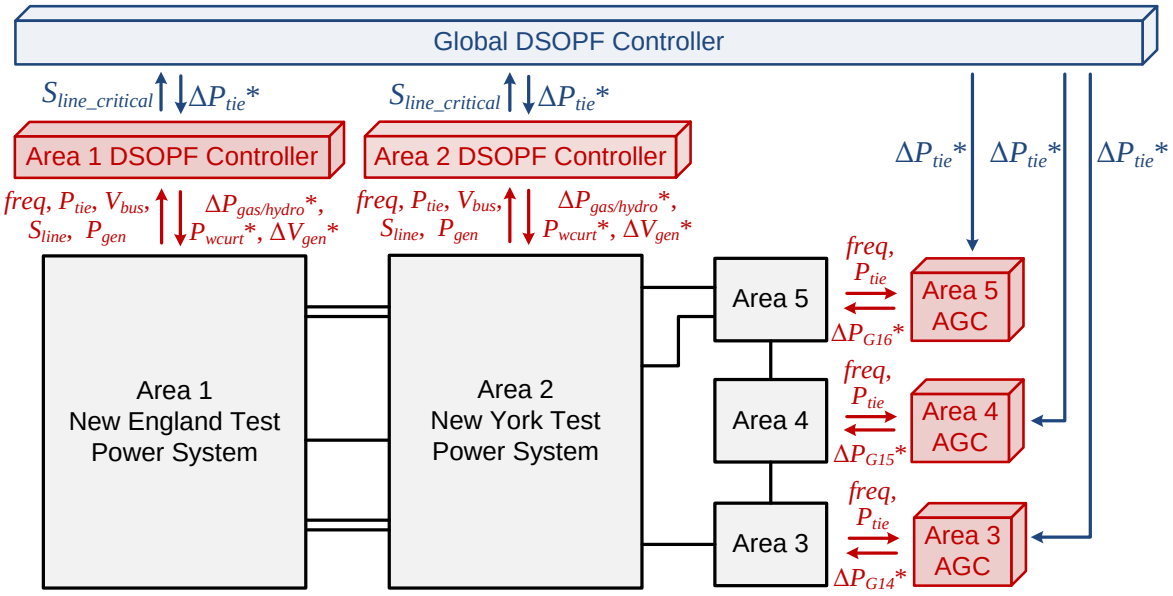

Figure 5.6 Two-level DSOPF control architecture of the 70-bus system.

5.4 Design of Area DSOPF Controllers

The two area dynamic stochastic optimal power flow (DSOPF) controllers are at the same control level and interact with each other. Changes (due to weight updates) to one DSOPF controller will affect the plant dynamics "seen" by the other one. To minimize instability during the initial training stage, each area DSOPF controller is first designed and trained with the rest of the system controlled by fixed automatic generation controllers (AGCs), thereby learning the system dynamics with only AGCs present.

After the initial training stage, the two area DSOPF controllers are connected to the system at the same time, but updated sequentially. When one area DSOPF is being trained, the other one is fixed (no weight updates). In this step, one area DSOPF controller will learn

the system dynamics with the other area DSOPF controller present.

5.4.1 Initial Training of Area 1 DSOPF Controller

The area 1 DSOPF controller is designed to replace and expand the function of area 1 AGC. During the initial training and design of the area 1 DSOPF controller, areas 2 to 5 are controlled by AGCs.

5.4.1.1 Model Network of Area 1 DSOPF Controller

The nonlinear dynamic plant "seen" by the area 1 DSOPF controller is defined in Figure 5.7. The following 41 smoothed wide-area measurements are sampled at 1 Hz for the area 1 DSOPF controller: the area 1 frequency in Hz, f^{A1} (average rotor speeds of G1 to G9); the power exports in the three tie-lines in MW, $P_{tie8\text{-}9}$, $P_{tie27\text{-}1}$, and $P_{tie2\text{-}1}$; the RMS voltage at nine buses in per unit (pu), V_3, V_4, V_8, V_{12}, V_{14}, V_{16}, V_{24}, V_{27}, and V_{28}; the apparent power loading of 20 transmission lines in pu, $S_{2\text{-}3}$, $S_{2\text{-}25}$, $S_{3\text{-}4}$, $S_{3\text{-}18}$, $S_{4\text{-}5}$, $S_{4\text{-}14}$, $S_{5\text{-}6}$, $S_{5\text{-}8}$, $S_{6\text{-}7}$, $S_{7\text{-}8}$, $S_{13\text{-}14}$, $S_{14\text{-}15}$, $S_{15\text{-}16}$, $S_{16\text{-}17}$, $S_{16\text{-}21}$, $S_{16\text{-}24}$, $S_{17\text{-}18}$, $S_{17\text{-}27}$, $S_{25\text{-}16}$, and $S_{26\text{-}27}$; the active power outputs from six fast-ramping generators in MW, P_{G1}, P_{G2}, P_{G3}, P_{G5}, P_{G7}, and P_{G8}; the active power output from the wind plant G17 in MW, P_{w17}; and the total area 1 active power loss in MW, $P^{A1}{}_{loss}$. The monitored buses and lines are selected such that they cover a large portion of the area mesh network. These 41 measurements are then scaled linearly to have the same order of magnitude. The plant output for the area 1 DSOPF controller, $y^{A1}(k)$, is obtained.

The plant has 17 inputs, $u^{A1}(k)$, from the area 1 DSOPF controller. $u^{A1}{}_1(k)$ to $u\ u^{A1}{}_6(k)$ are adjustment signals to change the active power outputs of G1, G2, G3, G5, G7, and G8. $u^{A1}{}_7(k)$ is a positive curtailment signal to reduce the output power of wind plant G17. $u^{A1}{}_8(k)$ to $u^{A1}{}_{17}(k)$ are adjustment signals to change the terminal voltages of G1 to G9, and G17. These 17 inputs are then scaled and added to the steady-state dispatches obtained from the traditional OPF algorithm.

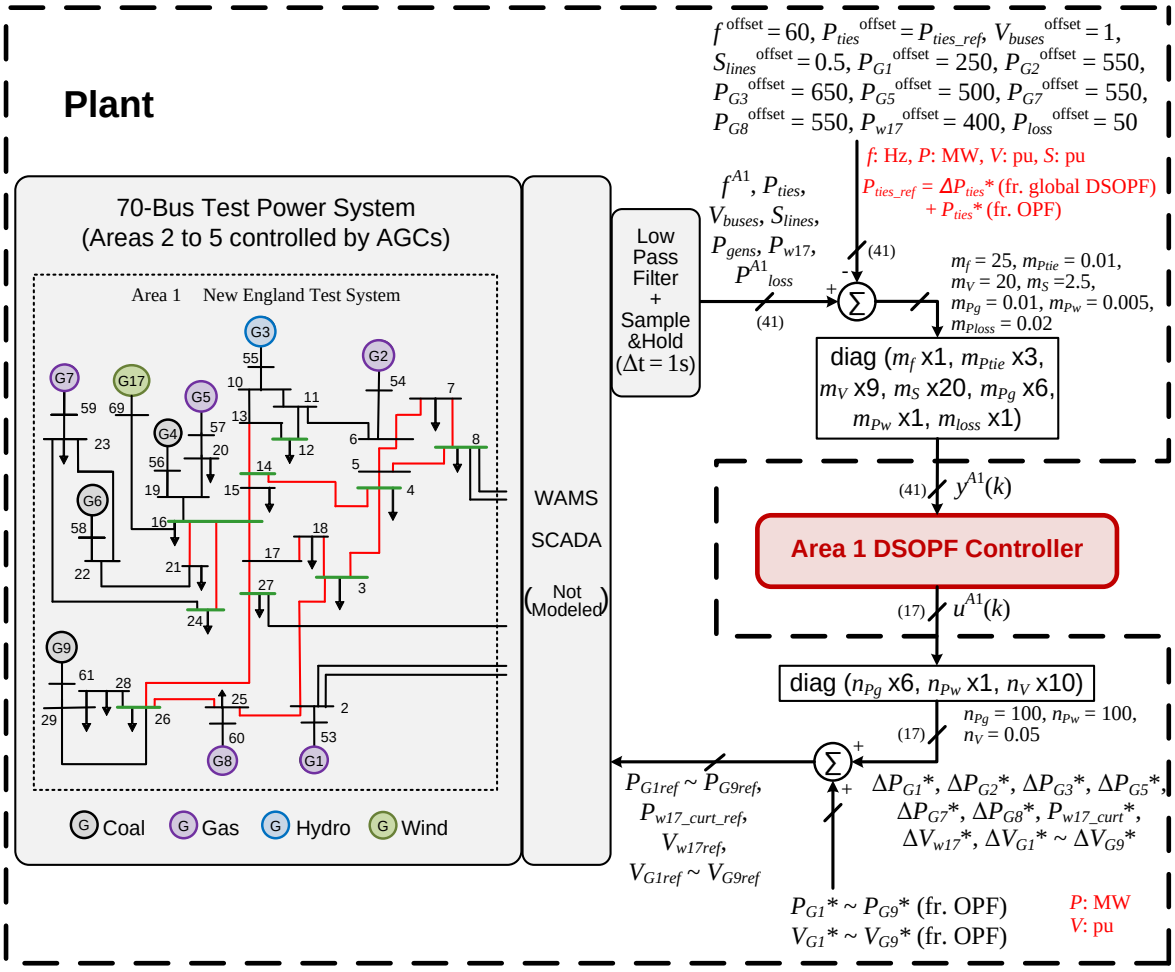

Figure 5.7 Nonlinear plant seen by the area 1 DSOPF controller (monitored power lines and buses are in red and green).

Based on the dual heuristic dynamic programming (DHP) scheme shown in Figure 4.5, a model network, using a recurrent neural network (RNN) with 80 internal weights, is first trained offline to identify the plant dynamics (see the model network offline training flowchart shown in Figure 4.6). Eight different dispatch cases listed in Table 5.1 are defined for training the DSOPF controller at different average wind speeds. Pseudo-random binary signal (PRBS) perturbations, as shown in Figure 5.8, are injected into the plant to collect date for model network offline training. During PRBS injections, the actual wind power outputs have small variation around the average wind power defined in Table 5.1. PRBSs

are first applied to $u^{A1}{}_1$ to $u^{A1}{}_7$ and then to $u^{A1}{}_8$ to $u^{A1}{}_{17}$. Only positive PRBSs are injected into $u^{A1}{}_7$ for wind curtailments. 600 s of data are collected at every dispatch case for model network offline training. The final testing result of the area 1 model network frequency prediction at case D1 is shown in Figure 5.9. A good prediction performance is achieved. After this initial offline training, the area 1 model network now learns the plant dynamics with AGCs for areas 2 to 5.

Table 5.1 Dispatch cases for 70-bus system DSOPF controller training.

Gen	*Dispatch Cases (MW)*							
	D1	D2	D3	D4	D5	D6	D7	D8
1	250	300	250	250	250	300	250	250
2	545	400	545	500	545	400	545	500
3	650	600	750	650	750	600	650	650
4	632	580	632	600	632	580	632	600
5	505.2	400	505.2	450	505.2	400	505.2	450
6	700	600	800	700	800	600	700	700
7	560	400	560	520	560	400	560	520
8	540	500	540	500	540	500	540	500
9	800	700	800	700	800	700	800	700
10	500	250	500	500	350	500	250	350
11	1000	850	1000	1000	950	1000	850	950
12	1350	1100	1620	1620	1150	1350	1100	1150
13	2888	2596	2858	2878	2908	2865	2618	2908
14	5785	5785	5785	5785	5785	5785	5785	5785
15	6000	6000	6000	6000	6000	6000	6000	6000
16	5500	5500	5500	5500	5500	5500	5500	5500
17	350 (9m/s)	1075 (13m/s)	146 (7m/s)	650 (11 m/s)	146 (7m/s)	1075 (13m/s)	350 (9m/s)	650 (11 m/s)
18	460 (9m/s)	1310 (13m/s)	191 (7m/s)	191 (7m/s)	851 (11m/s)	460 (9m/s)	1310 (13m/s)	851 (11m/s)

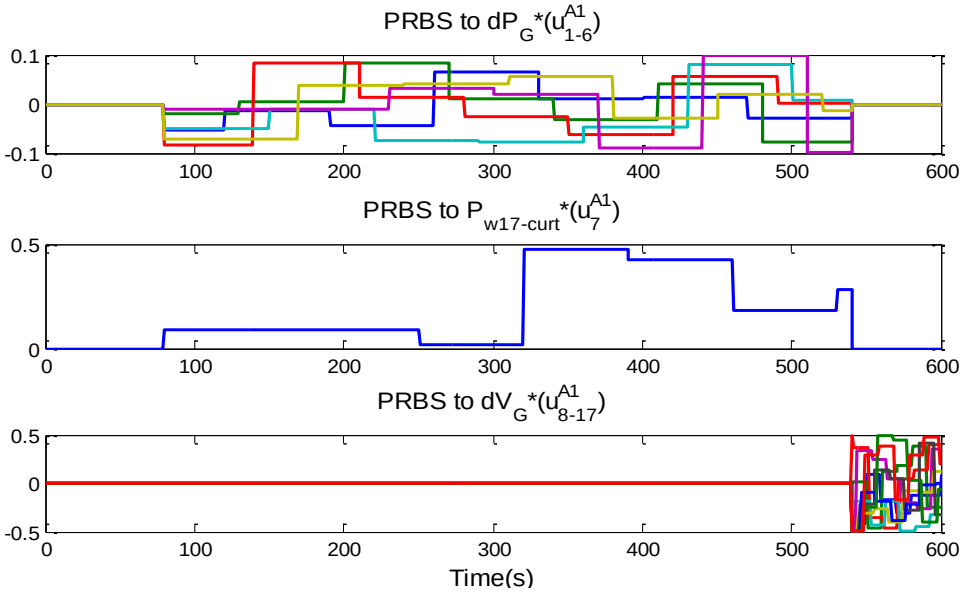

Figure 5.8 PRBS perturbations applied to area 1.

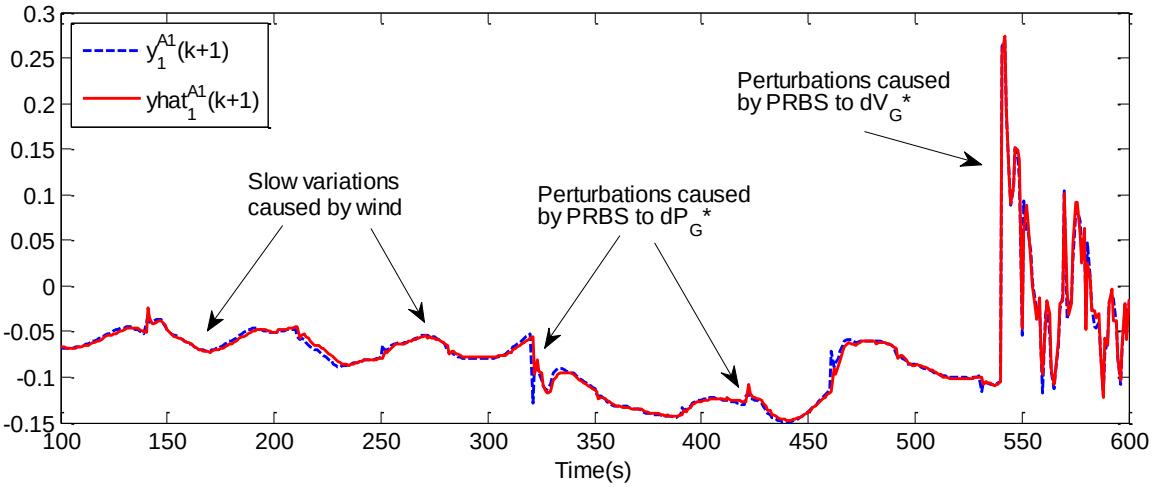

Figure 5.9 Testing result of area 1 model network frequency prediction at case D1.

5.4.1.2 Utility Function and Critic Network of Area 1 DSOPF Controller

Besides the six utility components defined in Chapter 4, an additional component is introduced to represent wind curtailment. The utility function for area 1 DSOPF controller is defined as

$$U^{A1}(k) = U^{A1}_{ACE}(k) + U^{A1}_{Volt}(k) + U^{A1}_{Line}(k) + U^{A1}_{Fuel}(k) + U^{A1}_{Wind}(k) + U^{A1}_{Loss}(k) + U^{A1}_{Ctrl}(k) \quad (5.1)$$

,

with

$$
\begin{aligned}
U^{A1}_{ACE}(k) &= w_{freq}\Delta f^{2}(k) + w_{tie}\left\|\Delta P_{tie}(k)\right\|^{2} \\
&= w_{freq} y^{A1}_{1}(k)^{2} / m^{2}_{f} + w_{tie}\left\| y^{A1}_{2-4}(k)\right\|^{2} / m^{2}_{Ptie} \\
U^{A1}_{Volt}(k) &= w_{volt} \,\|\, \Delta V(k) \,\|^{2} = w_{volt} \,\|\, y^{A1}_{5-13}(k) \,\|^{2} / m^{2}_{V} \\
U^{A1}_{Line}(k) &= w_{line} \sum e^{(S^{4}_{\text{lines}}(k)-1)} = w_{line} \sum e^{\{[y^{A1}_{14-33}(k)/m_{s} + S^{offset}_{lines}]^{4}-1\}} \\
U^{A1}_{Fuel}(k) &= w_{fuel}[\sum F_{G1,2,3,5,7,8}(k) - F^{offset}] \sim y^{A1}_{34-39}(k) \\
U^{A1}_{Wind}(k) &= w_{wind} P_{wind\_curt}(k) / [P_{wind\_curt}(k) + P_{wind}(k)] \\
&= w_{wind} n_{Pw} u^{A1}_{7}(k) / [n_{Pw} u^{A1}_{7}(k) + y^{A1}_{40}(k)/m_{Pw} + P^{offset}_{w17}] \\
U^{A1}_{Loss}(k) &= w_{loss} P_{loss}(k) = w_{loss}[y^{A1}_{41}(k)/m_{loss} + P^{offset}_{loss}] \\
U^{A1}_{Ctrl}(k) &= w_{Pg} \,\|\, \Delta P^{*}_{G}(k) \,\|^{2} + w_{Pw} P^{*}_{w17\_curt}(k)^{2} + w_{Vg} \,\|\, \Delta V^{*}_{G}(k) \,\|^{2} \\
&= w_{Pg} n^{2}_{Pg} \,\|\, u^{A1}_{1-6}(k) \,\|^{2} + w_{Pw} n^{2}_{Pw} u^{A1}_{7}(k)^{2} + w_{Vg} n^{2}_{Vg} \,\|\, u^{A1}_{8-17}(k) \,\|^{2}
\end{aligned}
\qquad (5.2)
$$

w_x's are various weighting factors. m_x's and n_x's are the plant input-output scaling factors shown in Figure 5.7. U^{A1}_{ACE}, U^{A1}_{Volt}, U^{A1}_{Line}, U^{A1}_{Fuel}, U^{A1}_{Loss}, and U^{A1}_{Ctrl} in (5.2) have the same meanings as those in the utility function for the 12-bus system DSOPF controller defined in Chapter 4. U^{A1}_{wind} in (5.2) is proportional to the percentage wind power curtailment.

From (5.1) and (5.2), the utility function for area 1 DSOPF controller, $U^{A1}(k)$, is a function of the plant output, $y^{A1}(k)$, and control action, $u^{A1}(k)$. The derivatives of $U^{A1}(k)$, $\partial U^{A1}(k)/\partial u^{A1}(k)$ and $\partial U^{A1}(k)/\partial y^{A1}(k)$, can be analytically obtained from (5.2) and used for training of critic and action networks.

An RNN DHP critic network, with 80 internal weights, is then trained online to approximate $\lambda^{A1}(k+1)$, the derivative of $J^{A1}(k+1)$ with respect to $y^{A1}(k+1)$. The online training of the critic network is carried out with the action network in the loop, following the flowchart shown in Figure 4.7.

5.4.1.3 Action Network of Area 1 DSOPF Controller

An RNN action network, with 80 internal weights, is trained to approximate the optimal control laws. The RNN action network uses *tansig*(·) as the hidden-layer activation functions,

and uses a linear output activation function for all output neurons except for $u^{A1}{}_7$. Since $u^{A1}{}_7$ needs to be a positive signal representing wind curtailment, the output activation function for $u^{A1}{}_7$ is an absolute function, $abs(\cdot)$. The output-layer gradient for $u^{A1}{}_7$ is thus a piecewise function of 1 or -1 depending on the sign before the $abs(\cdot)$ operation.

With the gradient information from the critic and model networks, the action network is trained online by minimizing $\partial J^{A1}(k)/\partial u^{A1}(k)$, as shown in Figure 4.7. The online training continues until the weights of both the critic and action networks converge. The area 1 DSOPF controller now becomes an optimal power flow controller for area 1, when areas 2 to 5 are controlled by AGCs.

5.4.2 Initial Training of Area 2 DSOPF Controller

The area 2 DSOPF controller is designed to replace and expand the function of area 2 AGC. During the initial training and design of the area 2 DSOPF controller, areas 1, 3, 4, and 5 are controlled by AGCs.

5.4.2.1 Model Network of Area 2 DSOPF Controller

The nonlinear dynamic plant "seen" by the area 2 DSOPF controller is defined in Figure 5.10. The following 42 smoothed wide-area measurements are sampled at 1 Hz for the area 2 DSOPF controller: the area 2 frequency in Hz, f^{A2} (average rotor speeds of G10 to G13); the power imports in the six tie lines in MW, $P_{tie8\text{-}9}$, $P_{tie27\text{-}1}$, $P_{tie2\text{-}1}$, $P_{tie52\text{-}50}$, $P_{tie52\text{-}49}$, and $P_{tie41\text{-}40}$; the RMS voltage at ten buses in per unit (pu), V_1, V_9, V_{30}, V_{33}, V_{35}, V_{38}, V_{44}, V_{46}, V_{48}, and V_{51}; the apparent power loading of 21 transmission lines in pu, $S_{1\text{-}30}$, $S_{1\text{-}31}$, $S_{1\text{-}47}$, $S_{9\text{-}30}$, $S_{9\text{-}36}$, $S_{30\text{-}31}$, $S_{30\text{-}32}$, $S_{31\text{-}38}$, $S_{32\text{-}33}$, $S_{33\text{-}34}$, $S_{33\text{-}38}$, $S_{34\text{-}36}$, $S_{35\text{-}45}$, $S_{36\text{-}37}$, $S_{37\text{-}43}$, $S_{38\text{-}46}$, $S_{39\text{-}44}$, $S_{39\text{-}45}$, $S_{43\text{-}44}$, $S_{44\text{-}45}$, and $S_{45\text{-}51}$; the active power outputs from two fast-ramping generators in MW, P_{G11} and P_{G13}; the active power output from the wind plant G18 in MW, P_{w18}; and the total area 2 active power loss in MW, $P^{A2}{}_{loss}$. The monitored buses and lines are selected such that they

cover a large portion of the area mesh network. These 42 measurements are then scaled linearly to have the same order of magnitude. The plant output for the area 2 DSOPF controller, $y^{A2}(k)$, is obtained.

The plant has eight inputs, $u^{A2}(k)$, from the area 2 DSOPF controller. $u^{A2}{}_1(k)$ and $u^{A2}{}_2(k)$ are adjustment signals to change the active power outputs of G11 and G13. $u^{A2}{}_3(k)$ is a positive curtailment signal to reduce the output power of wind plant G18. $u^{A2}{}_4(k)$ to $u^{A2}{}_8(k)$ are adjustment signals to change the terminal voltages of G10 to G13, and G18. These eight inputs are then scaled and added to the steady-state dispatches obtained from the traditional OPF algorithm.

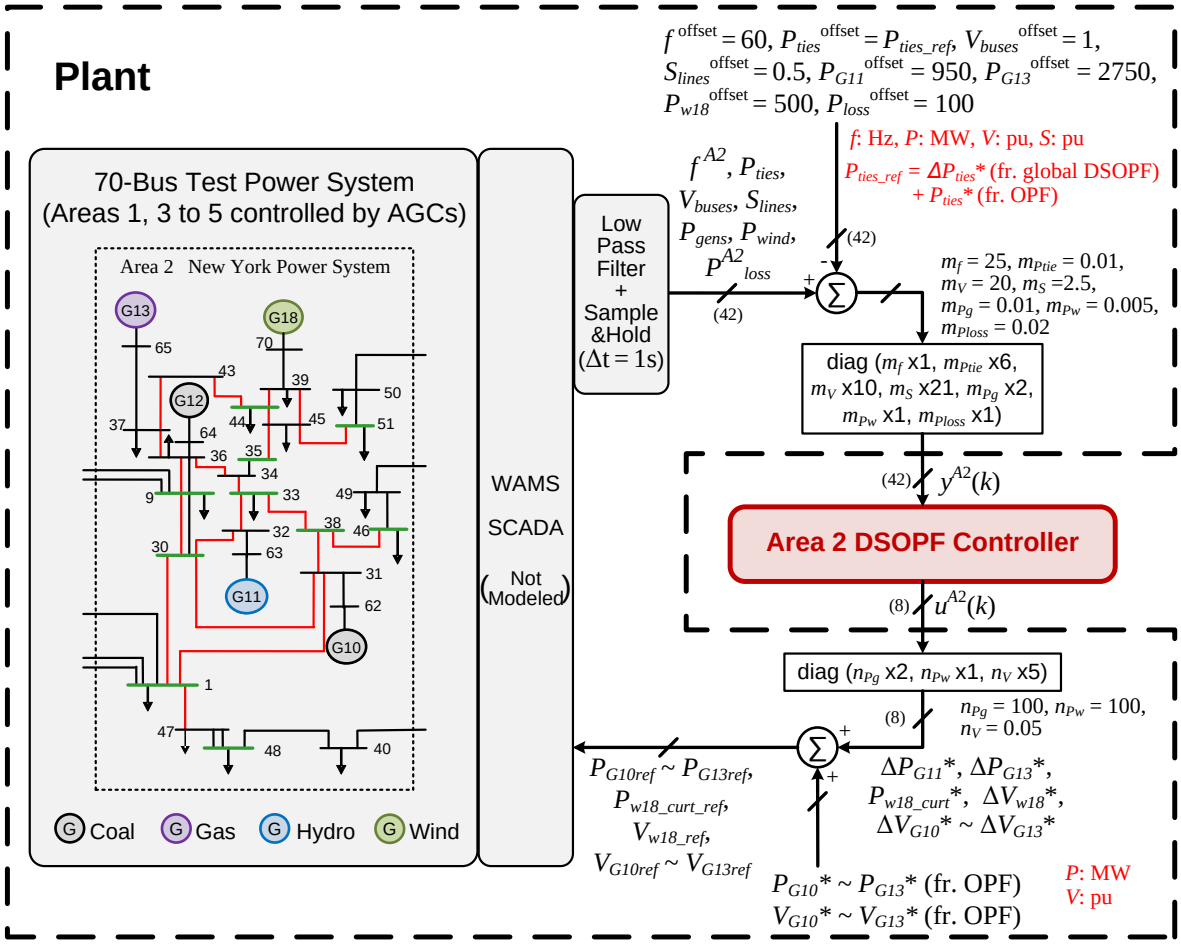

Figure 5.10 Nonlinear plant seen by the area 2 DSOPF controller (monitored power lines and buses are in red and green).

An RNN model network, with 80 internal weights, is trained offline to identify the plant dynamics. The same eight dispatch cases listed in Table 5.1 are used for generating training data. PRBS perturbations are injected into the plant through u^{A2}. Again, wind power variation is assumed to be low when PRBSs are injected. PRBSs are first applied to $u^{A2}{}_1$ to $u^{A2}{}_3$, and then to $u^{A2}{}_4$ to $u^{A2}{}_8$ with the same step size as that shown in Figure 5.8. Only positive PRBSs are injected into $u^{A2}{}_3$ for wind curtailments. 600 s of data are collected at each dispatch case shown in Table 5.1 for offline model network training. The testing result of the area 2 model network frequency prediction at case D1 is shown in Figure 5.11. A good prediction performance is achieved. After this initial offline training, the area 2 model network now learns the plant dynamics with AGCs for areas 1, 3, 4, and 5.

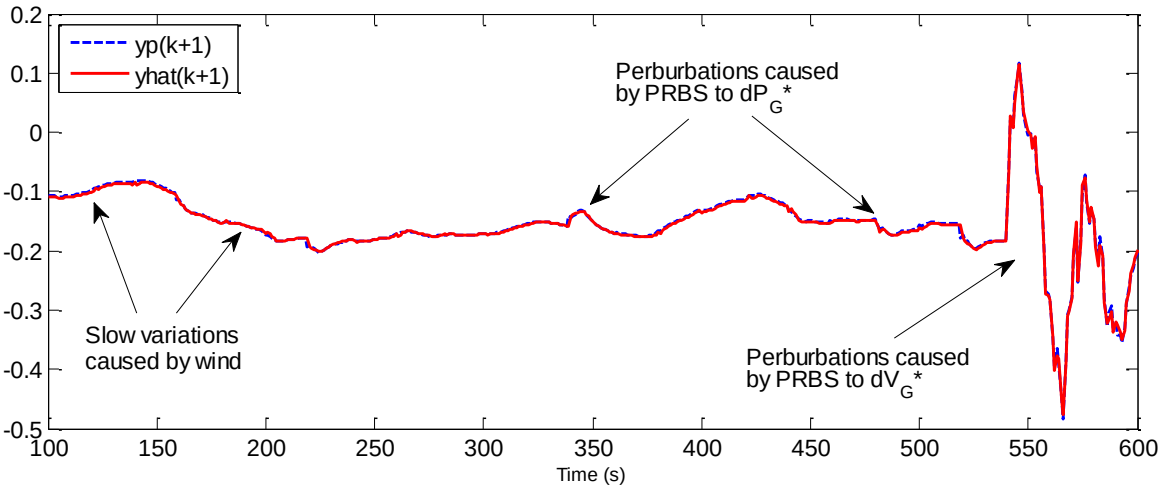

Figure 5.11 Testing result of area 2 model network frequency prediction at case D1.

5.4.2.2 Utility Function and Critic Network of Area 2 DSOPF Controller

Similar to the area 1 DSOPF controller, the utility function of the area 2 DSOPF controller has seven components, as in

$$U^{A2}(k) = U^{A2}_{ACE}(k) + U^{A2}_{Volt}(k) + U^{A2}_{Line}(k) + U^{A2}_{Fuel}(k) + U^{A2}_{Wind}(k) + U^{A2}_{Loss}(k) + U^{A2}_{Ctrl}(k) \quad (5.3)$$

,

with

$$
\begin{aligned}
U_{ACE}^{A2}(k) &= w_{freq}\Delta f^{2}(k) + w_{tie}\left\|\Delta P_{tie}(k)\right\|^{2} \\
&= w_{freq}y_{1}^{A2}(k)^{2}/m_{f}^{2} + w_{tie}\left\|y_{2-7}^{A2}(k)\right\|^{2}/m_{Ptie}^{2} \\
U_{Volt}^{A2}(k) &= w_{volt}\,\|\,\Delta V(k)\,\|^{2} = w_{volt}\,\|\,y_{8-17}^{A2}(k)\,\|^{2}/m_{V}^{2} \\
U_{Line}^{A2}(k) &= w_{line}\sum e^{(S_{\text{lines}}^{4}(k)-1)} = w_{line}\sum e^{\{[y_{18-38}^{A2}(k)/m_{s}+S_{lines}^{offset}]^{4}-1\}} \\
U_{Fuel}^{A2}(k) &= w_{fuel}[\sum F_{G11,13}(k) - F^{offset}] \sim y_{39,40}^{A1}(k) \\
U_{Wind}^{A2}(k) &= w_{wind}P_{wind\_curt}(k)/[P_{wind\_curt}(k) + P_{wind}(k)] \\
&= w_{wind}n_{Pw}u_{3}^{A2}(k)/[n_{Pw}u_{3}^{A2}(k) + y_{41}^{A2}(k)/m_{Pw} + P_{w18}^{offset}] \\
U_{Loss}^{A2}(k) &= w_{loss}P_{loss}(k) = w_{loss}[y_{42}^{A2}(k)/m_{loss} + P_{loss}^{offset}] \\
U_{Ctrl}^{A2}(k) &= w_{Pg}\,\|\,\Delta P_{G}^{*}(k)\,\|^{2} + w_{Pw}P_{w18\_curt}^{*}(k)^{2} + w_{Vg}\,\|\,\Delta V_{G}^{*}(k)\,\|^{2} \\
&= w_{Pg}n_{Pg}^{2}\,\|\,u_{1,2}^{A2}(k)\,\|^{2} + w_{Pw}n_{Pw}^{2}u_{3}^{A2}(k)^{2} + w_{Vg}n_{Vg}^{2}\,\|\,u_{4-8}^{A2}(k)\,\|^{2}
\end{aligned}
\qquad (5.4)
$$

w_x's are various weighting factors same as those in (5.2). m_x's and n_x's are the plant input-output scaling factors shown in Figure 5.10. From (5.3) and (5.4), the utility function for the area 2 DSOPF controller, $U^{A2}(k)$, is a function of the plant output, $y^{A2}(k)$, and control action, $u^{A2}(k)$. The derivatives of $U^{A2}(k)$, $\partial U^{A2}(k)/\partial u^{A2}(k)$ and $\partial U^{A2}(k)/\partial y^{A2}(k)$, can be analytically obtained from (5.4) and used for training of critic and action networks. An RNN DHP critic network, with 80 internal weights, is then trained online to approximate $\lambda^{A2}(k+1)$, the derivative of $J^{A2}(k+1)$ with respect to $y^{A2}(k+1)$, following the online training flowchart shown in Figure 4.7.

5.4.2.3 Action Network of Area 2 DSOPF Controller

An RNN action network, with 80 internal weights, is trained to approximate the optimal control laws for the area 2 DSOPF controller. To have a non-negative signal at $u^{A2}{}_3$, which is the command for wind curtailment, the output activation function for $u^{A2}{}_3$ is an absolute function, $abs(\cdot)$. With the gradient information from the critic and model networks, the action network is trained online with the critic network by minimizing $\partial J^{A2}(k)/\partial u^{A2}(k)$, as illustrated in Figure 4.7. The online training continues until the weights of both the critic and action networks converge. The area 2 DSOPF controller now becomes an optimal power

flow controller for area 2, when areas 1, 3, 4, and 5 are controlled by AGCs.

5.4.3 Sequential Training of Area 1 & 2 DSOPF Controllers

After the initial training stage, the two area DSOPF controllers are now connected to the system at the same time. The area 1 DSOPF controller needs further online adaptation to account for changes to the system dynamics introduced by the area 2 DSOPF controller. Similarly, the area 2 DSOPF controller also needs further online adaptation.

This online adaptation is done sequentially for the two area DSOPF controllers, as illustrated in Figure 5.12. When one area DSOPF is being trained, the other one is fixed (no weight updates). This back and forth training of the two area DSOPF controllers continue until the critic and action errors of both area DSOPF controllers drop below a certain level and the weights converge.

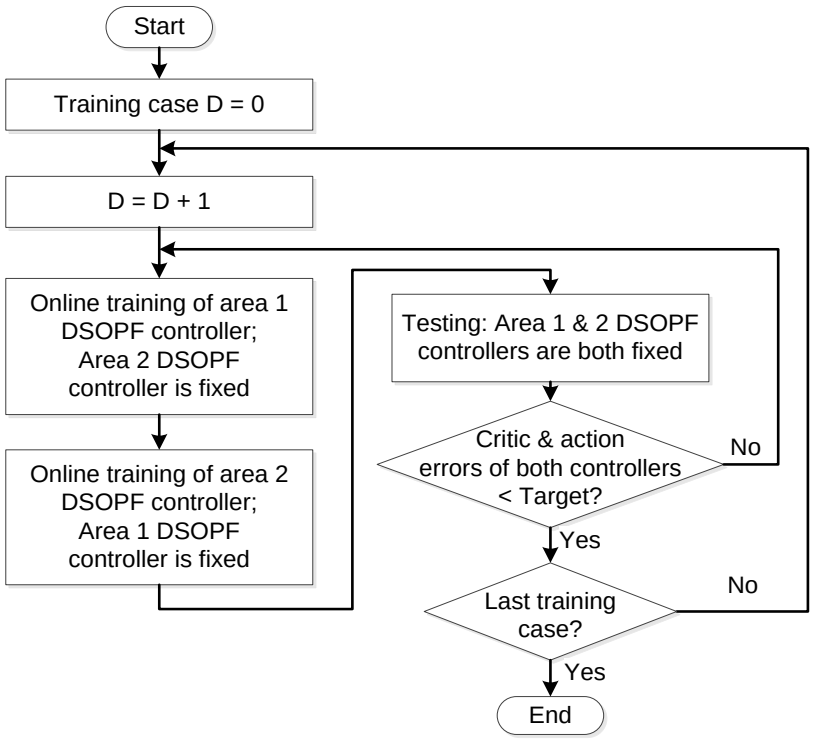

Figure 5.12 Flowchart of sequential training of area DSOPF controllers.

5.5 Simulation Studies for the Area DSOPF Controllers

To evaluate the control performance of the trained area dynamic stochastic optimal power flow (DSOPF) controllers, large varying wind profiles and wind ramps are applied to the system. Responses of the system using the area DSOPF controllers and using only the AGCs (see Figure 5.4) are compared.

5.5.1 Results for Large Wind Variation

To evaluate the performance of the area DSOPF controllers during large wind variation, the system initially operates at dispatch case D1 in Table 5.1, and large wind variation is applied to wind plants G17 and G18 starting at 300 s, as shown in the top graph in Figure 5.13. The responses of the70-bus system controlled by the automatic generation controllers (AGCs) and area DSOPF controllers, respectively, are compared below. When the DSOPF controllers are used, no wind curtailment command is generated. The wind power productions for G17 and G18, as shown in the bottom graph in Figure 5.13, are the same for both AGCs and DSOPF controllers. Between 500 s and 600 s, about 1400 MW (5% of total system load) of wind power change is applied to the system in one minute.

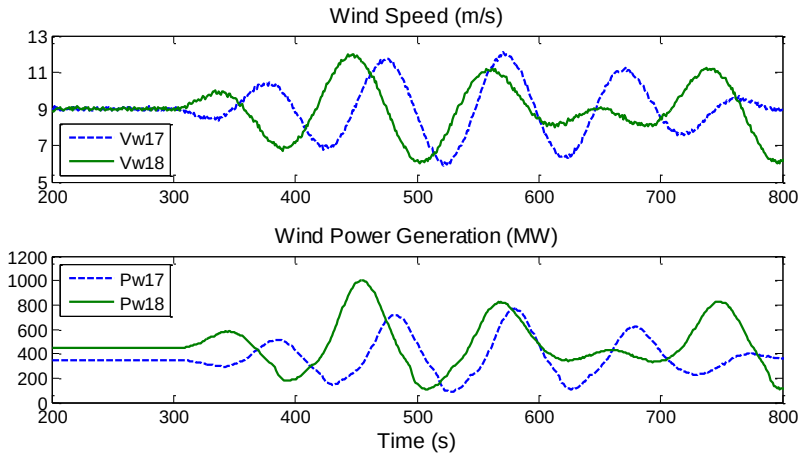

Figure 5.13 Wind variation from wind plants G17 and G18.

The overall utility functions for areas 1 and 2, defined in (5.1) and (5.3), are shown in

Figure 5.14. The time accumulation of the utility functions is the optimal control objective for the area DSOPF controllers. From Figure 5.14, this overall performance index is always lower for both areas when the DSOPF controllers are used. When the wind deviation is high, for example at around 580 s, the two area utility functions from the AGCs increase a lot more than those from the DSOPF controllers.

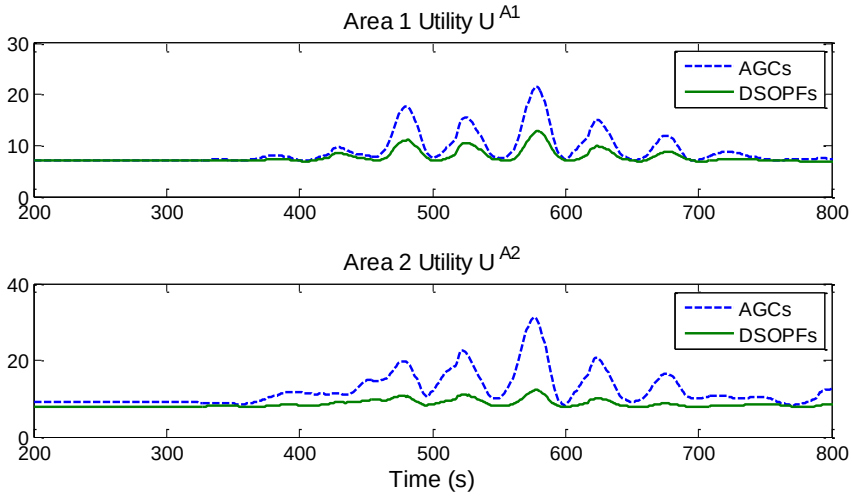

Figure 5.14 Area 1 & 2 utility functions during the large wind variation.

The frequency response is shown in Figure 5.15, and the active power flows in the three tie lines between areas 1 and 2 are plotted in Figure 5.16. During the steady state prior to 300 s, the AGCs can regulate the frequency to 60 Hz and regulate the tie-line flows to their respective commanded values with no error. The DSOPF controllers, in contrast, result in small steady-state errors for the frequency and tie-line flows, which is a compromise naturally results from the mulit-objective DSOPF controllers. When the wind starts to vary at 300 s, the frequency and tie-line flow deviations are higher when the AGCs are used, as compared to those from the DSOPF controllers. The area DSOPF controllers are able to regulate the frequency and tie-line flows closer to their reference values during large wind variation.

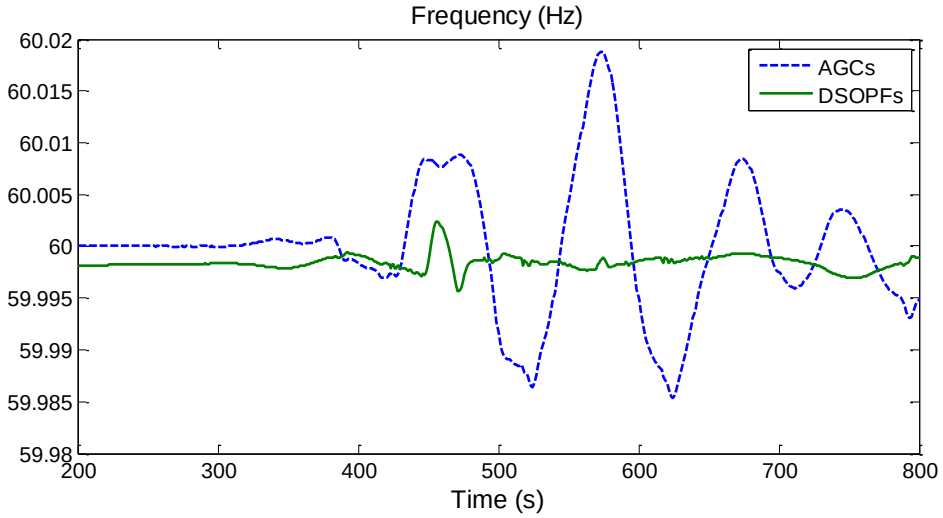

Figure 5.15 System frequency during the large wind variation.

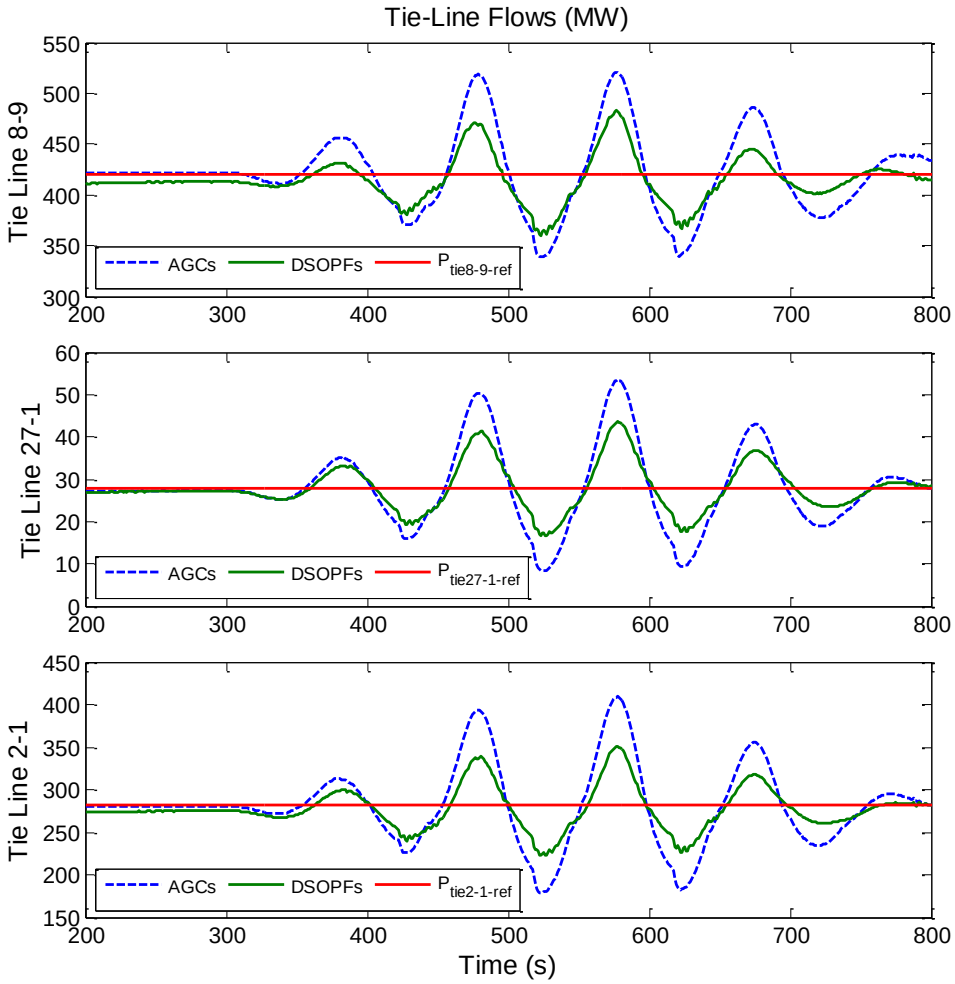

Figure 5.16 Tie-line flows between areas 1 & 2 during the large wind variation.

During this event of large wind variation, the voltages at all the buses are kept between 0.95 pu and 1.05 pu for both AGCs and DSOPFs. However, when the AGCs are used, the MVA loading of line 16-17, a transmission line close to the wind plant G17, exceeds 1 pu when the wind generation form G17 deviates above the average value. On the contrary, the DSOPF controllers are able to maintain this line loading below 1 pu, as shown in Figure 5.17. Notice that the loadings of line 16-17 are the same for both the AGCs and DSOPF controllers, when the wind generation from G17 is low (at around 520 s and 620 s). When the wind generation from G17 becomes higher, the DSOPF controllers are able to reroute some of the wind energy and reduce the loading of this line.

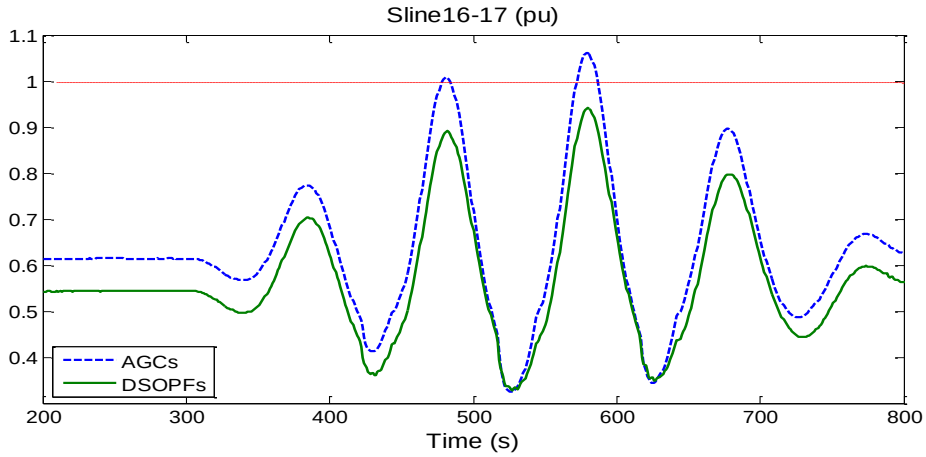

Figure 5.17 Loading of transmission line 16-17 during the large wind variation.

5.5.2 Results for an Unexpected Rise of Wind Power

To evaluate the performance of the area DSOPF controllers during an unexpected rise of wind power, the following events are applied to the 70-bus system: the system initially operates at dispatch case D8 in Table 5.1; the wind speed at wind plant 17 rises at 300 s from 11 m/s to 12.5 m/s (about 300 MW rise in 50 s); and the wind speed at wind plant 18 rises at 450 s from 11 m/s to 13 m/s (about 550 MW rise in 50 s), as shown in the top graph of Figure 5.18.

The resulting wind power generations from G17 and G18 are shown in the bottom two graphs of Figure 5.18. When the area 1 and 2 AGCs are used, the two wind plants output all of their available wind power. The AGCs balance the wind power rise by dropping the generation from traditional power plants. When the area DSOPF controllers are used, some of the wind power (about 30 MW from G17 and 50 MW from G18) is curtailed. This trade-off yet brings a better overall performance. The area DSOPF controllers result in lower (better) overall utilities [defined in (5.1) and (5.3)] than the AGCs do for both the area power networks, as shown in Figure 5.19.

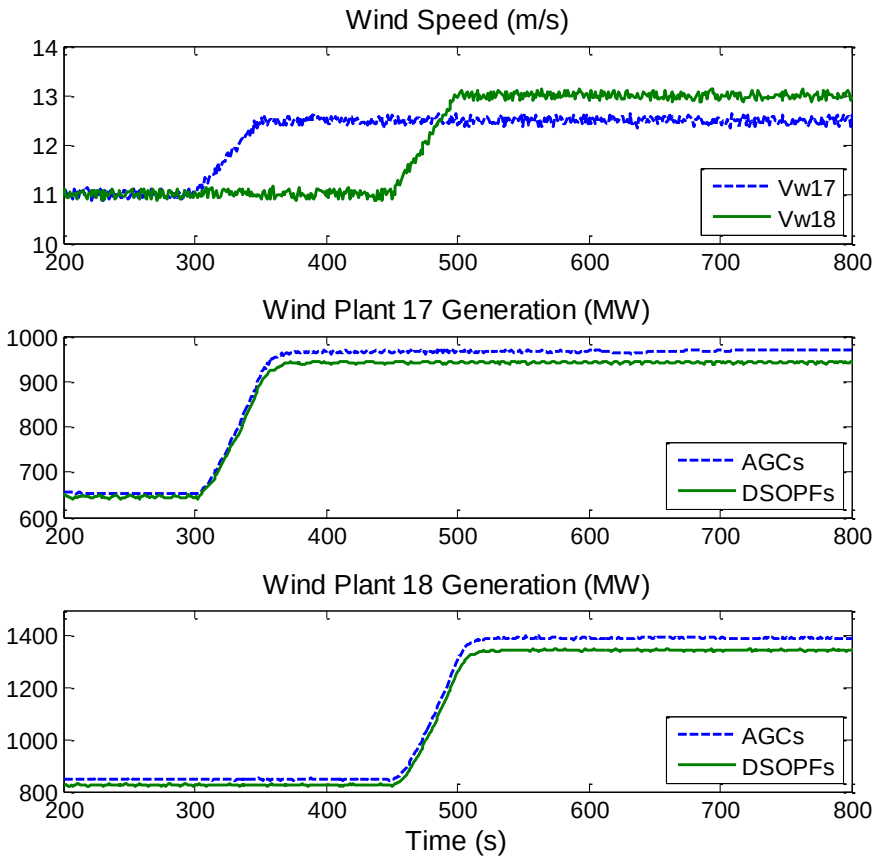

Figure 5.18 Rise of wind power from wind plants 17 and 18.

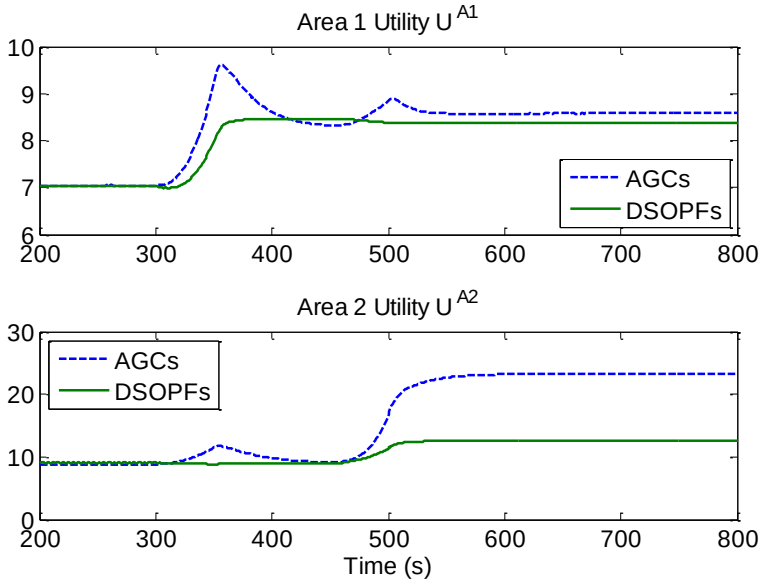

Figure 5.19 Area 1 and 2 overall utilities during the large wind power rise.

The system frequency response under this event of a large wind power rise is shown in Figure 5.28. When the wind power rises, the AGCs cannot mitigate the frequency deviation, because the AGCs control only the active power outputs of conventional generation units, which have relatively slow ramp rates. In contrast, the area DSOPF controllers coordinate both active and reactive power, and leverage the load-voltage characteristics to improve the system active power balancing. The area DSOPF controllers result in a smaller frequency deviation than that from the AGCs.

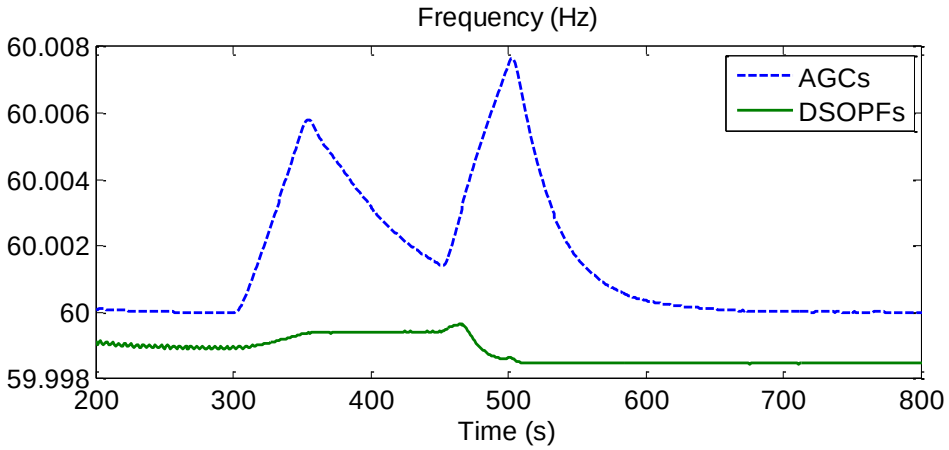

Figure 5.20 System frequency during the large wind power rise.

The DSOPF controllers result in lower (better) utility indices for bus voltages [defined in (5.2) and (5.4)] before and after the rise of wind power, as shown in Figure 5.21. Thus, the bus voltages across the system are closer to 1 pu when the DSOPF controllers are used. When the AGCs are used, the voltage of bus 43 drops below 0.95 pu after the unexpected wind power rise, as shown in Figure 5.22. The DSOPF controllers, on the contrary, are able to maintain this bus voltage almost unchanged.

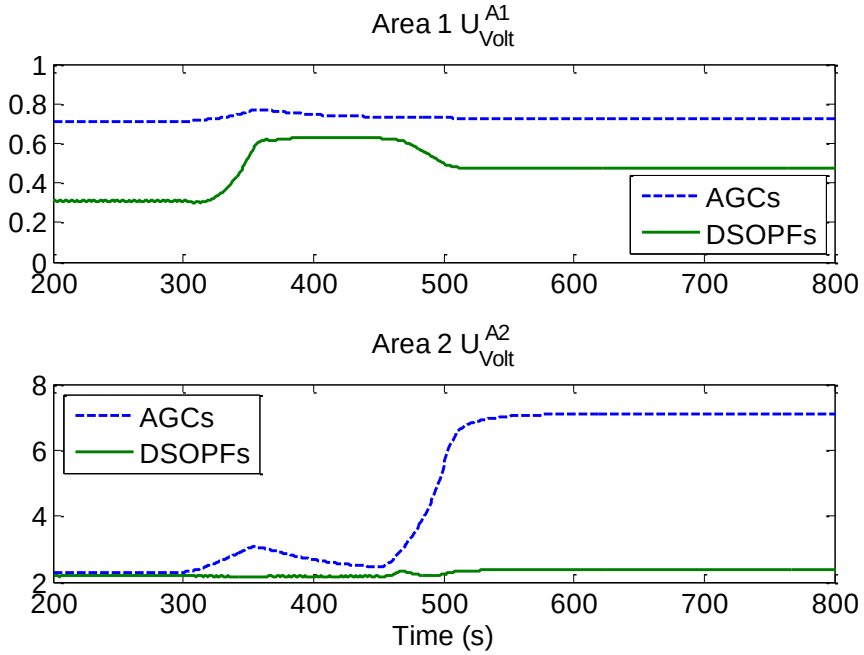

Figure 5.21 Bus voltage utility indices during the large wind power rise.

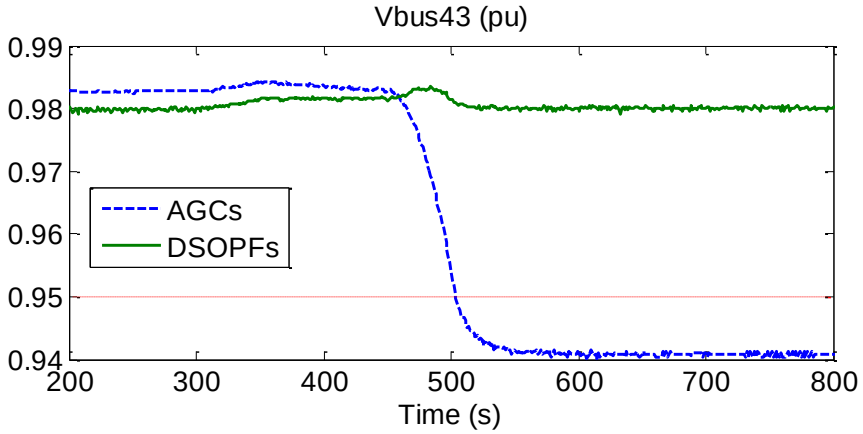

Figure 5.22 Voltage of bus 43 during the large wind power rise.

The DSOPF controllers also result in lower (better) utility indices for line loadings [in (5.2) and (5.4)] before and after the large unexpected wind power rise, as shown in Figure 5.23. Thus, the line loadings across the system are more even when the DSOPF controllers are used. Figure 5.24 and Figure 5.25 show the MVA loading of line 16-17 (close to G17) and line 37-43 (close to G18), respectively. The DSOPF controllers are able to reduce the loading of these two lines after the wind power rise, but at the cost of curtailing some of the wind power (see Figure 5.18).

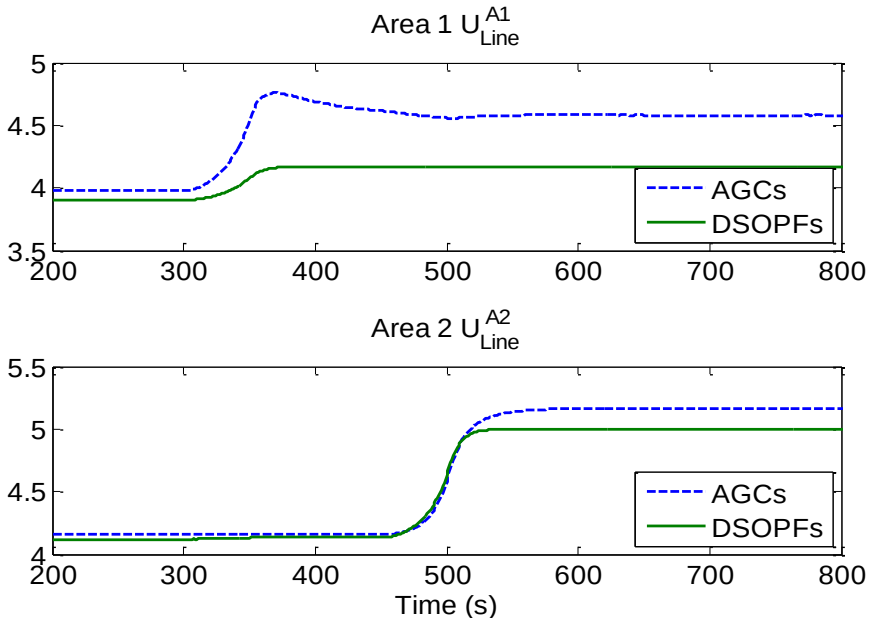

Figure 5.23 Line loading utility indices during the large wind power rise.

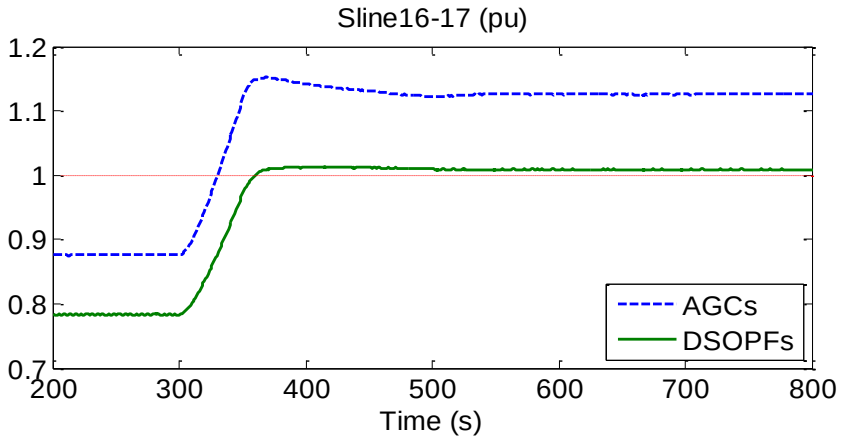

Figure 5.24 Loading of line 16-17 during the large wind power rise.

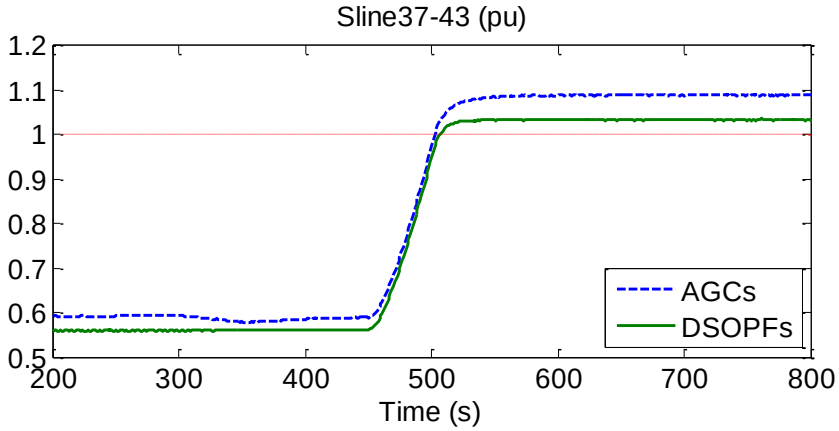

Figure 5.25 Loading of line 37-43 during the large wind power rise.

The area DSOPF controllers are able to improve the security of the 70-bus system by mitigating violations of bus-voltage and line-loading constraints in events of unexpected wind power changes. However, some wind power may need to be curtailed to achieve optimal performance for each local area network. A global DSOPF controller is thus designed in the next section to coordinate the area DSOPF controllers, allowing the whole 70-bus system to achieve a global optimum.

5.6 Design of Global DSOPF Controller

A global dynamic stochastic optimal power flow (DSOPF) controller is designed to coordinate the area 1 & 2 DSOPF controllers. The goal of the global DSOPF controller is to relieve the line loading of transmission line 16-17 in area 1 and line 37-43 in area 2, when the wind power from the two wind plants increases unexpectedly. The sampling and control frequency of the global DSOPF control is set to 0.1 Hz, one tenth of the sampling and control frequency of the area DSOPF controllers.

5.6.1.1 Model Network of Global DSOPF Controller

The nonlinear dynamic plant "seen" by the global DSOPF controller is defined in Figure 5.26. The apparent power loading of the two critical transmission lines in pu, $S_{16\text{-}17}$

and $S_{37\text{-}43}$, are sampled at 0.1 Hz and fed into the global DSOPF controller after a linear scaling. The plant output is denoted as $y^G(k)$.

The plant has six inputs, $u^G{}_1(k)$ to $u^G{}_6(k)$, form the global DSOPF controller. Each of the six control inputs is an adjustment signal to change one of the tie-line flow commands, as shown in Figure 5.26. These six inputs are then scaled and added to the steady-state dispatches obtained from the traditional OPF algorithm.

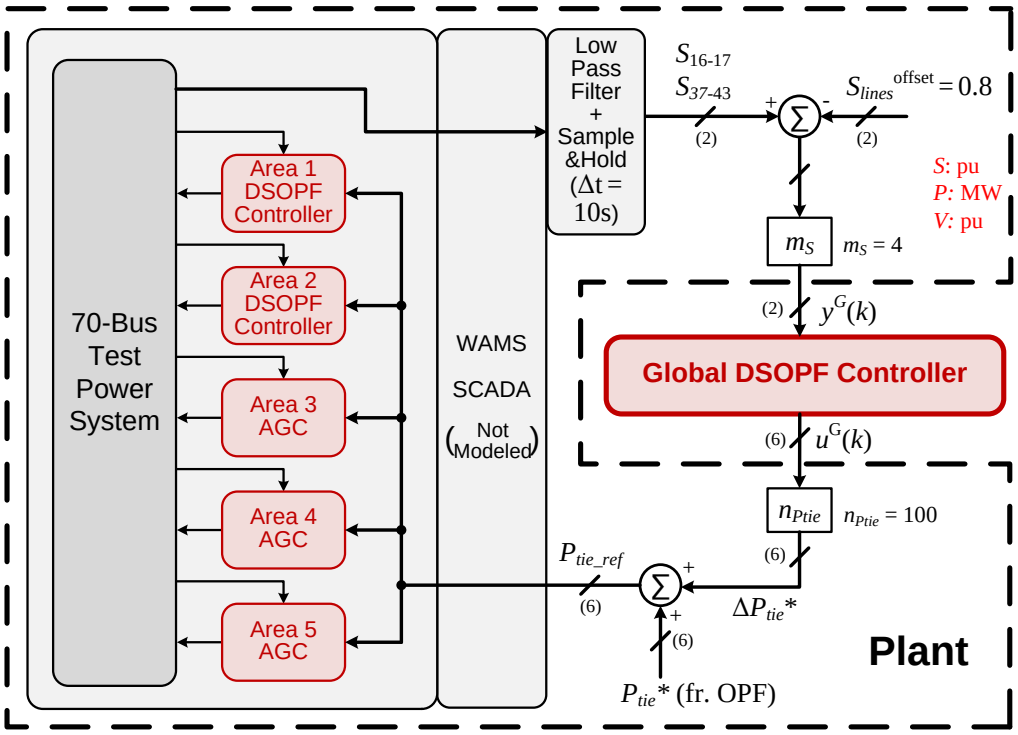

Figure 5.26 Nonlinear plant seen by the global DSOPF controller.

A recurrent neural network (RNN), with 20 internal weights, is used as the model network for the global DSOPF controller. PRBS perturbations, as shown in Figure 5.27, are injected into the plant through u^G. Wind power variation is assumed to be low when PRBSs are injected. 1100 s of data are collected at each dispatch case shown in Table 5.1 for offline model network training. The testing result of the global model network for line 16-17 loading prediction at dispatch case D8 is shown in Figure 5.28. After this initial offline

training, the global model network captures the plant dynamics with area 1 and 2 DSOPF controllers and area 3, 4, and 5 automatic generation controllers (AGCs).

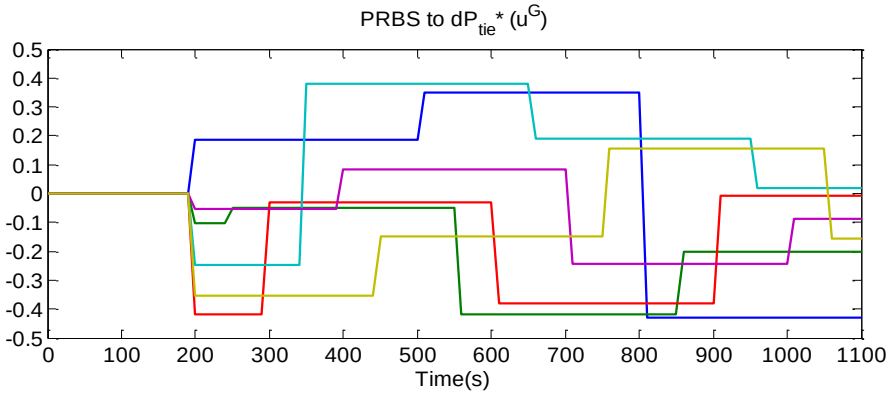

Figure 5.27 PRBS perturbations applied to the plant of global DSOPF controller.

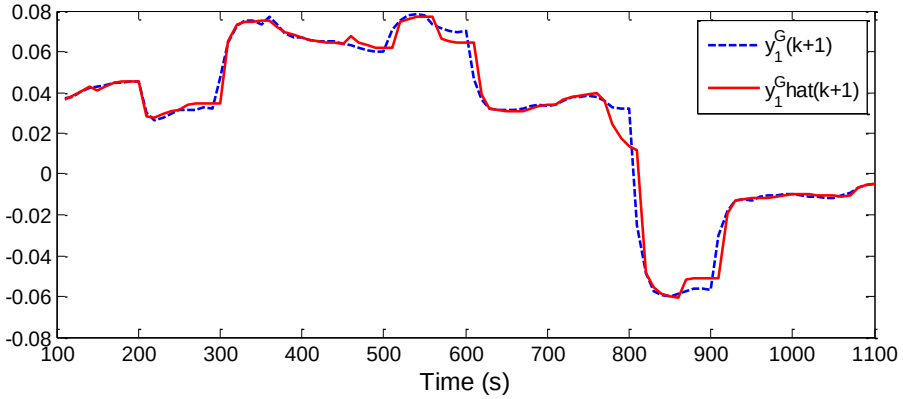

Figure 5.28 Global model network for line loading prediction at case D8.

5.6.1.2 Utility Function and Critic Network of Global DSOPF Controller

The utility function of the global DSOPF controller has two components, as in

$$U^G(k) = U^G_{Line}(k) + U^G_{Ctrl}(k), \tag{5.5}$$

where

$$\begin{aligned} U^G_{Line}(k) &= w^G_{line}[e^{(S^4_{16\text{-}17}(k)-1)} + e^{(S^4_{37\text{-}43}(k)-1)}] \\ &= w^G_{line}\{e^{[(y^G_1(k)/m_s + S^{offset}_{lines})^4 - 1]} + e^{[(y^G_2(k)/m_s + S^{offset}_{lines})^4 - 1]}\}. \\ U^G_{Ctrl}(k) &= w^G_{Ptie} \,\|\, \Delta P^*_{tie}(k) \,\|^2 = w_{Ptie} n^2_{Ptie} \,\|\, u^G(k) \,\|^2 \end{aligned} \tag{5.6}$$

$w_{line}{}^G$ and $w_{Ptie}{}^G$ are two weighting factors are selected heuristically. m_s and n_{Ptie} are the plant

input-output scaling factors shown in Figure 5.26. The utility function for the global DSOPF controller, $U^G(k)$, is then a function of the global plant output, $y^G(k)$, and the control action, $u^G(k)$. The derivatives of $U^G(k)$, $\partial U^G(k)/\partial u^G(k)$ and $\partial U^G(k)/\partial y^G(k)$, can be analytically obtained from (5.6) and used for training of the global critic and action networks. An RNN DHP global critic network, with 20 internal weights, is trained online to approximate $\lambda^G(k+1)$, the derivative of $J^G(k+1)$ with respect to $y^G(k+1)$, following the online training flowchart shown in Figure 4.7.

5.6.1.3 Action Network of Global DSOPF Controller

An RNN action network, with 20 internal weights, is trained to approximate the optimal control laws for the global DSOPF controller. With the gradient information from the global critic and model networks, the action network is trained online with the critic network by minimizing $\partial J^G(k)/\partial u^G(k)$, as illustrated in Figure 4.7. The online training continues until the weights of both the global critic and action networks converge.

5.7 Simulation Studies for the Global DSOPF Controller

To evaluate the performance of the global DSOPF controller, the 70-bus system is simulated under the same event of a large unexpected wind power rise as presented in Section 5.5.2. The system responses with the additional global DSOPF controller (see Figure 5.6 for the overall control structure) are compared with the results from using only the AGCs and using only the area DSOPF controllers without global coordination.

With the global DSOPF controller, the tie-line flows are now actively controlled, as illustrated in Figure 5.29. Compared to the case of using only the area DSOPF controllers, the global DSOPF controller reduces the wind power curtailment, as shown in Figure 5.30, and at the same time further relieves the two congested line, line 16-17 and line 37-43, as shown in Figure 5.31 and Figure 5.32. The global DSOPF controller provides the additional coordination between the local areas by adjusting their tie-lie flows.

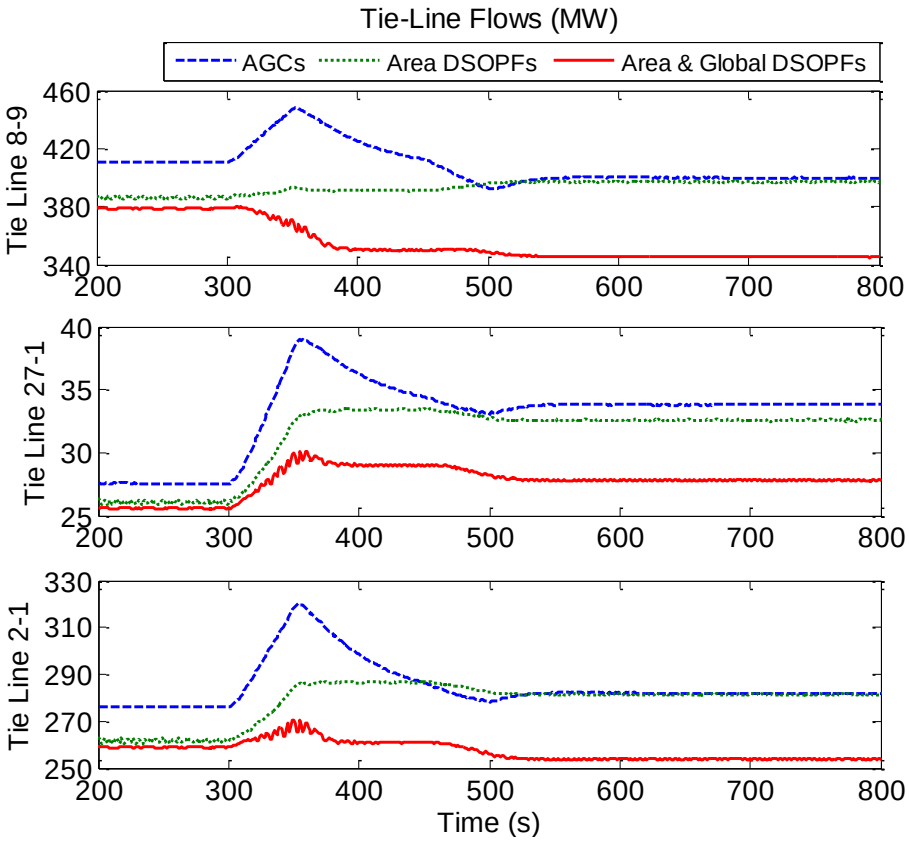

Figure 5.29 Tie-line flows with area and global DSOPF controllers.

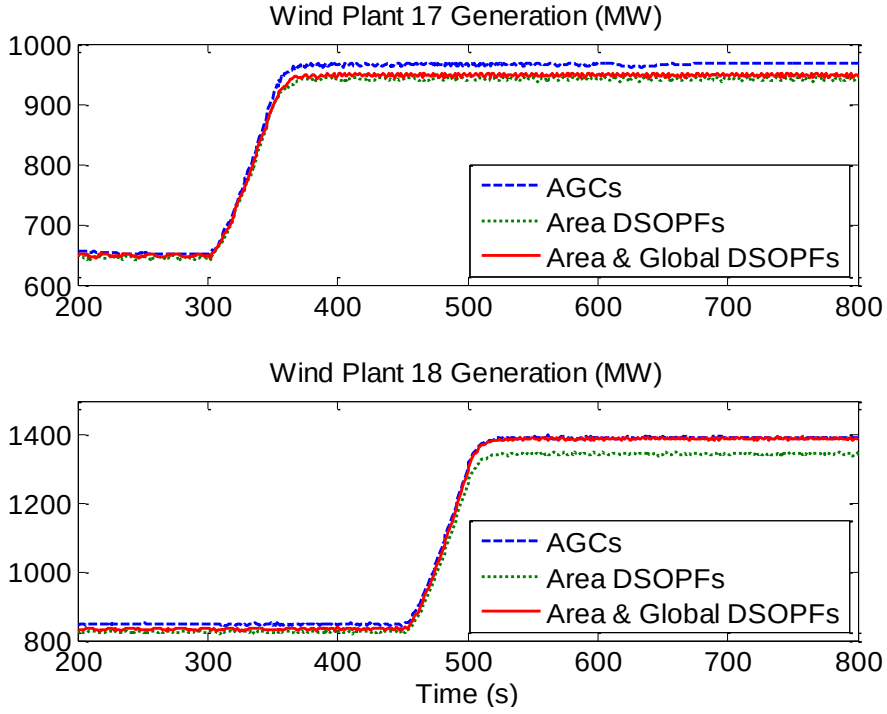

Figure 5.30 Wind power generation with area and global DSOPF controllers.

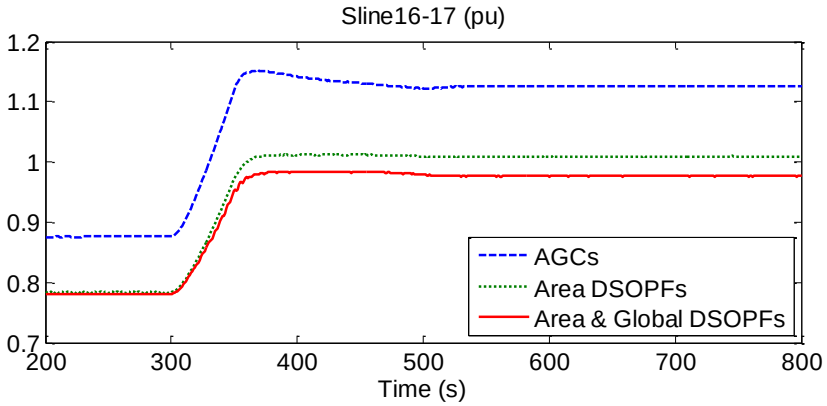

Figure 5.31 Line 16-17 loading with area and global DSOPF controllers.

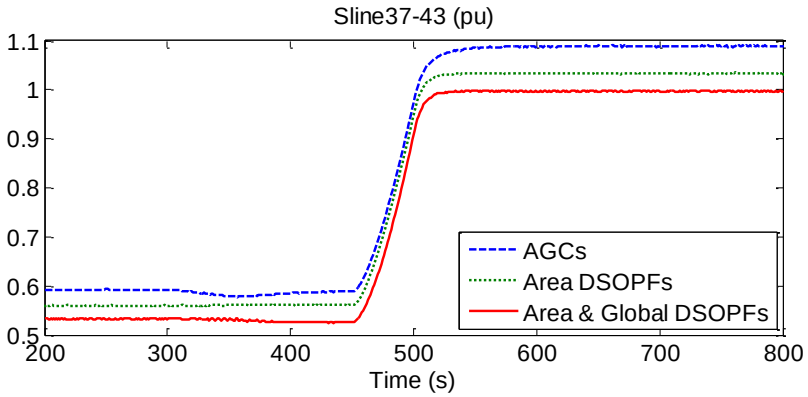

Figure 5.32 Line 37-43 loading with area and global DSOPF controllers.

When the global DSOPF controller is used, the system frequency has a higher deviation than using only the area DSOPF controllers, as shown in Figure 5.33. This is because the frequency response is not one of the objectives in the global DSOPF utility function, and changing the inter-area tie-line flows disturbs the power balance of each local area.

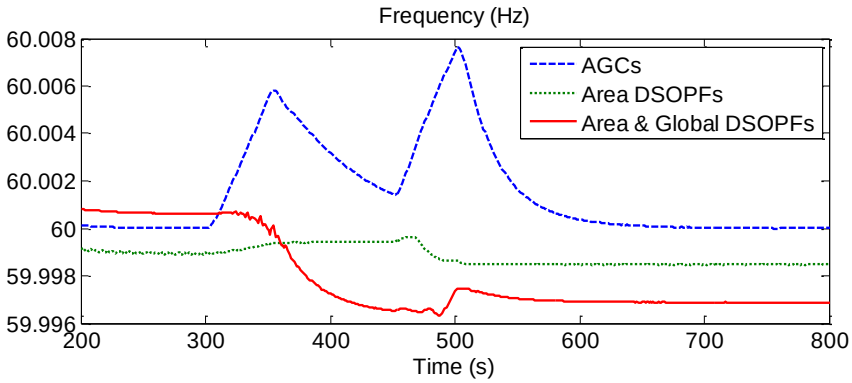

Figure 5.33 Frequency response with area and global DSOPF controllers.

5.8 Chapter Summary

A two-level dynamic stochastic optimal power flow (DSOPF) control scheme is proposed in this chapter to scale up the DSOPF control algorithm for large power systems. Two area DSOPF controllers are first developed to control the dynamic power flow of the two local areas in the 70-bus system. With the area DSOPF controllers, the security of the local area power networks is improved. Compared to traditional automatic generation controllers (AGCs), when the wind power generation varies, the area DSOPF controllers can better regulate the system frequency and inter-area tie-line flows, improve the overall system voltage profile, and mitigate line overloads, but at the cost of higher control effort and some wind power curtailment. An additional global DSOPF controller is designed to further coordinate the two area DSOPF controllers by adjusting the inter-area tie-line flows. The global coordination further relieves the congested lines, while minimizing wind power curtailment. This two-level architecture distributes the control and computation burden to multiple area DSOPF controllers, and reduces the training difficulty for implementing the DSOPF control for a large network.

The next chapter discusses the market operation layer (Figure 1.4) for efficient integration of wind power, and proposes a combined energy-and reserve market mechanism for wind power trading.

CHAPTER 6 COMBINED ENERGY-AND-RESERVE MARKET SCHEME FOR WIND POWER TRADING

6.1 Chapter Overview

To achieve high penetration of wind energy, system operators typically need to schedule a significant amount of additional reserve to balance unpredicted wind power variation. Meanwhile, wind producers participating in most electricity markets are subject to significant deviation penalties during market settlements. In this chapter, a combined energy-and-reserve market scheme is proposed for wind power trading. An additional wind reserve market is designed with lower deviation penalties, and thus lower risks for uncertainties. In the proposed wind market scheme, wind producers can increase their revenue by optimally bidding into the combined market and regulating their actual short-term energy production. The system benefits from facing less wind energy intra-hour variation, demanding less fast reserve for balancing wind variation, and having additional fast, although variable, reserve from wind plants. These benefits are likely to enhance grid security and operation in a scenario with high penetration of wind power.

6.2 Combined Energy-and-Reserve Market Design for Wind Power Trading

6.2.1 Existing Energy Market for Wind Power

With no congestion, a wind producer's revenue for a certain settling interval is related to its committed supply and the actual production, as in [98]

$$R_E = \pi_E P_c + T_E , \tag{6.1}$$

where R_E denotes the revenue from the energy market, π_E denotes the market price for energy (determined by solving the optimal power flow problem [19]), and P_c denotes the committed

output power (the power that the wind plant is supposed to output). T_E denotes the additional revenue (possibly negative) resulting from actual output power deviation, as in [98]

$$T_E = \begin{cases} \pi_{E+}(P - P_c) & P \geq P_c \\ \pi_{E-}(P - P_c) & P < P_c \end{cases}, \tag{6.2}$$

where P denotes the actual delivered power from the wind plant, π_{E+} and π_{E-} are the deviation prices for over-generation and under-generation, respectively. In general, $0 \leq \pi_{E+} \leq \pi_E \leq \pi_{E-}$. In other words, the excessive energy has a lower value and the energy deficits have a higher value.

Figure 6.1 illustrates that during real-time operation, given a committed output power, P_c, a wind producer's revenue in the energy market is maximized when all the available wind power is generated. It is because the wind plant revenue monotonically increases with the wind plant output power. The market does not affect the short-term wind plant output power. All of the wind power variation must then be absorbed by reserve from other controllable resources under the existing wind power market mechanism.

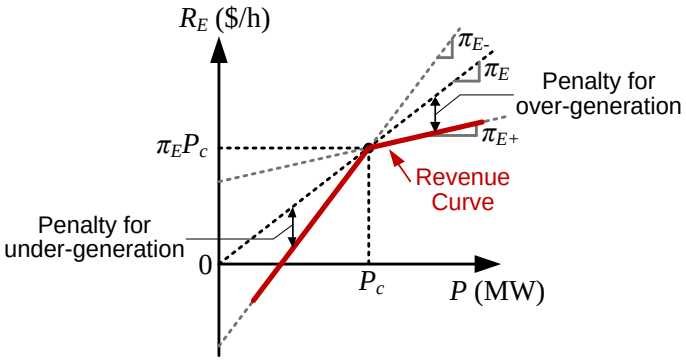

Figure 6.1 Revenue from energy market vs. actual output power.

6.2.2 Additional Reserve Market for Wind Power

In a reserve market, reserve products, which are distinguished in terms of ramp rates, typically include regulation reserve, spinning reserve, and non-spinning reserve [20]. Regulation reserve may include up regulation reserve and down regulation reserve, while

spinning and non-spinning reserve are up reserve services. Regulation reserve is typically most expensive because of its fast-ramping requirement. Since a wind plant has fast ramping capability, it may provide any type of reserve provided that the required wind power is available. Without loss of generality, in this study, different reserve products are not distinguished for wind power. Only up reserve (UR) and down reserve (DR) services are discussed below.

Usually in a reserve market, reserve products are firm with high certainty [20]. Thus, wind plants normally do not qualify for providing such firm reserve. In this dissertation, a reserve market allowing deviations, but with deviation penalties, is created below to allow wind plants to participate into the reserve market.

Since a wind plant can provide DR (down to its minimum output power) at virtually no cost, in a competitive market, the price for DR is expected to be low with the participation of wind plants. On the contrary, it depends on the availability of wind for a wind plant to provide UR. The price for UR is expected to be high. In the following discussions, the price for DR is assumed to be negligible and only the revenue from providing UR is considered. The revenue of a wind plant from the energy and reserve markets is then given by

$$R = R_E + R_{UR} = \pi_E P_c + T_E + \pi_{UR} UR_c + T_{UR}, \tag{6.3}$$

where π_{UR} is the market price for UR (determined by solving the simultaneous energy-and-reserve optimization problem [127]). UR_c is the committed UR from the wind plant (the up reserve that the wind plant is supposed to provide). T_{UR} denotes the revenue resulting from deviation of actual available UR during real-time operation, which is given by

$$T_{UR} = \begin{cases} \pi_{UR+}(UR - UR_c) & UR \geq UR_c \\ \pi_{UR-}(UR - UR_c) & UR < UR_c \end{cases}, \tag{6.4}$$

where UR is the actual available UR, π_{UR+} and π_{UR-} are deviation prices for the excessive UR

and UR deficits, respectively. Similar to the energy market, it is expected that the following price relationships hold:

$$Price\ Assumption\ I: 0 \le \pi_{UR+} \le \pi_{UR} \le \pi_{UR-}. \tag{6.5}$$

Note that monitoring of actual available UR from wind plants is needed to determine reserve deviation. Given a committed UR level, UR_c, Figure 6.2 shows the wind plant revenue by providing UR during real-time operation. It is also a monotonically increasing function. In other words, the more UR a wind plant provides during real time operation, the more money it earns from the reserve market.

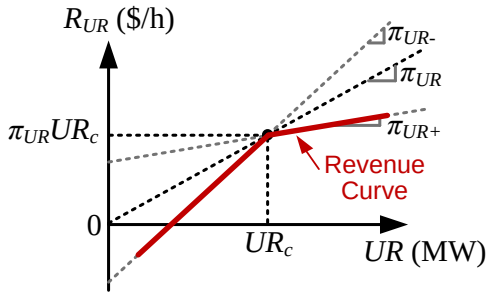

Figure 6.2 Revenue from reserve market vs. actual provision of up reserve.

For a certain settling interval during real-time operation, the market prices for energy and reserve, the deviation prices, and the energy and UR commitments from the wind plant are already determined. From (6.2) to (6.4), a wind plant's total revenue depends only on the actual delivered energy and UR. Note that providing either energy or UR requires the availability of wind. The next subsection discusses a wind plant's behavior during real-time operation: how to divide its available wind into energy and reserve to maximize its total reverne.

6.2.3 Wind Plant Revenue-Maximizing Operation in the Combined Market

The prices for energy and up reserve (UR), π_E and π_{UR}, are determined by the co-optimization of the energy and reserve markets [127]. Whenever the actual available wind

power deviates during real-time operation, a wind plant's most profitable operation (whether to change the energy output or UR) is determined by: 1) π_{E-} and π_{E+}, the marginal revenue of providing energy; and 2) π_{UR-} and π_{UR+}, the marginal revenue of providing UR.

In an electricity market, producing energy is associated with a fuel cost. The price of energy is often higher than the price of reserve [128]. Thus, it is expected that $\pi_{UR+} \leq \pi_{E+}$ and $\pi_{UR-} \leq \pi_{E-}$. In most existing reserve markets, the reserve demand is modeled as a single block, which tends to keep the reserve price low and create price spikes. It is expected that with a smooth demand curve for reserve, the reserve price would be higher and smoother. Besides, for example in the Texas nodal market, the price for over-generation is zero (π_{E+} = 0) after the generation exceeds a certain dead band. Thus, $\pi_{E+} \leq \pi_{UR-}$ is likely to be true under most circumstances. Assume that the electricity market for trading wind is designed such that the following relationships for deviation prices hold:

$$\textit{Price Assumption II}: 0 \leq \pi_{UR+} \leq \pi_{E+} \leq \pi_{UR-} \leq \pi_{E-}. \tag{6.6}$$

Denote the total available wind power during a certain settlement interval as P_w. P_w is then used to provide either energy or UR, as in

$$P_w = P + UR. \tag{6.7}$$

Under *Price Assumption II*, when P_w is less than $P_c + UR_c$, the wind plant will try to fulfill its committed output power first, because it results in a higher marginal revenue of π_{E-}. After the wind plant fulfills its committed output power, it will then provide UR for a marginal revenue of π_{UR-}. When the total available wind power is more than $P_c + UR_c$, the wind plant will output all of its excessive power, unless being called to curtail, since additional energy now yields a higher marginal revenue ($\pi_{UR+} \leq \pi_{E+}$).

Given a day-ahead commitment of energy and UR, (P_c, UR_c), if the wind plant operates optimally as described above, its maximum revenue during a certain settlement interval

depends only on P_w. From (6.1) to (6.4), this optimal revenue is illustrated in Figure 6.3 and given by

$$R(P_w \mid P_c, UR_c) = \begin{cases} \pi_{E+}P_w + (\pi_E - \pi_{E+})P_c + (\pi_{UR} - \pi_{E+})UR_c & P_w \in [P_c + UR_c, P_{\max}] \\ \pi_{UR-}P_w - (\pi_{UR-} - \pi_E)P_c - (\pi_{UR-} - \pi_{UR})UR_c & P_w \in [P_c, P_c + UR_c) \\ \pi_{E-}P_w - (\pi_{E-} - \pi_E)P_c - (\pi_{UR-} - \pi_{UR})UR_c & P_w \in [0, P_c) \end{cases}, \tag{6.8}$$

where P_{max} is the wind plant installed capacity.

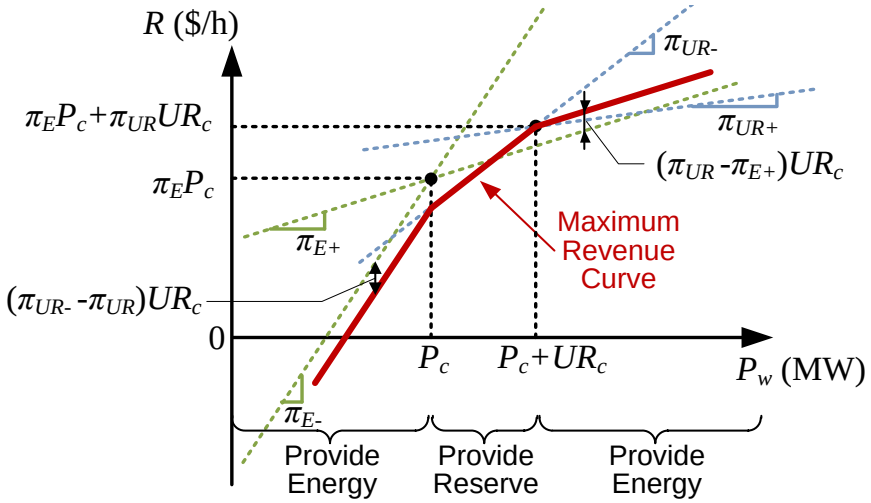

Figure 6.3 Maximum revenue vs. available wind power under *Price Assumption II*.

Under *Price Assumption II*, when a wind plant operates optimally, wind power variation between P_c and $P_c + UR_c$ appears as varying regulation reserve, and the grid is not directly exposed to such variation. Note that the resulting variable reserve from wind, which would have appeared in the energy market and required balancing from other conventional energy sources, can now be effectively used to counteract system active power imbalance.

6.3 Wind Plant Bidding Strategies in the Combined Market

Given a certain amount of available wind power, the amount of reserve provided depends on the day-ahead commitments, P_c and UR_c. This section discusses the wind plant's

optimal bidding scheme given price signals and probabilistic wind forecasts. It is assumed that the market prices are available by perfect estimation and both the energy and reserve markets are competitive, i.e., bids from any individual wind plant do not affect the market prices.

6.3.1 Wind Plant Revenues with Different Bidding Schemes

If only a point prediction is available, a simply bidding strategy is to commit the output power to be the same as the prediction. If the prediction is perfect, then this simple bidding strategy yields maximum revenue. However, in reality, wind power forecasts are subject to relatively large errors, especially for a single wind plant. Figure 6.4 shows an example of wind plant revenue curves from two bidding strategies. In strategy 1, the wind producer participates only in the energy market, resulting in *Revenue Curve 1*, where the optimal committed output power, P_{c1}, depends on the market prices and probabilistic wind forecast [98]. In strategy 2, it participates in both markets with commitments P_{c2} and UR_{c2}, and results in *Revenue Curve 2*. In this example, if the actual available wind power is around P_{c1}, strategy 1 results in a higher revenue; otherwise, strategy 2 yields a higher revenue.

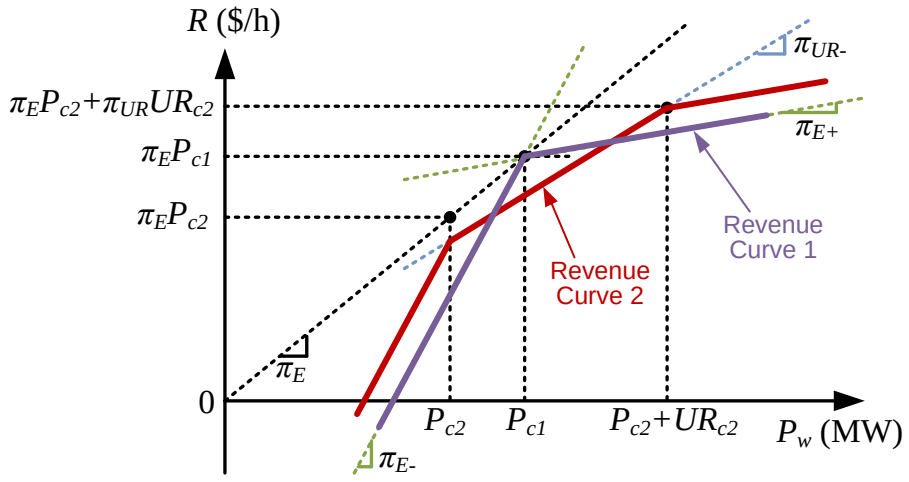

Figure 6.4 Example wind plant revenue curves with two different bidding schemes (0 $< \pi_{UR+} < \pi_{E+} < \pi_{UR} < \pi_{UR-} < \pi_E < \pi_{E-}$).

6.3.2 Optimal Bidding Scheme with Probabilistic Wind Forecasts

Given a probabilistic prediction of wind production, the expected revenue in a certain settlement interval is given by

$$E[R(P_c, UR_c)] = \int_0^{P_{\max}} R(P_w \mid P_c, UR_c)\, f(P_w) dP_w , \tag{6.9}$$

where $f(P_w)$ is the prediction probability density function with support over the interval $[0, P_{max}]$. The optimal bidding strategy is to maximize the expected revenue, i.e.,

$$\begin{aligned} &\max E[R(P_c, UR_c)] \\ &\text{s.t. } P_{\max} - P_c - UR_c \geq 0 \\ &P_c \geq 0, UR_c \geq 0 \end{aligned} \tag{6.10}$$

The necessary conditions for optimality are given by the Karush–Kuhn–Tucker (KKT) conditions [123]. Define

$$A = \frac{\pi_E - \pi_{UR}}{\pi_{E-} - \pi_{UR-}}, \quad B = \frac{\pi_{UR} - \pi_{E+}}{\pi_{UR-} - \pi_{E+}} . \tag{6.11}$$

Note that under *Price Assumption I*, $B \leq 1$. The optimal bidding scheme is conditional on the values of A and B [124] and summarized by the following cases (see Appendix F for detailed derivations):

Case 1: $0 < A < B$

It is optimal to bid in both energy and reserve markets, and the optimal strategy is

$$P_c^* = F^{-1}(A), \; UR_c^* = F^{-1}(B) - P_c^* , \tag{6.12}$$

where $F(P_w)$ is the cumulative distribution function of $f(P_w)$ and $F^{-1}(1) = P_{max}$. Note that when π_{E-} is larger (higher penalty for under-generation) and π_{UR-} is smaller (closer to π_{UR} and lower penalty for UR deficits), $B - A$ becomes larger. In other words, when bidding in the reserve market has less risk of revenue reduction, the region of providing reserve (see Figure 6.3) will be wider, and more wind variation will be diverted into the reserve market.

Case 2: $A > 0$ and $A \geq B$

In this case, it is optimal to bid only in the energy market, and the optimal strategy is

$$P_c^* = F^{-1}\left(\frac{\pi_E - \pi_{E+}}{\pi_{E-} - \pi_{E+}}\right), UR_c^* = 0 \quad (6.13)$$

Note that since $\pi_{E+} \leq \pi_E \leq \pi_{E-}$, $0 \leq (\pi_E - \pi_{E+})/(\pi_{E-} - \pi_{E+}) \leq 1$ and (6.13) is valid. The optimal solution in this case is the same as that shown in [98], where only the energy market was considered. To attract wind producers to participate into the reserve marker, it is necessary to have a lower deviation penalty π_{UR-} to ensure $A < B$.

Case 3: $A \leq 0$, i.e., $\pi_E \leq \pi_{UR}$

In this case, it is optimal to bid only in the reserve market, and the optimal strategy is

$$P_c^* = 0, UR_c^* = F^{-1}(B) \quad (6.14)$$

Note that $A \leq 0$ implies $\pi_{E+} \leq \pi_{UR}$. Thus, $B \geq 0$ in this case and $F^{-1}(B)$ is valid.

6.4 Simulation Studies

6.4.1 Wind Plant Probabilistic Forecasts

A simulated wind plant (site 0195) in north Texas with an installed capacity of 1089 MW is selected from the National Renewable Energy Laboratory (NREL) Eastern Wind Integration and Transmission Study (EWITS) dataset [125]. Day-ahead hourly point forecasts and actual outputs are available from the dataset.

Probabilistic forecasts are generated based on the 2006 data of the wind plant. It is assumed that the wind forecast probability distribution follows the beta distribution $B(\alpha, \beta)$ [94], [126], with a finite support between 0 and 1. When $\alpha > 1$ and $\beta > 1$, $B(\alpha, \beta)$ is a unimodal function, where the mode is the value with the highest probability. From the 2006 data, the forecast variance as a function of the point forecast is approximated by a quadratic

curve, as shown in Figure 6.5. For a normalized point forecast, P ($0 \le P \le 1$), $\alpha(P)$ and $\beta(P)$ are calculated such that $\alpha(P)$, $\beta(P) > 1$, P is the mode of $B[\alpha(P), \beta(P)]$, and the $B(\alpha(P), \beta(P))$ variance follows the fitted quadratic curve shown in Figure 6.5. Probabilistic forecasts are then generated from α, β, and the point forecasts.

The actual 10 min wind power outputs and the day-ahead hourly probabilistic forecasts for a historical day (July 19, 2006) are plotted in Figure 6.6, where the prediction confidence intervals are generated from the beta distribution.

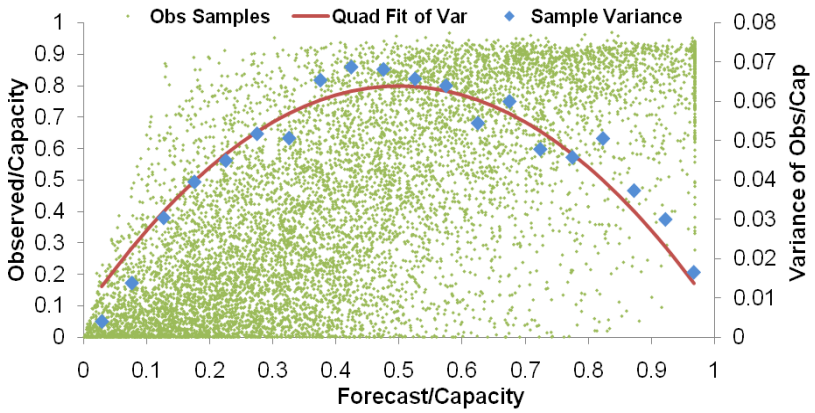

Figure 6.5 Normalized day-ahead hourly forecasts and actual outputs of wind site 0195 in year 2006, with sample variance and its fitted quadratic curve.

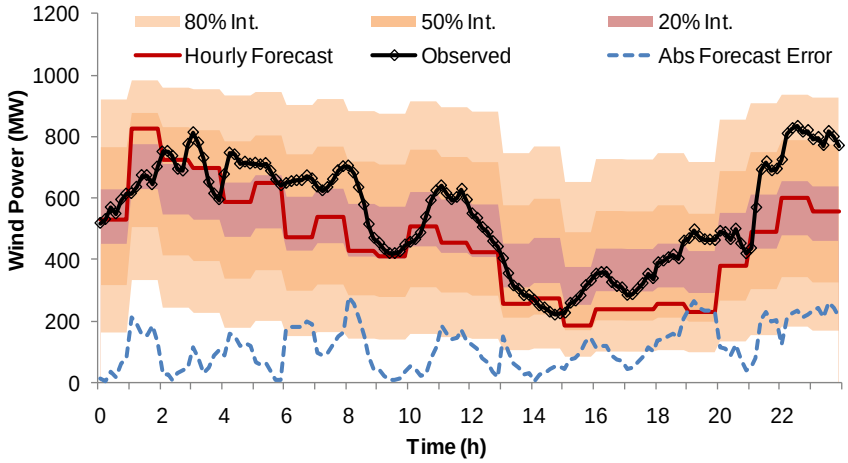

Figure 6.6 Day-ahead hourly wind power forecasts (highest-probability predictions), with confidence intervals, actual 10-min wind power, and the absolute forecast error.

6.4.2 Wind Plant Bids and Operation

Assume that any deviation from the dispatched levels is subject to penalties (no dead band). In this study, the market prices for energy and up reserve (UR), as shown in Figure 6.7, are selected from the ERCOT day-ahead nodal market on Dec 5, 2010. High deviation penalties are assumed for the energy market. The percentage penalties for over- and under-generation are 90%, i.e., $\pi_{E+} = 0.1\pi_E$ and $\pi_{E-} = 1.9\pi_E$. For the UR market, the penalty for excessive UR is assumed to be high ($\pi_{UR+} = 0.1\pi_{UR}$), and the penalty for UR deficits is assumed to be lower ($\pi_{UR-} = 1.3\pi_{UR}$) to incentivize wind producers to participate into the reserve market. *Price Assumptions I* and *II* are fulfilled with the above deviation price settings.

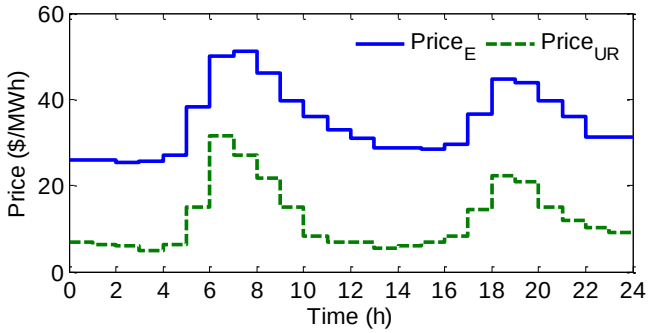

Figure 6.7 Day-ahead market prices for energy and UR.

Given the day-ahead probabilistic forecasts in Figure 6.6, from (6.12)-(6.14), the hourly optimal commitments in the energy and reserve markets, (P_c, UR_c), are obtained and shown in Figure 6.8. For comparison, the optimal commitments in only the energy market, denoted as $P_{cE\text{-}only}$, are obtained from (6.13) and plotted in Figure 6.8 as well.

Figure 6.9 shows the wind plant revenue-maximizing operation during the actual delivery day, where the output power and UR levels are updated every 10 min. When the wind power is traded only in the energy market, all available wind power is outputted to

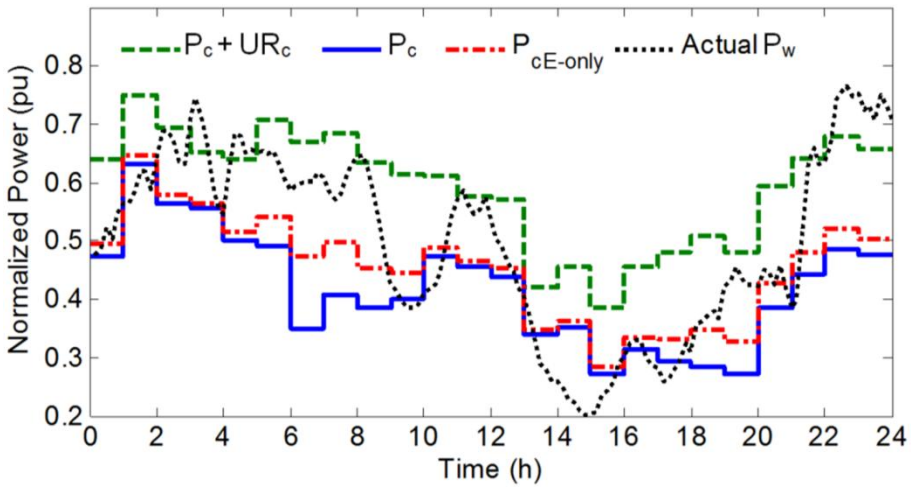

Figure 6.8 Optimal committed energy and UR when bidding in both markets (P_c and UR_c) and in the energy market only ($P_{cE\text{-}only}$).

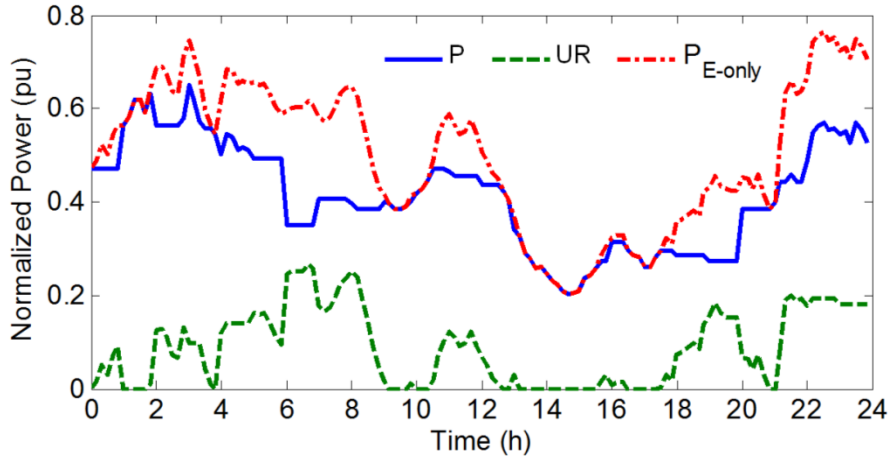

Figure 6.9 Output power and UR during actual delivery day: *P* and *UR* result from bidding in both markets; $P_{E\text{-}only}$ results from bidding in only the energy market.

maximize the revenue, resulting in the $P_{E\text{-}only}$ curve following the P_w curve. When the wind power is traded in both the energy and reserve markets, the wind power variation that falls between P_c and UR_c appear as system reserve. With the proposed market scheme, the actual wind plant output power *P* has less intra-hour short-term variation, and the inter-hour output follows the committed outputs more closely as compared to the energy-market-only case. Less variation in *P* requires less balancing reserve from the system, while the additional fast reserve from wind can be used to respond to system frequency deviation.

The new additional reserve from wind is less reliable because of its variability, and thus can be considered with a lower credit to replace part of the traditional reserve. However, because of the fast ramping capability of wind plants, the reserve from wind has better quality. A certain amount of reserve from wind can replace a larger amount of the traditional slower reserve, since the system reserve requirement also depends on the ramp rates of the units that provide the reserve.

6.4.3 Wind Plant Revenues

With the day-ahead commitments in Figure 6.8 and the actual delivery in Figure 6.9, the wind plant revenues, updated every 10 min, are obtained based on (6.2) to (6.4) and shown in Figure 6.10. Although bidding in both markets results in a lower level of output power, the revenue does not reduce because of the additional revenue from the reserve market. When the actual wind power deviates significantly from $P_{cE\text{-}only}$, such as during hours 8 and 23-24, bidding in both markets results in a higher revenue. In contrast, when the actual wind power is around $P_{cE\text{-}only}$, such as at hours 6 and 18, bidding only in the energy market results in a higher revenue. The revenue difference between the two schemes is amplified by the price signals.

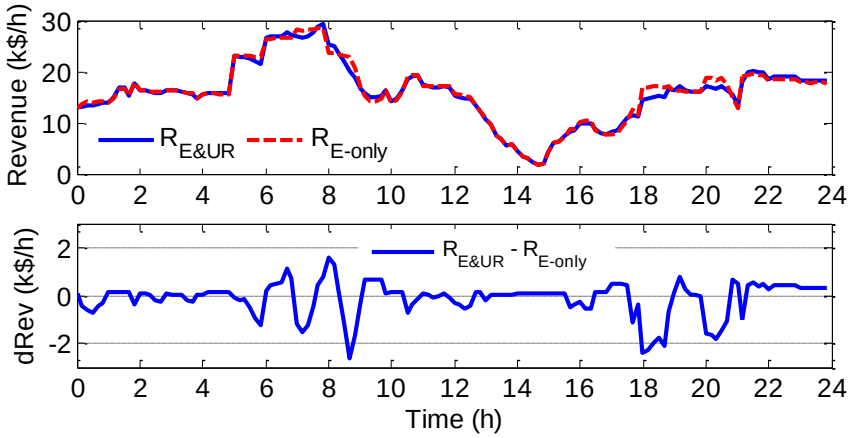

Figure 6.10 Wind plant revenues. Top: revenues when bidding in both markets ($R_{E\&UR}$) and in the energy market only ($R_{E\text{-}only}$). Bottom: difference between $R_{E\&UR}$ and $R_{E\text{-}only}$.

With the same daily prices for the whole year, Table 6.1 compares the monthly average revenues from these two bidding schemes. For example in January, the wind plant earns an average of \$11.23k/h when bidding in both the energy and up reserve (UR) markets, but earns only \$10.81k/h when bidding in only the energy market; a revenue increase of 3.88% is achieved from the combined market. Averaging the monthly revenues, bidding in the combined market yields a yearly average of 4.96% revenue increase, which is due to the fact that wind production deviates from the committed output significantly most of the time and is subject to the corresponding penalties. Suppose the rate of return for this wind project is 10% under the existing market rules. With the proposed market scheme, if a long-term revenue increase of 4.96% can be realized, the resulting rate of return becomes 15.5%, representing a 54.4% increase in profit. In reality, the market prices need to be forecasted, and the price forecast errors will cause some loss in the revenue.

Table 6.1 Monthly average revenue (no curtailment).

	$R_{E\&UR}$ (k\$/h)	$R_{E\text{-}only}$ (k\$/h)	R Inc. (%)		$R_{E\&UR}$ (k\$/h)	$R_{E\text{-}only}$ (k\$/h)	R Inc. (%)
Jan	11.23	10.81	3.88	Aug	4.96	4.63	7.25
Feb	9.36	8.99	4.06	Sep	4.92	4.49	9.59
Mar	13.08	12.70	2.97	Oct	7.80	7.42	5.07
Apr	13.32	12.96	2.76	Nov	9.02	8.64	4.38
May	6.53	6.12	6.71	Dec	8.48	8.15	4.12
Jun	10.06	9.71	3.62	Yearly Avg.	8.82	8.44	4.96
Jul	7.04	6.69	5.10				

6.4.4 Effects of Different Penalties for Up Reserve Deficits

As discussed in Section 6.3.2, the deviation price for up reserve (UR) deficits, $\pi_{UR\text{-}}$, affects the level of committed UR and thus the output power variation. Different levels of $\pi_{UR\text{-}}$ are simulated, and the resulting output power and UR are shown in Figure 6.11. When

the penalty for under-provision of UR is low ($\pi_{UR-} = 1.1\pi_{UR}$), the hourly wind plant outputs become constant and all the intra-hour wind variation is diverted into the regulation reserve. On the other hand, when this penalty is high ($\pi_{UR-} = 1.5\pi_{UR}$), the committed UR is low and the wind power variation saturates this reserve level most of the time, resulting in a more variable wind power output.

When $\pi_{UR-} = 1.1\pi_{UR}$, a yearly average revenue increase of 11.70% is observed when bidding in both markets. This revenue increase becomes 1.60% when $\pi_{UR-} = 1.5\pi_{UR}$.

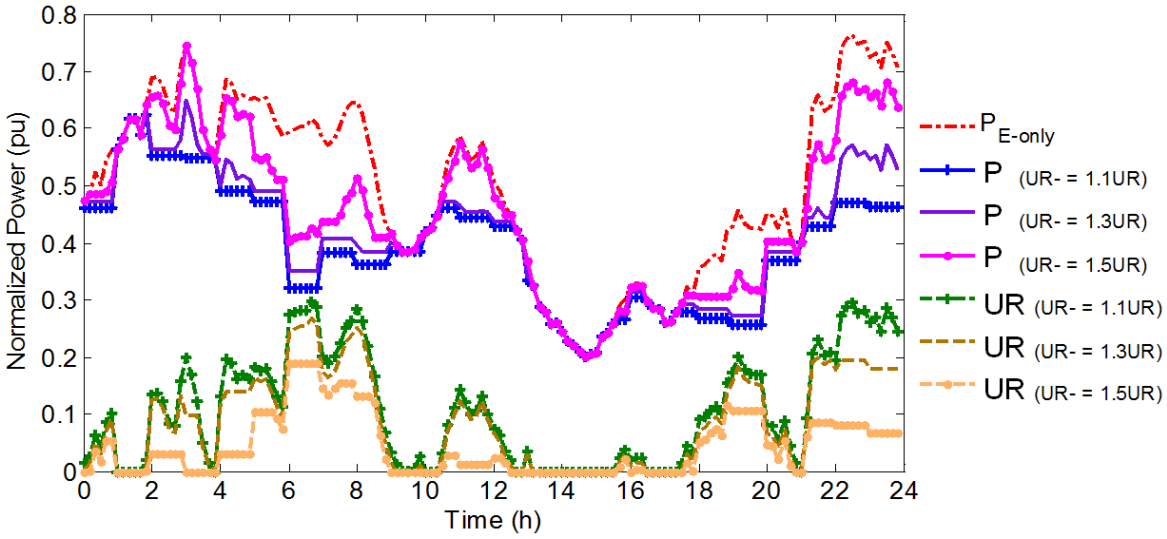

Figure 6.11 Output power and UR with different levels of π_{UR-}.

6.5 Chapter Summary

A combined energy-and-reserve wind market scheme is proposed in this chapter to incentivize wind producers to regulate their outputs. In the combined market, the penalty for up reserve deficit is designed to be low. Wind producers can thus hedge their risks of revenue reductions due to forecast errors in the reserve market. It is shown that wind producers can increase their revenues by optimally bidding into both the energy and reserve markets. As a result, part of the wind power variation is diverted into the system reserve,

reducing the need for additional reserve to balance wind power short-term variation. The system also benefits from having additional fast reserve from wind plants. These additional fast reserves may then be used to respond to system frequency deviations and increase system security. The proposed wind market scheme is likely to favor grid operation especially with high penetration of wind power.

The next chapter compares the proposed wind market scheme with two other existing wind market schemes in a single-bus power system with high wind penetration. The benefits of the proposed market scheme on grid operation and control are further investigated.

CHAPTER 7 COMPARISON OF DIFFERENT WIND MARKET SCHEMES IN A SINGLE-BUS POWER SYSTEM

7.1 Chapter Overview

The combined energy-and-reserve wind market scheme proposed in Chapter 6 is further evaluated in a single-bus power system with market operation and control interactions. Market operation is modeled by solving the day-ahead unit commitment problem using mixed integer quadratic programming. A simplified system dynamic model is developed with closed-loop frequency control to study the system dynamic responses. The proposed combined market scheme is compared with two existing wind market schemes (using conservative and optimal wind forecasts in only the energy market). Percentage wind energy generated, percentage load served, energy and reserve prices, and system frequency deviations under different wind market schemes are evaluated. The benefit of having fast reserve from wind is shown in a contingency study with loss of generation. The proposed combined energy-and-reserve wind market scheme provides better grid security and a way to adjust the impacts from wind plants on grid operation by changing the deviation prices.

7.2 Single-Bus Power System for Wind Market Comparison

The single-bus system under study consists of one aggregated load, one aggregated coal plant for supplying the base load, one aggregated gas plant for providing ramping capability, and some wind plants, as shown in Figure 7.1. To better represent the behavior of individual wind plants in a market environment, no aggregation is applied to wind plants. Each wind plant will operate and participate in the market based on the price signals. Transmission loss and congestions are not considered in this single-bus system.

In this study, only the day-ahead market is considered. Persistent price forecasts (using the actual market prices from the previous day) are used for wind plants to submit their supply bids. Wind plant bids will now affect the market prices. Load forecasting errors are assumed to be zero, since they are relatively small compared to the wind forecasting errors. Hourly energy and reserve schedules are first determined for the next day based on the load forecasts and supply bids from all generation resources. During real-time operation, up reserve (UR) and down reserve (DR) services are then used to balance unpredicted wind variation by a frequency control loop. Figure 7.2 shows the overall market operation and control process. Different wind power market schemes will be compared. Percentage of load served, percentage of wind used, etc. (see Figure 7.2) will be evaluated. The implementations of the day-ahead scheduling and frequency control schemes are described in the following sections.

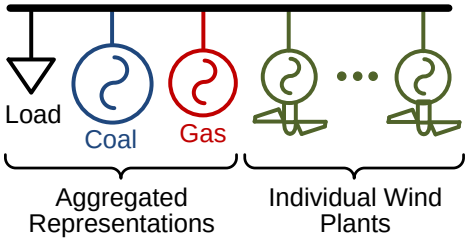

Figure 7.1 Single-bus system for wind market scheme comparison.

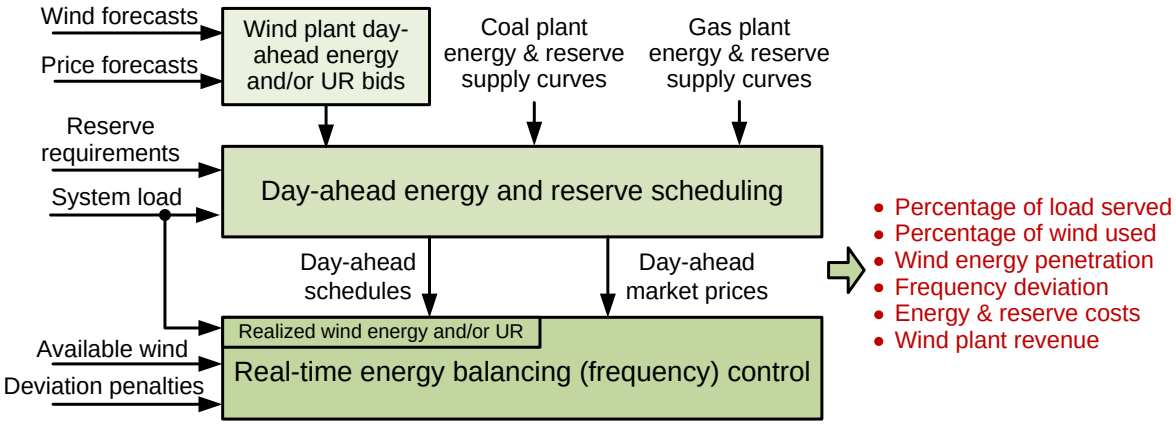

Figure 7.2 Overall market operation and control process.

7.3 Day-Ahead Scheduling of Energy and Reserve

The goal of the day-ahead scheduling problem, or the unit commitment problem, is to minimize the overall cost to procure energy and reserve services over the scheduling horizon, typically hourly for the next day.

7.3.1 Clearing of Energy and Up Reserve Bids from Wind Plants

Since the marginal cost of the wind power is close to zero, a wind plant normally submits a supply curve (price vs. power) that is low enough to get entirely dispatched. It is thus equivalent for the wind plant to submit only the highest supply bid. In this study, the energy and up reserve (UR) bids from wind plants are accepted first without market optimization. The remaining net load, net UR requirement, and down reserve (DR) requirement are then optimized among the conventional generators.

7.3.2 Co-optimization of Energy and Reserve Bids from Conventional Generators based on Mixed-Integer Programming

For the remaining conventional generation units, their bids are cleared by the co-optimization of energy and reserve [127]. The optimization objective is described by

$$\min \sum_{t=1}^{24} \sum_{k=1}^{Ng} [Z_k(t) \times C_{Ek}(P_k(t)) + Z_k(t) \times C_{URk}(UR_k(t)) + Z_k(t) \times C_{DRk}(DR_k(t)) + C_{onk}(Z_k(t), Z_k(t-1)) + C_{offk}(Z_k(t), Z_k(t-1))], \quad (7.1)$$

where t is the hourly time index, k is the index for conventional generators, and N_g is the total number of conventional generators. $Z_k(t)$ is an integer variable indicating the status of generator k at time t (1 means on, and 0 means off). $P_k(t)$, $UR_k(t)$, and $DR_k(t)$ are positive variables representing the scheduled output power, UR service, and DR service, respectively, for generator k. $C_{Ek}(\cdot)$, $C_{URk}(\cdot)$, $C_{DRk}(\cdot)$, $C_{onk}(\cdot,\cdot)$, and $C_{offk}(\cdot,\cdot)$ are functions representing the energy supply curve, UR supply curve, DR supply curve, turn-on cost, and turn-off cost, respectively, for generator k.

7.3.2.1 Power Balance Constraint

In a lossless power network, the scheduled energy supply should be equal to the forecasted energy demand over the scheduling horizon. In this study, since the wind bids are cleared first, the net load may be lower than the minimum output power of any thermal plant, but sometimes one or more thermal plant(s) may need to be on to meet the active power or reserve requirements. The power balance equality constraint is thus relaxed into an inequality constraint to first accept all wind power. Any excessive wind power will later be curtailed by an over-frequency protection loop during real-time operation. The power balance inequality is described by

$$\sum_{k=1}^{Ng} P_k(t) \geq D(t) - \sum_{i=1}^{Nw} P_{cw,i}(t), \ \forall t \quad . \tag{7.2}$$

$D(t)$ is the forecasted demand at time t. $P_{cw,i}(t)$ is the energy commitment of wind plant i at time t, and N_w is the total number of wind plants.

7.3.2.2 Reserve Requirement Constraints

The reserve requirement constraints are inequality constraints to ensure the required amounts of up and down reserve capacity are procured. These capacity requirements are defined offline based on the load forecasts and security/reliability standards. In this study, the load forecast error is assumed to be zero, and all procured reserve is used to balance wind variability and uncertainty. These reserve services are evaluated in 10 min, i.e., the procured reserve must appear as generator active power outputs in 10 min once it is called by the system operator. The constraints for the UR and DR requirements are described by

$$\begin{aligned} &\sum_{k=1}^{Ng} UR_k(t) \geq UR_{req}(t) - \sum_{i=1}^{Nw} G_{URw,i} UR_{cw,i}(t), \ \forall t \\ &\sum_{k=1}^{Ng} DR_k(t) \geq DR_{req}(t), \ \forall t \end{aligned} \quad , \tag{7.3}$$

where $UR_{req}(t)$ and $DR_{req}(t)$ are 10 min UR and DR requirements at time t. $UR_{cw,i}(t)$ is the UR commitment of wind plant i at time t. To account for the uncertainty of wind power, a discount factor, $G_{URw,i}$ ($0 < G_{URw,i} < 1$), is used to commit reserve from each wind plant. $G_{URw,i}$ can be set to a value lower than the wind plant capacity factor, which indicates the long-term average energy availability of the wind plant. A typical wind plant has a capacity factor of 0.25. In this study, $G_{URw,i}$ is set to 0.2 for all wind palnts.

7.3.2.3 Supply Min/Max Constraints

The active power output from a power plant is bounded by its physical limits. The total output power including both up and down reserve should not exceed these limits [127], as in

$$\begin{aligned} P_k(t) + UR_k(t) &\le P_{\max k} Z_k(t), \ \forall k,t \\ P_k(t) - DR_k(t) &\ge P_{\min k} Z_k(t), \ \forall k,t \end{aligned} \quad . \tag{7.4}$$

P_{maxk} and P_{mink} are the sustainable maximum and minimum outputs from generator k when it is on. When generator k is off, its maximum and minimum outputs become zero. Thus, in (7.4), P_{maxk} and P_{mink} are multiplied by $Z_k(t)$, the status of generator k.

7.3.2.4 Supply Ramping Constraints

Output power changes from a generator are subject to its ramping capability. This ramping capability adds two sets of constraints to a generator. Firstly, the 10 min reserve services a generator can provide are limited by its ramp rate [127], as in

$$\begin{aligned} UR_k(t) &\le UR_{\max k}, \ \forall k,t \\ DR_k(t) &\le DR_{\max k}, \ \forall k,t \end{aligned} \quad , \tag{7.5}$$

where UR_{maxk} and DR_{maxk} are the maximum up and down reserve generator k can provide in 10 min. Secondly, the output power change from t-1 to t is also limited by the generator's ramp rate in one hour. If generator k remains on from t-1 to t,

$$-6DR_{\max k}(t) \le P_k(t) - P_k(t-1) \le 6UR_{\max k},\ \forall k,t \quad . \tag{7.6}$$

In other words, $UR_{max,k}$ and $DR_{max,k}$ are the maximum up and down output power changes generator k can achieve in 10 min; $6UR_{max,k}$ and $6DR_{max,k}$ are the maximum up and down output power changes generator k can achieve in one hour, if generator k remains on during the hour. If generator k turns on from t-1 to t, $P_k(t\text{-}1) = 0$ and $P_k(t) \ge P_{mink}$. It is assumed that generator k can provide P_{mink} instantly, and $P_k(t)$ is limited by

$$\begin{aligned} &P_k(t) \le 6UR_{\max k} + P_{\min k} \\ &\forall k,t,\ \text{if } P_k(t-1) = 0 \end{aligned} \quad . \tag{7.7}$$

If generator k turns off from t-1 to t, $P_k(t\text{-}1) \ge P_{mink}$ and $P_k(t) = 0$. It is assumed that generator k can drop its output from P_{mink} to zero instantly. $P_k(t\text{-}1)$ is thus limited by

$$\begin{aligned} &P_k(t-1) \le 6DR_{\max k} + P_{\min k} \\ &\forall k,t,\ \text{if } P_k(t) = 0 \end{aligned} \quad . \tag{7.8}$$

7.3.2.5 Formulation into a Linearly-Constrained Mixed-Integer Quadratic Programming Problem

Quadratic supply curves [20] are used for energy, UR and DR services, as in

$$\begin{aligned} &C_{Ek}(P_k) = a_k + b_k P_k + c_k P_k^{\,2} \\ &C_{URk}(UR_k) = b_{URk} UR_k + c_{URk} UR_k^{\,2} \\ &C_{DRk}(DR_k) = b_{DRk} DR_k + c_{DRk} DR_k^{\,2} \end{aligned} \quad . \tag{7.9}$$

where a_k, b_k, and c_k are fixed, linear, and quadratic energy cost coefficients for generator k, b_{URk}, and c_{URk} are linear and quadratic UR cost coefficients, and b_{DRk}, and c_{DRk} are linear and quadratic DR cost coefficients.

Assume that these supply curves remain unchanged over the scheduling horizon. The energy-reserve co-optimization problem described by (7.1) to (7.8) can then be formulated into a linearly-constrained mixed-integer quadratic programming problem, as in

$$
\begin{aligned}
\min_{\substack{Z_k, P_k, \\ UR_k, DR_k}} \; & \sum_{t=1}^{24} \sum_{k=1}^{Ng} \{ a_k Z_k(t) + b_k P_k(t) + c_k P_k(t)^2 + c_{ak}[Z_k(t) - Z_k(t-1)]^2 + c_{bk}[Z_k(t) - Z_k(t-1)] \\
& + b_{URk} UR_k(t) + c_{URk} UR_k(t)^2 + b_{DRk} DR_k(t) + c_{DRk} DR_k(t)^2 \} \\
s.t. \; & \sum_{k=1}^{Ng} P_k(t) \geq D(t) - \sum_{k=i}^{Nw} P_{cw,i}(t) \\
& \sum_{k=1}^{Ng} UR_k(t) \geq UR_{req} - G_{URw} \sum_{i=1}^{Nw} UR_{cw,i}(t) \\
& \sum_{k=1}^{Ng} DR_k(t) \geq DR_{req} \\
& P_k(t) + UR_k(t) - P_{\max k} Z_k(t) \leq 0 \\
& P_k(t) - DR_k(t) - P_{\min k} Z_k(t) \geq 0 \\
& P_k(t) - P_k(t-1) - [Z_k(t) - Z_k(t-1)] P_{\min k} \leq 6 UR_{\max k} \\
& P_k(t) - P_k(t-1) - [Z_k(t) - Z_k(t-1)] P_{\min k} \geq -6 DR_{\max k} \\
& 0 \leq Z_k(t) \leq 1, \; 0 \leq P_k(t) \leq P_{\max k} \\
& 0 \leq UR_k(t) \leq UR_{\max k}, \; 0 \leq DR_k(t) \leq DR_{\max k}, \\
& Z_k(t) \in \mathbb{Z}, \; P_k(t) \in \mathbb{R}, \; UR_k(t) \in \mathbb{R}, \; DR_k(t) \in \mathbb{R} \\
& \forall k = 1, 2, ..., Ng, \; \forall t = 1 \, 2 \, \ldots \, 24
\end{aligned}
\qquad (7.10)
$$

c_{ak} and c_{bk} are costs derived from the turn-on cost, c_{onk}, and turn-off cost, c_{offk}, as in $c_{ak} = (c_{onk} + c_{offk})/2$, and $c_{bk} = (c_{onk} - c_{offk})/2$. The wind reserve discount factor G_{URw} equals 0.2. It is assumed in (7.10) that the up and down reserve requirements, UR_{req} and DR_{req}, remain unchanged over time and are set to 15% of the total installed wind capacity.

This mixed-integer optimization problem can then be solved using an existing optimization software package, such as MOSEK [129].

7.3.3 Day-Ahead Market Prices and Real-Time Settlements

The day-ahead market price for energy or reserve is defined as the price for procuring the next MW of energy or reserve [130]. For the studied system, the market price for energy, UR, or DR is determined by the highest marginal price, for providing the respective service, among all conventional plants, as in

$$\begin{aligned}\pi_E(t) &= \max(b_k + 2c_k P_k(t), \forall k)\\ \pi_{UR}(t) &= \max(b_{URk} + 2c_{URk} UR_k(t), \forall k)\\ \pi_{DR}(t) &= \max(b_{DRk} + 2c_{DRk} DR_k(t), \forall k)\end{aligned} \quad (7.11)$$

During real-time operation, conventional units have controllable primary energy inputs. They will provide the scheduled amounts of energy and reserve, and thus do not involve deviation penalties. For wind plants, the realized energy and/or UR may deviate from the scheduled values. Any deviations from the schedules are subject to penalties. All wind plants are assumed to operate optimally (maximizing their revenues) in real time based on their wind availability and the market deviation prices, as described in Section 6.2.3. Wind plant revenues are then settled based on (6.3).

7.4 Dynamic System Model with Frequency Control

Given the actual realized energy and reserve from coal, gas, and wind plants, the system frequency may deviate because of unpredicted wind variation and insufficient ramping capability to follow the wind variation. To evaluate the system frequency deviation and the benefits of having fast reserve from wind, a simplified dynamic system model is developed, as shown in Figure 7.3.

The system frequency response is modeled as a first-order dynamic process, where M is the equivalent system inertia in pu and D is the load-frequency response in pu [17]. Any frequency deviation is regulated by an AGC. The dispatch ratios, K_{Coal}, K_{Gas}, and K_{Wind}, in the AGC are proportional to the ramp rates of the respective generation resources. Thus, the ramping capabilities of all resources are fully used.

The output of the AGC is limited by the day-ahead-scheduled and/or actual-available reserve from all resources. If a large power unbalance occurs, under-frequency (or over-frequency) protection will kick in to shed load (or curtail wind).

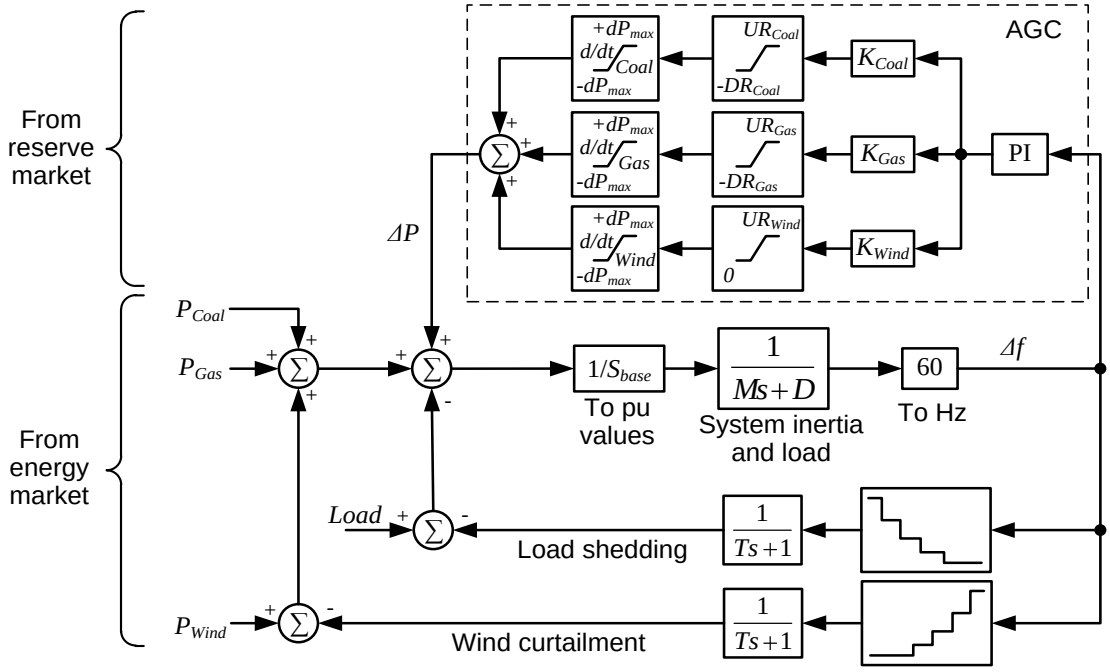

Figure 7.3 Dynamic system model with frequency control.

7.5 Simulation Studies

7.5.1 Simulation Data and Parameter Settings

The aggregated coal and gas plants in Figure 7.1 are rated at 1000 MW and 500 MW, respectively. Table 7.1 lists the detailed parameters for the two thermal plants. 10 individual wind plants are selected from the NREL EWITS database [125]. The total installed wind power capacity is 1000 MW, resulting in 40% capacity penetration. All 10 wind plants are located in one geographic region, so they are likely to be within one balancing area and their wind profiles are correlated. Figure 7.4 shows the forecasts and actual outputs from the 10 wind plants for a typical day. Wind probabilistic forecasts are generated using the Beta distribution discussed in Section 6.4.1.

Table 7.1 Parameters for the coal and gas plants.

Gen Unit	P_{min} (MW)	P_{max} (MW)	UR_{max} (MW in 10 min)	DR_{max} (MW in 10 min)	Turn On Cost ($)	Turn Off Cost ($)
Coal	100	1000	80	80	2000	1500
Gas	50	500	250	250	2500	2000

Gen Unit	Energy Supply Curve			UR Supply Curve		DR Supply Curve	
	a ($/h)	b ($/MWh)	c ($/MW^{2}h)	b_{UR} ($/MWh)	c_{UR} ($/MW^{2}h)	b_{DR} ($/MWh)	c_{DR} ($/MW^{2}h)
Coal	650	15	0.008	11	0.05	7	0.005
Gas	650	50	0.005	30	0.05	8	0.005

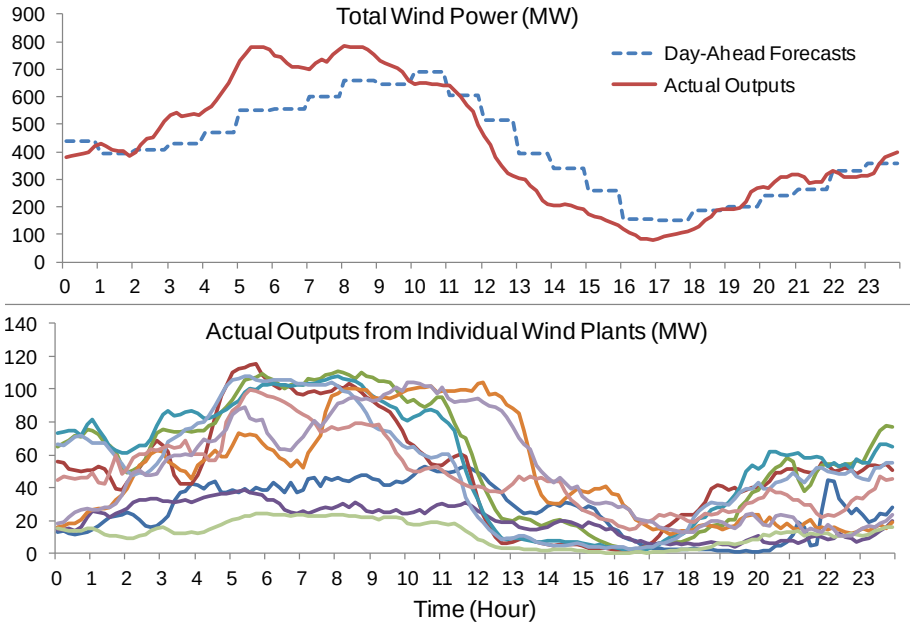

Figure 7.4 Wind profiles of a typical day.

Some typical load data are selected from an ISO. After scaling, the peak load becomes 1400MW, equal to 80% of the total installed generation capacity (taking 25% capacity factor for wind). Both up and down reserve requirements are set to 15% of the wind capacity, i.e., $UR_{req} = DR_{req} = 150$ MW.

The percentage penalties for over- and under-generation are both 70%, i.e., $\pi_{E+} = 0.3\pi_E$ and $\pi_{E-} = 1.7\pi_E$. The percentage penalties for over- and under-provision of UR are 90% ($\pi_{UR+} = 0.1\pi_{UR}$) and 30% ($\pi_{UR-} = 1.3\pi_{UR}$), respectively.

In the dynamic model shown in Figure 7.3, the equivalent system inertia, *M*, is assume to be 8 s on a 1500 MVA base. The ramp rates for coal, gas, and wind are assumed to be 0.8%, 5%, and 50% (based on the installed capacity) per minute, respectively. The frequency-based load shedding and wind curtailment schemes are shown in Table 7.2.

Table 7.2 Load shedding and wind curtailment schemes.

Δf (Hz)	Load Shedding (MW)	Δf (Hz)	Wind Curtailment (MW)
-0.7	60	0.7	60
-0.9	150	0.9	150
-1.1	250	1.1	250
-1.3	350	1.3	350
-1.5	450	1.5	450
-1.7	550	1.7	550
-1.9	650	1.9	650
-2.1	750	2.1	750

7.5.2 Scheduling and Real-time Operation Results

Three different wind power market schemes are compared: *Scheme 1* - using conservative wind forecasts (80% probability of exceedance) in only the energy market; *Scheme 2* - allowing wind plants to place optimal bids in only the energy market; and *Scheme 3*: allowing wind plants to place optimal bids in the combined energy-and-reserve market. The wind data shown in Figure 7.4 are used to perform the comparison. The day-ahead scheduling model is first run for a few days prior to the studied day to allow the price forecasts to converge.

Figure 7.5 shows the total day-ahead wind commitments under different wind market schemes. When *Schemes 1* and *2* are used, wind plants only participate in the energy market, resulting in no UR_c over the scheduling horizon. With *Scheme 1*, the wind plant energy bids are conservative and much lower than the forecasts. With *Scheme 2*, the wind plant energy

bids are higher and close to the day-ahead forecasts. When *Scheme 3* is used, the energy bids are somewhere between *Schemes 1* and *2*, and some wind power is committed as UR.

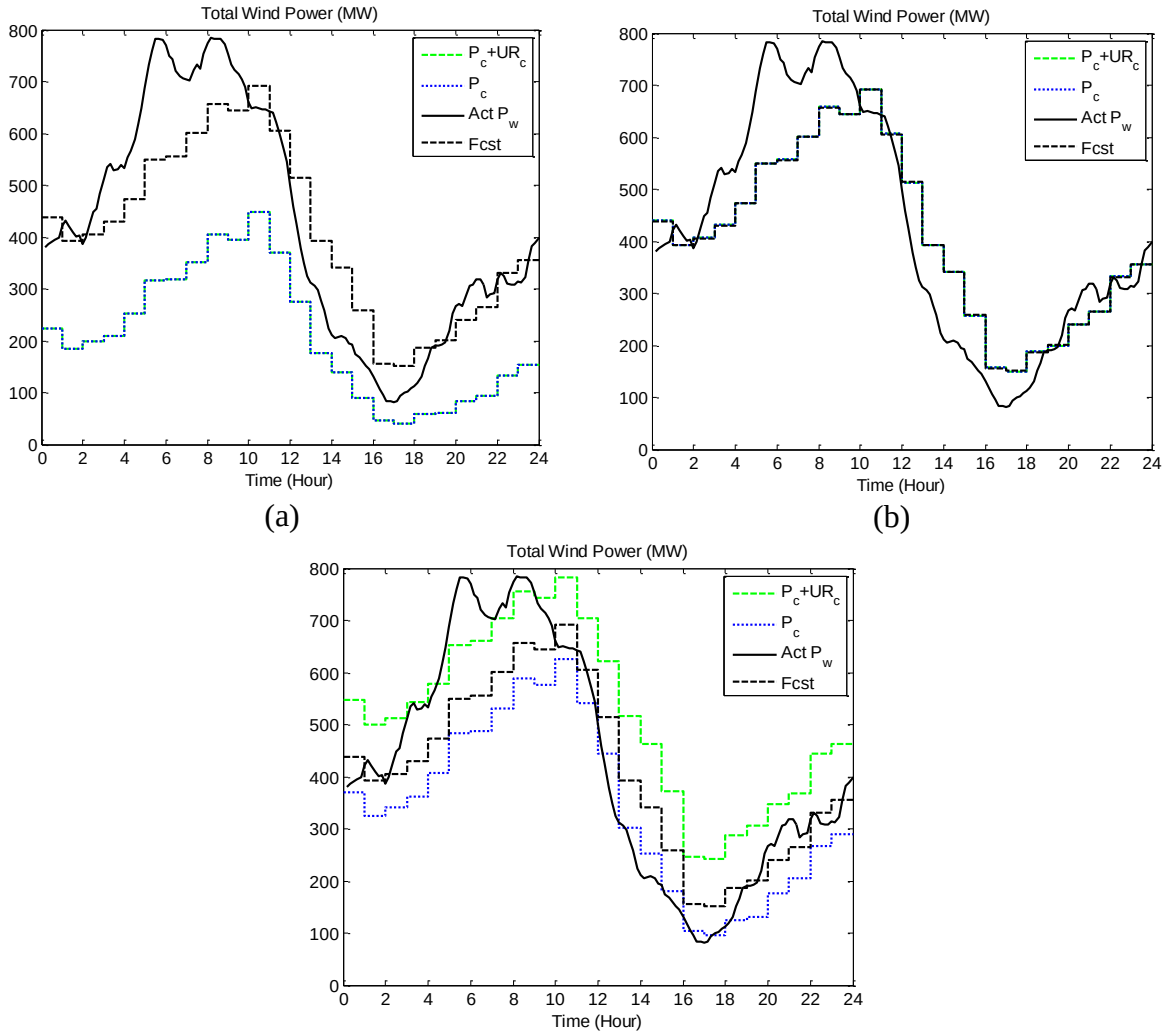

Figure 7.5 Total wind commitments under different day-ahead wind market schemes: (a) *Scheme 1*, (b) *Scheme 2*, and (c) *Scheme 3*.

The scheduling results for *Schemes 1* to *3* are shown in Figure 7.6 (a), Figure 7.7 (a), and Figure 7.8 (a), respectively. *Scheme 1* requires more energy to be scheduled from the conventional units than the other two schemes. *Scheme 3* allows wind plant to commit UR and results in less UR scheduled from conventional units (wind UR is accepted with a discount factor of 0.2).

When the actual available wind power is considered, all wind plants are assumed to operate optimally to maximize their revenues during real-time operation. All available wind energy will be generated in *Schemes 1* and *2*, as shown in Figure 7.6 (b) and Figure 7.7 (b). There is no supply deficit in *Scheme 1*, but any excessive wind power will need to be curtailed after all DR has been exhausted. *Scheme 2* uses more wind energy, but has some supply deficit. Some of the loads will need to be shed after all UR has been exhausted. When *Scheme 3* is used, some of the wind power appears as varying UR [see Figure 7.8 (b)]. Deviation of wind energy from the day-ahead schedules is reduced. Less supply deficit is observed. To better understand and illustrate the effects of *Scheme 3*, the system dynamic model is then simulated.

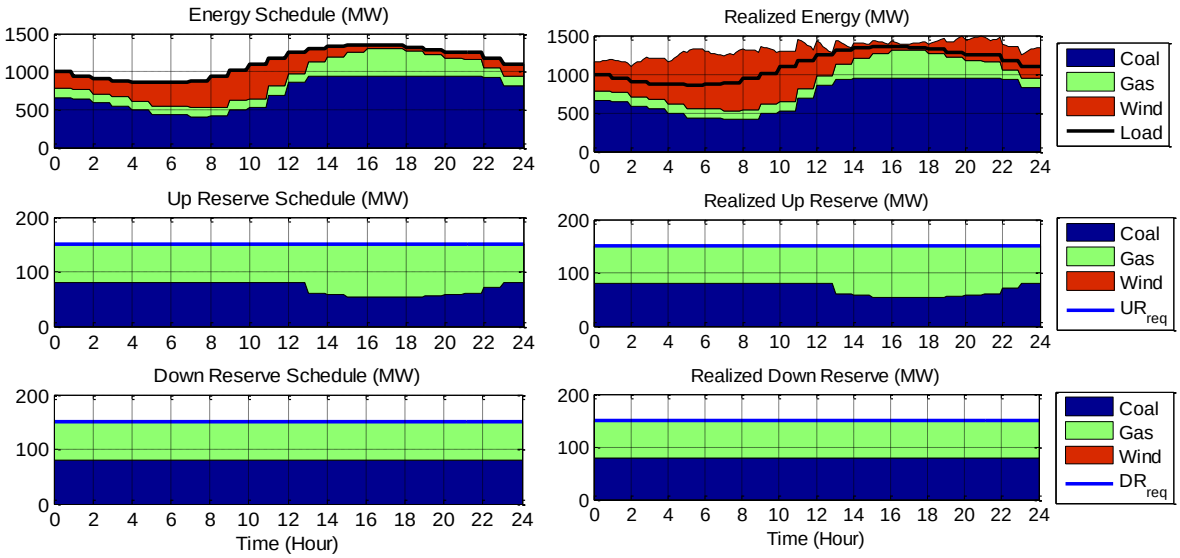

(a) (b)

Figure 7.6 Energy, UR and DR under wind market *Scheme 1*: (a) day-ahead schedules based on wind forecasts, and (b) realized quantities based on actual wind.

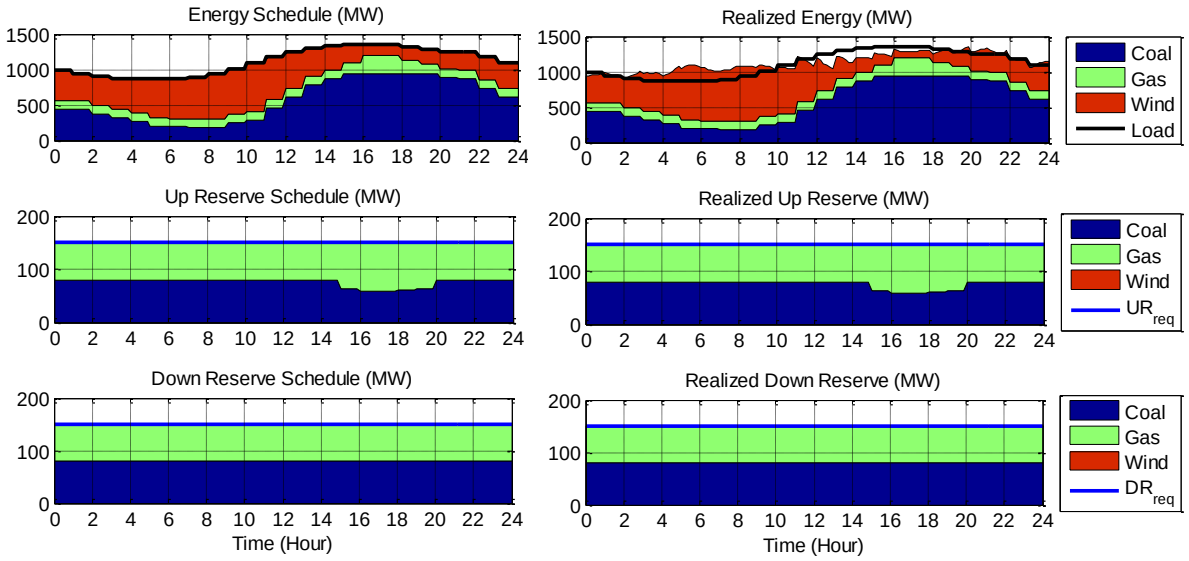

Figure 7.7 Energy, UR and DR under wind market *Scheme 2*: (a) day-ahead schedules based on wind forecasts, and (b) realized quantities based on actual wind.

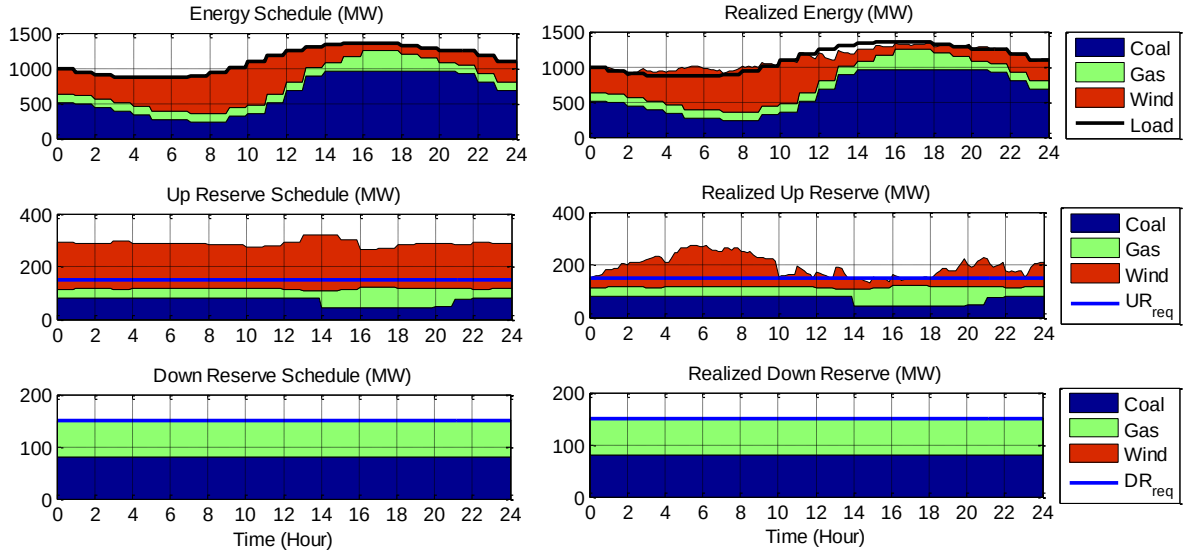

Figure 7.8 Energy, UR and DR under wind market *Scheme 3*: (a) day-ahead schedules based on wind forecasts, and (b) realized quantities based on actual wind.

The frequency deviation and reserve usage under the three wind market schemes are shown in Figure 7.9 to Figure 7.11. Note that since the UR dispatch ratios are set to be proportional the ramp rates, when UR is called, most of the UR supply will come from wind. When *Scheme 1* is used, the system frequency deviation stays above zero most of the time,

and the scheduled DR is not enough to absorb all excessive wind power. As a result, any unabsorbed wind power is curtailed, as shown in Figure 7.9. When *Scheme 2* is used, wind plants become less reliable. During the hours with wind shortage, some of the loads are shed, as shown in Figure 7.10. *Scheme 3* results in less frequency deviation (because of less wind energy deviation from the day-ahead schedules), and provides a trade-off between the wind energy usage and reliability. Table 7.3 summarizes different performance indices for the three wind market schemes for the studied day. 99.99% of the loads are served in *Scheme 3*, while only 99.92% of the loads are served in *Scheme 2*. The percentage wind energy generated (based on the actual wind power that can be captured) from *Scheme 3* is between the other two schemes. The wind energy penetration in Table 7.3 is calculated as the generated wind energy over the served load. Over 30% wind energy penetration is obtained for the studied day.

Scheme 3 results in the highest average wind revenue of $16.87k/h, since wind plants are allowed to optimally bid into both the energy and reserve markets, and hedge their risks of forecast uncertainties. As expected, *Scheme 1* results in the least wind revenue and highest energy price, since less wind energy is used and wind plants are subject to a lot of

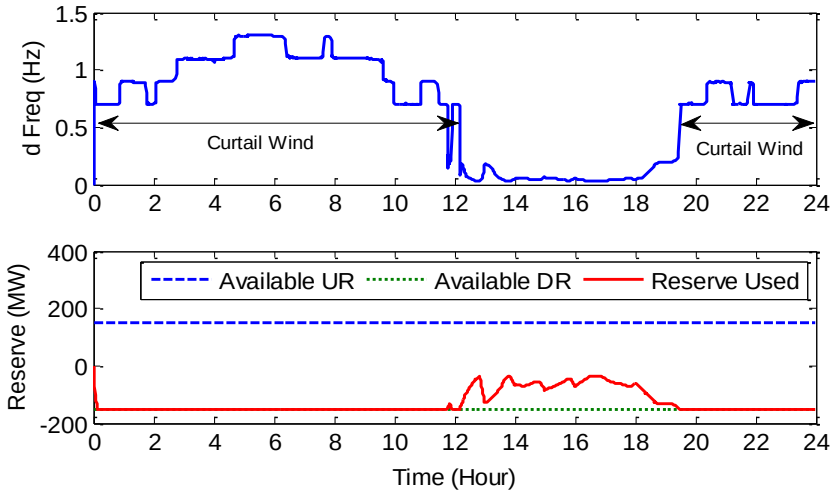

Figure 7.9 Frequency deviation and reserve usage under wind market *Scheme 1*.

deviation penalties. The price of UR is lower in *Scheme 3*, because some of the UR is now supplied by wind, which has low marginal cost.

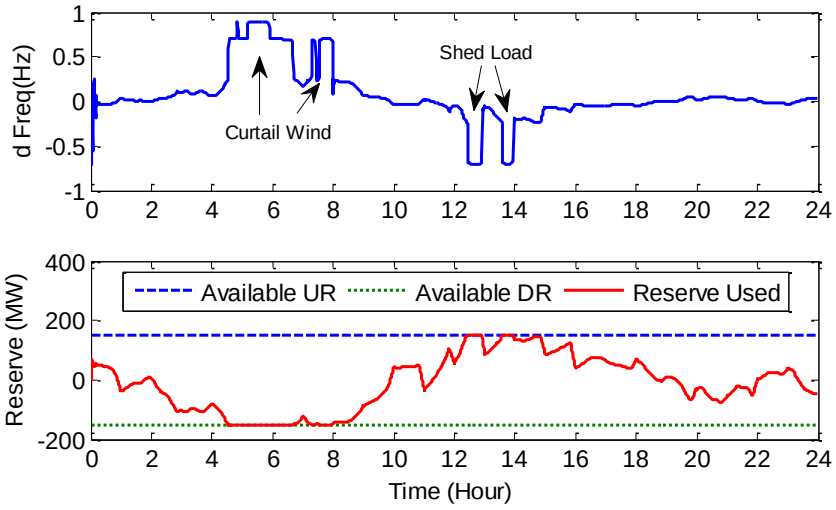

Figure 7.10 Frequency deviation and reserve usage under wind market *Scheme 2*.

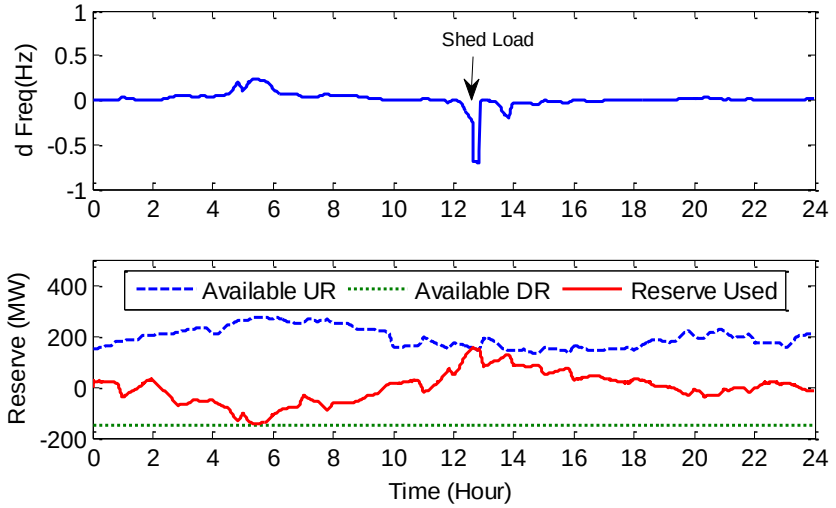

Figure 7.11 Frequency deviation and reserve usage under wind market *Scheme 3*.

Table 7.3 Comparison of different wind market schemes.

Market Scheme	Load Ser.(%)	Wind Energy Gen.(%)	Wind Energy Pen.(%)	Avg. Wind Rev.(k$/h)	Avg. Energy Price($/MWh)	Avg. UR Price ($/MWh)
1	100.00	79.26	30.14	13.55	51.80	37.92
2	99.92	98.93	37.65	16.66	51.37	37.41
3	99.99	84.42	32.11	16.87	51.47	34.61

7.5.3 Benefit of Fast Wind Reserve during Loss of Generation

A unique product from the combined energy-and-reserve wind market is the fast reserve from wind. The benefit of having this fast wind reserve is evaluated by applying a grid contingency, a loss of 75 MW of generation from the coal plant, at the 20th hour. The system frequency and reserve responses are shown in Figure 7.12.

Without the fast wind reserve, simulation results under *Scheme 2* show that some of the loads need to be shed until UR from the coal and gas plants picks up the supply deficit. On the contrary, in Scheme 3, there is about 100 MW of UR available from the wind plants at the 20th hour [see Figure 7.8 (b)]. This fast wind reserve responds to the frequency drop much faster than the reserve from the coal and gas plants. As a result, the frequency drop is corrected right after the contingency and load shedding is not necessary. *Scheme 3* results in high quality fast reserve from wind and improves the system security.

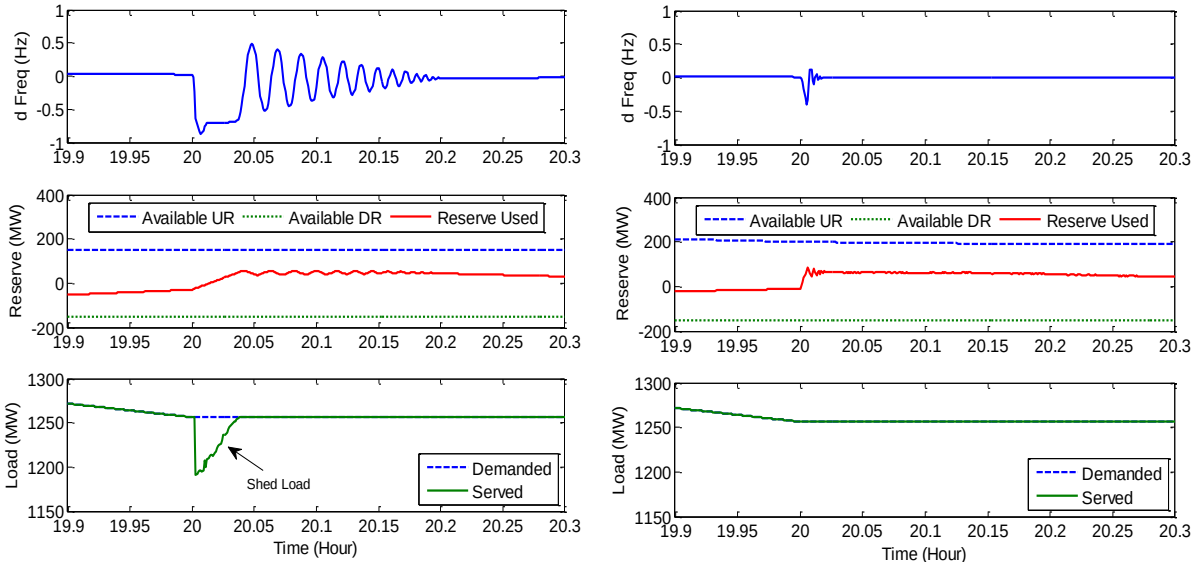

Figure 7.12 System response during sudden loss of 75 MW generation: (a) without fast wind reserve (*Scheme 2*), and (b) with fast wind reserve (*Scheme 3*).

7.5.4 Sensitivity Analysis of Deviation Penalty Factors

As mentioned above, the proposed wind market scheme provides a trade-off between the wind energy usage and reliability. From the discussions in Chapter 6, the market deviation penalties affect the wind plant day-ahead commitments and real-time behavior. Thus, this trade-off that *Scheme 3* provides depends on the market deviation penalties. Define the deviation penalty factors, f_E and f_{UR}, as

$$\begin{aligned} \pi_{E-} &= (1+ f_E)\pi_E \\ \pi_{E+} &= (1- f_E)\pi_E \\ \pi_{UR-} &= (1+ f_{UR})\pi_{UR}. \end{aligned} \tag{7.12}$$

In the previous analysis, f_E = 0.7 and f_{UR} = 0.3. The deviation penalty factor for excessive UR is fixed at 0.9, i.e., $\pi_{UR+} = (1-0.9)\pi_{UR}$. Thus, excessive UR is valued at a very low price.

Table 7.4 lists the percentage load served and wind energy generated for the same day with different values of f_E and f_{UR}. Figure 7.13 (plotted upside down for better illustration) and Figure 7.14 plot these two metrics into two 3D graphs. When f_E is low ($\leq$ 0.3 in Table 7.4), wind power is committed into only the energy market, resulting in a lower percentage of load served, and *Scheme 3* converges to *Scheme 2*. With a higher f_E, different f_{UR} results in a different trade-off between the wind energy usage and reliability. In general, a lower f_{UR} results in more wind being diverted into the reserve market, a higher percentage of load served, but a lower wind energy usage.

An extreme case happens when f_E = 0.9 and f_{UR} = 0.1. Too much wind is committed into the reserve market. The system becomes less secure when wind shortage occurs. This scenario should be avoided when setting the market deviation penalties.

Table 7.4 Deviaiton Penalty Factor Sensitivity.

f_E	f_{UR}	0.1	0.2	0.3	0.4	0.5	0.6	0.7	0.8	0.9
0.1	Load Served (%)	99.92	99.92	99.92	99.92	99.92	99.92	99.92	99.92	99.92
	Wind Generated (%)	98.93	98.93	98.93	98.93	98.93	98.93	98.93	98.93	98.93
0.2	Load Served (%)	99.92	99.92	99.92	99.92	99.92	99.92	99.92	99.92	99.92
	Wind Generated (%)	98.93	98.93	98.93	98.93	98.93	98.93	98.93	98.93	98.93
0.3	Load Served (%)	99.92	99.92	99.92	99.92	99.92	99.92	99.92	99.92	99.92
	Wind Generated (%)	98.93	98.93	98.93	98.93	98.93	98.93	98.93	98.93	98.93
0.4	Load Served (%)	99.92	99.92	99.92	99.92	99.92	99.92	99.92	99.92	99.92
	Wind Generated (%)	97.01	98.92	98.93	98.93	98.93	98.93	98.93	98.93	98.93
0.5	Load Served (%)	99.94	99.95	99.92	99.92	99.92	99.92	99.92	99.92	99.92
	Wind Generated (%)	86.09	93.05	98.54	98.93	98.93	98.93	98.93	98.93	98.93
0.6	Load Served (%)	99.96	99.98	99.98	99.95	99.92	99.92	99.92	99.92	99.92
	Wind Generated (%)	80.57	85.56	91.23	96.69	98.93	98.93	98.93	98.93	98.93
0.7	Load Served (%)	100	99.99	99.99	99.99	99.97	99.92	99.92	99.92	99.92
	Wind Generated (%)	70	79.58	84.42	89.57	94.65	98.93	98.93	98.93	98.93
0.8	Load Served (%)	100	100	100	100	100	99.99	99.94	99.92	99.92
	Wind Generated (%)	70.15	74.97	78.65	83.15	87.94	92.83	97.81	98.93	98.93
0.9	Load Served (%)	99.92	100	100	100	100	100	99.99	99.97	99.92
	Wind Generated (%)	71.92	69.48	73.97	77.68	81.87	86.31	91.02	95.9	98.93

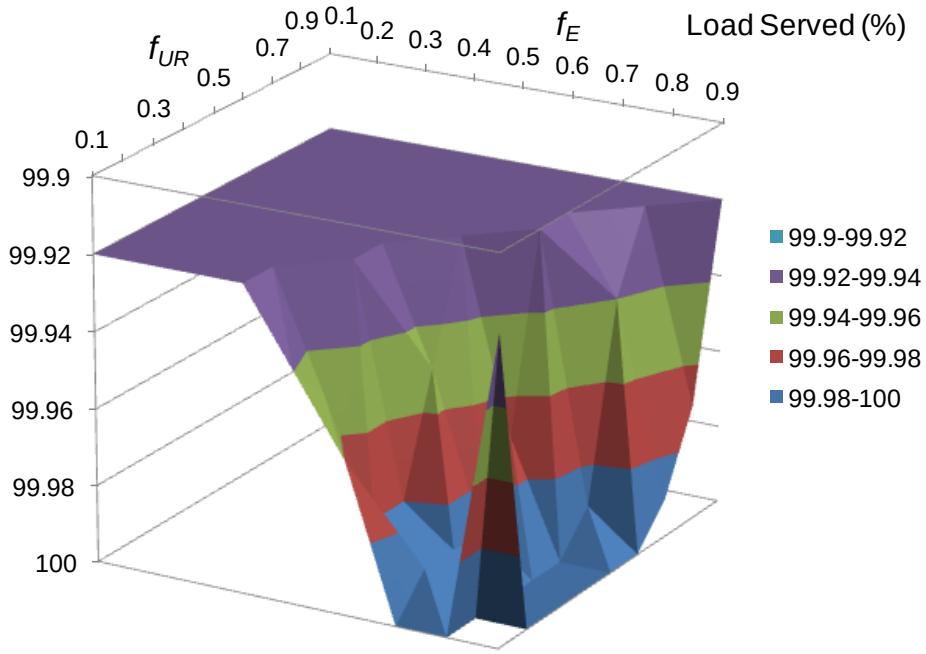

Figure 7.13 Percentage load served for different deviation penalty factors.

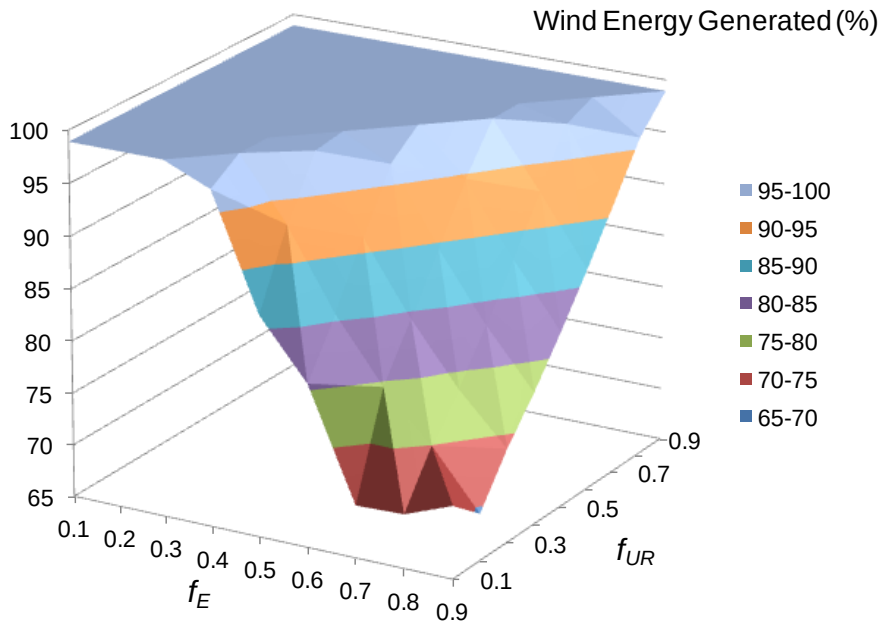

Figure 7.14 Percentage wind generated for different deviation penalty factors.

7.6 Chapter Summary

This chapter investigates the benefits of the combined energy-and-reserve wind market scheme on grid operation and control. The day-ahead unit commitment problem is modeled and solved using mixed-integer quadratic programming. The system dynamic model is simulated with closed-loop frequency control to analyze the system dynamic responses.

The proposed wind market scheme allows wind producers to participate and hedge their forecast uncertainties in the reserve market, which is designed to have a lower penalty for reserve deficits. Less wind production deviation from the day-ahead schedules is observed, resulting in less frequency deviation during real-time operation. The proposed wind market scheme provides a trade-off between the wind energy usage and supply reliability. Changing the market deviation penalties changes the wind plant behavior and thereby this trade-off. The proposed scheme provides the grid a mean to adjust the impacts of wind power

according to the grid conditions. In addition, the resulting reserve product from wind has a high ramping rate and can significantly improve grid security. The proposed wind market scheme is a promising method to incorporate wind energy in a high-wind-penetration scenario.

CHAPTER 8 CONCLUSIONS, CONTRIBUTIONS, AND RECOMMENDATIONS FOR FUTURE WORK

8.1 Conclusions

Achieving a high penetration level of sustainable renewable energy, most of which unfortunately has high uncertainty and variability, is a challenge that has to be conquered. The power systems that have been developed for the past century heavily rely on firm generation resources, well predictable loads, deterministic operation methods, and linear local/suboptimal control. Large-scale integration of wind energy for sustainability requires innovations from many different areas of power engineering. The proposed research focuses on three aspects of wind power integration: improving the interconnection robustness of double-fed induction generator (DFIG) based wind turbine systems, improving the real-time dynamic active and reactive power flow control capability of power systems, and better handling the wind power forecast uncertainty at the market operation level.

DFIG-based wind turbines are low cost due to their fractionally rated power electronic converters, but they are sensitive to grid faults. The proposed feed-forward transient compensation control scheme introduces compensations for the transient impacts of grid faults on the DFIG rotor circuit. The impacts from both balanced and unbalanced grid faults are considered. This control scheme improves the transient current control capability of DFIGs, and reduces the electrical stress on the power electronic converters. Torque ripples are also reduced by the proposed feed-forward transient compensation control during unbalanced grid conditions. Gearbox mechanical stress is thus reduced. Theoretical analysis, simulation studies, and experimental results under different operating conditions with different grid faults are presented. The feed-forward transient compensation control scheme

can reduce DFIG operation and control interruptions caused by grid faults, and improve the low-voltage ride-through capability and reliability of DFIG wind turbines.

Enhancing the equipment robustness and reliability provides more reliable wind power generation, but issues arising from wind variability and uncertainty still need to be solved. The dynamic stochastic optimal power flow (DSOPF) control scheme is proposed to handle fast unexpected wind power variation by coordinating multiple resources across the power system. The DSOPF control is implemented using a nonlinear optimal neurocontrol theory called adaptive critic designs. A small 12-bus test system is first used to demonstrate the DSOPF control concept. Design procedures are presented in detail. The DSOPF controller shows promising steady-state and dynamic performance at different operating conditions. To further evaluate the feasibility of implementing the DSOPF control for a large system, the dynamic model of a 70-bus test system is developed and used to demonstrate the design and performance of a two-level DSOPF control scheme. The DSOPF control scheme opens up opportunities to optimally control real-time active and reactive power flow with multiple control objectives, and optimally absorb the impacts of short-time fast wind power variation.

A combined energy-and-reserve wind market scheme is proposed to better handle the day-ahead wind forecast uncertainty. The additional reserve market is designed with a lower deficit penalty and allows wind producers to manage their risks of revenue loss caused by forecasting errors. Compared to participations in only the energy market, numerical studies show that wind producers can increase their profits by optimally committing into both the energy and reserve markets. As a result, the additional wind reserve market absorbs part of the wind power uncertainty and variability, resulting in less actual production deviation from the day-ahead schedules. Dynamic simulations show that frequency deviation caused by wind variability is reduced during real-time operation. In a scenario with high wind power

penetration, the proposed wind market scheme can provide a trade-off between the wind energy usage and supply reliability. In addition, the wind reserve products created from the proposed market scheme can quickly respond to system frequency deviation and significantly improve system security.

A lot more still need to be done to achieve a high penetration of wind power and energy sustainability. The methods and discussions presented in this dissertation provide some insights into solving the challenge of large-scale renewable integration.

8.2 Contributions

The contributions from this dissertation research are summarized as follows:

- A feed-forward transient compensation control algorithm is designed to enhance the low-voltage ride-though capability of DFIG wind turbines during both balanced and unbalanced grid faults. Theoretical analysis on the design steps and ride-though capability of the proposed control algorithm is provided. Simulation and experimental studies are carried out to verify the effectiveness of the proposed control algorithm.
- An experimental DFIG system is developed with a three-phase voltage sag generation circuit. Experimental measurements on DFIG fault dynamics under different operating conditions, different grid fault types, and different control schemes are presented.
- A dynamic model of a 70-bus power system with two wind plants is developed from existing steady-state data. The model can be used to develop and compare control algorithms for damping inter-area oscillation and dynamic power flow control.
- The feasibility of using recurrent neural networks to implement adaptive critic design based neurocontrol is analyzed. Detailed training steps and derivations for gradients are presented.

- The dynamic stochastic optimal power flow (DSOPF) control concept is elaborated and its feasibility is studied in a small 12-bus test power system. The control of dynamic power flow is achieved using an optimal recurrent neurocontoller based on Adaptive Critic Designs. Control performances under different operating points and large disturbances are presented.
- The scalability of the intelligent DSOPF controller is investigated in a 70-bus test power system. A two-level DSOPF control architecture is proposed and its performance for absorbing short-term fast wind variation is demonstrated.
- A combined energy-and-reserve wind power market is proposed to better integrate individual wind plants into power system daily scheduling and dispatching operations. Fast variable wind reserve product is created to absorb part of the wind production variation. Wind producers can make more profits by optimally participating into the combined market.
- The benefits of the combined energy-and-reserve wind power market on grid operation are investigated in a single-bus test system. Different wind market schemes are compared using mixed integer programming and dynamic simulations. The combined wind market scheme can reduce system frequency deviation caused by wind variation, reduce balancing reserve requirements, and improve system security.

Three journal papers and eight conference papers have been published from the proposed dissertation research:

- Jiaqi Liang, Ganesh K. Venayagamoorthy and Ronald G. Harley,"Wide-Area measurement based Dynamic Stochastic Optimal Power Flow Control for Smart Grids with High Variability and Uncertainty," *IEEE Trans. Smart Grid*, vol. 3, no. 1, pp. 59-

69, Mar. 2012.

- Jiaqi Liang, Santiago Grijalva, and Ronald G. Harley, "Increased wind revenue and system security by trading wind power in energy and regulation reserve markets," *IEEE Trans. Sustainable Energy*, vol. 2, no. 3, pp. 340-347, July 2011.
- Jiaqi Liang, Wei Qiao, and Ronald G. Harley, "Feed-forward transient current control for low-voltage ride-through enhancement of DFIG wind turbines," *IEEE Trans. Energy Conversion*, vol. 25, no. 3, pp. 836-843, Sept. 2010.
- Jiaqi Liang and Ronald G. Harley, "Feed-forward transient compensation control for DFIG wind generators during both balanced and unbalanced grid disturbances," in *Proc. 2011 IEEE Energy Conversion Congress and Exposition (ECCE)*, Phoenix, AZ, USA, Sept. 17-22, 2011.
- Wei Qiao, Jiaqi Liang, Ganesh K. Venayagamoorthy, Ronald G. Harley, "Computational intelligence for control of wind turbine generators," in *Proc. 2011 IEEE PES General Meeting*, Detroit, MI, July 24-29, 2011.
- Jiaqi Liang, Ronald G. Harley, and Ganesh K. Venayagamoorthy, "Adaptive critic design based dynamic optimal power flow controller for a smart grid," in *Proc. 2011 IEEE Symposium Series on Computational Intelligence – Computation Intelligence Applications in Smart Grid (CIASG)*, Paris, France, Apr. 11-15, 2011.
- Diogenes Molina, Jiaqi Liang, Ronald G. Harley, and Ganesh K. Venayagamoorthy, "Comparison of TDNN and RNN performances for neuro-identification on small to medium-sized power systems," in *Proc. 2011 IEEE Symposium Series on Computational Intelligence –CIASG*, Paris, France, Apr. 11-15, 2011.
- Jiaqi Liang, Wei Qiao, and Ronald G. Harley, "Feed-forward transient current control for low-voltage ride-through enhancement of DFIG wind turbines," in *Proc. 2011 IEEE*

Power Systems Conference & Exposition (PSCE), Phoenix, AZ, Mar. 20-23, 2011.

- Jiaqi Liang and Ronald G. Harley, "Pumped storage hydro-plant models for system transient and long-term dynamic studies," in *Proc. 2010 IEEE PES general meeting*, Minneapolis, MN, USA, July 25-29, 2010.
- Jiaqi Liang, Jing Dai, Ganesh K. Venayagamoorthy and Ronald G. Harley, "Dynamic system eigenvalue extraction using linear echo state network for small-signal stability analysis - a novel application," in *Proc. 2010 International Joint Conference on Neural Networks (IJCNN)*, Barcelona, Spain, July 18-23, 2010.
- Jiaqi Liang, Wei Qiao, and Ronald G. Harley, "Direct transient control of wind turbine driven DFIG for low voltage ride-through," in *Proc. 2009 IEEE Symposium on Power Electronics and Machines in Wind Applications (PEMWA)*, Lincoln, NE, USA, June 24-26, 2009.

8.3 Recommendations for Future Work

The following investigations are recommended for continuing research based on the results presented in this dissertation work.

8.3.1 Small-Signal Analysis of DFIG Systems

The full nonlinear model of the DFIG system has been derived and presented. Experimental results show that there is an under-damped oscillating mode for the lab machine at super-synchronous operation with the traditional current control method. This under-damped oscillating mode becomes well-damped at sub-synchronous operation or when the feed-forward transient compensation control is used. It would be interesting to derive the linear models of a DFIG system at different operating conditions and with different control methods. Small-signal analysis should be able to identify this oscillation

mode and show a clear effect of the feed-forward transient compensation control on the system eigenvalues.

8.3.2 Redesign of the DSOPF Control based on Actual Wide-Area Monitoring Systems (WAMSs)

The DSOPF control scheme presented in Chapters 4 and 5 neglects the WAMS and simply assumes the availability of various synchronized measurements. It would be interesting to consider the signal availability, random communication delays, and other limitations of an actual WAMS. There is also critical information that may be available from an actual WAMS but is not yet included in the presented DSOPF control design, such as generator rotor angles and voltage phasor angles. A new DSOPF control objective can be formulated to include such information as a system stability index.

8.3.3 Coordination of FACTS or Power-Electronics-Augmented Devices for Dynamic Power Flow Control

FACTS (or power-electronics-augmented) devices can be added to the system model for better control of dynamic power flow. A FACTS device has a much faster response than traditional generator units, and can provide direct control to the power flow of a particular line. While generator units are controlled to ensure power balance, better dynamic power flow control is expected with additional FACTS devices. With coordination from a DSOPF controller, a few FACTS devices in a large power network may provide sufficient control capability to reroute variable wind power injections. The wind power transfer capability of the power network would thus be increased.

8.3.4 Adding an Adjustment Market for Wind Market Investigations

The discussions presented in Chapters 6 and 7 neglect the effects of adjustment markets. In most existing electricity markets nowadays, hour-ahead or intra-hour adjustment markets

have been implemented to adjust the day-ahead energy (but not reserve) schedules. Although the MW volume is smaller in an adjustment market, it can adjust the energy schedules based on more accurate wind forecasts. Wind plants can be allowed to adjust their commitments in the adjustment market. An additional reserve adjustment market may be added, since day-ahead wind reserve is subject to uncertainty. With the adjustment market, the electricity market dynamics can be more accurately modeled, and the benefits of the combined energy-and-reserve wind market scheme can be better evaluated.

8.3.5 Investigations of the Combined Energy-and-Reserve Wind Market with Power Network Constraints

The combined energy-and-reserve wind market may be further investigated in a small and then a large power system with network constraints. Line congestions and locational pricing can then be included. The presented combined wind market design focuses mostly on dealing with wind variation and reserve, but has not considered line congestions. Modifications to the wind market rules and new market ideas may be needed to handle wind variation and reserve in the case of line congestions.

APPENDIX A MODELING AND CONTROL OF DFIG-BASED WIND TURBINE SYSTEMS

The reference directions for the various quantities discussed in this Appendix A are shown in Figure A.1.

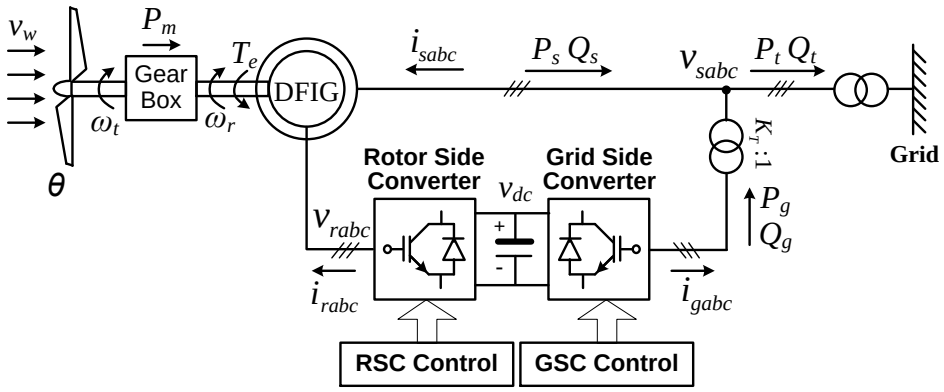

Figure A.1 A DFIG wind turbine and reference directions for various quantities.

A.1 Modeling of Wind Turbines

The wind power captured by a wind turbine is given by [29], [30]

$$P_m = P_{wind} C_P(\lambda,\theta) = \frac{1}{2}\rho A_r v_w^3 C_P(\lambda,\theta), \tag{A.1}$$

where P_{wind} is the input wind power, C_P is the wind turbine efficiency, ρ is the air density, A_r is the area swept by the turbine rotor blades, and v_w is the wind speed. The turbine efficiency depends on the blade pitch angle, θ, and the tip-speed ratio, λ, defined by

$$\lambda = \omega_t R / v_w, \tag{A.2}$$

where R is the blade length and ω_t is the turbine rotating speed. Figure A.2 shows an example C_P-λ-θ curves of a 3.6 MW wind turbine model used in this dissertation. In Figure A.2, C_p is approximated by a polynomial, as in

$$Cp(\theta,\lambda)=\sum_{i=0}^{4}\sum_{j=0}^{4}a_{ij}\theta^{i}\lambda^{j}, \tag{A.3}$$

where the coefficients a_{ij}'s are listed in Table A.1.

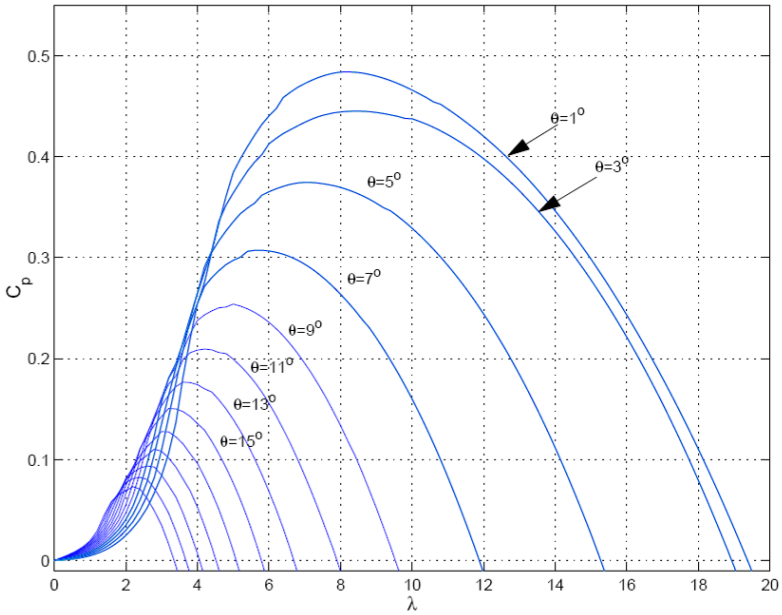

Figure A.2 C_p curves of a 3.6 MW wind turbine model [29].

Table A.1 Coeffiecients of turbine C_p curves [29].

i	j	a_{ij}	i	j	a_{ij}	i	j	a_{ij}
4	4	4.9686E-10	3	0	-8.6018E-04	1	2	-1.3934E-02
4	3	-7.1535E-08	2	4	2.7937E-06	1	1	6.0405E-02
4	2	1.6167E-06	2	3	-1.4855E-04	1	0	-6.7606E-02
4	1	-9.4839E-06	2	2	2.1495E-03	0	4	1.1524E-05
4	0	1.4787E-05	2	1	-1.0996E-02	0	3	-1.3365E-04
3	4	-8.9194E-08	2	0	1.5727E-02	0	2	-1.2406E-02
3	3	5.9924E-06	1	4	-2.3895E-05	0	1	2.1808E-01
3	2	-1.0479E-04	1	3	1.0683E-03	0	0	-4.1909E-01
3	1	5.7051E-04						

For a certain pitch angle, θ, the optimal λ and the maximum C_p are fixed. Thus from (A.1) and (A.2), the maximum turbine output power is proportional to the cube of the wind

speed, and the turbine rotor speed, ω_t, needs to be proportional to the wind speed to achieve this maximum power. Figure A.3 illustrates the turbine output power at a certain pitch angle but at various wind speeds and turbine rotor speeds. When the pitch angle is increased, the same set of power curves will drop in magnitude.

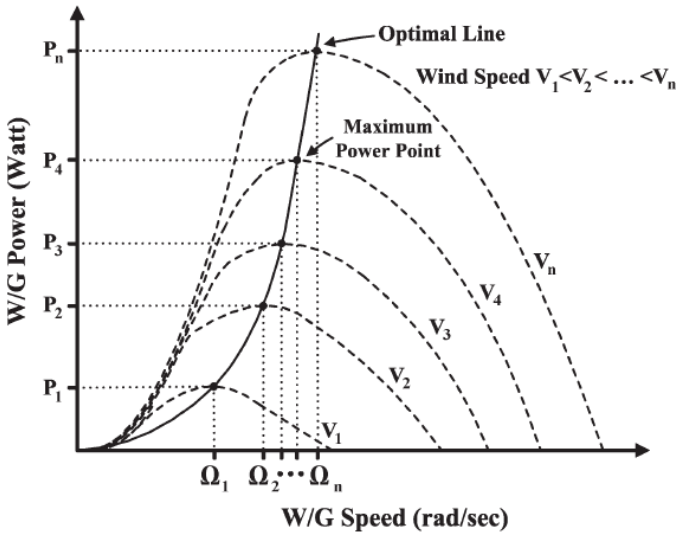

Figure A.3 Wind turbine power curves at different wind and turbine speeds [33].

A.2 Control of Wind Turbines

When the wind speed is below the cut-in wind speed, the wind turbine is kept offline. When the wind speed is between the cut-in and rated wind speeds, the wind turbine operates in the maximum power point tracking (MPPT) region, when the wind speed is between the rated and cut-out wind speeds, the turbine operates in the maximum turbine capacity region. When the turbine is connected to a DFIG, the rotor speed needs to be maintained between 0.7 to 1.3 pu.

A.2.1 Control in MPPT and Maximum Turbine Capacity Regions

When the turbine operates in the MPPT region, the pitch angle is typically fixed at the optimal position (1° for the turbine model shown in Figure A.2). The MPPT control used in

this dissertation takes the turbine rotor speed as input, and commands the total electrical output power to follow the optimal power line shown in Figure A.3. The block diagram of this MPPT control is shown in Figure A.4. At the output of the MPPT control, an under-speed protection control branch is used to prevent the turbine speed to drop below 0.7 pu.

In the maximum turbine capacity region, the MPPT control shown in Figure A.4 continues to operate, but limits the maximum electrical power command to be the turbine capacity. When the wind speed is above the rated wind speed, the input wind power will be greater than the output electrical power. The pitch-angle control now increases the pitch angle (reduces the captured wind power) and maintains the rotor speed at 1.3 pu. The block diagram of the pitch-angle control is shown in Figure A.5. The overall turbine operating curve is shown in Figure A.6.

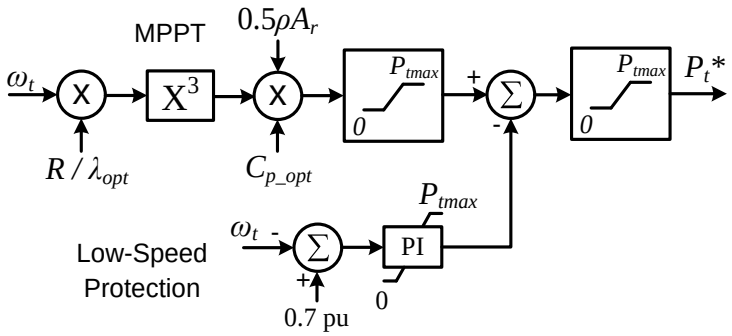

Figure A.4 Wind turbine output power control.

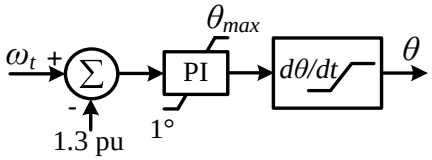

Figure A.5 Wind turbine pitch-angle control.

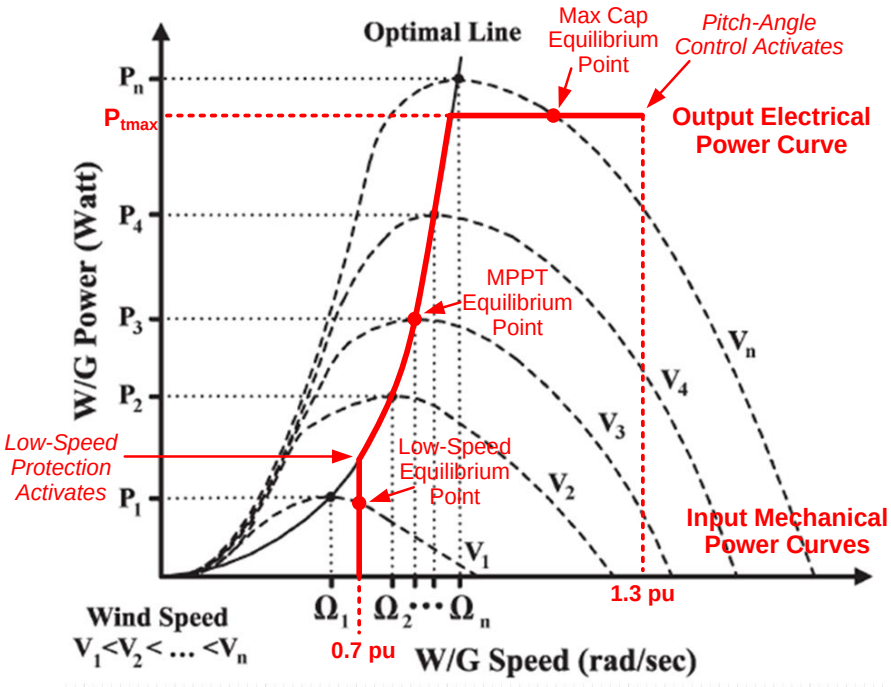

Figure A.6 Overall wind turbine operating curve.

A.2.2 Control for Wind Curtailment

To follow a curtailment command in MW, the output of the turbine power control shown in Figure A.4 is subtracted by the curtailment command. The operating curve shown in Figure A.6 will then be down shifted by the corresponding MW amount.

A.3 Derivations for DFIG Dynamic Model and Rotor-Side Converter Vector Control

The dynamics of a double-fed induction machine can be described by the well known *dq* equations (motor convention) in an arbitrary reference frame [35]:

$$\begin{aligned} v_{ds} &= R_s i_{ds} + p\lambda_{ds} - \omega\lambda_{qs} & \lambda_{ds} &= L_s i_{ds} + L_m i_{dr} \\ v_{qs} &= R_s i_{qs} + p\lambda_{qs} + \omega\lambda_{ds} & \lambda_{qs} &= L_s i_{qs} + L_m i_{qr} \\ v_{dr} &= R_r i_{dr} + p\lambda_{dr} - (\omega - \omega_r)\lambda_{qr} & \lambda_{dr} &= L_m i_{ds} + L_r i_{dr} \\ v_{qr} &= R_r i_{qr} + p\lambda_{qr} + (\omega - \omega_r)\lambda_{dr} & \lambda_{qr} &= L_m i_{qs} + L_r i_{qr} \end{aligned}, \qquad \text{(A.4)}$$

where all symbols have their usual meanings, and ω is the rotating speed of the arbitrary reference frame. Equation (A.4) holds in both steady-state and transient conditions (including

stator-voltage transients during grid faults). Neglecting R_s and substituting the flux equations into the voltage equations yield

$$\begin{bmatrix} v_{ds} \\ v_{qs} \end{bmatrix} = L_s \begin{bmatrix} p & -\omega \\ \omega & p \end{bmatrix} \begin{bmatrix} i_{ds} \\ i_{qs} \end{bmatrix} + L_m \begin{bmatrix} p & -\omega \\ \omega & p \end{bmatrix} \begin{bmatrix} i_{dr} \\ i_{qr} \end{bmatrix}, \tag{A.5}$$

$$\begin{bmatrix} v_{dr} \\ v_{qr} \end{bmatrix} = \begin{bmatrix} R_r + L_r p & -(\omega - \omega_r) L_r \\ (\omega - \omega_r) L_r & R_r + L_r p \end{bmatrix} \begin{bmatrix} i_{dr} \\ i_{qr} \end{bmatrix} + L_m \begin{bmatrix} p & -(\omega - \omega_r) \\ (\omega - \omega_r) & p \end{bmatrix} \begin{bmatrix} i_{ds} \\ i_{qs} \end{bmatrix}. \tag{A.6}$$

To derive the control algorithm from the rotor side, equation (A.5) is used to replace the *dq* stator currents in (A.6). From (A.5),

$$\begin{aligned} L_m \begin{bmatrix} p & -(\omega - \omega_r) \\ (\omega - \omega_r) & p \end{bmatrix} \begin{bmatrix} i_{ds} \\ i_{qs} \end{bmatrix} &= \frac{L_m}{L_s} \begin{bmatrix} v_{ds} \\ v_{qs} \end{bmatrix} + L_m \omega_r \begin{bmatrix} i_{qs} \\ -i_{ds} \end{bmatrix} - \frac{L_m^2}{L_s} \begin{bmatrix} p & -\omega \\ \omega & p \end{bmatrix} \begin{bmatrix} i_{dr} \\ i_{qr} \end{bmatrix} \\ &= \frac{L_m}{L_s} \begin{bmatrix} v_{ds} + \omega_r \lambda_{qs} \\ v_{qs} - \omega_r \lambda_{ds} \end{bmatrix} - \frac{L_m^2}{L_s} \begin{bmatrix} p & -(\omega - \omega_r) \\ (\omega - \omega_r) & p \end{bmatrix} \begin{bmatrix} i_{dr} \\ i_{qr} \end{bmatrix}. \end{aligned} \tag{A.7}$$

Substituting (A.7) into (A.6) yield

$$\begin{bmatrix} v_{dr} \\ v_{qr} \end{bmatrix} = \begin{bmatrix} R_r + L_r' p & -(\omega - \omega_r) L_r' \\ (\omega - \omega_r) L_r' & R_r + L_r' p \end{bmatrix} \cdot \begin{bmatrix} i_{dr} \\ i_{qr} \end{bmatrix} + \frac{L_m}{L_s} \begin{bmatrix} v_{ds} + \omega_r \lambda_{qs} \\ v_{qs} - \omega_r \lambda_{ds} \end{bmatrix}, \tag{A.8}$$

where L_r' is the rotor transient inductance, $L_r' = \sigma L_r$ with $\sigma = 1 - L_m^2 / (L_s L_r)$.

In the synchronous reference frame with the *d* axis aligned to the stator flux, the following equations hold in steady-state balanced stator-voltage conditions:

$$\begin{aligned} &\lambda_{ds}^e = \lambda_s, \lambda_{qs}^e = 0 \\ &v_{ds}^e = 0, v_{qs}^e = v_s = \omega_s \lambda_{ds}^e, \end{aligned} \tag{A.9}$$

where the superscript *e* denotes quantities in the synchronous reference frame, λ_s and v_s are the magnitudes of the stator flux and stator voltage vectors. Equation (A.8) is simplified to

$$\begin{bmatrix} v_{dr}^e \\ v_{qr}^e \end{bmatrix} = \begin{bmatrix} R_r + L_r' p & -s\omega_s L_r' \\ s\omega_s L_r' & R_r + L_r' p \end{bmatrix} \cdot \begin{bmatrix} i_{dr}^e \\ i_{qr}^e \end{bmatrix} + s \frac{L_m}{L_s} \begin{bmatrix} 0 \\ v_{qs}^e \end{bmatrix}. \tag{A.10}$$

where *s* is slip.

The instantaneous electromagnetic torque of a DFIG is given by

$$T_e = \frac{3}{2}\frac{P}{2}\frac{L_m}{L_s}(\lambda_{ds} i_{qr} - \lambda_{qs} i_{dr}) \quad , \tag{A.11}$$

where a positive torque means generating electrical power. Under the synchronous reference frame and steady-state balanced stator-voltage conditions, the torque equation in (A.11) is then simplified into

$$T_e = \frac{3}{2}\frac{P}{2}\frac{L_m}{L_s}\lambda_s i_{qr}^e \quad . \tag{A.12}$$

The instantaneous active and reactive power outputs (generation) from the DFIG stator are given by

$$\begin{aligned} P_s &= -\frac{3}{2}(v_{ds} i_{ds} + v_{qs} i_{qs}) \\ Q_s &= -\frac{3}{2}(v_{qs} i_{ds} - v_{ds} i_{qs}) \end{aligned} \quad . \tag{A.13}$$

Under the synchronous reference frame and steady-state balanced stator-voltage conditions, applying (A.9) to (A.13) yield

$$\begin{aligned} P_s &= -\frac{3}{2} v_{qs}^e i_{qs}^e = \frac{3}{2}\frac{L_m}{L_s} v_s i_{qr}^e \\ Q_s &= -\frac{3}{2} v_{qs}^e i_{ds}^e = \frac{3}{2}\frac{L_m}{L_s} v_s (i_{dr}^e - \frac{v_s}{\omega_s L_m}) \end{aligned} \quad . \tag{A.14}$$

From (A.10), with proper decoupling, $i_{dr}{}^e$ and $i_{qr}{}^e$ can be controlled by changing $v_{dr}{}^e$ and $v_{qr}{}^e$, respectively. From (A.12) and (A.14), the stator active power output or rotor speed (torque) can be controlled by changing $i_{qr}{}^e$, and the stator reactive power output can be controlled by changing $i_{dr}{}^e$.

A.4 Derivations for DFIG Grid-Side Converter Vector Control

The *abc* voltage and current outputs from the grid-side converter (GSC) are given by

$$\begin{aligned} v_{ag} &= R_g i_{ag} + L_g p i_{ag} + v_{as} / K_T \\ v_{bg} &= R_g i_{bg} + L_g p i_{bg} + v_{bs} / K_T \\ v_{cg} &= R_g i_{cg} + L_g p i_{cg} + v_{cs} / K_T \end{aligned}, \tag{A.15}$$

where R_g is the equivalent resistance between the GSC and the grid, L_g is the equivalent inductance between the GSC and the grid, and K_T is the transformer ratio. After the Park Transformation with an arbitrary reference frame, equation (A.15) becomes

$$\begin{bmatrix} v_{dg} \\ v_{qg} \end{bmatrix} = \begin{bmatrix} R_g + L_g p & -\omega L_g \\ \omega L_g & R_g + L_g p \end{bmatrix} \cdot \begin{bmatrix} i_{dg} \\ i_{qg} \end{bmatrix} + \frac{1}{K_T} \begin{bmatrix} v_{ds} \\ v_{qs} \end{bmatrix}, \tag{A.16}$$

Define a new synchronous reference frame, where the *d* axis is aligned to the stator voltage vector. During steady-state balanced stator-voltage conditions,

$$v_{ds}^e = v_s,\ v_{qs}^e = 0, \tag{A.17}$$

Equation (A.16) then becomes

$$\begin{bmatrix} v_{dg}^e \\ v_{qg}^e \end{bmatrix} = \begin{bmatrix} R_g + L_g p & -\omega L_g \\ \omega L_g & R_g + L_g p \end{bmatrix} \cdot \begin{bmatrix} i_{dg}^e \\ i_{qg}^e \end{bmatrix} + \frac{1}{K_T} \begin{bmatrix} v_s \\ 0 \end{bmatrix}, \tag{A.18}$$

The instantaneous active and reactive power outputs from the GSC are given by

$$\begin{aligned} P_g &= \frac{3}{2} \frac{1}{K_T} (v_{ds} i_{dg} + v_{qs} i_{qg}) \\ Q_g &= \frac{3}{2} \frac{1}{K_T} (v_{qs} i_{dg} - v_{ds} i_{qg}) \end{aligned}. \tag{A.19}$$

Under the synchronous reference frame and steady-state balanced stator-voltage conditions, equation (A.19) is simplified to

$$P_g = \frac{3}{2}\frac{v_s}{K_T} i_{dg}^e$$
$$Q_g = -\frac{3}{2}\frac{v_s}{K_T} i_{qg}^e \quad . \tag{A.20}$$

From (A.18), with proper decoupling, i_{dg}^e and i_{qg}^e can be controlled by changing v_{dg}^e and v_{qg}^e, respectively. From (A.20), the GSC active power output can be controlled by changing i_{dg}^e, and the GSC reactive power output can be controlled by changing i_{qg}^e.

A.5 Parameters of the 3.6 MW DFIG Wind Turbine Model Parameters

The parameters of the simulation 3.6 MW DFIG wind turbine system are listed in Table A.2 and Table A.3.

Table A.2 Parameters for the 3.6 MW wind turbine model.

Quantity	Value
P_{rated} (MW)	3.6
V_{wind_rated} (m/s)	14
Inertia (s)	4.29

Table A.3 Parameters for the 4 MVA DFIG model.

Quantity	Value	Quantity	Value
MVA Rating	4	R_s (pu)	0.017
V_{rated} (kV)	4.16	R_r (pu)	0.015
Inertia (s)	0.9	L_m (pu)	4.4
S-to-R Turns Ratio	1	L_{ls} (pu)	0.179
$V_{DC\text{-}Bus}$ (kV)	3	L_{lr} (pu)	0.156

APPENDIX B LABORATORY IMPLEMENTATION OF A VOLTAGE SAG GENERATOR

B.1 Power Stage Schematic of the Three-Phase Voltage Sag Generator

Figure B.1 shows the power stage schematic of the three-phase voltage sag generator. The series triacs are normally on to bypass the current-limiting resistors (12 Ω). To generate a fault, all three series triacs are first turned off, and then the three shunt triacs are turned on. Depending on the connections and the states of the mechanical switches, the shunt resistor networks can have different values for generating different levels of sags. To generate an unbalanced fault, the power circuit connections may be manually changed.

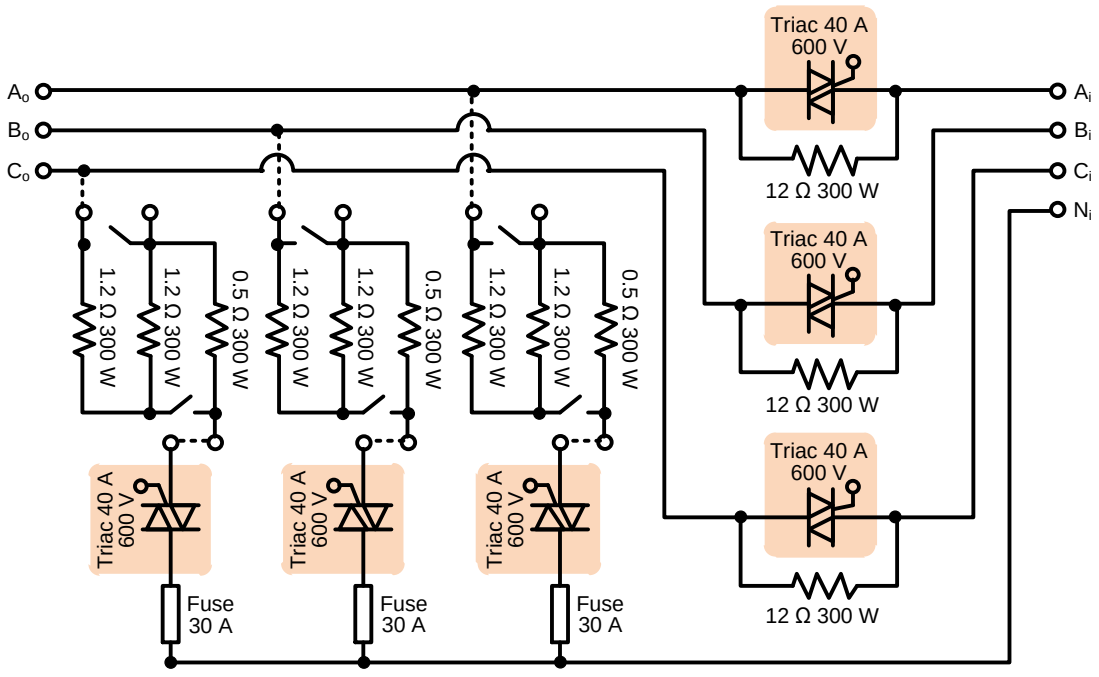

Figure B.1 Power stage of three-phase voltage sag generator.

B.2 MCU and Gate Driver Schematic and PCB

The microcontroller-unit (MCU) and gate-driver PCB, as shown in Figure B.2 was originally designed by Dr. Jose Alex Restrepo for controlling and driving IGBTs. The PCB is then adapted to control and drive the triacs, as shown in Figure B.3. High commutation triacs are used in the power stage. High commutation triacs operate only in quadrants 1, 2, and 3, i.e., when the gate current is positive (into the gate), the triac conducts only in the positive half cycle (current flows from MT2 to MT1). Thus, a diode (see Figure B.3) is used to block positive voltage from the IGBT gate driver. When the IGBT gate driver outputs negative voltage, the triac is turned on (conducting in both directions). 5 kHz negative gating pulses are generated by the MCU to maintain the triac at "on" state. When the IGBT gate driver outputs positive voltage, the triac is turned off (blocking in both directions).

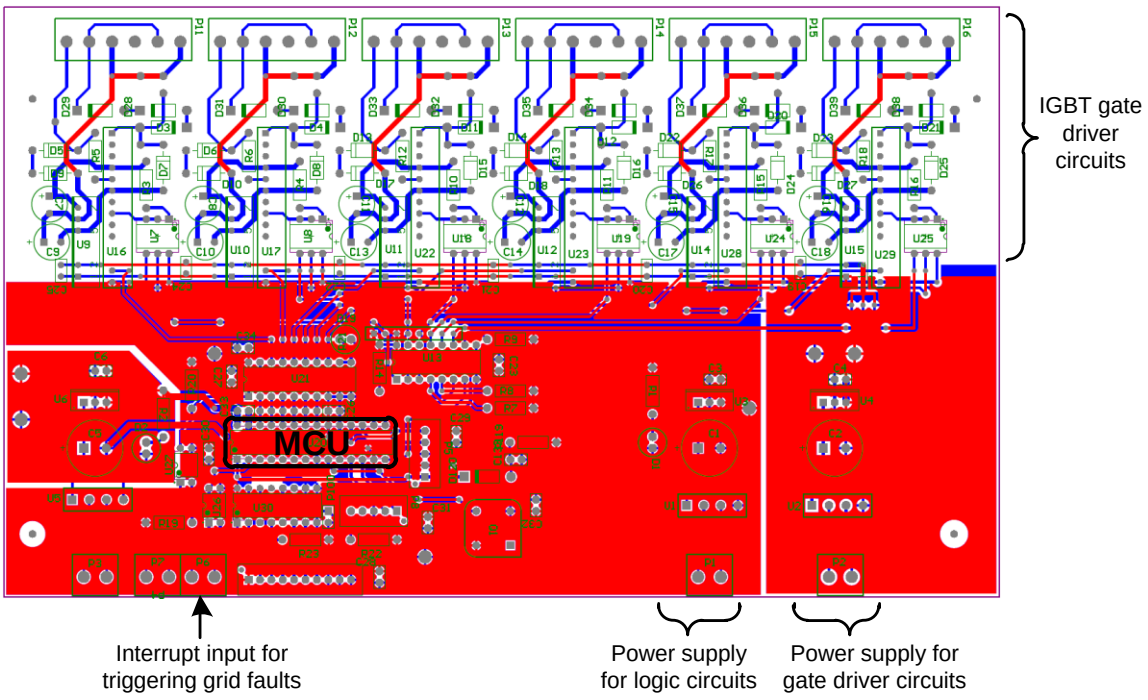

Figure B.2 Layout of MCU and gate-driver PCB for voltage sag generator.

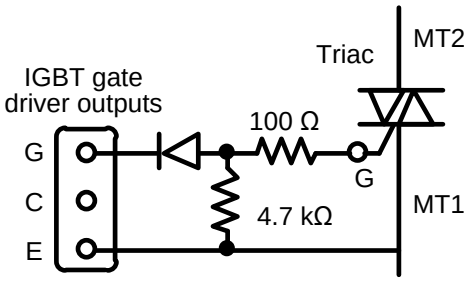

Figure B.3 Modification of IGBT gate driver outputs for driving triacs.

B.3 Flowchart of MCU Codes for Controlling Sag Generator

The Microchip dsPIC30F2010 is used to control the voltage sag generator. Figure B.4 shows the flowchart of the codes used in dsPIC30F2010.

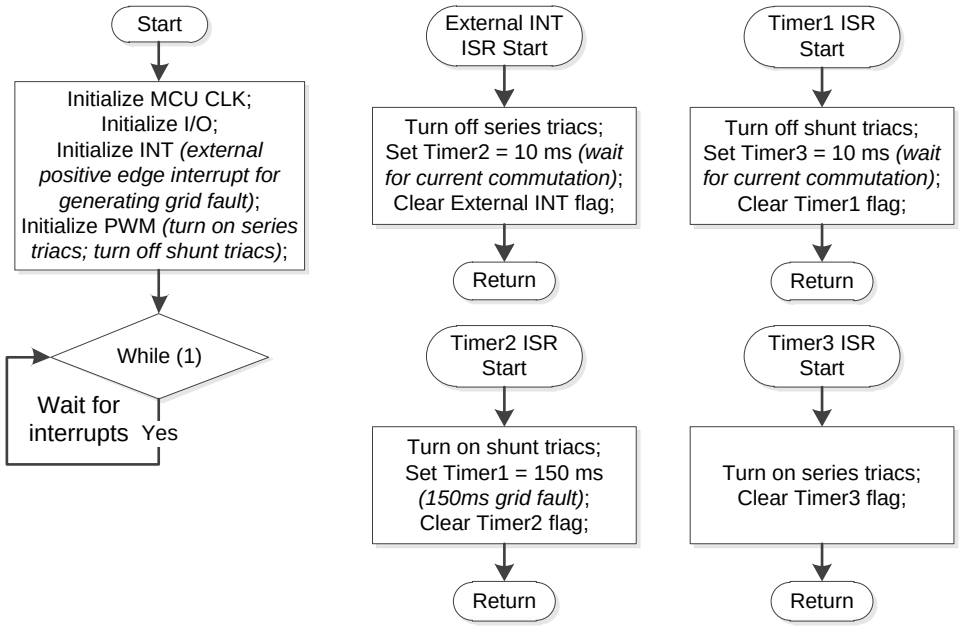

Figure B.4 Flowchart MCU codes for controlling the voltage sag generator.

APPENDIX C LABORATORY IMPLEMENTATION OF A DOUBLY-FED INDUCTION GENERATOR

C.1 Power Electronic Converter Schematic of the 7.5 hp 230 V DFIG

Figure C.1 and Figure C.2 show the detailed schematics of the DFIG power electronic converter hardware. The GSC and DC-bus precharge circuit reside on one heat sink with a cooling fan. The RSC, AC active crowbar, and DC dynamic brake reside on another heat sink also with a cooling fan. The DC bus outlets from the GSC and RSC are connected through wires.

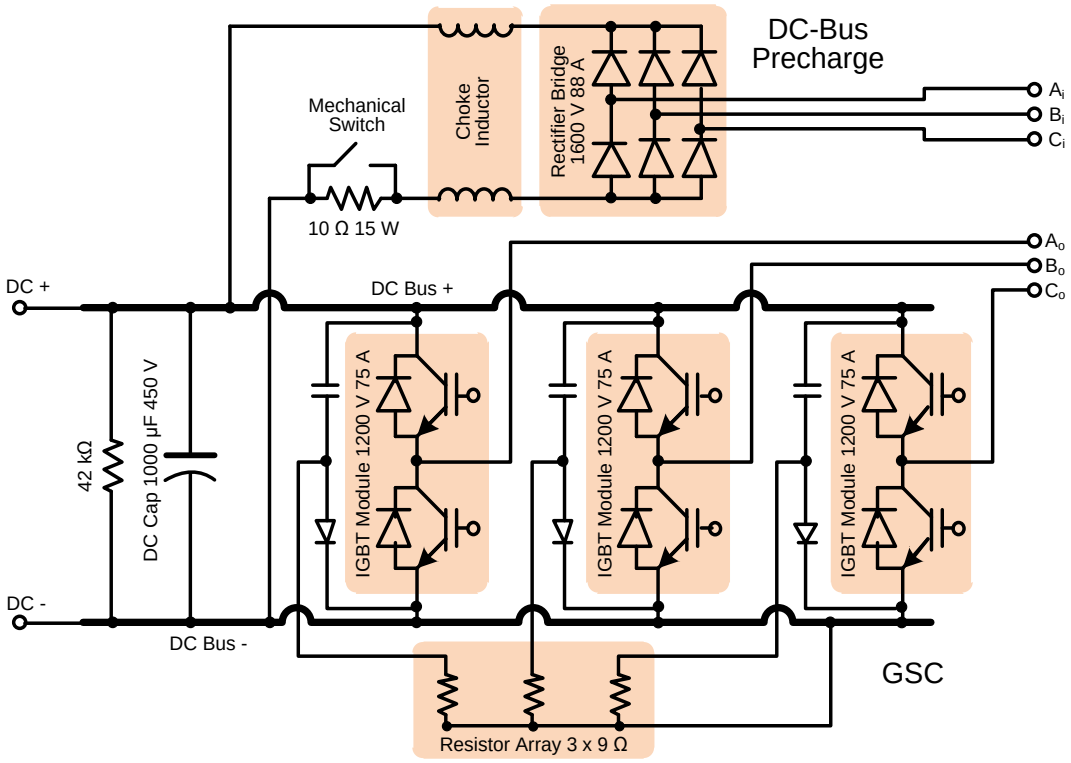

Figure C.1 GSC power stage with DC-bus precharge circuit.

A 10 Ω resistor (see Figure C.1) is used to limit the DC-bus precharge current. The mechanical switch may be used to bypass this precharge resistor when the GSC works as a

regular motor drive without the RSC. The 42 kΩ resistor across the DC bus is used to dissipate DC bus energy when the system is deenergized.

Three small inductors between the RSC AC-side terminals and the AC crowbar terminals (see Figure C.2) are required to limit the RSC *di/dt*. When the DFIG is operated around the synchronous speed, the voltage across the DFIG rotor terminals is close to zero, and so is the voltage across the snubber capacitor of the AC crowbar IGBT. Without the three inductors, current spikes appear when the RSC starts to switch and the DC-bus capacitor discharges into this snubber capacitor though the 2 Ω power resistor.

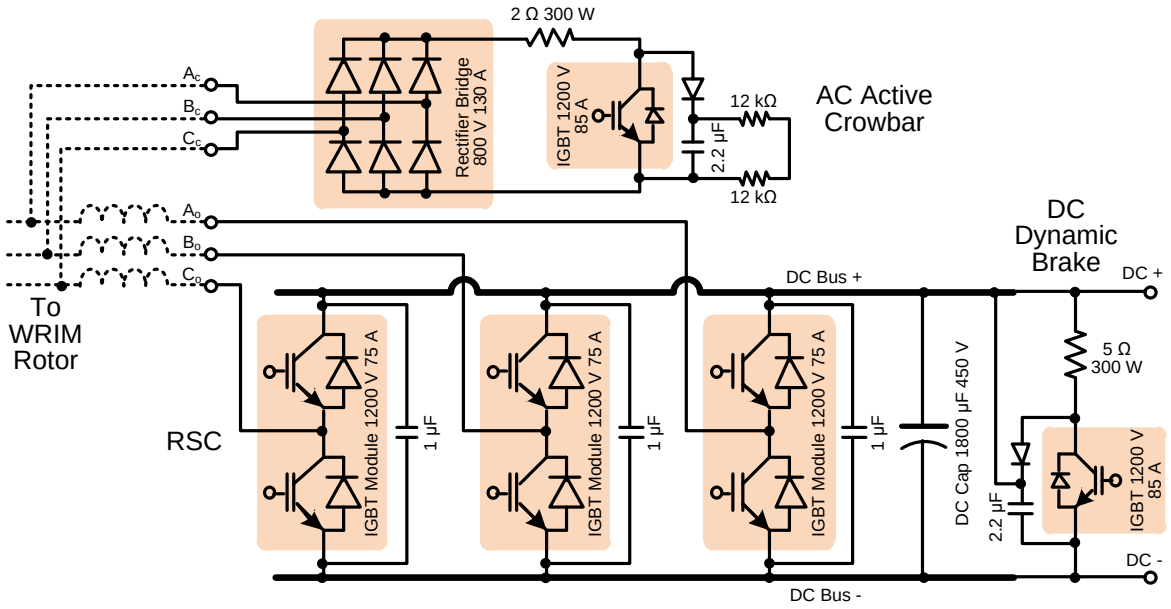

Figure C.2 RSC power stage with AC crowbar and DC dynamic brake.

C.2 Gate-Driver, Sensor, and Controller Schematics and PCBs

The PCBs for the gate-drivers, sensor measurements, and DSP/FPGA controller was originally designed by Dr. Jose Alex Restrepo and Siwei Cheng. Their PCB designs are adapted in this research to control the DFIG GSC and RSC. The overall control architecture is shown in Figure 3.29. The schematic of each PCB is briefly described below.

C.2.1 Gate-Driver PCB Design

The PCB layout for the gate-driver board is shown in Figure C.3, which includes six identical gate-driver circuits. The schematic of one gate-driver circuit is shown in Figure C.4. Each gate-driver circuit has three outputs connecting to the gate, collector, and emitter, respectively, of one IGBT. The TTL control signal input is isolated from the power circuit by the gate-driver chip, M57959L.

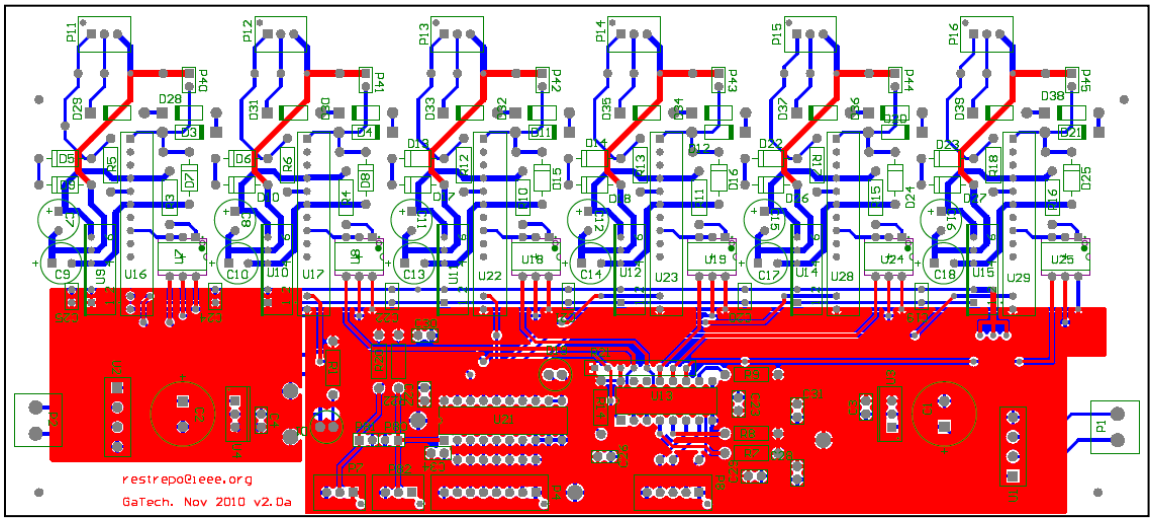

Figure C.3 Gate-driver PCB layout.

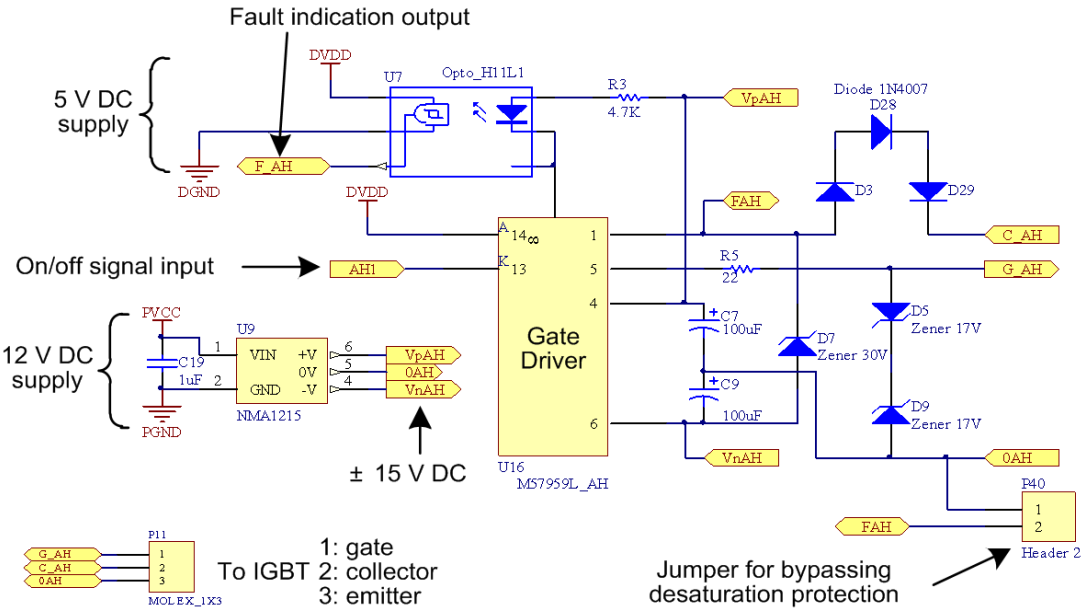

Figure C.4 Schematic of gate-driver circuitry for one IGBT.

A front-end line driver (see Figure C.5) can block all the gate triggering signals from the FPGA to the gate drivers by outputting high impedance. One the triggering signals are blocked, all six IGBTs are turned off. The blocking signal comes from the sensor board when over-current is detected.

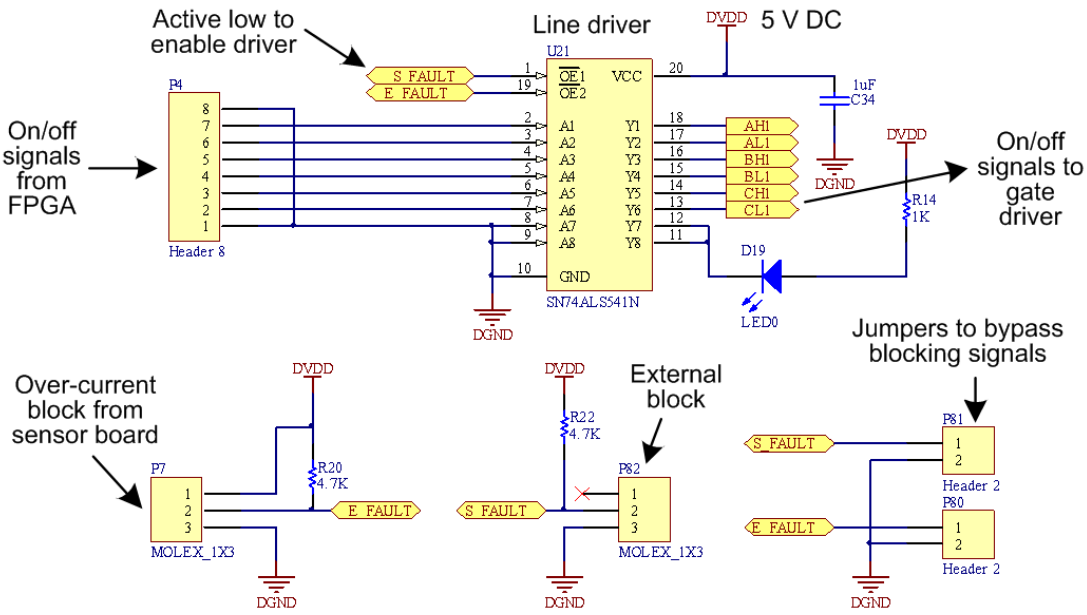

Figure C.5 Schematic of line driver and over-current block.

C.2.2 Sensor Measurement and Signal Conditioning PCB Design

Figure C.6 shows the PCB layout of the sensor board, which includes two current-measurement channels, one voltage-measurement channel, and one extra channel that can be used for either voltage or current measurement. Hall-effect sensors are used for isolation. The signal conditioning circuit includes amplification, level shifting, and 12-bit A/D conversion, as shown in Figure C.7. Two Schottky diodes (D1 and D2 in Figure C.7) are used to protect the analog-to-digital conversion (ADC) chip input pin. A comparator logic circuit, as shown in Figure C.8, is used to detect over-current and generate blocking signals to the gate-driver board.

For the GSC sensor board, two of the three GSC output currents and two of the three stator voltages are measured. For the RSC sensor board, two of the three RSC output currents and the DC-bus voltage are measured.

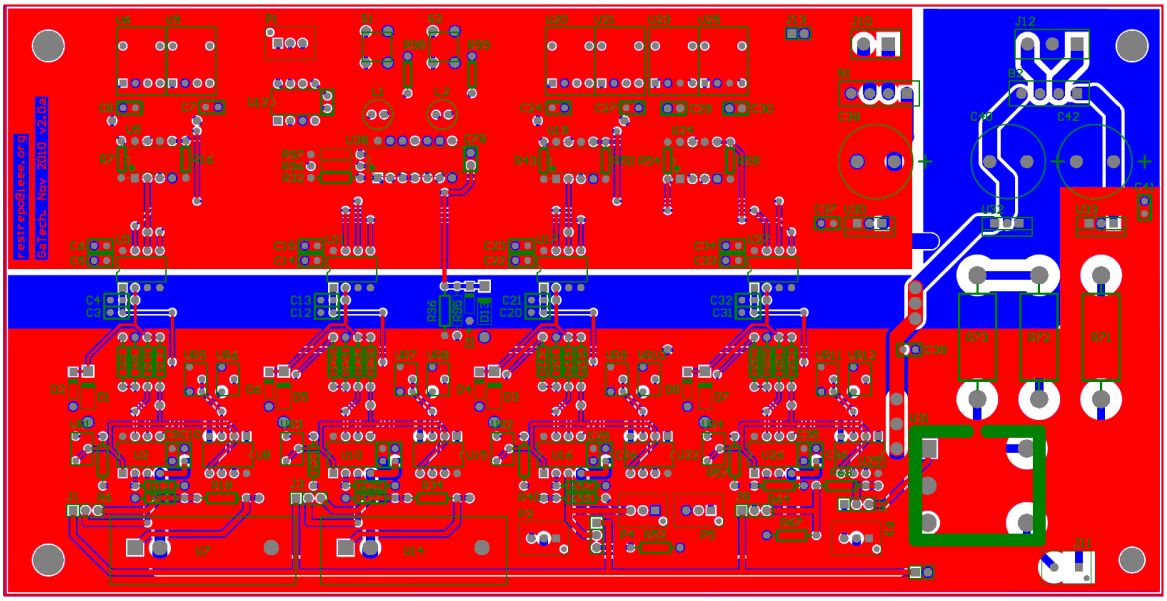

Figure C.6 Sensor measurement PCB layout.

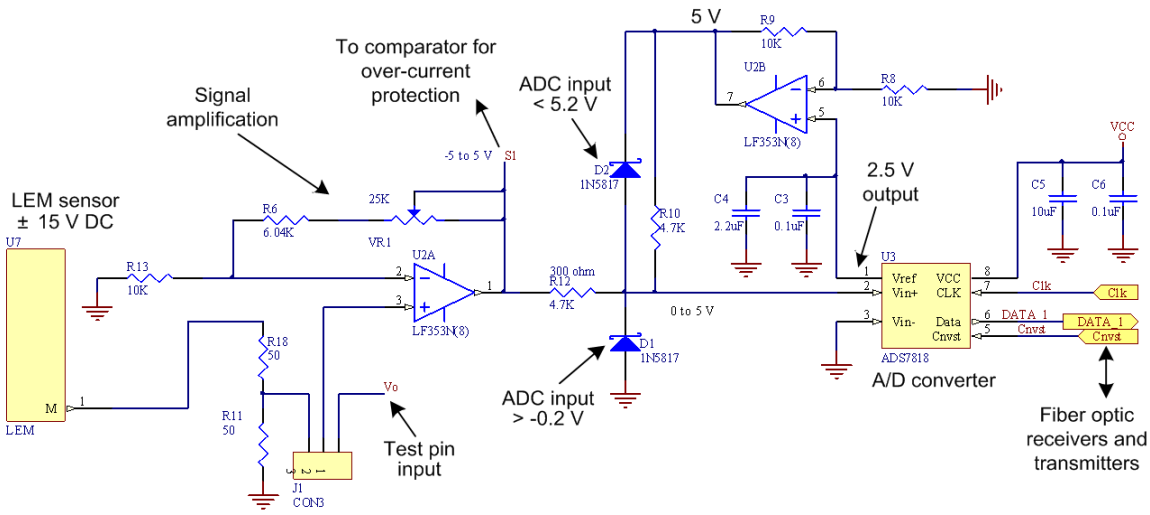

Figure C.7 Schematic of signal conditioning and A/D converter for one sensor channel.

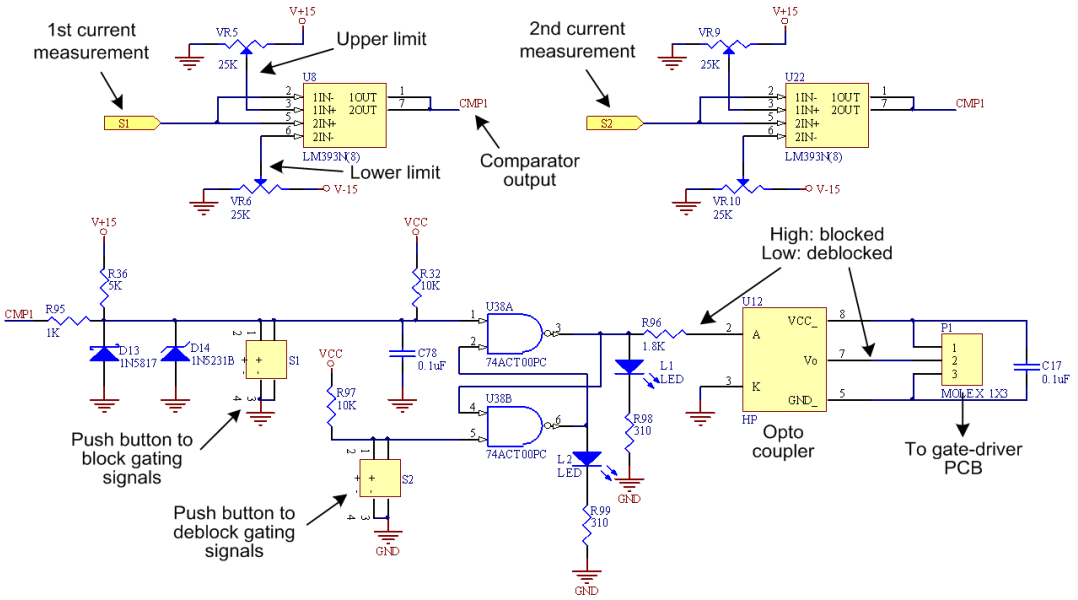

Figure C.8 Schematic of over-current protection logics.

C.2.3 FPGA PCB Design

The PCB layout of the FPGA interfacing board is shown in Figure C.9. It connects to the Analog Device ADSP-21369 EZ-KIT through three 90-pin TFC-145-32-F-D-A

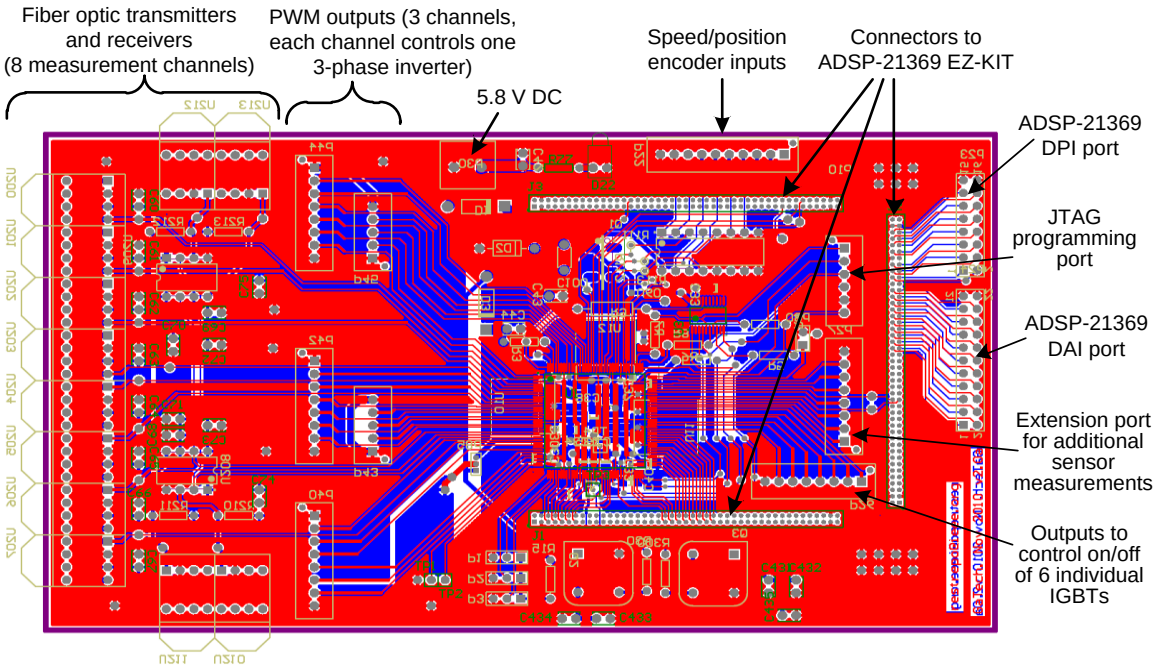

Figure C.9 FPGA PCB layout.

connectors. The FPGA board has eight measurement channels, and three three-phase PWM output channels. Two PWM channels are used to control the GSC and RSC. The AC crowbar and DC dynamic brake IGBTs are controlled using the output port at the bottom right of Figure C.9.

C.3 Flowchart of DSP Codes

The flowchart of the DSP codes for RSC and GSC control is shown in Figure C.10. The additional computation for implementing the proposed feed-forward transient compensation (FFTC) control scheme is highlighted in red.

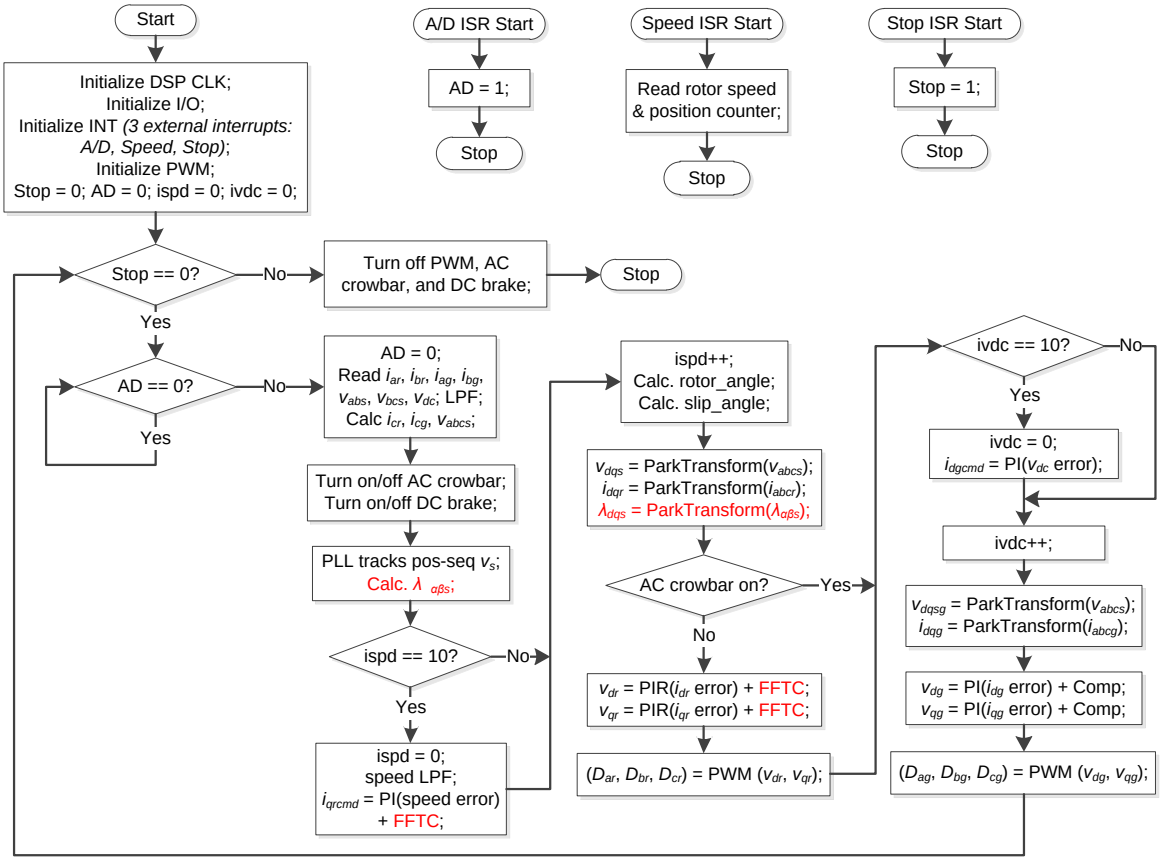

Figure C.10 Flowchart of DSP codes for RSC and GSC control.

C.4 Laboratory DFIG System Parameters

The parameters for the laboratory DFIG system are listed in Table C.1.

Table C.1 Parameters of the laboratory DFIG system.

Component	Name	Value	Name	Value
WRIM	P_{rated} (hp)	7.5	L_m (pu)	1.268
	V_{rated} (V)	230	L_s (pu)	0.04634
	I_{srated} (A)	17	L_r (pu)	0.04634
	Poles	4	R_s (pu)	0.02247
	S/R Turns Ratio	1	R_r (pu)	0.01035
GSC Transformer (Single Phase)	P_{rated} (kVA)	3	$L_{leakage}$ (pu)	0.067
	$V_{primary}$ / $V_{secondary}$	480V:115V		
Three-Phase Line Inductor	I_{rated}(A)	60	L (mH)	0.35
GSC & RSC	$V_{DC\text{-}bus}$ (V)	160	F_{switch} (Hz)	10k

C.5 Experimental Test Results

C.5.1 Sub-Synchronous Operation

The DFIG is driven by a DC motor, which is supplied with constant armature and field voltage. The DFIG initially rotates at 1700 rpm at no load (RSC and GSC are both off). The DSP controller then starts both power electronic converters and changes the speed command. Experimental results are shown in Figure C.11. The harmonics (120 Hz) in the *dq* rotor currents are due to the asymmetry of the WRIG and the limited 120 Hz regulation capability of the PI current controllers.

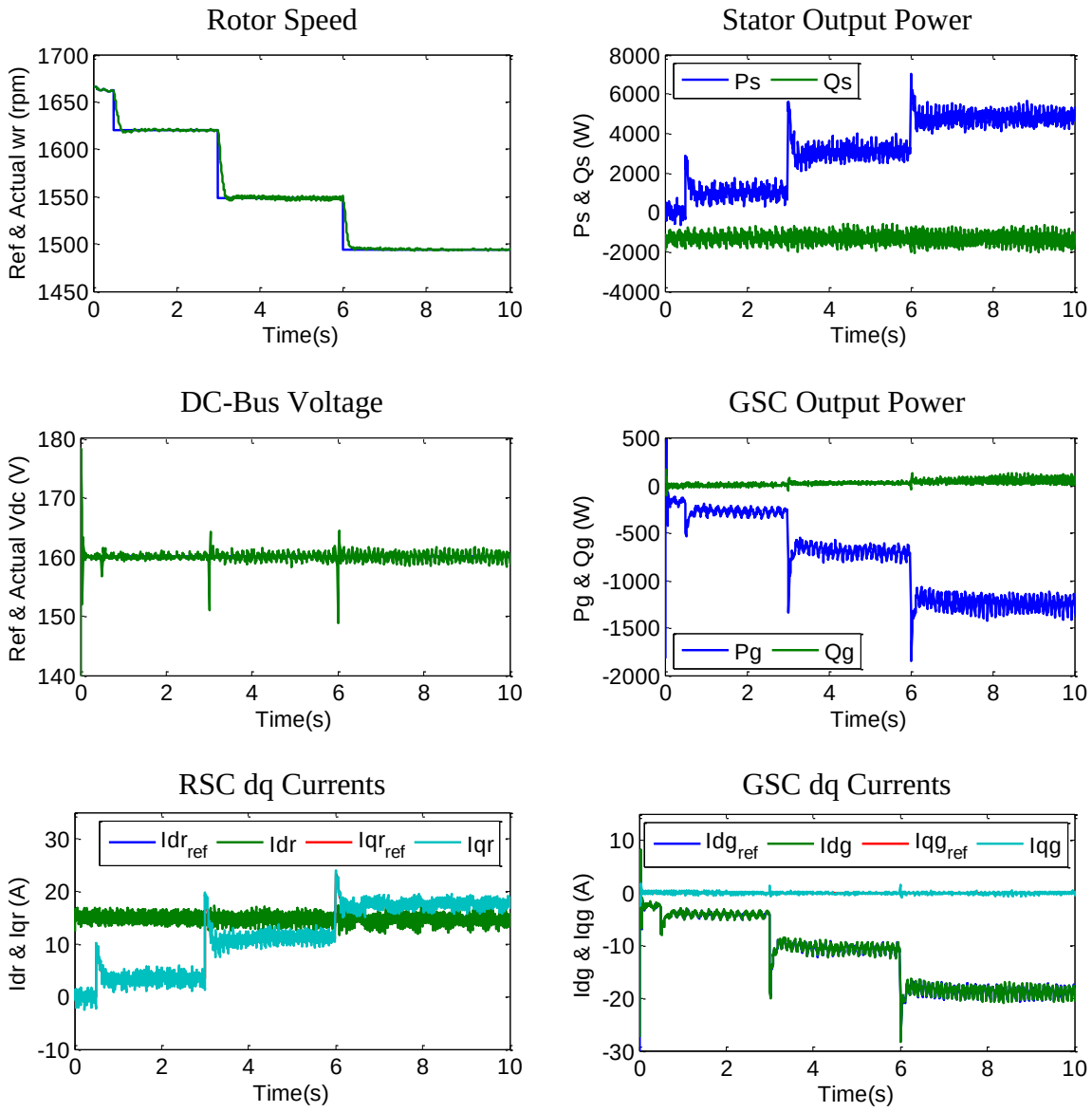

Figure C.11 Experimental results of DFIG sub-synchronous operation.

C.5.2 Super-Synchronous Operation

The DFIG is again driven by a DC motor and rotates at super-synchronous speed. The DSP controller maintains the DFIG speed at 2070 rpm (s = -0.15). The DC motor armature voltage is then manually increased and decreased to change the DC motor mechanical power output. Experimental results are shown in Figure C.12, where regular PI current controllers are used.

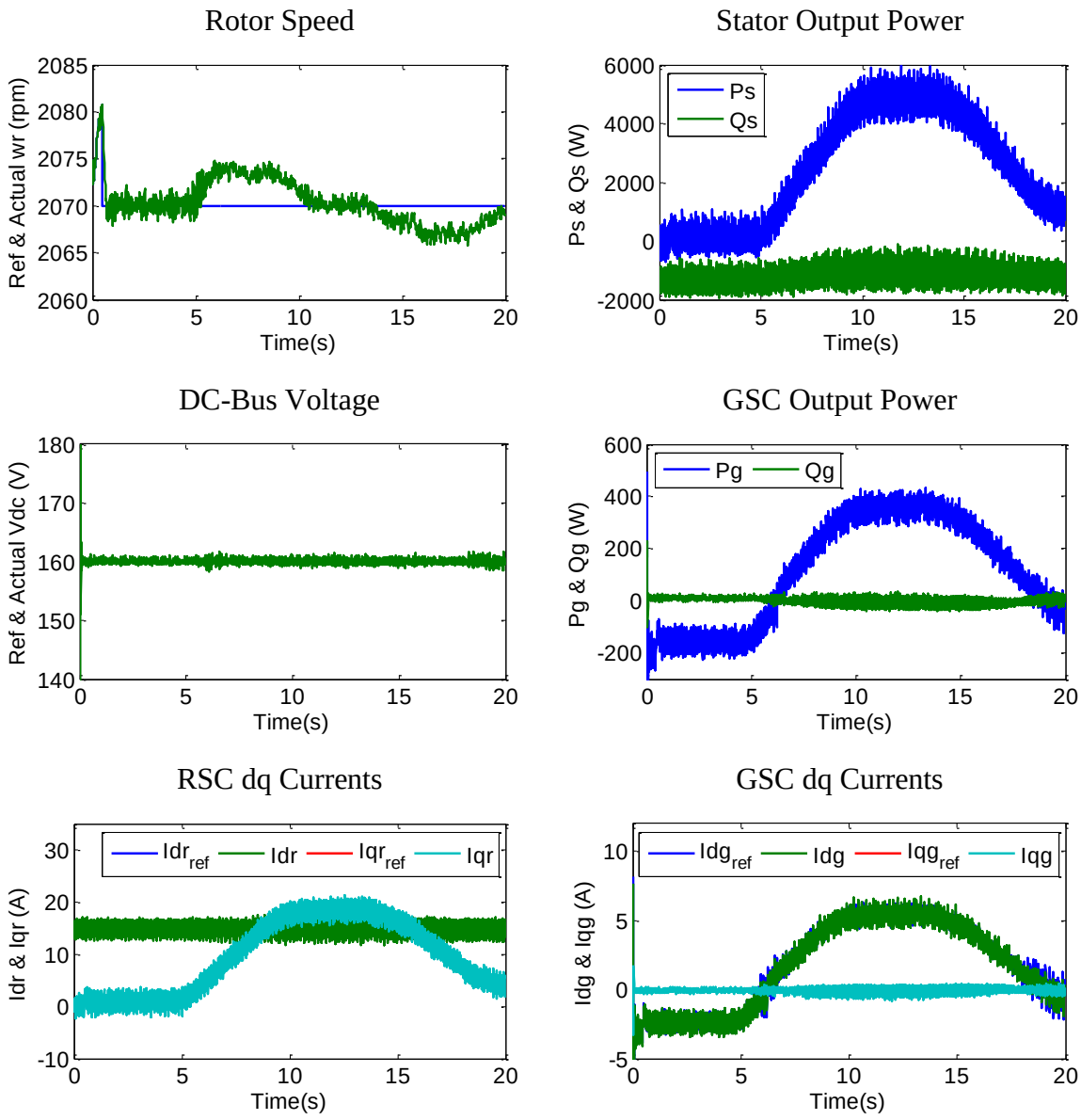

Figure C.12 Experimental results of DFIG super-synchronous operation.

APPENDIX D PARAMETERS OF THE 12-BUS AND 70-BUS POWER SYSTEMS

D.1 Parameters of the 4-Machine 12-Bus Test Power System

The parameters for the 12-bus test system are modified based on [114].

D.1.1 Generator Unit Parameters of the 12-Bus System

Table D.1 Generator parameters of the 12-bus system.

Gen	Bus	kV	MVA	R_s	X_{ls}	X_d	X_d'	X_d''	T_{do}'	T_{do}''	X_q	X_q''	T_{qo}''	H
1	9	22	1000	0.002	0.15	1.5	0.4	0.35	5.0	0.002	1.20	0.30	0.002	5.0
2	10	22	700	0.002	0.15	1.5	0.4	0.35	5.0	0.002	1.20	0.30	0.002	5.0
3	11	22	500	0.002	0.15	1.4	0.3	0.28	6.0	0.002	1.35	0.27	0.002	3.0
4	12	22	500	0.002	0.15	1.5	0.4	0.35	5.0	0.002	1.20	0.30	0.002	5.0

Table D.2 Parameters of AVRs and speed govenors of the 12-bus system.

Gen	Bus	T_r	K_A	T_A	E_{fmax}	E_{fmin}	1/R	T_{max}	T_{min}	T_G	T_1	T_2	T_3
1	9	0.01	20	0.05	5	-5	20	1.1	0	0.2	0.1	2.5	8
2	10	0.01	20	0.05	5	-5	20	1.1	0	0.2	0.1	2.5	8
3	11	0.01	20	0.05	5	-5	20	1.1	0	0.2	0.1	2.5	8
4	12	0.01	20	0.05	5	-5	20	1.1	0	0.2	0.1	2.5	8

D.1.2 Network Parameters of the 12-Bus System

Table D.3 Bus parameters of the 12-bus power system.

Bus	Base kV	Load (MVA)	Shunt (MVAr)	Bus	Base kV	V_{gen} (pu)	P_{gen} (MW)
1	230	0	0	7	345	1	0
2	230	280 + j200	0	8	345	1	0
3	230	320 + j240	0	9	22	1.02	480
4	230	320 + j240	160	10	22	1.02	500
5	230	100 + j60	80	11	22	1.01	200
6	230	440 + j300	180	12	22	1.02	300

Table D.4 Line parameters of the 12-bus system (100 MVA base).

Fr. bus	To bus	R (pu)	X (pu)	B (pu)	Rating (MVA)	Fr. bus	To bus	R (pu)	X (pu)	B (pu)	Rating (MVA)
1	2	0.01144	0.09111	0.18261	250	1	7	0	0.01	0	1000
1	6	0.03356	0.26656	0.55477	250	1	9	0	0.01	0	1000
2	5	0.03356	0.26656	0.55477	250	2	10	0	0.01	0	1000
3	4	0.01144	0.09111	0.18261	250	3	8	0	0.01	0	1000
3	4	0.01144	0.09111	0.18261	250	3	11	0	0.01	0	1000
4	5	0.03356	0.26656	0.55477	250	6	12	0	0.02	0	500
4	6	0.03356	0.26656	0.55477	250						
7	8	0.01595	0.17214	3.2853	350						

D.2 Parameters of the 18-Machine 70-Bus Test Power System

The parameters for the 70-bus system are derived from the 68-bus system in [120].

D.2.1 Generator Unit Parameters of the 70-Bus System

Table D.5 Synchrnous generator dynamic parameters of the 70-bus system.

Gen	Bus	kV	MVA	R_s	X_d	X_d'	X_d''	T_{do}'	T_{do}''
1	53	22	800	0.002	0.800	0.248	0.200	10.200	0.050
2	54	22	850	0.002	2.508	0.592	0.425	6.560	0.050
3	55	22	1000	0.002	2.495	0.531	0.450	5.700	0.050
4	56	22	800	0.002	2.096	0.349	0.280	5.690	0.050
5	57	22	750	0.002	2.475	0.495	0.375	5.400	0.050
6	58	22	1000	0.002	2.540	0.500	0.400	7.300	0.050
7	59	22	750	0.002	2.213	0.368	0.300	5.660	0.050
8	60	22	700	0.002	2.030	0.399	0.315	6.700	0.050
9	61	22	1000	0.002	2.106	0.570	0.450	4.790	0.050
10	62	22	875	0.002	1.479	0.400	0.350	9.370	0.050
11	63	22	1300	0.002	1.664	0.234	0.156	4.100	0.050
12	64	22	2000	0.002	2.020	0.620	0.500	7.400	0.050
13	65	345	10000	0.002	1.480	0.275	0.200	5.900	0.050
14	66	345	10000	0.002	1.800	0.285	0.230	4.100	0.050
15	67	345	10000	0.002	1.800	0.285	0.230	4.100	0.050
16	68	345	10000	0.002	1.780	0.355	0.275	7.800	0.050

Table D.5 (continued).

Gen	Bus	X_{ls}	X_q	X_q'	X_q''	T_{qo}'	T_{qo}''	H
1	53	0.100	0.552	0.224	0.200	1.500	0.035	5.250
2	54	0.298	2.397	0.510	0.425	1.500	0.035	3.553
3	55	0.304	2.370	0.500	0.450	1.500	0.035	3.580
4	56	0.236	2.064	0.320	0.280	1.500	0.035	3.575
5	57	0.203	2.325	0.450	0.375	0.440	0.035	3.467
6	58	0.224	2.410	0.450	0.400	0.400	0.035	3.480
7	59	0.242	2.190	0.338	0.300	1.500	0.035	3.520
8	60	0.196	1.960	0.350	0.315	0.410	0.035	3.471
9	61	0.298	2.050	0.500	0.450	1.960	0.035	3.450
10	62	0.174	1.006	0.394	0.350	1.500	0.035	3.543
11	63	0.134	1.599	0.195	0.156	1.500	0.035	2.169
12	64	0.440	1.900	0.560	0.500	1.500	0.035	4.615
13	65	0.150	1.430	0.250	0.200	1.500	0.035	4.960
14	66	0.170	1.730	0.250	0.230	1.500	0.035	3.000
15	67	0.170	1.730	0.250	0.230	1.500	0.035	3.000
16	68	0.205	1.670	0.300	0.275	1.500	0.035	4.500

Table D.6 AVR and speed govenor parameters of the 70-bus system.

Gen	Bus	T_r	K_A	T_A	K_F	T_F	E_{fmax}	E_{fmin}	1/R	T_{max}	T_{min}	T_G	T_1	T_2	T_3
1	53	0.01	50	0.02	0.1	0.5	4	-4	20	1.1	0	0.1	0.1	0	0
2	54	0.01	50	0.02	0.1	0.5	4	-4	20	1.1	0	0.1	0.1	0	0
3	55	0.01	50	0.02	0.15	0.5	4	-4	20	1.1	0	0.2	0.5	0	0
4	56	0.01	50	0.02	0.15	0.5	4	-4	20	1.1	0	0.2	0.1	2.5	8
5	57	0.01	50	0.02	0.15	0.5	4	-4	20	1.1	0	0.1	0.1	0	0
6	58	0.01	50	0.02	0.15	0.5	4	-4	20	1.1	0	0.2	0.1	2.5	8
7	59	0.01	50	0.02	0.15	0.5	4	-4	20	1.1	0	0.1	0.1	0	0
8	60	0.01	50	0.02	0.025	0.5	4	-4	20	1.1	0	0.1	0.1	0	0
9	61	0.01	50	0.02	0.1	0.5	4	-4	20	1.1	0	0.2	0.1	2.5	8
10	62	0.01	50	0.02	0.025	0.5	4	-4	20	1.1	0	0.2	0.1	2.5	8
11	63	0.01	50	0.02	0.025	0.5	4	-4	20	1.1	0	0.2	0.5	0	0
12	64	0.01	50	0.02	0.1	0.5	4	-4	20	1.1	0	0.2	0.1	2.5	8
13	65	0.01	50	0.02	0.1	0.5	4	-4	20	1.1	0	0.1	0.1	0	0
14	66	0.01	50	0.02	0.05	0.5	4	-4	20	1.1	0	0.2	0.1	2.5	8
15	67	0.01	50	0.02	0.05	0.5	4	-4	20	1.1	0	0.2	0.1	2.5	8
16	68	0.01	50	0.02	0.05	0.5	4	-4	20	1.1	0	0.2	0.1	2.5	8

Table D.7 PSS parameters of the 70-bus system.

Gen	Bus	G_w	T_w	T_1	T_2	T_3	T_4	dV_{max}	dV_{min}
3	54	40	1.5	0.24	0.08	0.24	0.08	0.2	-0.2
9	61	40	1.5	0.25	0.1	0.25	0.1	0.2	-0.2
10	62	40	1.5	0.21	0.07	0.21	0.07	0.2	-0.2
12	64	40	1.5	0.24	0.08	0.24	0.08	0.2	-0.2
14	66	20	1.5	0.6	0.2	0.6	0.2	0.2	-0.2
15	67	20	1.5	0.36	0.11	0.36	0.11	0.2	-0.2
16	68	20	1.5	0.69	0.23	0.69	0.23	0.2	-0.2

Table D.8 Wind plant parameters of the 70-bus system.

Gen	Bus	kV	MVA	MW	Gen Type	V_{wrated} (m/s)
17	69	345	1560	1404	3.6 MW DFIG	14
18	70	345	2040	1836	3.6 MW DFIG	14

D.2.2 Network Parameters of the 70-Bus System

Table D.9 Bus parameters of the 70-bus system (100 MVA base).

Bus	Volt	P_{gen}	P_{load}	Q_{load}	Bus	Volt	P_{gen}	P_{load}	Q_{load}
1	1	0	2.527	1.1856	19	1	0	0	0
2	1	0	0	0	20	1	0	6.8	1.03
3	1	0	3.22	0.02	21	1	0	2.74	1.15
4	1	0	2	0.736	22	1	0	0	0
5	1	0	0	0	23	1	0	2.48	0.85
6	1	0	0	0	24	1	0	4.84	-0.8
7	1	0	2.34	0.84	25	1	0	2.24	0.47
8	1	0	2.088	0.708	26	1	0	1.39	0.17
9	1	0	1.04	1.25	27	1	0	2.81	0.76
10	1	0	0	0	28	1	0	2.06	0.28
11	1	0	0	0	29	1	0	2.84	0.27
12	1	0	0.09	0.88	30	1	0	0	0
13	1	0	0	0	31	1	0	0	0
14	1	0	0	0	32	1	0	0	0
15	1	0	3.2	1.53	33	1	0	3.52	0.24
16	1	0	5.04	0.44	34	1	0	0	0
17	1	0	0	0	35	1	0	0	0
18	1	0	1.58	0.3	36	1	0	1.02	-0.1946

Table D.9 (continued).

Bus	Volt	P_{gen}	P_{load}	Q_{load}	Bus	Volt	P_{gen}	P_{load}	Q_{load}
37	1	0	60	3	54	0.98	5.45	0	0
38	1	0	0	0	55	0.983	6.5	0	0
39	1	0	2.67	0.126	56	0.997	6.32	0	0
40	1	0	0.6563	0.2353	57	1.011	5.052	0	0
41	1	0	50	4	58	1.02	7	0	0
42	1	0	61.5	4	59	1.02	5.6	0	0
43	1	0	0	0	60	1	5.4	0	0
44	1	0	2.6755	0.0484	61	1.01	8	0	0
45	1	0	4.48	0.45	62	1.01	5	0	0
46	1	0	1.507	0.285	63	1	10	0	0
47	1	0	2.0312	0.3259	64	1	13.5	0	0
48	1	0	2.412	0.022	65	1.011	27.96	0	0
49	1	0	1.64	0.29	66	1	57.85	0	0
50	1	0	1	-1.47	67	1.01	60	0	0
51	1	0	3.37	-1.22	68	1.01	55	0	0
52	1	0	39.7	2.23	69	1.00	P_{wind}	0	0
53	1	2.5	0	0	70	1.00	P_{wind}	0	0

Table D.10 Line parameters of the 70-bus system (100 MVA base).

Fr Bus	To Bus	MVA	R (pu)	X (pu)	B (pu)	Tap Ratio	Fr Bus	To Bus	MVA	R (pu)	X (pu)	B (pu)	Tap Ratio
2	3	500	0.0013	0.0151	0.2572	0	13	14	500	0.0009	0.0101	0.1723	0
2	25	500	0.007	0.0086	0.146	0	14	15	700	0.0018	0.0217	0.366	0
3	4	500	0.0013	0.0213	0.2214	0	15	16	700	0.0009	0.0094	0.171	0
3	18	500	0.0011	0.0133	0.2138	0	16	17	500	0.0007	0.0089	0.1342	0
4	5	700	0.0008	0.0128	0.1342	0	16	19	700	0.0016	0.0195	0.304	0
4	14	700	0.0008	0.0129	0.1382	0	16	21	700	0.0008	0.0135	0.2548	0
5	6	700	0.0002	0.0026	0.0434	0	16	24	700	0.0003	0.0059	0.068	0
5	8	700	0.0008	0.0112	0.1476	0	17	18	500	0.0007	0.0082	0.1319	0
6	7	700	0.0006	0.0092	0.113	0	17	27	500	0.0013	0.0173	0.3216	0
6	11	500	0.0007	0.0082	0.1389	0	19	20	500	0.0007	0.0138	0	1.02
7	8	500	0.0004	0.0046	0.078	0	21	22	900	0.0008	0.014	0.2565	0
10	11	700	0.0004	0.0043	0.0729	0	22	23	500	0.0006	0.0096	0.1846	0
10	13	700	0.0004	0.0043	0.0729	0	23	24	500	0.0022	0.035	0.361	0
11	12	500	0.0016	0.0435	0	0.9804	25	26	500	0.0032	0.0323	0.531	0
12	13	500	0.0016	0.0435	0	1.02	26	27	500	0.0014	0.0147	0.2396	0

Table D.10 (continued).

Fr Bus	To Bus	MVA	R (pu)	X (pu)	B (pu)	Tap Ratio	Fr Bus	To Bus	MVA	R (pu)	X (pu)	B (pu)	Tap Ratio
26	28	500	0.0043	0.0474	0.7802	0	44	45	700	0.0025	0.073	0	0
26	29	500	0.0057	0.0625	1.029	0	45	51	1100	0.0004	0.0105	0.72	0
28	29	500	0.0014	0.0151	0.249	0	46	49	500	0.0018	0.0274	0.27	0
1	2	500	0.007	0.0822	0.34935	0	47	48	500	0.0025	0.0268	0.4	0
1	2	500	0.007	0.0822	0.34935	0	47	48	500	0.0025	0.0268	0.4	0
1	27	500	0.032	0.32	0.41	0	50	51	1500	0.0009	0.0221	1.62	0
8	9	500	0.0046	0.0726	0.1902	0	40	41	900	0.006	0.084	3.15	0
8	9	500	0.0046	0.0726	0.1902	0	49	52	500	0.0076	0.1141	1.16	0
1	30	500	0.0008	0.0074	0.48	0	50	52	1500	0.0012	0.0288	2.06	0
1	31	500	0.0016	0.0163	0.25	0	41	42	500	0.004	0.06	2.25	0
1	47	500	0.0013	0.0188	1.31	0	42	52	500	0.004	0.06	2.25	0
9	30	700	0.0019	0.0183	0.29	0	16	69	1600	0.0012	0.0155	0.304	0
9	30	700	0.0019	0.0183	0.29	0	39	70	2000	0.0008	0.0078	0.36	0
9	36	900	0.0022	0.0196	0.34	0	2	53	1000	0	0.0181	0	1
9	36	900	0.0022	0.0196	0.34	0	6	54	1000	0	0.025	0	1.07
30	31	500	0.0013	0.0187	0.333	0	10	55	1000	0	0.02	0	1.07
30	32	500	0.0024	0.0288	0.488	0	19	56	1000	0.0007	0.0142	0	1.03
31	38	500	0.0011	0.0147	0.247	0	20	57	1000	0.0009	0.018	0	1.009
32	33	1100	0.0008	0.0099	0.168	0	22	58	1000	0	0.0143	0	1.01
33	34	1100	0.0011	0.0157	0.202	0	23	59	1000	0.0005	0.0272	0	1
33	38	500	0.0036	0.0444	0.693	0	25	60	1000	0.0006	0.0232	0	1.01
34	35	700	0.0001	0.0074	0	1	29	61	1000	0.0008	0.0156	0	1.01
34	36	1100	0.0033	0.0111	1.45	0	31	62	1000	0	0.026	0	1
35	45	700	0.0007	0.0175	1.39	0	32	63	1500	0	0.013	0	1
36	37	4000	0.0005	0.0045	0.32	0	36	64	2000	0	0.0075	0	1
37	43	700	0.0005	0.0276	0	0	37	65	10000	0	0.0033	0	1.02
38	46	500	0.0022	0.0284	0.43	0	41	66	10000	0	0.0015	0	1
39	44	1000	0	0.0411	0	0	42	67	10000	0	0.0015	0	1
39	45	700	0	0.0839	0	0	52	68	10000	0	0.003	0	1
40	48	900	0.002	0.022	1.28		16	69	1600	0.0012	0.0155	0.304	0
43	44	700	0.0001	0.0011	0	0	39	70	2000	0.0008	0.0078	0.36	

APPENDIX E TRAINING OF RECURRENT NEURAL NETWORKS

E.1 Recurrent Neural Networks (RNNs)

An in-depth description on RNNs, RNN training algorithms, and RNN control applications is provided in [131]. This appendix is intended to provide a brief summary on the RNN structure and training algorithm used in this dissertation work.

A typical RNN with one hidden layer is shown in Figure E.1, where $f(\cdot)$ is the activation function for the hidden layer and $g(\cdot)$ is the activation function for the output layer. For an n-dimensional input vector, $x(k)$, an m-dimensional internal vector, $s(k)$, and a o-dimensional output vector, $y(k)$, an RNN can be expressed as

$$\begin{aligned} s(k) &= f[W_s s(k-1) + W_i x(k)] \\ y(k) &= g[W_o s(k)] \end{aligned} \quad . \tag{E.1}$$

Unfolding (E.1) yields

$$\begin{aligned} y(k) &= g\{W_o \cdot f_1[W_s s(k-1) + W_i x(k)]\} \\ &= g\{W_o \cdot f_1[W_s f_2[W_s s(k-2) + W_i x(k-1)] + W_i x(k)]\} \\ &= g\{W_o \cdot f_1[W_s f_2[W_s f_3[W_s s(k-3) + W_i x(k-2)] + W_i x(k-1)] + W_i x(k)]\} \\ &= \cdots\cdots \end{aligned} \quad , \tag{E.2}$$

where the subscript for $f(\cdot)$ is an index for unfolding depth. All $f_i(\cdot)$'s are the same function but have different gradients. Figure E.2 shows this RNN unfolded with a depth of three.

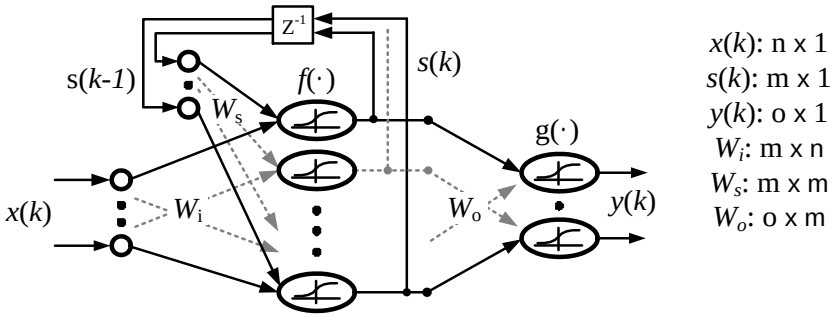

Figure E.1 A typical RNN with one hidden layer.

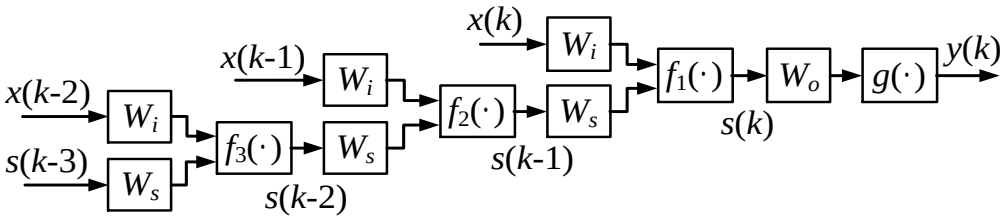

Figure E.2 An RNN with an unfolded depth of three.

E.2 Calculating the Gradients for an RNN

Because of the recurrent loop, the gradient of an RNN output with respect to its weights may depend on all of the historical inputs. A look-back parameter, the truncated depth *h*, is thus defined when calculating the gradient of an RNN. For an error scalar $E(k)$, the gradient of $E(k)$ with respect to W_o is given by

$$\left.\frac{\partial E(k)}{\partial W_o}\right|_{o\times m} = [\nabla g]\big|_{o\times o} \cdot \left.\frac{\partial E(k)}{\partial y(k)}\right|_{o\times 1} \cdot s(k)'\big|_{1\times m} \quad \text{(E.3)}$$

where the dimension of each quantity is given behind the "|" symbol, $[\nabla g]$ is an $o\times o$ diagonal matrix of the gradients of g(·), and the upper-right prime symbol means transpose. The gradient of $E(k)$ with respect to W_s for a truncated depth of *h* is given by

$$
\begin{aligned}
h=1:\ & \left.\frac{\partial E(k)}{\partial W_s}\right|_{m\times m} = [\nabla f_1]\big|_{m\times m}\cdot W_o'\big|_{m\times o}\cdot[\nabla g]\big|_{o\times o}\cdot\left.\frac{\partial E(k)}{\partial y(k)}\right|_{o\times 1}\cdot s(k-1)'\big|_{1\times m} \\
h=2:\ & \left.\frac{\partial E(k)}{\partial W_s}\right|_{m\times m} = [\nabla f_1]\cdot W_o'\cdot[\nabla g]\cdot\frac{\partial E(k)}{\partial y(k)}\cdot s(k-1)' \\
& \qquad + [\nabla f_2]\cdot W_s'\cdot[\nabla f_1]\cdot W_o'\cdot[\nabla g]\cdot\frac{\partial E(k)}{\partial y(k)}\cdot s(k-2)' \\
h=3:\ & \left.\frac{\partial E(k)}{\partial W_s}\right|_{m\times m} = [\nabla f_1]\cdot W_o'\cdot[\nabla g]\cdot\frac{\partial E(k)}{\partial y(k)}\cdot s(k-1)' \\
& \qquad + [\nabla f_2]\cdot W_s'\cdot[\nabla f_1]\cdot W_o'\cdot[\nabla g]\cdot\frac{\partial E(k)}{\partial y(k)}\cdot s(k-2)' \\
& \qquad + [\nabla f_3]\cdot W_s'\cdot[\nabla f_2]\cdot W_s'\cdot[\nabla f_1]\cdot W_o'\cdot[\nabla g]\cdot\frac{\partial E(k)}{\partial y(k)}\cdot s(k-3)' \\
&\cdots\cdots .
\end{aligned}
\tag{E.4}
$$

where all $[\nabla f_i]$'s are $m\times m$ diagonal matrices containing the gradients of $f_i(\cdot)$.The gradient of $E(k)$ with respect to W_i for a truncated depth of h is given by

$$
\begin{aligned}
h=1:\ & \left.\frac{\partial E(k)}{\partial W_i}\right|_{m\times n} = [\nabla f_1]\big|_{m\times m}\cdot W_o'\big|_{m\times o}\cdot[\nabla g]\big|_{o\times o}\cdot\left.\frac{\partial E(k)}{\partial y(k)}\right|_{o\times 1}\cdot x(k)'\big|_{1\times n} \\
h=2:\ & \left.\frac{\partial E(k)}{\partial W_i}\right|_{m\times n} = [\nabla f_1]\cdot W_o'\cdot[\nabla g]\cdot\frac{\partial E(k)}{\partial y(k)}\cdot x(k)' \\
& \qquad + [\nabla f_2]\cdot W_s'\cdot[\nabla f_1]\cdot W_o'\cdot[\nabla g]\cdot\frac{\partial E(k)}{\partial y(k)}\cdot x(k-1)' \\
h=3:\ & \left.\frac{\partial E(k)}{\partial W_i}\right|_{m\times n} = [\nabla f_1]\cdot W_o'\cdot[\nabla g]\cdot\frac{\partial E(k)}{\partial y(k)}\cdot x(k)' \\
& \qquad + [\nabla f_2]\cdot W_s'\cdot[\nabla f_1]\cdot W_o'\cdot[\nabla g]\cdot\frac{\partial E(k)}{\partial y(k)}\cdot x(k-1)' \\
& \qquad + [\nabla f_3]\cdot W_s'\cdot[\nabla f_2]\cdot W_s'\cdot[\nabla f_1]\cdot W_o'\cdot[\nabla g]\cdot\frac{\partial E(k)}{\partial y(k)}\cdot x(k-2)' \\
&\cdots\cdots .
\end{aligned}
\tag{E.5}
$$

A larger truncated depth results in a more accurate gradient, but requires more computation effort (although some code optimization can be made to avoid duplicate computations). More importantly, for a certain truncated depth h, weights should remain unchanged within this backward depth. In other words, weight updates can only be carried

out every *h* steps.

For the numerical simulations performed in this dissertation work, it is found that a truncated depth of one can yield sufficiently good training results. A truncated depth of one is used for training all the RNNs in the DSOPF controller presented in Chapters 4 and 5. In the following derivations, the truncated depth is set to one.

E.3 Incremental Gradient Descent for Training an RNN

After obtaining the gradients, to minimize $E(k)$, the incremental gradient descent algorithm is used to update the RNN weights. The following weight updates are carried out in every samping step k:

$$\begin{aligned} W_o(k+1) &= W_o(k) - r_o \frac{\partial E(k)}{\partial W_o} \\ W_s(k+1) &= W_s(k) - r_s \frac{\partial E(k)}{\partial W_s} \\ W_i(k+1) &= W_i(k) - r_i \frac{\partial E(k)}{\partial W_i} \end{aligned} \quad . \tag{E.6}$$

where r_o, r_s, and r_i are gains controlling the step size of the weight updates. When *tansig*(·) or *sigmoid*(·) is used for the activation functions, their gradients are small in the saturation regions. Thus, r_s and r_i are usually larger (say five times larger for a truncated depth of one) than r_o to compensate for the magnitude drops introduced by the additional gradient operations. r_o could be in the range of 0.0001 to 0.01 depending on the applications and the maturity of the neural network.

APPENDIX F WIND OPTIMAL BIDDING IN COMBINED ENERGY-AND-RESERVE MARKET

An optimal wind plant bidding scheme is to maximize the expected revenue, as in

$$\begin{aligned} &\max E[R(P_c, UR_c)] \\ &\text{s.t. } P_{\max} - P_c - UR_c \geq 0, \\ &P_c \geq 0,\ UR_c \geq 0 \end{aligned} \quad \text{(F.1)}$$

.

Given a probabilistic wind forecast, $f(P_w)$, using the revenue equation (6.8), the expected revenue is given by

$$\begin{aligned} &E[R(P_c, UR_c)] \\ &= \int_0^{P_{\max}} R(P_w \mid P_c, UR_c) f(P_w) dP_w \\ &= \pi_{E-} \int_0^{P_c} P_w f(P_w) dP_w - [(\pi_{E-} - \pi_E) P_c + (\pi_{UR-} - \pi_{UR}) UR_c] \int_0^{P_c} f(P_w) dP_w \\ &\quad + \pi_{UR-} \int_{P_c}^{P_c+UR_c} P_w f(P_w) dP_w - [(\pi_{UR-} - \pi_E) P_c + (\pi_{UR-} - \pi_{UR}) UR_c] \int_{P_c}^{P_c+UR_c} f(P_w) dP_w \\ &\quad + \pi_{E+} \int_{P_c+UR_c}^{P_{\max}} P_w f(P_w) dP_w + [(\pi_E - \pi_{E+}) P_c + (\pi_{UR} - \pi_{E+}) UR_c] \int_{P_c+UR_c}^{P_{\max}} f(P_w) dP_w \\ &= \pi_{E-} \int_0^{P_c} P_w f(P_w) dP_w + \pi_{UR-} \int_{P_c}^{P_c+UR_c} P_w f(P_w) dP_w + \pi_{E+} \int_{P_c+UR_c}^{P_{\max}} P_w f(P_w) dP_w \\ &\quad - (\pi_{E-} - \pi_{UR-}) P_c F(P_c) - (\pi_{UR-} - \pi_{E+})(P_c + UR_c) F(P_c + UR_c) \\ &\quad + (\pi_E - \pi_{E+}) P_c + (\pi_{UR} - \pi_{E+}) UR_c \end{aligned} \quad \text{(F.2)}$$

.

The expected revenue's partial derivatives with respect to P_c and UR_c are given by

$$\frac{\partial E[R(P_c, UR_c)]}{\partial P_c} = (\pi_E - \pi_{E+}) - (\pi_{E-} - \pi_{UR-}) F(P_c) - (\pi_{UR-} - \pi_{E+}) F(P_c + UR_c) \quad \text{(F.3)}$$

,

$$\frac{\partial E[R(P_c, UR_c)]}{\partial UR_c} = (\pi_{UR} - \pi_{E+}) - (\pi_{UR-} - \pi_{E+}) F(P_c + UR_c) \quad \text{(F.4)}$$

.

The optimal bidding scheme problem, (F.1), has three inequality constraints. The necessary conditions for optimality are given by the Karush–Kuhn–Tucker (KKT) conditions [123], as in

$$\begin{aligned}
&\frac{\partial E[R(P_c,UR_c)]}{\partial P_c} - \lambda_1 + \lambda_2 = 0, \;\; \frac{\partial E[R(P_c,UR_c)]}{\partial UR_c} - \lambda_1 + \lambda_3 = 0, \\
&\lambda_1(P_{\max} - P_c - UR_c) = 0, \;\; \lambda_2 P_c = 0, \;\; \lambda_3 UR_c = 0 \\
&\lambda_1, \;\lambda_2, \;\lambda_3, \;(P_{\max} - P_c - UR_c), \;P_c, \;UR_c \geq 0
\end{aligned} \quad , \tag{F.5}$$

which are solved by the following analysis. Define

$$A = \frac{\pi_E - \pi_{UR}}{\pi_{E-} - \pi_{UR-}}, \;\; B = \frac{\pi_{UR} - \pi_{E+}}{\pi_{UR-} - \pi_{E+}} \; . \tag{F.6}$$

a) If none of the constraints is binding, i.e., P_{max} - P_c - UR_c > 0, P_c > 0, and UR_c > 0, from (F.5),

$$\frac{\partial E[R(P_c,UR_c)]}{\partial P_c} = \frac{\partial E[R(P_c,UR_c)]}{\partial UR_c} = 0 \quad , \tag{F.7}$$

From (F.3) and (F.4), solution to (F.7) is given by

$$P_c^* = F^{-1}(A) \; , \; UR_c^* = F^{-1}(B) - P_c^* \; , \tag{F.8}$$

In order for the assumption of no binding constraint to be true, from (F.8), it is required that 0 < A < B < 1. Note that

$$\begin{aligned}
P_c + UR_c < P_{max} \;\; &\Leftrightarrow \;\; B < 1 \\
P_c > 0 \;\; &\Leftrightarrow \;\; A > 0 \\
UR_c > 0 \;\; &\Leftrightarrow \;\; B - A > 0
\end{aligned} \tag{F.9}$$

Also note that under *Price Assumption I*, $B \leq 1$. Thus, the maximum power inequality can only be boundary binding, which has the same optimal solution as when it is not binding. From (F.9), (F.8) is the optimal strategy when $0 < A < B \leq 1$. In the following analysis, the maximum power inequality is not considered as a binding constraint.

b) If $A > 0$ and $A \geq B$, from (F.9), only UR_c becomes a binding constraint, i.e., P_{max} - P_c - $UR_c \geq 0$, $P_c > 0$, and $UR_c = 0$. From (F.5),

$$\frac{\partial E[R(P_c, UR_c)]}{\partial P_c} = 0, \quad \frac{\partial E[R(P_c, UR_c)]}{\partial UR_c} = -\lambda_3 \leq 0 \tag{F.10}$$

,

The solution to $UR_c = 0$ and $\partial E[R(P_c, UR_c)] / \partial P_c = 0$ is given by

$$P_c^* = F^{-1}\left(\frac{\pi_E - \pi_{E+}}{\pi_{E-} - \pi_{E+}}\right), UR_c^* = 0 \tag{F.11}$$

.

With (F.11) and $A \geq B$, $\partial E[R(P_c, UR_c)] / \partial UR_c \leq 0$ and (F.10) is satisfied. Therefore, (F.11) is the optimal strategy when $A > 0$ and $A \geq B$.

c) If $A \leq 0$, from (F.9), P_c becomes a binding constraint, i.e., $P_c = 0$. Note that when $A \leq 0$, $\pi_{E+} \leq \pi_E \leq \pi_{UR}$ and $B \geq 0$, which implies $A \leq B$. Thus, whenever P_c becomes a binding constraint, UR_c will be either nonbinding or boundary binding. UR_c can then be treated as nonbinding in this case. From (F.5),

$$\frac{\partial E[R(P_c, UR_c)]}{\partial UR_c} = -\lambda_2 \leq 0, \quad \frac{\partial E[R(P_c, UR_c)]}{\partial UR_c} = 0 \tag{F.12}$$

.

The solution to $P_c = 0$ and $\partial E[R(P_c, UR_c)] / \partial UR_c = 0$ is given by

$$P_c^* = 0, UR_c^* = F^{-1}(B) \tag{F.13}$$

.

With $A \leq 0$, $\partial E[R(P_c, UR_c)] / \partial P_c \leq 0$ and (F.12) is satisfied. Therefore, (F.13) is the optimal strategy when $A \leq 0$.

REFERENCES

[1] "The EU climate and energy package," European Commission Climate Action, [Online]. Available: http://ec.europa.eu /clima/policies/brief/eu/package_en.htm.

[2] "20% wind energy by 2030: increasing wind energy's contribution to U.S. electricity supply," U.S. Department of Energy report, July 2008, [Online]. Available: http://www1.eere.energy.gov/windandhydro/pdfs/41869.pdf.

[3] "States with renewable portfolio standards," U.S. Department of Energy information resources, May 2009, [Online]. Available: http://apps1.eere.energy.gov/states/maps /renewable_portfolio_states.cfm.

[4] "World wind energy report 2009," World Wind Energy Association, Mar. 2010, [Online]. Available: http://www.wwindea.org/home/images/stories/worldwindenergy report 2009_s.pdf.

[5] "AWEA year end 2009 market report," American Wind Energy Association, Jan. 2010, [Online]. Available: http://www.awea.org/documents/reports/4Q09.pdf.

[6] "International energy statistics," U.S. Energy Information Administration, data retrieved Dec. 2010, [Online]. Available: http://tonto.eia.gov/cfapps/ipdbproject/IED Index3.cfm?tid=2&pid=2&aid=2.

[7] J. M. Carrasco, L. G. Franquelo, J. T. Bialasiewicz, E. Galván, R. C. Portillo-Guisado, M. Á. Martín-Prats, J. I. León, and N. Moreno-Alfonso, "Power-electronic systems for the grid integration of renewable energy sources: a survey," *IEEE Trans. Ind. Electron.*, vol. 53, no. 4, pp. 1002-1016, Aug. 2006.

[8] Z. Chen, J. M. Guerrero, and F. Blaabjerg, "A review of the state of the art of power electronics for wind turbines," *IEEE Trans. Power Electron.*, vol. 24, no. 8, pp. 1859-1875, Aug. 2009.

[9] J. Matevosyan, T. Ackermann, S. Bolik, and L. Sder, "Comparison of international regulations for connection of wind turbines to the network," in *Proc. Nordic Wind Power Conf. (NWPC'2004)*, Gothenburg, Sweden, Mar. 2004.

[10] W. Qiao, and R. G. Harley, "Grid connection requirements and solutions for DFIG wind turbines," in *Proc. IEEE Energy 2030 Conf.*, Atlanta, GA, Nov. 17-18, 2008.

[11] P. B. Eriksen, T. Ackermann, H. Abildgaard, P. Smith, W. Winter, and J. M. Rodriguez Garcia, "System operation with high wind penetration," *IEEE Power Energy Mag.*, vol. 3, no. 6, pp. 65-74, Nov./Dec. 2005.

[12] "Regulatory order No. 661: interconnection for wind energy," Federal Energy Regulatory Commission, Jun. 2, 2005, [Online]. Available: http://www.ferc.gov /industries/electric/indus-act/gi/wind.asp.

[13] "Regulatory order No. 661-A: interconnection for wind energy," Federal Energy Regulatory Commission, Dec. 12, 2005, [Online]. Available: http://www.ferc.gov /industries/electric/indus-act/gi/wind.asp.

[14] J. Lopez, P. Sanchis, X. Roboam, and L. Marroyo, "Dynamic behavior of the doubly fed induction generator during three-phase voltage dips," *IEEE Trans. Energy Convers.*, vol. 22, no. 3, pp. 709–717, Sept. 2007.

[15] M. Mohseni, S. Islam, and M. Masoum, "Impacts of symmetrical and asymmetrical voltage sags on DFIG-based wind turbines considering phase-angle jump, voltage recovery, and sag parameters," *IEEE Trans. Power Electron.*, vol. 26, no. 5, pp. 1587-1598, May 2011.

[16] T. K. Brekken, and N. Mohan, "Control of a doubly fed induction wind generator under unbalanced grid voltage conditions," *IEEE Trans. Energy Convers.*, vol. 22, no. 1, pp. 129-135, Mar. 2007.

[17] P. Kundur, *Power System Stability and Control*, New York: McGraw-Hill, 1994. ISBN-13: 978-0070359581.

[18] N. G. Hingorani and L. Gyugyi, *Understanding FACTS: Concepts and Technology of Flexible AC Transmission Systems*, Wiley-IEEE Press, Dec. 1999. ISBN-13: ISBN-13: 978-0780334557.

[19] J. Wood and B. F. Wollenberg, *Power Generation, Operation, and Control*, Wiley-Interscience, 2nd ed., Jan. 1996. ISBN-13: 978-0471586999.

[20] M. Shahidehpour, H. Yamin, and Z. Li, *Market Operations in Electric Power Systems: Forecasting, Scheduling, and Risk Management*, Wiley-IEEE Press, 2002. ISBN-13: 978-0471224129

[21] K. Porter and J. Rogers, "Status of centralized wind power forecasting in North America: May 2009 – May 2010," NREL subcontract report, NREL/SR-550-47853, Apr. 2010.

[22] A. Botterud, J. Wang, V. Miranda and R. J. Bessa, "Wind power forecasting in U.S. electricity markets," *The Electricity Journal*, vol. 23, no. 3, pp. 71-82, Apr. 2010.

[23] S. Fink, C. Mudd, K. Porter, and B. Morgenstern, "Wind energy curtailment case studies," NREL subcontract report, NREL/SR-550-46716, Oct. 2009.

[24] M. Robinson, "Role of balancing markets in wind integration," in *Proc. 2006 IEEE Power Systems Conference & Exhibition (PSCE)*, Atlanta, GA, Oct. 29-Nov. 1, 2006, pp. 232-233.

[25] C. Brunetto, M. Nicita and G. Tina, "Wind generation in day-ahead energy markets in Italy: imbalances penalties," in *Proc. 2007 IEEE Lausanne Power Tech Conf.*, Lausanne, Switzerland, July 1-5, 2007.

[26] D. Maggio, C. D'Annunzio, S. Huang, C. Thompson, "Outstanding questions around increasing variable generation penetration in the ERCOT system," in *Proc. 2010 IEEE PES General Meeting*, Minneapolis, MN, 25-29 July 2010.

[27] S. Grijalva and M. U. Tariq, "Prosumer-based smart grid architecture enables a flat, sustainable electricity industry," in *Proc. IEEE Innovative Smart Grid Technologies Conference (ISGT)*, Anaheim, CA, Jan. 2011.

[28] D. Prokhorov and D. Wunsch, "Adaptive critic designs," *IEEE Trans. Neural Netw.*, vol. 8, no. 5, pp. 997-1007, Sept. 1997.

[29] K. Clark, N. W. Miller, and J. J. Sanchez-Gasca, "Modeling of GE wind turbine-generators for grid studies," General Electric International, Inc., Schenectady, NY, USA, Sept. 9, 2009.

[30] W. Qiao, "Integrated control of wind farms, facts devices and the power network using neural networks and adaptive critic designs," PhD Dissertation, Georgia Institute of Technology, July 2008.

[31] E. Muljadi and C. P. Butterfield, "Pitch-controlled variable-speed wind turbine generation," *IEEE Trans. Ind. Appl.*, vol. 37, no. 1, pp. 240-246, Jan./Feb. 2001.

[32] W. Qiao, W. Zhou, J. M. Aller, and R. G. Harley, "Wind speed estimation based sensorless output maximization control for a wind turbine driving a DFIG," *IEEE Trans. Power Electron.*, vol. 23, no. 3, pp. 1156-1169, May 2008.

[33] E. Koutroulis and K. Kalaitzakis, "Design of a maximum power tracking system for wind-energy-conversion applications," *IEEE Trans. Ind. Electron.*, vol. 53, no. 2, pp. 486-494, Apr. 2006.

[34] V. Agarwal, R. K. Aggarwal, P. Patidar, and C. Patki, "A novel scheme for rapid tracking of maximum power point in wind energy generation systems," *IEEE Trans. Energy Convers.*, vol. 25, no. 1, pp. 228-236, Mar. 2010.

[35] D. W. Novotny and T. A. Lipo, *Vector Control and Dynamics of AC Drives*, Oxford University Press, 2000. ISBN-13: 978-0198564393.

[36] R. Lorenz and D. Lawson, “Performance of feedforward current regulators for field-oriented induction machine controllers,” *IEEE Trans. Ind. Appl.*, vol. IA-23, no. 4, pp. 597-602, July/Aug., 1987.

[37] I. Takahashi and Y. Ohmori, “High-performance direct torque control of an induction motor,” *IEEE Trans. Ind. Appl.*, vol. 25, no. 2, pp. 1090–1093, May 1989.

[38] D. Casadei, F. Profumo, G. Serra, and A. Tani, “FOC and DTC: Two viable schemes for induction motors torque control,” *IEEE Trans. Power Electron.*, vol. 17, no. 5, pp. 779-787, Sept. 2002.

[39] S. Seman, J. Niiranen, and A. Arkkio, “Ride-through analysis of doubly fed induction wind-power generator under unsymmetrical network disturbance,” *IEEE Trans. Power Syst.*, vol. 21, no. 4, pp. 1782-1789, Nov. 2006.

[40] L. Xu and P. Cartwright, “Direct active and reactive power control of DFIG for wind energy generation,” *IEEE Trans. Energy Convers.*, vol. 21, no. 3, pp. 750–758, Sept. 2006.

[41] D. Zhi and L. Xu, “Direct power control of DFIG with constant switching frequency and improved transient performance,” *IEEE Trans. Energy Convers.*, vol. 22, no. 1, pp. 110–118, Mar. 2007.

[42] K. Niiranen, “Simulation of doubly fed induction generator wind turbine with an active crowbar,” in *Proc. 11th Int’l Conf. Power Electronics and Motion Control (EPE-PEMC)*, Riga, Latvia, 2004.

[43] J. Morren and S. W. H. de Hann, “Ride through of wind turbines with doubly-fed induction generator during a voltage dip,” *IEEE Trans. Energy Convers.*, vol. 20, no. 2, pp. 435-441, June 2005.

[44] I. Erlich, H. Wrede, and C. Feltes, “Dynamic behavior of DFIG-based wind turbines during grid faults,” in *Proc. Power Conversion Conference (PCC) 2007*, Nagoya, Apr. 2-5, 2007, pp. 1195–1200.

[45] D. Hansena, G. Michalke, “Fault ride-through capability of DFIG wind turbines,” *Renewable Energy*, vol. 32, no. 9, pp. 1594-1619, July 2007.

[46] Z. Peng, H. Yikang, “Control Strategy of an Active Crowbar for DFIG Based Wind Turbine under Grid Voltage Dips,” in *Proc. Int’l Conf. Electrical Machines and Systems 2007*, Seoul, Korea, Oct. 2007.

[47] W. Qiao, G. K. Venayagamoorthy, and R. G. Harley, "Real-time implementation of a STATCOM on a wind farm equipped with doubly fed induction generators," *IEEE Trans. Ind. Appl.*, vol. 45, no. 1, pp.98-107, Jan./Feb. 2009.

[48] W. Qiao, R. G. Harley, and G. K. Vanayagamoorthy, "Coordinated reactive power control of a large wind farm and a STATCOM using heuristic dynamic programming," *IEEE Trans. Energy Convers.*, vol. 24, no. 2, pp. 493-503, June 2009.

[49] M. Molinas, J. A.Suul, and T. Undeland, "Low voltage ride through of wind farms with cage generators: STATCOM versus SVC," *IEEE Trans. Power Electron.*, vol. 23, no. 3, pp. 1104-1117, May 2008.

[50] J. López, E. Gubía, E. Olea, J. Ruiz, and L. Marroyo, "Ride through of wind turbines with doubly fed induction generator under symmetrical voltage dips," *IEEE Trans. Ind. Electron.*, vol. 56, no. 10, pp. 4246-4254, Oct. 2009.

[51] G. Pannell, D. J. Atkinson, and B. Zahawi, "Minimum-threshold crowbar for a fault-ride-through grid-code-compliant DFIG wind turbine," *IEEE Trans. Energy Convers.*, vol. 25, no. 3, pp. 750-759, Sept. 2010.

[52] P. Flannery and G. Venkataramanan, "A fault tolerant doubly fed induction generator wind turbine using a parallel grid side rectifier and series grid side converter," *IEEE Trans. Power Electron.*, vol. 23, no. 3, pp. 1126-1135, May 2008.

[53] O. Abdel-Baqi and A. Nasiri, "A dynamic LVRT solution for doubly-fed induction generators," *IEEE Trans. Power Electron.*, vol. 25, no. 1, pp. 193-196, Jan. 2010.

[54] J. Yang, J. E. Fletcher, and J. O'Reilly, "A series-dynamic-resistor-based converter protection scheme for doubly-fed induction generator during various fault conditions," *IEEE Trans. Energy Convers.*, vol. 25, no. 2, pp. 422-432, June 2010.

[55] X. Yan, G. Venkataramanan, P. S. Flannery, Y. Wang, Q. Dong, and B. Zhang, "Voltage-sag tolerance of DFIG wind turbine with a series grid side passive-impedance network," *IEEE Trans. Energy Convers.*, vol. 25, no. 4, pp. 1048-1056, Dec. 2010.

[56] O. Gomis-Bellmunt, A. Junyent-Ferre, A. Sumper, and J. Bergas-Jane, "Ride-through control of a doubly fed induction generator under unbalanced voltage sags," *IEEE Trans. Energy Convers.*, vol. 23, no. 4, pp. 1036-1045, Dec. 2008.

[57] L. Xu and Y. Wang, "Dynamic modeling and control of DFIG-based wind turbines under unbalanced network conditions," *IEEE Trans. Power Syst.*, vol. 22, no. 1, pp. 314-323, Feb. 2007.

[58] J. Hu, Y. He, L. Xu, and B. W. Williams, "Improved control of DFIG systems during network unbalance using PI–R current regulators," *IEEE Trans. Ind. Electron.*, vol. 56, no. 2, pp. 439-451, Feb. 2009.

[59] L. Xu, "Coordinated control of DFIG's rotor and grid side converters during network unbalance," *IEEE Trans. Power Electron.*, vol. 23, no. 3, pp. 1041-1049, May 2008.

[60] D. Santos-Martin, J. L. Rodriguez-Amenedo, and S. Arnaltes, "Direct power control applied to doubly fed induction generator under unbalanced grid voltage conditions," *IEEE Trans. Power Electron.*, vol. 23, no. 5, pp. 2328-2336, Sept. 2008.

[61] D. Santos-Martin, J. L. Rodriguez-Amenedo, and S. Arnaltes, "Providing ride-through capability to a doubly fed induction generator under unbalanced voltage dips," *IEEE Trans. Power Electron.*, vol. 24, no. 7, pp. 1747-1757, July 2009.

[62] G. Abad, M. A. Rodriguez, G. Iwanski, and J. Poza, "Direct power control of doubly-fed-induction-generator-based wind turbines under unbalanced grid voltage," *IEEE Trans. Power Electron.*, vol. 25, no. 2, pp. 442-452, Feb. 2010.

[63] P. S. Flannery and G. Venkataramanan, "Unbalanced voltage sag ride-through of a doubly fed induction generator wind turbine with series grid-side converter," *IEEE Trans. Ind. Appl.*, vol. 45, no. 5, pp. 1879-1887, Sept./Oct. 2009.

[64] J. De La Ree, V. Centeno, J. Thorp, and A. Phadke, "Synchronized phasor measurement applications in power systems," *IEEE Trans. Smart Grid*, vol. 1, no. 1, pp. 20-27, June 2010.

[65] D. Karlsson, M. Hemmingsson, and S. Lindahl, "Wide area system monitoring and control - terminology, phenomena, and solution implementation strategies," *IEEE Power Energy Mag.*, vol. 2, no. 5, pp. 68-76, Sept.-Oct. 2004.

[66] E. Farantatos, G. K. Stefopoulos, G. J. Cokkinides, A. P. Meliopoulos, "PMU-Based Dynamic State Estimation for Electric Power Systems," in *Proc. 2009 PES General Meeting*, Calgary, Alberta, Canada, July 2009.

[67] R. Huang, E. Farantatos, G. J. Cokkinides, and A. P. Meliopoulos, "Substation based dynamic state estimator - numerical experiment," in *Proc. 2010 IEEE PES T&D Conference and Exposition*, New Orleans, LA, USA, Apr. 19-22, 2010.

[68] X. Xie, Y. Xin, J. Xiao, J. Wu, and Y. Han, "WAMS applications in Chinese power systems," *IEEE Power Energy Mag.*, vol. 4, no. 1, pp. 54-63, Jan.-Feb. 2006.

[69] K. Tomsovic, D. Bakken, V. Venkatasubramanian, and A. Bose, "Designing the next generation of real-time control, communication, and computations for large power systems," *Proc. IEEE*, vol. 93, no. 5, pp. 965-979, May 2005.

[70] I. Kamwa, R. Grondin, and Y. Hébert, "Wide-Area measurement based stabilizing control of large power systems- a decentralized/hierarchical approach," *IEEE Trans. Power Syst.*, vol. 16, no. 1, pp. 136–153, Feb. 2001.

[71] R. Majumder, B. Chaudhuri, and B. C. Pal, "A probabilistic approach to model-based adaptive control for damping of interarea oscillations," *IEEE Trans. Power Syst.*, vol. 20, no. 1, pp. 367-374, Feb. 2005.

[72] H. Ni, G. T. Heydt, and L. Mili, "Power system stability agents using robust wide area control," *IEEE Trans. Power Syst.*, vol. 17, no. 4, pp. 1123–1131, Nov. 2002.

[73] F. Okou, L. A. Dessaint, and O. Akhrif, "Power systems stability enhancement using a wind-area signals based hierarchical controller," *IEEE Trans. Power Syst.*, vol. 20, no. 3, pp. 1465-1477, Aug. 2005.

[74] G. Yu, B. Zhang, H. Xie, C. Wang, "Wide-area measurement-based nonlinear robust control of power system considering signals' delay and incompleteness," in *Proc. 2007 IEEE PES General Meeting*, Tampa, FL, 24-28 June 2007.

[75] S. Ray and G. K. Venayagamoorthy, "Wide-area signal-based optimal neurocontroller for a UPFC," *IEEE Trans. Power Del.*, vol. 23, no. 3, pp. 1597-1605, July 2008.

[76] S. Mohagheghi, G. K. Venayagamoorthy, and R. G. Harley, "Optimal wide area controller and state predictor for a power system," *IEEE Trans. Power Syst.*, vol. 22, no. 2, pp. 693-705, May 2007.

[77] S. Ray, G. K. Venayagamoorthy, B. Chaudhuri, and R. Majumder, "Comparison of adaptive critic-based and classical wide-area controllers for power systems," *IEEE Trans. Syst., Man, Cybern. B, Cybern.*, vol. 38, no. 4, pp. 1002-1007, Aug. 2008.

[78] S. Corsi, M. Pozzi, C. Sabelli, and A. Serrani, "The coordinated automatic voltage control of the Italian transmission grid-part I: reasons of the choice and overview of the consolidated hierarchical system," *IEEE Trans. Power Syst.*, vol. 19, no. 4, pp. 1723-1732, Nov. 2004.

[79] S. Corsi, M. Pozzi, M. Sforna, and G. Dell'Olio, "The coordinated automatic voltage control of the Italian transmission grid-part II: control apparatuses and field performance of the consolidated hierarchical system," *IEEE Trans. Power Syst.*, vol. 19, no. 4, pp. 1733-1741, Nov. 2004.

[80] H. Wang, H. Li, and H. Chen, "Coordinated secondary voltage control to eliminate voltage violations in power system contingencies," *IEEE Trans. Power Syst.*, vol. 18, no. 2, pp. 588-595, May 2003.

[81] J. Wen, Q. Wu, D. Turner, S. Cheng, and J. Fitch, "Optimal coordinated voltage control for power system voltage stability," *IEEE Trans. Power Syst.*, vol. 19, no. 2, pp. 1115-1122, May 2004.

[82] B. Fardanesh, "Future trends in power system control," *IEEE Comput. Appl. Power*, vol. 15, no. 3, pp. 24-31, July 2002.

[83] G. K. Venayagamoorthy, "CAREER: Scalable learning and adaptation with intelligent techniques and neural networks for reconfiguration and survivability of complex systems," NSF CAREER Award # 0348221, Jun. 2004.

[84] J. Momoh, "Towards dynamic stochastic optimal power flow," in *Hanbook of Learning and Approximate Dynamic Programming*, Wiley-IEEE Press, 2004. ISBN-13: 978-0471660545.

[85] P. Werbos, "New directions in ACDs: keys to intelligent control and understanding the brain," in *Proc. Int'l Joint Conf. Neural Networks (IJCNN) 2000*, vol. 3, pp. 61-66, Como, Italy, July 24, 2000.

[86] J. Si, A. Barto, W. Powell, and D. Wunsch, *Hanbook of Learning and Approximate Dynamic Programming*, Wiley-IEEE Press, 2004. ISBN-13: 978-0471660545.

[87] S. Haykin, *Neural Networks: A Comprehensive Foundation*, 2nd ed., Prentice Hall, July 1998. ISBN-13: 978-0132733502.

[88] K. Narendra, "Neural networks for control theory and practice," *Proc. IEEE*, vol. 84, no. 10, pp. 1385-1406, Oct. 1996.

[89] G. K. Venayagamoorthy, R. G. Harley, and D. Wunsch, "Implementation of adaptive critic-based neurocontrollers for turbogenerators in a multimachine power system," *IEEE Trans. Neural Netw.*, vol. 14, no. 5, pp. 1047-1064, Sept. 2003.

[90] "ERCOT 101 for wind generation," Electric Reliability Council of Texas (ERCOT) Nodal Market Training, [Online]. Available: http://nodal.ercot.com/training/courses /nc14.html#materials.

[91] "Section 6: adjustment period and real-time operations," ERCOT Nodal Protocols, Aug. 1, 2010 [Online]. Available: http://www.ercot.com/mktrules/nprotocols/current.

[92] "Spanish royal decree 661/2007," Boletín Oficial del Estado, vol. 126, Ministry of Industry, Tourism and Trade, pp.22846–22886, 2007.

[93] J. R. Abbad, "Electricity market participation of wind farms: the success story of the Spanish pragmatism," *Energy Policy*, vol. 38, no. 7, pp. 3174-3179, July 2010.

[94] A. Fabbri, T. G. San Roman, J. R. Abbad, V. H. Mendez Quezada, "Assessment of the cost associated with wind generation prediction errors in a liberalized electricity market," *IEEE Trans. Power Syst.*, vol. 20, no. 3, pp. 1440-1446, Aug. 2005.

[95] F. Bourry, L. Costa, and G. Kariniotakis, "Risk-based strategies for wind/pumped-hydro coordination under electricity markets," in *Proc. 2009 IEEE Bucharest Power Tech Conf.*, Bucharest, Romania, June 28 - July 2, 2009.

[96] G. Bathurst, J. Weatherill, G. Strbac, "Trading wind generation in short term energy markets," *IEEE Trans. Power Syst.*, vol 17, no. 3, pp. 782-789, Aug. 2002.

[97] J. Matevosyan and L. Söder, "Minimization of imbalance cost trading wind power on the short-term power market," *IEEE Trans. Power Syst.*, vol. 21, no. 3, pp. 1396-1404, Aug. 2006.

[98] P. Pinson, C. Chevallier, G. Kariniotakis, "Trading wind generation from short-term probabilistic forecasts of wind power", *IEEE Trans. Power Syst.*, vol. 22, no. 3, pp. 1148-1156, Aug. 2007.

[99] J. Usaola, J. Angarita, "Bidding wind energy under uncertainty," in *Proc. of 2007 Int'l Conf. Clean Electrical Power (ICCEP)*, Capri, Italy, May 2007.

[100] J. Usaola and M. Angeles Moreno, "Optimal bidding of wind energy in intraday markets," in *Proc. 6th Int'l Conf. European Energy Market (EEM) 2009*, Leuven, Belgium, May 2009.

[101] Y. Xue, B. Venkatesh, and L. Chang, "Bidding wind power in short-term electricity market based on multiple-objective fuzzy optimization," in *Proc. Canadian Conf. Electrical and Computer Engineering (CCECE) 2008*, Niagara Falls, ON, Canada, May 2008.

[102] A. Botterud, J. Wang, R.J. Bessa, H. Keko, and V. Miranda, "Risk management and optimal bidding for a wind power producer," in *Proc. 2010 IEEE PES General Meeting*, Minneapolis, MN, July 25-29, 2010.

[103] J. Liang, W. Qiao, and R. G. Harley, "Feed-forward transient current control for low-voltage ride-through enhancement of DFIG wind turbines," *IEEE Trans. Energy Convers.*, vol. 25, no. 3, pp. 836-843, Sept. 2010.

[104] J. Liang and R. G. Harley, "Feed-forward transient compensation control for DFIG wind generators during both balanced and unbalanced grid disturbances," in *Proc. 2011 IEEE Energy Conversion Congress and Exposition (ECCE)*, Phoenix, AZ, USA, Sept. 17-22, 2011.

[105] M. Mohseni, S. M. Islam, and M. A. S. Masoum, "Impacts of symmetrical and asymmetrical voltage sags on DFIG-based wind turbines considering phase-angle jump, voltage recovery, and sag parameters," *IEEE Trans. Power Electron.*, vol. 26, no. 5, pp. 1587-1598, May 2011.

[106] S.-K.Chung, "Phase-locked loop for grid-connected three-phase power conversion systems," *IEE Proc-Electr. Power Appl.*, vol. 147, no. 3, pp. 213-219, May 2000.

[107] F. D. Freijedo, A. G. Yepes, O. Lopez, A. Vidal, and J. Doval-Gandoy, "Three-phase PLLs with fast postfault retracking and steady-state rejection of voltage unbalance and harmonics by means of lead compensation," *IEEE Trans. Power Electron.*, vol. 26, no. 1, pp. 85-97, Jan. 2011.

[108] M. García-Gracia, M. Paz Comech, J. Sallán, D. López-Andía, O. Alonso, "Voltage dip generator for wind energy systems up to 5 MW," *Applied Energy*, vol. 86, no. 4, pp. 565-574, Apr. 2009.

[109] M. Liserre, R. Teodorescu, and F. Blaabjerg, "Multiple harmonics control for three-phase grid converter systems with the use of PI–RES current controller in a rotating frame," *IEEE Trans. Power Electron.*, vol. 21, no. 3, pp. 1–6, May 2006.

[110] M. H. Bollen, Understanding Power Quality Problems: Voltage Sags and Interruptions, Wiley - IEEE Press, 1999. ISBN-13: 978-0780347137.

[111] D. Prokhorov, G. Puskorius, and L. Feldkamp, "Dynamical recurrent networks in control," in *A Field Guide to Dynamical Recurrent Networks*, Wiley-IEEE Press, 2001. ISBN-13: 978-0780353695.

[112] J. Liang, J. Dai, G. Venayagamoorthy, and R. Harley, "Dynamic system eigenvalue extraction using a linear echo state network for small-signal stability analysis – a novel application," in *Proc. IEEE Int'l Joint Conf. Neural Networks (IJCNN) 2010*, Barcelona, Spain, 18-23 July 2010.

[113] P. Werbos, "Backpropagation through time: what it does and how to do it," *Proc. IEEE*, vol. 78, no. 10, pp. 1550-1560, Oct. 1990.

[114] S. Jiang, U. D. Annakkage, and A. M. Gole, "A platform for validation of FACTS models," *IEEE Trans. Power Del.*, vol. 21, no. 1, pp. 484-491, Jan. 2006.

[115] B. Kirby and M. Milligan, "A method and case study for estimating the ramping capacity of a control area or balancing authority and implications for moderate or high wind penetration," NREL report, NREL/CP-500-38153, May 2005.

[116] "Load representation for dynamic performance analysis," IEEE Task Force on Load Representation for Dynamic Performance, *IEEE Trans. Power Syst.*, vol. 8, no. 2, pp. 472-482, May 1993.

[117] R. Zimmerman, "MATPOWER user's manual," May 2010, [Online]. Available: http://www.pserc.cornell.edu/matpower/manual.pdf.

[118] J. Liang, R. G. Harley, and G. K. Venayagamoorthy, "Wide-area measurement based dynamic stochastic optimal power flow control for smart grids with high variability and uncertainty," *IEEE Trans. Smart Grid*, vol. 3, no. 1, pp. 59-69, Mar. 2012.

[119] J. Liang, R. G. Harley, and G. K. Venayagamoorthy, "Adaptive critic design based dynamic optimal power flow controller for a smart grid," in *proc. 2011 IEEE Symposium Series on Computational Intelligence – Computation Intelligence Applications in Smart Grid (CIASG)*, Paris, France, Apr. 2011.

[120] B. Pal and B. Chaudhuri, *Robust Control in Power Systems*, Springer, June 2005. ISBN-13: 978-0387259499.

[121] G. Rogers, *Power System Oscillations*, Springer, Dec. 1999. ISBN-13: 978-0792377122.

[122] P. Anderson and A. Fouad, *Power System Control and Stability*, 2nd ed., Piscataway, N.J.: IEEE Press, 2003. ISBN-13: 978-0471238621.

[123] M. Bazaraa, H. Sherali, and C. Shetty, *Nonlinear Programming: Theory and Algorithms*, Wiley-Interscience, 3rd ed., May 5, 2006. ISBN-13: 978-0471486008.

[124] J. Liang, S. Grijalva, and R. G. Harley, "Increased wind revenue and system security by trading wind power in energy and regulation reserve markets," *IEEE Trans. Sustainable Energy*, vol. 2, no. 3, pp. 340-347, July 2011.

[125] "Eastern wind integration and transmission study (EWITS)," National Renewable Energy Laboratory, [Online]. Available: http://www.nrel.gov/wind/systemsintegration/ewits.html.

[126] S. Bofinger, A. Luig, and H. Beyer, "Qualification of wind power forecasts," in *Proc. Global Wind Power Conf.*, Paris, France, Apr. 2–5, 2002.

[127] J. F. Restrepo and F. D. Galiana, "Unit commitment with primary frequency regulation constraints," *IEEE Trans. Power Syst.*, vol. 20, no. 4, pp. 1836-1842, Nov. 2005.

[128] Market Information, Electric Reliability Council of Texas (ERCOT), [Online]. Available: http://ercot.com/mktinfo/.

[129] MOSEK optimization software, [Online]. Available: http://www.mosek.com/.

[130] T. Wu, M. Rothleder, Z. Alaywan, and A. D. Papalexopoulos, "Pricing energy and ancillary services in integrated market systems by an optimal power flow," *IEEE Trans. Power Syst.*, vol. 19, no. 1, pp. 339-347, Feb. 2004.

[131] J. Kolen, S. Kremer, *A Field Guide to Dynamical Recurrent Networks*, Wiley-IEEE Press, 2001. ISBN-13: 978-0780353695.

VITA

Jiaqi Liang was born in Guangdong, China in 1984. He obtained his Bachelor's Degree in Electrical Engineering from Tsinghua University in Beijing, China in 2007. He then joined Georgia Institute of Technology in Atlanta, GA, USA in August 2007, where he obtained his Master's Degree in Electrical Engineering in 2009 and has been working towards his Ph.D. degree.

After he joined Georgia Tech, Jiaqi has been a graduate research assistant working on electric machine dynamics and control, power systems operation and control, and intelligent control applied to power systems. During his study at Georgia Tech, he lectured various undergraduate and graduate classes in electric machines, energy conversion systems, power system analysis, intelligent control, and applications of computational intelligence in power systems. He worked as a mentor for undergraduate research in the Opportunity Research Scholars program in the School of Electrical and Computer Engineering at Georgia Tech between 2009 and 2011. In summer 2008, he worked as an R&D intern in the motor control design group at Phoenix International-A John Deer Company.

Jiaqi Liang is the recipient of the Colonel Oscar P. Cleaver Award for the outstanding graduate student in the School of Electrical and Computer Engineering at Georgia Tech in 2007.